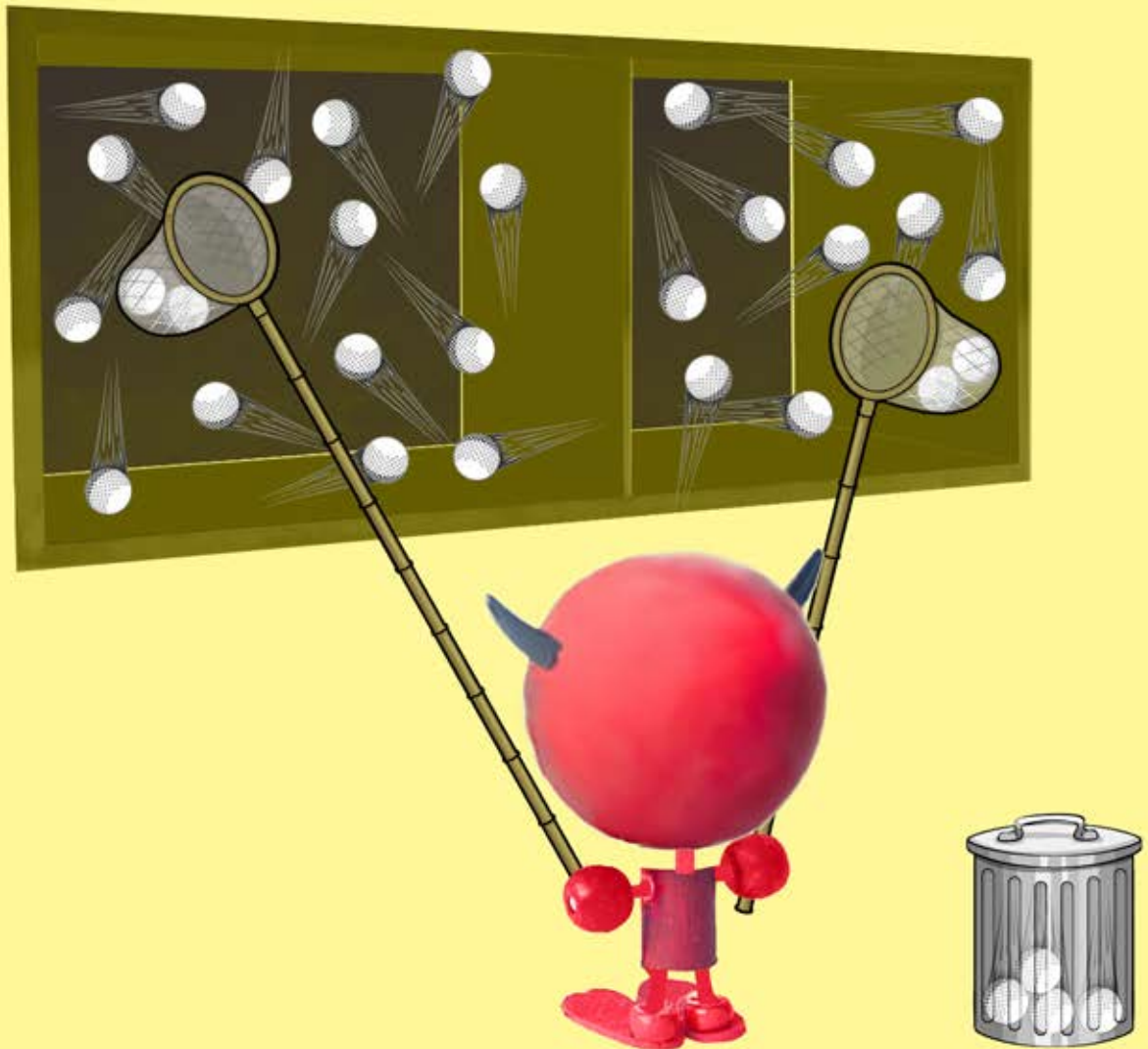


Hardware-Efficient Autonomous Quantum Error Correction



Shantanu Mundhada

Dissertation Director: Prof. Michel H. Devoret

Abstract

Hardware-Efficient Autonomous Quantum Error Correction

Shantanu Mundhada

2020

Quantum error correction (QEC) is a crucial area of research since the susceptibility of quantum information to noise prevents the implementation of useful quantum algorithms. Standard QEC protocols, however, come with an overwhelming hardware and software overhead. For superconducting quantum circuits, it is possible to minimize this overhead by hardware-efficient encoding which takes advantage of the infinite dimensional Hilbert spaces offered by high-Q harmonic oscillators. Error mitigation using autonomous feedback further increases the hardware efficiency. Such autonomous feedback requires specific highly nonlinear interactions between various modes of a quantum system. How does one engineer such interactions? In this thesis, we explore the Hamiltonian engineering techniques geared towards realizing the required interactions for a promising class of hardware efficient QEC codes, namely the Schrödinger cat codes.

In particular, we focus on the four-component Schrödinger cat code, which allows for first-order protection against all error channels of a harmonic oscillator. Autonomously stabilizing the decoherence free subspace for this code requires the harmonic oscillator to gain and lose photons in sets of four, that is, a four-photon driven-dissipative process. We propose a scheme for engineering such a process through a Raman-assisted cascading of readily available four-wave mixing interactions, and experimentally demonstrate the feasibility of this cascading. Furthermore, an improved four-wave mixing device that cancels unwanted, always-on interactions is studied. We also propose an implementation of a new error-correction code, the pair-cat code, which offers autonomous protection against all the error channels using low-order parametric interactions.

Hardware-Efficient Autonomous Quantum Error Correction

A Dissertation
Presented to the Faculty of the Graduate School
of
Yale University
in Candidacy for the Degree of
Doctor of Philosophy

by
Shantanu Mundhada

Dissertation Director: Prof. Michel H. Devoret

May 2020

© 2020 by Shantanu Mundhada
All rights reserved.

Contents

Contents	iii
List of Figures	vi
List of Tables	viii
List of Symbols	ix
Acknowledgments	xiii
0 Thesis overview	1
0.1 Motivation and central question	1
0.2 Outline of the chapters to come	4
1 Preliminary concepts	7
1.1 Notation for describing quantum system	7
1.1.1 Isolated quantum systems	7
1.1.2 Open quantum systems	9
1.1.3 Time evolution in presence of decoherence	11
1.2 Basic quantum systems	13
1.2.1 Spin-1/2 Qubits	13
1.2.2 Quantum harmonic oscillators	19
1.3 Summary and prelude to the next chapter	27
2 Introduction to quantum error correction	29
2.1 Basic principles	30
2.1.1 The Knill-Laflamme conditions	31
2.1.2 Examples of QEC codes	34
2.1.3 Failure modes of QEC and fault tolerance	40
2.2 Hardware efficient encoding	43
2.3 Autonomous Quantum Error Correction (AQEC)	45
2.4 Summary and prelude to the next chapter	52

3	Cat codes: Hardware efficiency and autonomous error correction	54
3.1	The cat codes	55
3.1.1	Two-component cats	56
3.1.2	Four-component cats and protection against photon loss	60
3.1.3	Effect of energy relaxation and dephasing	67
3.2	Autonomously stabilizing coherent state manifolds	70
3.2.1	Single-photon driven-dissipative process	72
3.2.2	Multi-photon driven-dissipative processes	74
3.3	Fault tolerance and cat codes	78
3.4	Summary and prelude to the next chapter	79
4	Engineering nonlinear driven-dissipative processes	81
4.1	Nonlinearity in cQED	82
4.1.1	Josephson junction and transmon	82
4.1.2	Transmon-cavity system	87
4.1.3	Modeling off-resonant drives and dissipation	93
4.2	Engineering two-photon drive and dissipation	97
4.2.1	Effective equation of motion of the oscillator	98
4.3	Engineering four-photon driven-dissipative process	103
4.3.1	Four-photon exchange using six-wave mixing	103
4.3.2	Four-photon exchange with Raman-assisted cascading	106
4.3.3	Including dissipation on the transmon	114
4.3.4	Required pump strengths to overcome Cross-Kerr	120
4.4	Summary and prelude to the next chapter	121
5	Demonstration of a cascaded process	123
5.1	Theory of $ f, 0\rangle \leftrightarrow g, 4\rangle$ transition	125
5.2	Experimental setup	129
5.3	System tuneup	134
5.3.1	Locating $ f, 0\rangle \leftrightarrow g, 4\rangle$ transition	134
5.3.2	Pump-strength calibration	136
5.4	Characterization of four-photon exchange	138
5.4.1	Partial tomography and comparison with simulations	139
5.4.2	Coherence of the oscillations	141
5.5	Summary and prelude to the next chapter	143
6	Cross-Kerr-free four-wave mixing	145
6.1	Required circuit elements	146
6.1.1	SQUID	147
6.1.2	SNAIL	149
6.1.3	Effect of series linear inductance	154
6.2	Circuit design	157
6.2.1	Formal analysis	161

6.2.2	Permissible parameter space	165
6.2.3	Numerical simulations	167
6.3	Experimental design	172
6.3.1	Magnetic field in 3D aluminum cavities	172
6.3.2	Enclosure for the cancellation circuit	177
6.4	Preliminary experimental results	178
6.5	Comparison with a different implementation	184
6.6	Summary and prelude to the next chapter	188
7	Fully autonomous QEC with pair cat code	191
7.1	Introduction to pair-cat states	193
7.1.1	Pair-coherent states	193
7.1.2	Pair-cat states and information storage	196
7.1.3	Tomography and representation	202
7.1.4	Autonomous protection of pair-cats	205
7.2	Engineering fully autonomous protection	208
7.2.1	Driven-dissipative stabilization	211
7.2.2	Correction against single-mode photon losses	215
7.3	Summary and prelude to the next chapter	223
8	Conclusion and perspective	225
8.1	Conclusion	225
8.2	Perspective	227
A	Second order RWA in presence of dissipation	229
B	Validity of adiabatic elimination	234
	Bibliography	237

List of Figures

1.1	Bloch sphere representation of a qubit	13
1.2	Important quantum gates	15
1.3	Common error channels for qubits	17
1.4	Quantum harmonic oscillator	19
1.5	Coherent state of a quantum harmonic oscillator	21
1.6	Examples of Wigner functions	23
1.7	Common error channels for harmonic oscillators	25
2.1	Three qubit bit flip code	34
2.2	Error detection and correction for the Steane code	39
2.3	Failure modes for Steane code	41
2.4	Examples of autonomous feedback in classical systems	47
2.5	Discrete and continuous autonomous feedback for bit-flip code	48
3.1	Two-component cat states	56
3.2	Information storage using two-component cat states	58
3.3	Four-component cat states	60
3.4	Protection against photon loss errors	62
3.5	Pulse sequence for measuring photon-number parity	65
3.6	Effect of photon loss, energy relaxation and dephasing errors	70
3.7	Single-photon driven-dissipative process and steady state	71
3.8	Two-photon driven-dissipative process and steady states	76
4.1	Josephson junction and transmon	83
4.2	Transmon coupled to a harmonic oscillator	88
4.3	Implementation of two-photon driven-dissipative process	99
4.4	Four-photon exchange with six-wave mixing	104
4.5	Four-photon driven-dissipative process with Raman-assisted cascading	107
4.6	Simulations of $ g, 4\rangle \leftrightarrow f, 0\rangle$ oscillations	113
4.7	Engineered vs ordinary f to g dissipation	115
4.8	Engineered vs ordinary f to g dissipation	118
4.9	Effect of stronger χ_{ab} on the stabilization	121
5.1	Intuitive picture of the demonstrated process	124

5.2	Design and pictures of the experimental system	128
5.3	Wiring diagram of the measurement setup	132
5.4	Locating $ f, 0\rangle \leftrightarrow g, 4\rangle$ oscillations	135
5.5	Stark-shift vs pump strength for conversion transmon	137
5.6	Partial tomography and comparison with numerical simulations	140
5.7	Pulse sequence for conditional Wigner tomography	142
5.8	Conditional Wigner tomography of $(f, 0\rangle + g, 4\rangle)/\sqrt{2}$	143
6.1	SQUID circuit and amplitude of fourth order nonlinearity	147
6.2	SNAIL circuit and amplitude of fourth order nonlinearity	150
6.3	SNAIL inserted in a transmon like circuit	153
6.4	Design of the cancellation circuit	158
6.5	Permissible values of α_{sn} for achieving cross-Kerr cancellation	166
6.6	Bare frequencies of the modes as function of flux	169
6.7	Numerical diagonalization of the cancellation circuit	171
6.8	Magnetic field in 3D aluminum enclosure	173
6.9	Enclosure for the cancellation circuit	177
6.10	Readout spectroscopy and the two-tone spectroscopy.	179
6.11	Spectroscopy of the readout resonator as function of flux	180
6.12	Two tone spectroscopy with SNAIL at half flux	181
6.13	Phase response amplitude as function of external flux	183
6.14	Comparison with another implementation	185
7.1	Information storage using pair-cat states	197
7.2	$\langle 1_L \hat{a}_1^\dagger \hat{a}_1 1_L \rangle - \langle 0_L \hat{a}_1^\dagger \hat{a}_1 0_L \rangle$ as function of γ and ∂	201
7.3	γ -plane Wigner functions	204
7.4	Proposed experimental setup for implementing a pair-cat qubit	209
7.5	Engineering driven-dissipative process for stabilizing pair-cat states	210
7.6	Engineering positive and negative cross-Kerr	214
7.7	Continuous correction against photon loss errors	220
B.1	Rate of stabilization vs strength of transmon dissipation	235

List of Tables

2.1	Error syndrome of the bit-flip code	36
5.1	System parameters for $ f, 0\rangle \leftrightarrow g, 4\rangle$ oscillations experiment	131
6.1	Simulation parameters for cancellation circuit	168
7.1	Proposed interaction strengths for implementing pair-cat code	222

List of symbols

Constants

h	Planck's constant
\hbar	Reduced Planck's constant
e	Electron charge
Φ_0	Magnetic flux quantum ($\Phi_0 = h/2e$)
ϕ_0	Reduced flux quantum ($\phi_0 = \Phi_0/2\pi$)

Qubits and operations on qubits

$\hat{\sigma}_x, \hat{\sigma}_y, \hat{\sigma}_z$	Pauli operators for spin 1/2 system
$\hat{\sigma}_+, \hat{\sigma}_-$	Raising and lowering operators for spin 1/2 system
$\mathbf{X}_\varphi, \mathbf{Y}_\varphi, \mathbf{Z}_\varphi$	Rotation of a qubit around X, Y, Z axis by angle φ respectively
$\hat{\sigma}_{jk}$	$\hat{\sigma}_{jk} = k\rangle\langle j $

Superconducting Circuits

\hat{H}	Hamiltonian of a quantum circuit
$\hat{Q}, \hat{\Phi}$	Charge and flux operators for superconducting circuits $[\hat{\Phi}, \hat{Q}] = i\hbar$

$\hat{\varphi}$	Superconducting phase operator across an element ($\hat{\varphi} = \hat{\Phi}/\phi_0$)
\hat{N}	Cooper pair number operator (Conjugate of $\hat{\varphi}$)
Z_0	Characteristic impedance of an L-C circuit ($Z_0 = \sqrt{L/C}$)
Φ_{ZPF}	Zero point fluctuations of the flux ($\Phi_{\text{ZPF}} = \sqrt{\hbar Z_0/2}$)
φ_{ZPF}	Zero point fluctuation of superconducting phase ($\varphi_{\text{ZPF}} = \Phi_{\text{ZPF}}/\phi_0$)
Q_{ZPF}	Zero point fluctuations of the charge ($Q_{\text{ZPF}} = \sqrt{\hbar/2Z_0}$)
E_J	Josephson energy
L_J	Josephson inductance (ϕ_0^2/E_J)
E_C	Charging energy of a capacitor ($E_C = e^2/2C$, $C \Rightarrow$ Capacitance)
Φ_{ext}^k	External flux through loop k
$c_{2,k}, c_{3,k}, \dots$	Constants in Taylor-expansion of potential of an inductive circuit element k
\hat{a}^\dagger, \hat{a}	Raising and lowering operators for harmonic oscillator mode a
\hat{b}^\dagger, \hat{b}	Raising and lowering operators for a transmon mode b
\hat{r}^\dagger, \hat{r}	Raising and lowering operators for a low-Q resonator mode r
\hat{n}	Photon number operator ($\hat{n} = \hat{a}^\dagger \hat{a}$)
$\hat{D}(\alpha)$	Displacement operator ($\hat{D}(\alpha) = e^{\alpha \hat{a}^\dagger - \alpha^* \hat{a}}$, $\alpha \in \mathbb{C}$)
$\hat{\Pi}$	Photon number parity operator $\hat{\Pi} = \exp(i\pi \hat{n})$
$\sqrt{\hat{\Pi}}$	Super parity operator
$\hat{\Pi}_{\text{joint}}$	Joint parity operator ($\hat{\Pi}_{\text{joint}} = \exp i\pi(\hat{n}_1 + \hat{n}_2)$)
$\hat{\partial}$	Photon number difference operator ($\hat{\partial} = \hat{a}_2^\dagger \hat{a}_2 - \hat{a}_1^\dagger \hat{a}_1$)
T_{parity}	Time for mapping parity of a cavity on a qubit $T_{\text{parity}} = \pi/\chi_{aq}$
ω_k	Angular frequency of mode k
$\tilde{\omega}_k$	Renormalized and Stark-shifted frequency of mode k
χ_{jk}	Cross-Kerr between mode j and mode k
χ_{kk}	Self-Kerr of mode k

Quantum states

ρ	Density matrix of a system
$\text{Tr}(\hat{k})$	Trace of operator \hat{k}
$\text{Tr}_j(\hat{k})$	Partial trace of operator \hat{k} over Hilbert space of system j
$\text{Tr}(\rho^2)$	Purity of a quantum system
$ 0\rangle, 1\rangle$	States of a two level system (qubit)
$ g\rangle, e\rangle, f\rangle$	Ground, first excited and second excited states of a transmon
$ n\rangle$	Fock states of a harmonic oscillator ($n \in \mathbb{W}$). Not to be confused with states of a qubit.
$ 0_L\rangle, 1_L\rangle$	States of a logical qubit as indicated by subscript L
$ \mathcal{C}_\alpha^{(m \bmod p)}\rangle$	$m \bmod p$ cat state
$ \mathcal{Y}_\alpha^{(m \pm in \bmod p)}\rangle$	$ \mathcal{C}_\alpha^{(m \bmod p)}\rangle + i \mathcal{C}_\alpha^{(n \bmod p)}\rangle$
$ \gamma_\partial\rangle$	Pair-coherent state with $\hat{a}_1\hat{a}_2 \gamma_\partial\rangle = \gamma^2 \gamma_\partial\rangle$ and $\hat{\partial} \gamma_\partial\rangle = \partial \gamma_\partial\rangle$
$ \mathcal{P}_{\gamma,\partial}^{(k \bmod 2)}\rangle$	Pair-cat states

Quantum errors

$\mathcal{D}[\hat{L}_k]$	Lindblad dissipator with a jump operator \hat{L}_k
\mathcal{M}	Kraus-map describing a process on a quantum systems
\hat{M}_k	Kraus-operators corresponding to a Kraus-map \mathcal{M}
$\Gamma_\downarrow, T_\downarrow$	Amplitude damping rate and time for a qubit ($\Gamma_\downarrow = 1/T_\downarrow$)
$\Gamma_\uparrow, T_\uparrow$	Heating rate and time for a qubit ($\Gamma_\uparrow = 1/T_\uparrow$)
Γ_1, T_1	Rate and time of relaxation or equilibration for a qubit ($\Gamma_1 = 1/T_1 = \Gamma_\downarrow + \Gamma_\uparrow$)
Γ_ϕ, T_ϕ	Pure dephasing rate and time of a mode ($\Gamma_\phi = 1/T_\phi$)
Γ_2, T_2	Dephasing rate and time of a mode ($\Gamma_2 = 1/T_2 = \Gamma_1/2 + \Gamma_\phi$)

$\Gamma_{\text{flip}}, T_{\text{flip}}$	Bit-flip rate and time
$\kappa_{n\text{ph}}$	n -photon dissipation rate for a harmonic oscillator
κ_{ϕ}	Dephasing rate for a harmonic oscillator
κ_{\uparrow}	Heating rate for a harmonic oscillator

Acronyms and abbreviations

QEC	Quantum Error Correction
AQEC	Autonomous Quantum Error Correction
QIP	Quantum Information Processing
NISQ	Noisy Intermediate-Scale Quantum (devices / technology)
cQED	Circuit Quantum ElectroDynamics
BBQ	Black-Box Quantization
RWA	Rotating Wave Approximation
Qubit	Quantum bit
Qumode	Quantum mode
CMOS	Complementary Metal-Oxide Semiconductor
SQUID	Superconducting Quantum Interference Device
SNAIL	Superconducting Nonlinear Asymmetric Inductive eLement
SPAM	State Preparation and Measurement Errors
FTQC	Fault-Tolerant Quantum Computation
Subscript sq	A quantity relating to a SQUID
Subscript sn	A quantity relating to a SNAIL
i.e.	id est (meaning ‘that is’)

Acknowledgments

There is a proverb in Africa which goes as, "It takes a village to raise a child". That couldn't have been more true in case of a graduate student like myself. Over the period of my PhD, I have had a pleasure to interact with and learn from many professors, post-docs and colleagues at Yale University. They have played a major role in my development as a physicist and shaped my understanding of the subject matter presented in this thesis. Although it is impossible to properly acknowledge all of them, in this section I briefly thank the people with whom I have worked closely.

First and foremost, I would like to thank my advisor Michel Devoret for his guidance, support and encouragement over the past six years. Michel's deep understanding of physics, constant curiosity and excellent mentorship have made for a wonderful PhD experience. I will be eternally grateful towards him for providing me the opportunity to work on these very interesting topics, and for allowing me the freedom to explore and come up with independent ideas. Michel's professional skills are only exceeded by his kindness. He supported me through all the ups and downs of the PhD life and was always very understanding. I hope in the future I can emulate him as a scientist and as a person.

I would also like to thank my thesis committee members: Steven (Steve) Girvin, Peter Rakich and Robert (Rob) Schoelkopf. I had a pleasure of working directly with Steve during an undergraduate internship. He introduced me to the world of circuit quantum electrodynamics. The concepts taught by him all those years back have been re-applied

in many different situations throughout my work. Although, I did not collaborate as closely with Peter and Rob, I had many opportunities to have very fruitful discussions with them. Every such discussion made me aware of different ideas and perspectives, and was always very educational.

Other professors at Yale have also helped me tremendously during the course of my PhD. Especially Mazyar Mirrahimi and Liang Jiang have made major contribution to the work presented in this thesis. The theoretical calculations for Raman assisted four-photon exchange technique were developed under the guidance of Mazyar while I was visiting him at INRIA, Paris. Liang played an important role in the development of the pair-cat codes which is essentially the punchline of this thesis. In addition, I will like to extend a special thanks to Luigi Frunzio who not only maintained the fabrication facilities but also kept up the lab morale with his jovial nature, booming voice and a constant smile. Moreover, he has made a direct contribution to this thesis by reading every chapter and suggesting important corrections.

Over the course of my PhD I worked closely with many postdocs. Especially Shyam Shankar, who acted as my mentor throughout the PhD program, has a huge contribution to my development as an experimental physicist. I hope in the future I can adopt the methodical and thorough approach towards science that Shyam epitomizes. In addition Alexander Grimm, Michael Hatridge, Zaki Leghtas, Shruti Puri and Ioannis Tsioutasios are the other post docs at Yale with whom I have worked closely. Each of them, with their different styles and approaches to science, shaped my understanding of physics and I will be eternally grateful to them. Especially Alexander Grimm has collaborated with me on virtually all the work presented in this thesis. I will also like to thank Benjamin Chapman, Nicolas Didier, Philippe Campagne-Ibarq, Valla Fatemi, Angela Kou, Gijs de Lange, Gangqiang Liu, Ioan Pop and Serge Rosenblum for all the great discussions we have had.

Many fellow graduate students have also contributed to the ideas presented in this thesis. This includes: Victor Albert, Nick Frattini, Akshay Koottandavida, Zlatko Minev, Philip Reinhold, Vladimir Sivak, Katrina Sliwa, Steven Touzard, Jaya Venkatraman and Uri Vool. Similarly, Christopher Axline, Luke Burkhart, Alec Eickbusch, Max Hays, Yehan Liu, Anirudh Narla, Kyungjoo Noh, Alex Read, Kyle Serniak, Clarke Smith, Zhixin Wang, Xu Xiao, Evan Zalys-Geller have also helped and supported me throughout my PhD career. I will be forever grateful towards all of them.

Finally I will like to thank my parents Omprakash Mundhada and Shubhangi Mundhada for guiding and encouraging me throughout my life, my elder brother Rohit Mundhada for always setting a great example for me to follow, and lovely wife Kanu Shree Maheshwari for firmly standing with me through the final leg of my PhD. I couldn't have made it this far without their constant support and understanding.

Chapter 0

Thesis overview

The goal of this chapter is to state and explain the central problem that we will be addressing in this thesis, and to provide a guide to how we further generalize as well as answer this problem. We motivate and phrase the central question of the thesis in the next section. This is followed by a chapter wise outline of the thesis which indicates how all the aspects of the question are addressed and answered.

0.1 Motivation and central question

We are witnessing, at the time of this writing, the realizations of noisy intermediate scale quantum (NISQ) computers, with 20 to 100 noisy qubits. Although progress is being made with proof of principle demonstrations of quantum algorithms [Kandala *et al.*, 2017, Nam *et al.*, 2019], quantum simulations [Wang *et al.*, 2019], and so-called quantum supremacy [Preskill, 2012, Arute *et al.*, 2019], it is unclear whether NISQ devices will have any practical applications [Preskill, 2018]. In fact, most quantum algorithms are expected to provide little, or no quantum advantage, due to the errors plaguing these early implementations. Therefore, in order to access the vast computational power afforded by

quantum information processing (QIP), it is imperative to protect the calculations against these errors.

The efforts for addressing quantum errors, are focused on both preventive and corrective strategies. Error prevention is accomplished by reducing the noise acting on a quantum system or by reducing the susceptibility of the system to the noise. So far, especially in the case of superconducting circuits, noise insensitive qubit designs have been the major driving force behind the increase in qubit lifetimes. The evolution of the transmon from the Cooper pair box is a great example of this accomplishment [Koch *et al.*, 2007]. Decoupling further from noisy elements by using 3D transmons [Paik *et al.*, 2011] demonstrated a major leap in coherence times. Improved qubit designs like fluxonium [Manucharyan *et al.*, 2009], heavy-fluxonium [Earnest *et al.*, 2018], $0 - \pi$ qubit [Brooks *et al.*, 2013, Gyenis *et al.*, 2019] are attempts at further increasing qubit coherence through particular circuit design. However, such qubit designs often come with less controllability, and trade insensitivity to one noise channel for a heightened sensitivity to another. Moreover, the error prevention strategies do not account for imperfect quantum gates which themselves add errors. Therefore, it is equally important to employ corrective strategies for combating quantum errors. Hence, quantum error correction (QEC) has emerged as an essential building block for robust fault-tolerant QIP.

A QEC protocol has three essential requirements: (i) redundant storage of information in higher-dimensional Hilbert space, (ii) error detection, and (iii) error correction. The majority of QEC protocols employ multiple finite dimensional systems to store information, and a measurement based classical feedback to detect and correct for the errors. Such a strategy invariably leads to significant hardware and software overheads, thus limiting the scalability of quantum computers. Furthermore, the permissible error threshold on individual components used for these traditional protocols are typically very low, thus making the implementation of fault-tolerant quantum computation a formidable engi-

neering challenge.

It is possible to greatly reduce the hardware overhead associated with multiple quantum systems, by encoding information in infinite dimensional Hilbert spaces. This is called hardware efficient encoding. In the case of superconducting circuits, such Hilbert spaces are readily available through the use of high-Q cavities to engineer long-lived quantum harmonic oscillators. Storing information with the help of these oscillators has multiple advantages. Firstly, the lifetime of these high-Q cavities is typically an order of magnitude higher than the transmon qubits. Second, these cavities have a single dominant error channel called amplitude-damping which causes the photons in the cavity to leak to the environment. Furthermore, it is possible to store an entire logical qubit with the help of a single cavity. Although, such hardware efficient error correction also requires ancillary nonlinear systems, like transmons, for control and error syndrome measurements, the total hardware complexity is a mere fraction of the traditional QEC codes.

The hardware overhead can be further mitigated by utilizing autonomous feed mechanisms that do not require any real-time decision making. These feedback mechanisms continuously correct against errors on the system and only require ‘always-on’ continuous wave (CW) tones which, once tuned, keep protecting the system from errors. Moreover, these protocols are typically insensitive to the errors on the ancillary systems including the state preparation and measurement (SPAM) errors. Therefore autonomous feedback is a desirable component of a QEC system.

On the other hand, the interactions required for engineering autonomous feedback mechanisms tend to be highly nonlinear and in general, are not available naturally. **Is it possible to engineer these interactions? More generally, is it possible to engineer fully autonomous protection of a hardware efficient logical qubit?** Through the work in this thesis, we propose Hamiltonian engineering techniques for engineering such autonomous protection and experimentally demonstrate the realization of these

techniques. We also engineer a novel superconducting circuit which suppresses the spurious interactions in our Hamiltonian while preserving the useful terms. The next section consists of a chapter by chapter breakdown of how we further develop and address the central goal of building an autonomous logical qubit.

0.2 Outline of the chapters to come

We begin our discussion in the next chapter (Ch. 1) by introducing some preliminary concepts. The first half of the chapter develops the notation for describing open quantum systems with an emphasis on the density matrix representation, Lindblad master equation and Kraus maps. The next half introduces two basic quantum systems, (i) the spin-1/2 qubits and (ii) the quantum harmonic oscillator. We put a special emphasis on the description of the errors such as, photon loss and dephasing errors, which affect these systems. A reader, familiar with these concepts, should feel free to skip to the next chapters, while keeping in mind to check back in case of an unfamiliar notation.

Ch. 2 provides a brief introduction to QEC with a special focus on the Knill-Laflamme conditions, the necessary and sufficient conditions for protection against a set of errors. We also give examples of some traditional error correction schemes and describe fault tolerance in this context. This naturally leads into a discussion of hardware-efficient and autonomous QEC. We elaborate these concepts in some detail and leave the discussion of the particular codes of interest, the cat-codes, to the following chapter.

Ch. 3 discusses the cat codes in detail. We first explain how information can be stored and protected from photon loss errors with the help of these codes. Such protection has been implemented elsewhere, using measurement-based feedback. We go beyond photon loss errors and focus on the stabilization these codes against the dephasing-like error channels using multi-photon driven-dissipative processes. Such protection is autonomous

and continuous. Therefore, these multi-photon driven-dissipative processes are the main focus of this thesis and the following three chapters are geared towards developing the Hamiltonian engineering techniques for realizing these highly nonlinear processes. The continuous protection against photon loss, on the other hand, requires a more complicated nonlinearity. We propose an alternate code to step around this issue in a later chapter.

Ch. 4 dives into the theoretical considerations behind implementation of the multi-photon driven-dissipative processes in the realm of superconducting circuits. We begin with an introduction to Josephson junctions and transmons which provide the much needed nonlinearity for implementing the required interaction. The Hamiltonian of the joint transmon plus harmonic oscillator system, as well a modeling of off-resonant drives is also elaborated here. This is followed by an explanation of how the four-wave mixing property of the Josephson junctions has been utilized for implementing two-photon driven-dissipative processes. However, for building the crucial four-photon driven-dissipative process, the required higher-order nonlinearity turns out to be very weak. We propose a scheme of cascading two four-wave mixing processes to obtain the required nonlinearity and show how such a process could be used for implementing four-photon drive and dissipation. This concept of cascading is very general and can be used as a starting point for generating many other useful nonlinear interactions.

In Ch. 5 we focus on the experimental demonstration of the cascading technique. This is achieved by inducing cascaded oscillations between the $|f, 0\rangle$ and $|g, 4\rangle$ states of the joint transmon-cavity system. Here f is the second excited state and g is the ground state of the transmon. The chapter details experimental design, system tune up and tomographic characterization of the oscillations. We also emphasize the limitations of the experimental system which prevent the stabilization of cat-states. Lifting these limitations is the goal of the next chapter.

Ch. 6 focuses on engineering a better four-wave mixing element. Typically, the four-

wave mixing interaction comes with always-on cross-Kerr term between the transmon and the cavity. Although useful in many cases, it creates havoc in the particular case of four-wave mixing that we are interested in. We propose and demonstrate a novel circuit which cancels the cross-Kerr term, while preserving the other interesting four-wave mixing interactions. This circuit requires the presence of magnetic field for operation. Therefore we also demonstrate a new simple way to introduce magnetic field in superconducting cavities.

In Ch. 7 we combine all the techniques learned in the previous chapters, to propose a way to build fully autonomous and continuous first-order error correction against all error channels. We accomplish this goal by introducing a new hardware efficient QEC code, called the pair-cat code, which stores the encoded states in two entangled harmonic oscillators. The slight increase in the hardware complexity of the pair-cat code is completely compensated by the reduction in the order of nonlinearity required to correct against photon loss errors in either of the modes. Moreover, the pair-cat code can tolerate multiple photon losses as long as they only affect a single mode. This is beneficial for engineering the particular Raman-assisted multi-photon driven-dissipative process required for protecting this code against dephasing-like errors.

We conclude the thesis in Ch. 8 with a summary of the work accomplished and the future directions.

Chapter 1

Preliminary concepts

This chapter builds up the preliminary knowledge required for understanding the material in this thesis. We begin our discussion in Sec. 1.1 by introducing the general notation for modeling open quantum systems and errors. With the help of this notation we describe two basic quantum systems, spin-1/2 qubits and quantum harmonic oscillators, in Sec. 1.2 with a special emphasis on the errors that affect these systems.

1.1 Notation for describing quantum system

The goal of this section is to introduce the notation used in this thesis for describing isolated and open quantum systems. Moreover we also describe the Lindblad master equation and the Kraus maps which model the time evolution of an open quantum system.

1.1.1 Isolated quantum systems

Let us assume that the Hilbert space \mathcal{H} of a quantum system is spanned by a set of orthonormal state vectors $\mathcal{S} = \{|\alpha\rangle, |\beta\rangle, |\gamma\rangle, \dots\}$. It is helpful to write the identity on this

Hilbert space as a sum of projectors given by

$$\hat{I}_{\mathcal{H}} = \sum_{|k\rangle \in \mathcal{S}} \hat{P}_k. \quad (1.1)$$

where $\hat{P}_k = |k\rangle\langle k|$. The quantum system can exist in superposition of two or more of these states, for example $|\psi\rangle = c_\alpha|\alpha\rangle + c_\beta|\beta\rangle$ where $\{c_\alpha, c_\beta\} \in \mathbb{C}$ and $|c_\alpha|^2 + |c_\beta|^2 = 1$. Such superposition states are called pure states. When the system is isolated the time evolution of the system is governed by the Schrödinger equation

$$i\hbar \frac{\partial}{\partial t} |\psi\rangle = \hat{H} |\psi\rangle, \quad (1.2)$$

where \hbar is the reduced Plank's constant, \hat{H} is the Hamiltonian of the system, and $\frac{\partial}{\partial t}$ is the partial derivative with respect to time. From now on we will denote the time derivative, even if partial, with a dot over the quantity of concern. The evolution under Schrödinger's equation is reversible and leads to unitary dynamics of the system given by

$$|\psi\rangle(t) = \hat{U} |\psi(0)\rangle = \mathcal{T} e^{-\frac{i}{\hbar} \int_0^t dt' \hat{H}(t')} |\psi(0)\rangle. \quad (1.3)$$

Here \mathcal{T} indicates the time ordering operator [Sakurai and Napolitano, 2017]. For the cases where $[\hat{H}(t_1), \hat{H}(t_2)] = 0$, such time ordering is not required and the integral turns into the normal integration. One of the major tasks in QIP applications is to engineer the desired unitary evolution, which allows for the execution of quantum algorithms.

Quantum processors typically include multiple subsystems interacting with each other. The Hilbert space of the joint system is spanned by the inner products of the state vectors of the individual systems. For example, the Hilbert space of system 1 and 2 is spanned by

$$\mathcal{S}_{\text{joint}} = \mathcal{S}_1 \otimes \mathcal{S}_2 = \{|\alpha_1, \alpha_2\rangle, |\alpha_1, \beta_2\rangle, \dots, |\beta_1, \alpha_2\rangle, |\beta_1, \beta_2\rangle, \dots\} \quad (1.4)$$

As a consequence of quantum superposition in this higher dimensional Hilbert space, we get entangled states which cannot be separated in terms of the products of the individual states. A famous example of entangled states is

$$|\text{Bell}\rangle = \frac{|\alpha_1, \alpha_2\rangle + |\beta_1, \beta_2\rangle}{\sqrt{2}}. \quad (1.5)$$

Quantum entanglement acts as the major resource as well as causes errors in QIP as we will see later.

1.1.2 Open quantum systems

Systems which couple to the environmental degrees of freedom are called “open” quantum systems, by opposition to isolated quantum systems which are also called “closed”. In order to describe our system in such a situation, we utilize the density matrix representation, which allows us to represent the effective state of the system when the environmental degrees of freedom are ignored. The density matrix of the system is obtained by performing the so called partial trace on the environmental degrees of freedom. Let the Hilbert space $\mathcal{H} \otimes \mathcal{H}_{\text{env}}$ of the system and its environment be spanned by $\mathcal{S} \otimes \mathcal{S}_{\text{env}}$ where $\mathcal{S}_{\text{env}} = \{|\alpha_{\text{env}}\rangle, |\beta_{\text{env}}\rangle, |\gamma_{\text{env}}\rangle, \dots\}$ is the set of state vectors describing environmental degrees of freedom. The density matrix of the system and the environment is defined as

$$\rho_{\text{tot}} = |\Psi_{\text{tot}}\rangle\langle\Psi_{\text{tot}}| \quad (1.6)$$

where $|\Psi_{\text{tot}}\rangle$ is a pure superposition state of the system and the environment together. The density matrix of the system, after ignoring the environmental degrees of freedom, is

then denoted by ρ and is obtained by

$$\rho = \text{Tr}_{\text{env}}(\rho_{\text{tot}}) = \sum_{|j_{\text{env}}\rangle \in \mathcal{S}_{\text{env}}} \left(\hat{I}_{\mathcal{H}} \otimes \langle j_{\text{env}}| \right) \rho_{\text{tot}} \left(\hat{I}_{\mathcal{H}} \otimes |j_{\text{env}}\rangle \right). \quad (1.7)$$

As a toy example, let us consider the two entangled systems considered in the previous section with $|\Psi_{\text{tot}}\rangle = |\text{Bell}\rangle$. If we consider system 1 as our system of interest and system 2 as the environment, then the density matrix of 1 is given by

$$\rho = |\alpha\rangle\langle\alpha| + |\beta\rangle\langle\beta|. \quad (1.8)$$

It is clear that the first system is no longer in a pure superposition of $|\alpha\rangle$ and $|\beta\rangle$. Instead, due to our lack of information about system 2, the first system is in either $|\alpha\rangle$ or $|\beta\rangle$.

In general, the density matrix of a system is represented as

$$\rho = \sum_{|i\rangle, |j\rangle \in \mathcal{S}} c_{ij} |i\rangle\langle j|. \quad (1.9)$$

The following points regarding the density matrix are useful for our discussions:

1. The density matrix is positive semi-definite, i.e. $\langle\psi|\rho|\psi\rangle > 0$ for every nonzero $|\psi\rangle$, and Hermitian, i.e. $\rho^\dagger = \rho$.
2. The trace of density matrix is always 1, i.e. $\text{Tr}(\rho) = \sum_{|j\rangle \in \mathcal{S}} \langle j|\rho|j\rangle = 1$.
3. The quantity $\text{Tr}(\rho^2)$ is 1 for pure states, and between 0 and 1 for mixed states. Hence this quantity is defined as the purity of the system.
4. Expectation value of an observable \hat{k} is given by $\text{Tr}(\hat{k}\rho)$.
5. Action of a unitary \hat{U} on the density matrix is given by $\hat{U}\rho\hat{U}^\dagger$.

6. In general, it is possible to trace out any subsystem from the density matrix. Such a partial trace with respect to a subsystem k is given by

$$\mathrm{Tr}_k(\rho) = \sum_{|j\rangle \in \mathcal{S}_k} \left(\hat{I}_{\mathcal{H}-\mathcal{H}_k} \otimes \langle j| \right) \rho \left(\hat{I}_{\mathcal{H}-\mathcal{H}_k} \otimes |j\rangle \right) \quad (1.10)$$

where $\hat{I}_{\mathcal{H}-\mathcal{H}_k}$ is the identity operator over the remaining part of the system.

7. The partial trace of a subsystem, entangled with the rest of the system, leads to a mixed state for the rest of the system as we have already seen.

1.1.3 Time evolution in presence of decoherence

The unavoidable interactions between the system and its environment results in entanglement with these spurious degrees of freedom. However, since we do not observe or control the environmental degrees of freedom, the evolution of the system is given by taking a partial trace with respect to those degrees of freedom. This leads to decoherence and dissipation in the system. Typically, such dissipation is harmful for QIP since it leads to errors. We model the dynamics of a system in presence of dissipation with the help of a differential equation called the Lindblad master equation [Haroche and Raimond, 2006, Gardiner and Zoller, 2015]. It is given by

$$\dot{\rho} = -\frac{i}{\hbar} [\hat{H}, \rho] + \sum_{i \neq 0} \mathcal{D}[\hat{L}_i] \rho. \quad (1.11)$$

Here, the first term $[\hat{H}, \rho]$ describes the Hamiltonian dynamics of the system, with the square brackets denoting commutation $[\hat{k}_1, \hat{k}_2] = \hat{k}_1 \hat{k}_2 - \hat{k}_2 \hat{k}_1$. The second term describes

various dissipation channels on the system, with

$$\mathcal{D}[\hat{L}_i]\rho = \hat{L}_i\rho\hat{L}_i^\dagger - \frac{1}{2}\{\hat{L}_i\hat{L}_i^\dagger, \rho\}, \quad (1.12)$$

where the curly brackets denote anti-commutation $\{\hat{k}_1, \hat{k}_2\} = \hat{k}_1\hat{k}_2 + \hat{k}_2\hat{k}_1$. The operators \hat{L}_i are called the Lindblad jump operators associated with the dissipation channels.

It is also possible to write down the time evolution of the density matrix under the action of dissipation in an **integrated form** with the help of the so called Kraus sum representation. In this representation, the density matrix after a time step τ is given by

$$\rho(t + \tau) = \mathcal{M}(\rho(t)) = \sum_{\mu} \hat{M}_{\mu}(\tau)\rho(t)\hat{M}_{\mu}^\dagger(\tau). \quad (1.13)$$

Here \mathcal{M} is known as a Kraus map which should preserve the positivity, Hermiticity and trace of the density matrix. The operators \hat{M}_{μ} are called Kraus operators. For a time-step τ much less than the characteristic time of the system evolution, the Kraus operators are given by

$$\begin{aligned} \hat{M}_0(\tau) &= \hat{I} - i\frac{\hat{H}}{\hbar}\tau - \frac{\tau}{2}\sum_i \hat{L}_i^\dagger\hat{L}_i, \\ \hat{M}_{\mu=i} &= \sqrt{\tau}\hat{L}_i, \end{aligned} \quad (1.14)$$

where L_i are the Lindblad jump operators. Knowing the Kraus operators that describe an error on the system is very helpful since the QEC codes that we develop will correct for the actions of a certain set of these operators.

Having built a general notational framework for describing open quantum systems, we now proceed to study this notation in the specific cases of spin-1/2 qubits and quantum harmonic oscillators.

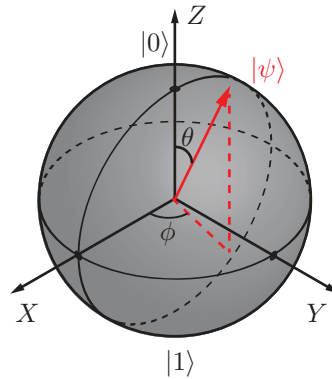


Figure 1.1: Bloch sphere representation. An arbitrary pure state $|\psi\rangle$ of a qubit is represented as a point on the surface of a unit sphere, called the Bloch sphere. Such a state can be represented as a superposition of the eigenstates of $\hat{\sigma}_z$, i.e. $|0\rangle$ and $|1\rangle$, by utilizing the polar angle θ and azimuthal angle ϕ as parameters (see Eq. 1.19).

1.2 Basic quantum systems

Here we discuss two basic quantum systems that are important for understanding the material in this thesis. First qubits are described along with some of the useful quantum gates, followed by the common error channels for the qubits. We then describe the quantum harmonic oscillators and introduce the Wigner function representation for visualizing the density matrix of a harmonic oscillator. The dominant error channels for this quantum system are also discussed.

1.2.1 Spin-1/2 Qubits

In this section we brush up on some of the important quantum gates and study quantum errors in the context of spin-1/2 qubits. The dynamics of such a qubit is governed by Pauli

operators

$$\hat{\sigma}_x = \begin{pmatrix} 0 & 1 \\ 1 & 0 \end{pmatrix}, \hat{\sigma}_y = \begin{pmatrix} 0 & i \\ -i & 0 \end{pmatrix}, \text{ and } \hat{\sigma}_z = \begin{pmatrix} 1 & 0 \\ 0 & -1 \end{pmatrix}, \quad (1.15)$$

and the identity operator

$$\hat{I} = \begin{pmatrix} 1 & 0 \\ 0 & 1 \end{pmatrix}. \quad (1.16)$$

As an example, the Hamiltonian of the system is given by

$$\hat{H} = -\frac{\hbar\omega_q}{2}\hat{\sigma}_z, \quad (1.17)$$

where ω_q is the transition frequency between the two energy eigenstates, that is the eigenstates of the $\hat{\sigma}_z$ operator. The lower energy state (eigenvalue $+1$) is denoted as $|0\rangle$ and sometimes called the ground state. The higher energy state is called the excited state and we denote it by $|1\rangle$. These states are described in matrix format as

$$|0\rangle = \begin{pmatrix} 1 \\ 0 \end{pmatrix} \text{ and } |1\rangle = \begin{pmatrix} 0 \\ 1 \end{pmatrix}. \quad (1.18)$$

Arbitrary pure states of a qubit are expressed in terms of $\mathcal{S} = \{|0\rangle, |1\rangle\}$ by the following expression:

$$|\psi\rangle = \cos\left(\frac{\theta}{2}\right)|0\rangle + e^{i\phi}\sin\left(\frac{\theta}{2}\right)|1\rangle, \quad (1.19)$$

where $\theta \in [0, \pi]$ and $\phi \in [0, 2\pi]$. It is helpful to visualize this superposition as a point on the surface of a unit sphere, called the Bloch sphere, with θ and ϕ as polar and azimuthal angles of the Bloch vector as shown in Fig. 1.1. Under the action of the qubit Hamiltonian, the Bloch vector will continuously precess around the Z -axis. However, here onwards we

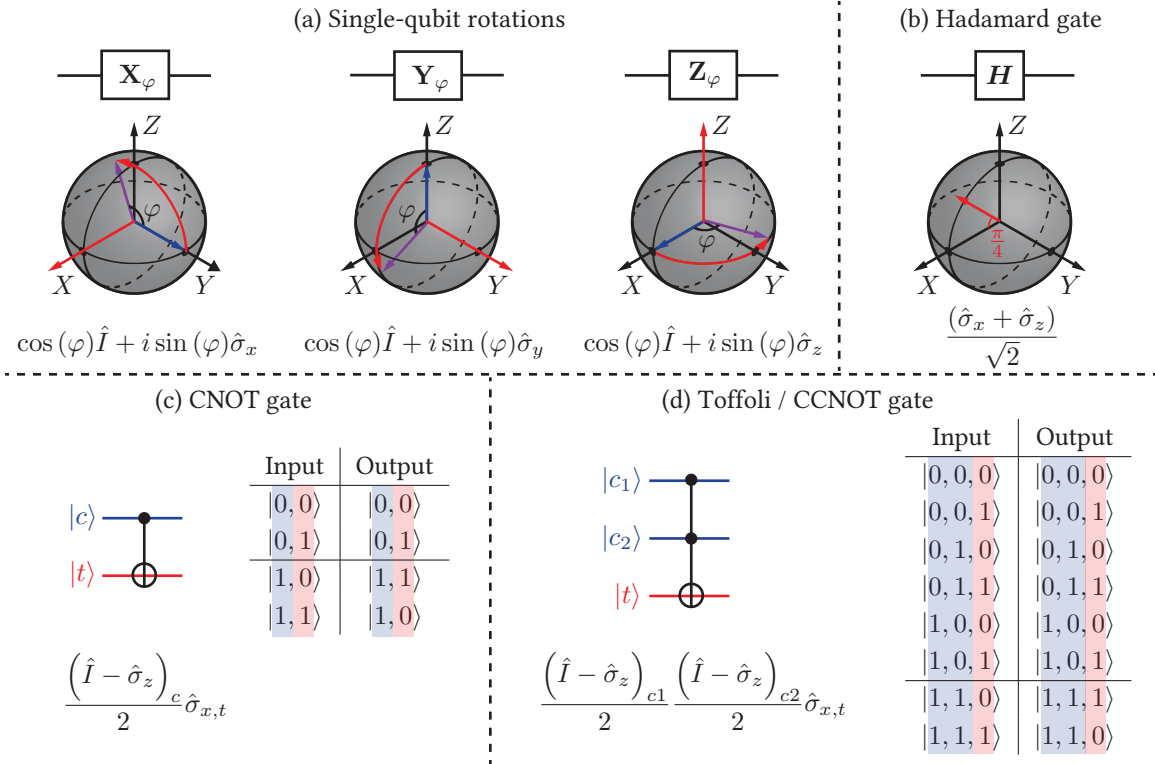


Figure 1.2: (a) Arbitrary single-qubit rotations (\mathbf{X}_φ , \mathbf{Y}_φ and \mathbf{Z}_φ). The Bloch spheres indicate the axis and arc of rotations (red arrows), generic initial states (blue arrows), and the resultant final states (purple arrows). (b) The Hadamard gate (\mathbf{H}). This gate is a rotation by π around an axis in the XZ -plane, making an angle of $\pi/4$ with the X -axis as shown. (c) Controlled-NOT (CNOT) gate. This is a two qubit gate with one qubit acting as the control (blue) and the other acting as the target (red). The target qubit is flipped if and only if the control is in $|1\rangle$, as shown in the truth table. The arbitrary single qubit rotations along with the CNOT gates form a universal gate set. (d) Toffoli or Controlled-Controlled-NOT (CCNOT) gate. The target qubit (red) is flipped, if and only if the two control qubits (blue) are both in respective $|1\rangle$ state as shown in the truth table. The unitary corresponding to each gate is specified at the bottom of the respective panels.

will work in a frame rotating in the same direction around the Z -axis with the same rate of precession. This will allow us to focus on the more interesting parts of qubit dynamics.

Important quantum gates

Figure 1.2 shows some of the important quantum gates that we will encounter over the course of this thesis. In case of the transmon, as we will discuss in a latter chapter, all the

single qubit rotations are possible. This allows for universal control of single qubits, i.e. we can construct arbitrary unitary operations on the qubits. Another important single qubit gate, the Hadamard, is shown in panel b of Fig. 1.2. This gate is essentially a combination of a rotation by π around the Z -axis followed by a rotation through $\pi/2$ around the Y -axis. Hadamard plays an important role in the discussion of error correction in the next section. In order to perform QIP and QEC, one requires the ability to control a multi-qubit system. This is achieved by engineering controlled interactions between two or more qubits. Two qubit gates like CNOT, CPHASE, SWAP and $\sqrt{i\text{SWAP}}$ have been demonstrated with increasing fidelity [Krantz *et al.*, 2019, Barends *et al.*, 2019, Hong *et al.*, 2019]. Panels c and d of Fig. 1.2 show the actions of Controlled-NOT (CNOT) and Toffoli gates. These multi-qubit gates are important for our discussion of QEC. Experimentally, we only require single qubit rotations for the purpose of this thesis.

Errors on qubits

Having discussed the unitary operations, let us turn our attention to studying qubits in presence of decoherence. An arbitrary density matrix of a single qubit is represented as

$$\rho = \frac{1}{2} \left(\hat{I} + r_x \hat{\sigma}_x + r_y \hat{\sigma}_y + r_z \hat{\sigma}_z \right). \quad (1.20)$$

Note that the trace of the density matrix is automatically preserved to 1. The constants $r_{x,y,z} \in [0, 1]$ and

$$|r_x|^2 + |r_y|^2 + |r_z|^2 = \text{Tr}(\rho^2) \leq 1. \quad (1.21)$$

These constants can be thought of as coordinates of the Bloch vector corresponding to the qubit. For pure states $\text{Tr}(\rho^2) = 1$ and as expected, the state lies on the surface of the Bloch sphere. For mixed states, however, $\text{Tr}(\rho^2) < 1$ and hence these states lie in the interior of the Bloch sphere. Moreover, this implies that the Bloch sphere contains the

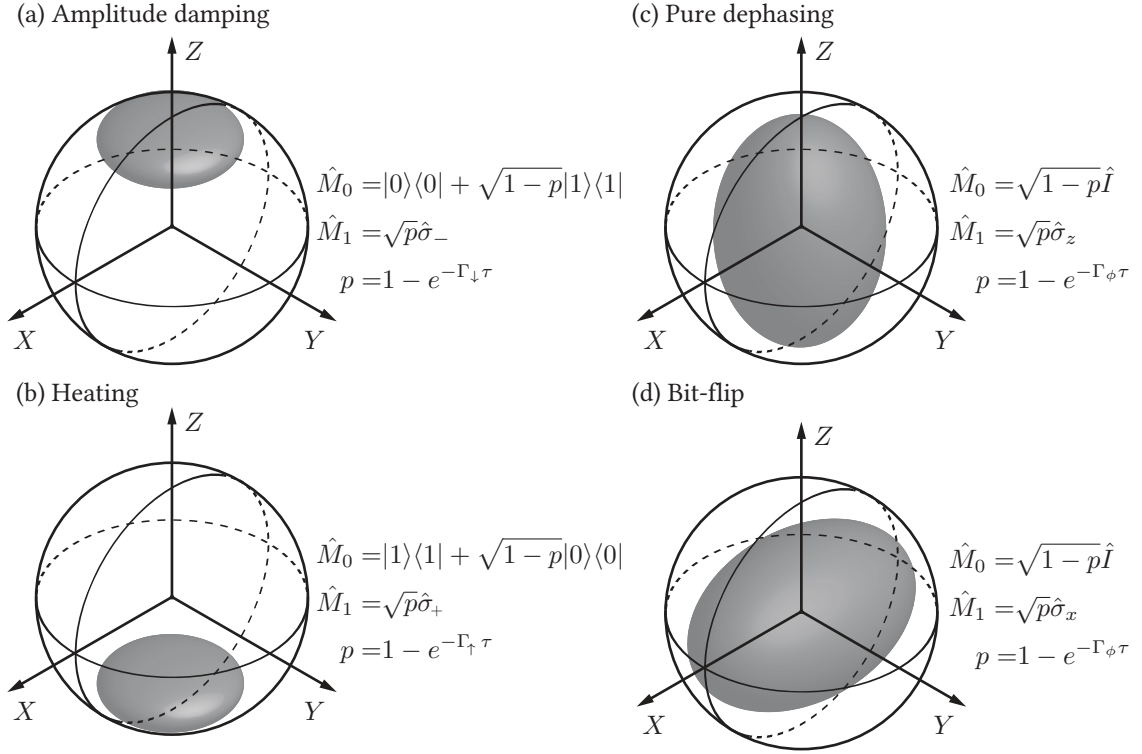


Figure 1.3: (a) Amplitude damping error occurs due to the excitation of the qubit leaking to the environment. This results in all the Bloch-vectors of the qubit shrinking towards the $|0\rangle$ state. (b) The opposite of amplitude damping is the heating error which incoherently adds an excitation from the environment to the qubit. (c) Dephasing error is introduced by random rotation of Bloch vectors around the Z -axis. Such an error results in all the Bloch vectors shrinking towards the Z -axis, except for the eigenstates of $\hat{\sigma}_z$, i.e. $|0\rangle$ and $|1\rangle$. (d) Bit-flip error is defined as the random rotation of the Bloch-vector around the X -axis. Such an error results in all the Bloch-vectors shrinking towards the X -axis, except for the eigenstates of $\hat{\sigma}_x$, i.e. $|+\rangle = (|0\rangle + |1\rangle)/\sqrt{2}$ and $|-\rangle = (|0\rangle - |1\rangle)/\sqrt{2}$, which remain unchanged. The random rotations around y -axis (not shown) are trivial since they can be thought as a combination of bit-flip and pure dephasing errors. Each panel specifies the Kraus operators for the respective error channels, where p indicates the probability of the error in a given time-step τ , and $\Gamma_{1,\phi,\text{flip}}$ are the rates of the respective errors on a qubit.

same information as the density matrix of a single qubit. We utilize this knowledge to illustrate some of the common error channels for a qubit in Fig. 1.3.

Panel a of Fig. 1.3 describes amplitude damping error. The effect of this error channel is to destroy qubit excitation by leaking it to the environment. As a result, all the

Bloch-vectors of the qubit shrink towards the lower energy state $|0\rangle$ as shown in Fig. 1.3a. Amplitude damping is modeled by $\mathcal{D}[\sqrt{\Gamma_\downarrow}\hat{\sigma}_-]$, where Γ_\downarrow is the rate of amplitude damping and $\hat{\sigma}_- = \hat{\sigma}_x + i\hat{\sigma}_y$ is the destruction operator for the qubit excitation. This operator destroys a single excitation on the qubit, thus taking $|1\rangle$ to $|0\rangle$. The conjugate of this error, where the qubit receives incoherent excitation from the environment, is known as the heating of the qubit (Fig. 1.3b). Heating is modeled by $\mathcal{D}[\sqrt{\Gamma_\uparrow}\hat{\sigma}_+]$ where Γ_\uparrow is the rate of heating for the qubit and $\hat{\sigma}_+ = \hat{\sigma}_-^\dagger$ is the creation operator. Typically, for a well cooled superconducting qubit Γ_\uparrow is around two orders of magnitude smaller than Γ_\downarrow . Panel c and d of Fig. 1.3 represent, respectively, the pure dephasing and bit-flip error channels for a qubit. Pure dephasing is random rotations of qubit Bloch-vector around Z -axis, modeled by $\mathcal{D}[\sqrt{\Gamma_\phi}\hat{\sigma}_z]$, whereas the bit-flip error is random rotations around the X -axis, modeled by $\mathcal{D}[\sqrt{\Gamma_{\text{flip}}}\hat{\sigma}_x]$. Here Γ_ϕ and Γ_{flip} are the rates of the respective errors. The figure also shows the Kraus operators, previously discussed in section 1.1.3, for the respective errors acting in isolation. It is important to note that all Kraus operators describing the errors on the qubits can be expressed as linear combinations of \hat{I} , $\hat{\sigma}_x$, $\hat{\sigma}_y$ and $\hat{\sigma}_z$. While building a QEC code, it will suffice to correct for the errors described by the identity and the Pauli-operators for complete protection against single-qubit errors. Amplitude damping, heating and dephasing form the major sources of errors in case of superconducting transmon qubits. The decoherence rates of a qubit are usually reported as the rate of relaxation $\Gamma_1 = \Gamma_\downarrow + \Gamma_\uparrow$, and the rate of total dephasing $\Gamma_2 = \Gamma_1/2 + \Gamma_\phi$.

An observant reader will note that the sources of errors on the qubit are not independent. For example, Kraus operators for the amplitude damping error can be expressed as a combination \hat{I} , $\hat{\sigma}_x$, $\hat{\sigma}_y$ and $\hat{\sigma}_z$ operators. The total dephasing error $\Gamma_2 = \Gamma_1/2 + \Gamma_\phi$, is essentially a combination of relaxation and dephasing. In general, the error channels of the spin-1/2 qubit can be broken in terms of the set of Pauli-operators and the identity operator. This leads to an important simplification for QEC as we will see in the next

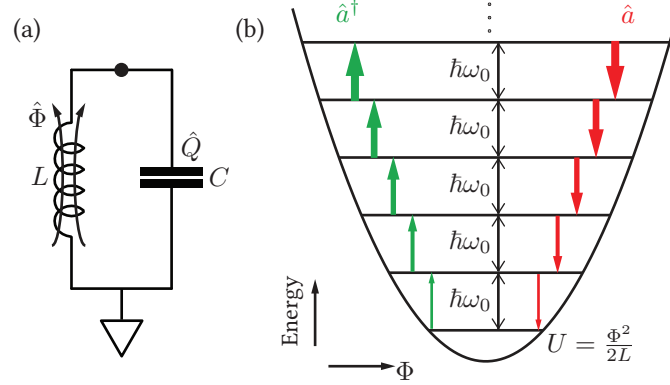


Figure 1.4: (a) Electrical LC circuit as an example of a quantum harmonic oscillator. The operator \hat{Q} indicates the charge on the capacitor C and the operator $\hat{\Phi}$ indicates the flux through the inductor L . (b) Parabolic potential and energy eigenstates, that is Fock states, of a quantum harmonic oscillator. The energy eigenstates are equally spaced with the energy difference $\hbar\omega_0$ between successive states. The green arrows represent the action of the creation operator \hat{a}^\dagger and red arrows represent the action of the destruction \hat{a} on each of the states. The widths of the arrows are increased up the ladder to signify the increasing strength of the respective matrix elements.

chapter (Ch. 2).

1.2.2 Quantum harmonic oscillators

The quantum harmonic oscillator is another important quantum system for the purpose of this thesis. An example of a harmonic oscillator is an LC circuit which is a fundamental building block for superconducting circuits. A circuit diagram of an LC circuit is represented in Fig. 1.4a. The Hamiltonian of this system is given by

$$\hat{H} = \frac{\hat{Q}^2}{2C} + \frac{\hat{\Phi}^2}{2L}, \quad (1.22)$$

where \hat{Q} is an operator describing the charge on the capacitor C , and $\hat{\Phi}$ is an operator describing the magnetic flux through the inductor L as shown in Fig. 1.4a. By convention, $\hat{\Phi}$ is the position coordinate of the oscillator and \hat{Q} is the conjugate momentum satisfying

the canonical commutation relation $[\hat{\Phi}, \hat{Q}] = i\hbar$. It is helpful to redefine $\hat{\Phi}$ and \hat{Q} in terms of ladder operators \hat{a}^\dagger and \hat{a} as

$$\begin{aligned}\hat{\Phi} &= \Phi_{\text{ZPF}} (\hat{a}^\dagger + \hat{a}) \\ \hat{Q} &= iQ_{\text{ZPF}} (\hat{a}^\dagger - \hat{a}).\end{aligned}\tag{1.23}$$

The operators \hat{a}^\dagger and \hat{a} satisfy $[\hat{a}^\dagger, \hat{a}] = 1$ in order to fulfill the canonical commutation relation. The constants Φ_{ZPF} and Q_{ZPF} are given by

$$\begin{aligned}\Phi_{\text{ZPF}} &= \sqrt{\frac{\hbar Z_0}{2}} \\ Q_{\text{ZPF}} &= \sqrt{\frac{\hbar}{2Z_0}}\end{aligned}\tag{1.24}$$

where Z_0 is the characteristic impedance of the oscillator defined as $Z_0 = \sqrt{L/C}$. In terms of the ladder operators the Hamiltonian of the oscillator is now given by

$$\hat{H} = \hbar\omega_0 \left(\hat{a}^\dagger \hat{a} + \frac{1}{2} \right) = \hbar\omega_0 \left(\hat{n}_a + \frac{1}{2} \right)\tag{1.25}$$

where ω_0 is the resonant frequency of the harmonic oscillator given by $\omega_0 = 1/\sqrt{LC}$ and $\hat{n}_a = \hat{a}^\dagger \hat{a}$ is called the number operator. The energy eigenstates of this Hamiltonian are the eigenstates of the number operator called the Fock states, and are denoted by $|n\rangle$ where $n \in \mathbb{N}$. The effect of the ladder operators on the Fock states is given by

$$\begin{aligned}\hat{a}^\dagger |n\rangle &= \sqrt{n+1} |n+1\rangle, \\ \hat{a} |n\rangle &= \sqrt{n} |n-1\rangle,\end{aligned}\tag{1.26}$$

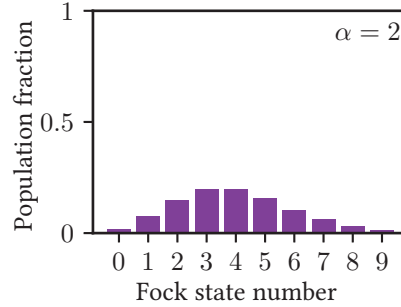


Figure 1.5: The population fractions $|\langle \alpha | n \rangle|^2$ of various Fock states $|n\rangle$ in a coherent state $|\alpha = 2\rangle$, as a function of Fock state number n . The population fractions have a Poissonion distribution.

i.e. \hat{a}^\dagger creates an excitation in the harmonic oscillator and \hat{a} destroys an excitation. It is clear from the above relations that Fock states are indeed energy eigenstates since

$$\hat{n}|n\rangle = \hat{a}^\dagger \hat{a}|n\rangle = n|n\rangle \Rightarrow E_n = \hbar\omega_0 \left(n + \frac{1}{2} \right). \quad (1.27)$$

Here E_n denotes the energy of the n^{th} Fock state. There are two important properties that one should emphasize at this point: (i) The Hilbert space of a harmonic oscillator is infinite dimensional since n is an integer ≥ 0 and (ii) the harmonic oscillator is a linear system with a constant energy difference of $\Delta E_{n,n+1} = \hbar\omega_0$ between the successive levels. These properties and the action of the ladder operators are represented as a cartoon in Fig. 1.4b.

Another important class of states for harmonic oscillators are known as the coherent states denoted as $|\alpha\rangle$ where $\alpha \in \mathbb{C}$. These are eigenstates of the destruction operator, that is

$$\hat{a}|\alpha\rangle = \alpha|\alpha\rangle \quad (1.28)$$

and are represented in the Fock state basis as

$$|\alpha\rangle = e^{-\frac{|\alpha|^2}{2}} \sum_{n=0}^{\infty} \frac{\alpha^n}{\sqrt{n!}} |n\rangle. \quad (1.29)$$

The population fraction $|\langle n|\alpha\rangle|^2$ of individual Fock-states n are shown in Fig. 1.5 for the particular case of $\alpha = 2$. They have a Poisson distribution. Note that the coherent states are pure superposition of Fock states, that is coherent states are themselves pure states. Moreover, the coherent state $|\alpha = 0\rangle$ is nothing but the 0th Fock state $|0\rangle$.

Wigner function representation

Just as in the case of qubits, it will be helpful to have a pictorial representation of the harmonic oscillator states and density matrices. In this thesis we will be using the Wigner function for the purpose of such visualization. In order to provide a useful definition of the Wigner function, we first introduce two important operations on the harmonic oscillator, (i) displacement and (ii) the photon number parity. The displacement operator $\hat{D}(\alpha)$, is defined as

$$\hat{D}(\alpha) = e^{\alpha\hat{a}^\dagger - \alpha^*\hat{a}} \quad (1.30)$$

where $\alpha \in \mathbb{C}$. The properties of this operator are summarized through the following equations:

$$\hat{D}(\alpha)|0\rangle = |\alpha\rangle, \quad (1.31a)$$

$$\hat{D}^\dagger(\alpha) = \hat{D}(-\alpha) \Rightarrow \hat{D}^\dagger(\alpha)\hat{D}(\alpha) = \hat{I}, \quad (1.31b)$$

$$\forall \beta \in \mathbb{C}, \hat{D}(\alpha)\hat{D}(\beta) = e^{(\alpha\beta^* - \alpha^*\beta)}\hat{D}(\alpha + \beta) \Rightarrow \hat{D}(\alpha)|\beta\rangle = e^{(\alpha\beta^* - \alpha^*\beta)}|\alpha + \beta\rangle, \quad (1.31c)$$

$$\hat{D}^\dagger(\alpha)\hat{a}\hat{D}(\alpha) = \hat{a} + \alpha. \quad (1.31d)$$

From these properties, we understand that the displacement operator is unitary and induces a translation in the phase space of the harmonic oscillator. The photon number parity operator $\hat{\Pi}$ is defined as

$$\hat{\Pi} = e^{i\pi\hat{a}^\dagger\hat{a}}. \quad (1.32)$$

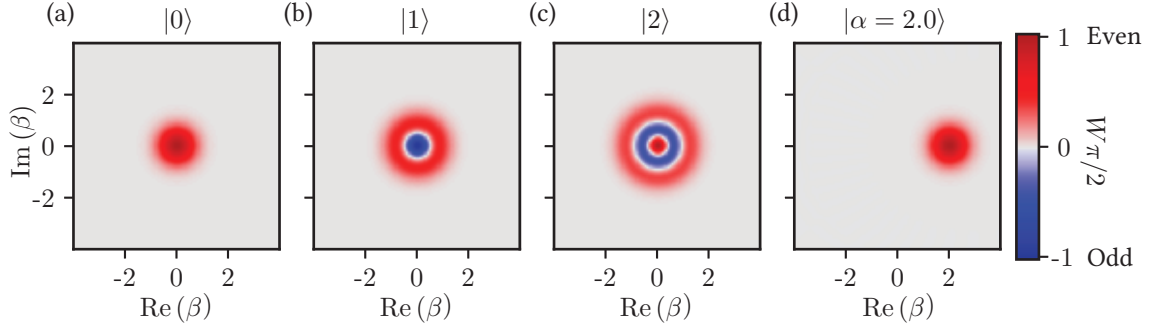


Figure 1.6: Examples of Wigner functions. Panels (a), (b) and (c) show the Wigner functions of Fock states $|0\rangle$, $|1\rangle$ and $|2\rangle$ respectively. Note that these Wigner functions are radially symmetric. Moreover, the value of Wigner function at the origin $\beta = 0$ indicates the parity of the state. Panel (d) shows the Wigner function of coherent state $|\alpha = 2\rangle$. The coherent state looks like a displaced ground state as one would expect.

It is easy to see that the parity operator is Hermitian, i.e. $\hat{\Pi}^\dagger = \hat{\Pi}$, and the Fock states are eigenstates of this operator with

$$\hat{\Pi}|n\rangle = -1^n|n\rangle. \quad (1.33)$$

In words, the parity is $+1$ for even Fock states and -1 for odd Fock states.

In terms of the displacement and parity operators, the Wigner function $W(\beta)$ is defined as

$$W(\beta) = \frac{2}{\pi} \text{Tr} \left(\hat{\Pi} \hat{D}(-\beta) \rho \hat{D}(\beta) \right), \quad (1.34)$$

where ρ is the density matrix of the harmonic oscillator. Therefore, the Wigner function is proportional to the expectation value of the parity operator calculated on the displaced density matrix. It is possible to show that the Wigner functions contain the same amount of information as the density matrices (see [Haroche and Raimond, 2006, Appendix A.2] for proof). We provide Wigner functions of Fock states $|0\rangle$, $|1\rangle$, $|2\rangle$ and the coherent state $|\alpha = 2\rangle$ in Fig. 1.6, for the purpose of illustration. The Wigner functions of the Fock states are azimuthally symmetric. The coherent state, on the other hand, looks like a displaced

version of $|0\rangle$. This is to be expected since the coherent states are indeed obtained by acting the displacement operator on $|0\rangle$ (Eq. 1.31a). Furthermore, the value of a Wigner function at $\beta = 0$ is simply the expectation value of $\hat{\Pi}$. This realization is useful for inferring the parity of harmonic oscillator states from this visual representation. Finally, in the lab frame, the coherent state will rotate around the origin due to time evolution under the action of the Hamiltonian of the oscillator. However, as in the case of qubits, we will work in a rotating frame in order to eliminate this trivial rotation.

Errors on harmonic oscillators

Having established a visualization scheme for the density matrix, let us now turn our attention to the errors that affect harmonic oscillators. The dominant error channel for this system is typically the amplitude damping error. This error channel is modeled by the dissipation of the form $\mathcal{D}[\sqrt{\kappa_{1\text{ph}}}\hat{a}]$, where we have used $\kappa_{1\text{ph}}$ to denote the rate of dissipation. The subscript ‘1ph’ in this notation refers to the power of \hat{a} in the jump operator. The Kraus operators (see Sec. 1.1.3) for describing the evolution of density matrix in presence of this error is given by

$$\hat{M}_k = \sqrt{\frac{(1 - e^{-\kappa_{1\text{ph}}\tau})^k}{k!}} e^{-\frac{1}{2}\kappa_{1\text{ph}}\tau\hat{a}^\dagger\hat{a}} \hat{a}^k, \quad (1.35)$$

where $k \in \mathbb{N}$. The $e^{-\frac{1}{2}\kappa_{1\text{ph}}\tau\hat{a}^\dagger\hat{a}}$ part of the Kraus operators is due to the back-action of the environment when no photon-loss events are detected. Such lack of photons reduces the relative probability of higher Fock states being occupied (as suggested by the $e^{-\frac{1}{2}\kappa_{1\text{ph}}\tau\hat{a}^\dagger\hat{a}}$ operator). We sometimes use the term energy relaxation error to describe this no photon jump evolution. The Kraus operators with $k > 0$ describe the consequence of the environment detecting k photon jump events. We call such jumps as photon loss errors. This division of the amplitude damping error channel into energy relaxation errors and

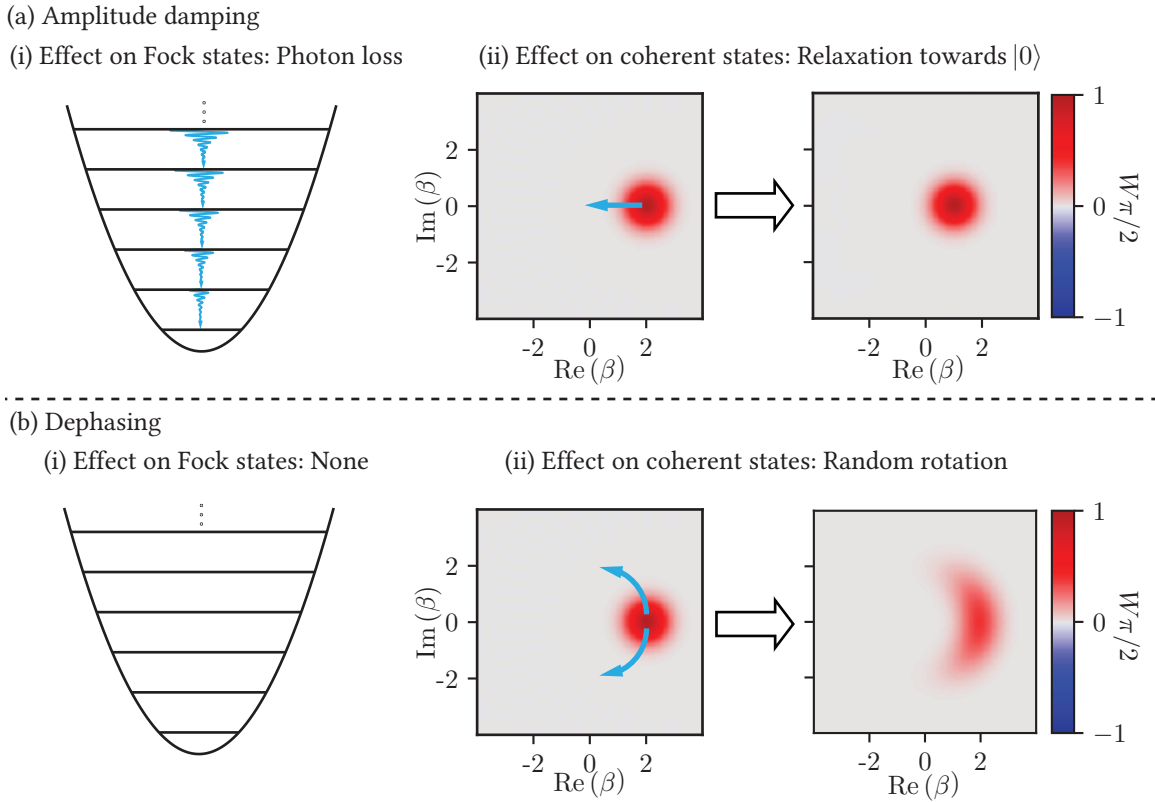


Figure 1.7: (a) Amplitude damping error channel for harmonic oscillator. We divide this error into two separate effects. Sub-panel (i) describes the stochastic photon-loss effect. This error is induced when the environment detects a leaked photon, thus causing a jump from $|n\rangle$ to $|n-1\rangle$ as indicated by the decaying wavy arrows. The widths of these arrows are increased as we climb the ladder to indicate the increasing probability of decay for higher Fock states. Sub-panel (ii) describes the energy relaxation effect. This deterministic evolution is induced by the back action of the environment when it does not detect any leaking photons. Pure Fock states are unaffected by energy relaxation while coherent states are pulled towards the ground state as shown. (b) Dephasing error channel for harmonic oscillator. This error induces random rotations in the phase space of the harmonic oscillator. Sub-panel (i) shows that individual Fock states are immune to this error since they are eigenstates of $\hat{a}^\dagger \hat{a}$. Only superposition of Fock states are affected. For example, panel (ii) shows how this error distorts the shape of a coherent state. The resulting banana shaped state is no longer a pure state.

photon-loss errors will prove useful while discussing QEC. We illustrate the separate effects of photon-loss and energy relaxation in Fig. 1.7a. Sub-panel (i) of the figure shows the result of a single photon loss on Fock states with the help of decaying wavy arrows.

The width of the arrows are increased as we climb up the ladder to depict the higher probability of decay. Sub-panel (ii) illustrates the effect of energy relaxation by showing the evolution of a coherent state under the action of amplitude damping error. The coherent states, being eigenstates of the destruction operator, are essentially immune to the photon losses up to a global phase. However, under the action of $e^{-\frac{1}{2}\kappa_{1\text{ph}}\tau\hat{a}^\dagger\hat{a}}$ operator, the coherent states are pulled towards the center of the phase space, i.e. towards the ground state $|0\rangle$, as shown in the figure.

The conjugate of amplitude damping is heating described by $\mathcal{D}[\sqrt{\kappa_\uparrow}\hat{a}^\dagger]$ where κ_\uparrow is the rate of heating. Typically, $\kappa_\uparrow \ll \kappa_{1\text{ph}}$. Therefore, we will not consider heating error in this thesis. On the other hand, a harmonic oscillator might inherit frequency fluctuations due to its coupling to other noisy systems. These fluctuations generate random rotations around the origin in Wigner function representation. The resulting error channel is called the dephasing error and it is described by a dissipator of the form $\mathcal{D}[\sqrt{\kappa_\phi}\hat{a}^\dagger\hat{a}]$ where κ_ϕ is the rate of dephasing for the harmonic oscillators. The Kraus operators for this error are given by

$$\hat{M}_{l,\text{dephasing}} = \sqrt{\frac{(\kappa_\phi t)^l}{l!}} e^{-\frac{1}{2}\kappa_\phi\tau\hat{n}^2} \hat{n}^l \text{ for } l \in \mathbb{N}. \quad (1.36)$$

where $l \in \mathbb{N}$. The effect of dephasing is illustrated in Fig. 1.7b. As shown, individual Fock-states are immune to this error since they are eigenstates of $\hat{a}^\dagger\hat{a}$ and have radially symmetric Wigner functions. Only superpositions of Fock states are affected. As an example, this error distorts the shape of coherent states as shown in Fig. 1.7b sub-panel (ii).

1.3 Summary and prelude to the next chapter

In this chapter we have developed the basic notation required for understanding the rest of this thesis. The important takeaway points from this chapter are as follows:

- (i) The density matrix can be used for describing arbitrary states of a quantum system including pure and the mixed states.
- (ii) The Lindblad master equation describes the time evolution of the density matrix in the differential form. An integral representation of the time evolution of the density matrix for a given time-step τ is given by the Kraus maps. The operators describing the Kraus maps depend on time step τ . The Kraus map representation is extremely useful for describing errors on the quantum systems.
- (iii) The Bloch sphere can be used as a visualization tool for the density matrices of the qubit. In case of harmonic oscillators, the Wigner function is the tool of choice in our case.
- (iv) The major sources of errors on the qubits are amplitude damping and pure dephasing. We also introduced the bit-flip error on the qubit which replaces amplitude damping as the dominant source of error in certain cases.
- (v) In the case of harmonic oscillator, amplitude damping is the dominant error channel. For sake of convenience, we divide amplitude damping in photon loss errors and energy relaxation. Photon loss corresponds to the cases where the environment detects leaked photons and the energy relaxation arises due the back-action of the environment when no photon loss events are detected.
- (vi) Another source of error in the harmonic oscillator is dephasing. This error can be

significant when frequency fluctuations are induced in the oscillators due to coupling with other nonlinear systems.

Having introduced these basic quantum systems and the errors which affect them, we are now ready to discuss how to correct them. We provide a brief introduction to QEC in the next chapter.

Chapter 2

Introduction to quantum error correction

In this chapter we turn our attention to some of the important concepts behind quantum error correction. The following section (Sec. 2.1) introduces the basic principles. This task is accomplished by first introducing the necessary and sufficient conditions for an encoding to protect against a given set of errors and giving an explicit construction for detection and recovery from these errors. We then discuss, in some depth, a few well known examples of QEC codes. These examples provide us opportunities to demonstrate QEC in action and also to discuss the limitations of QEC. It becomes clear that the hardware overhead in traditional QEC makes the task of error correction quite challenging. As a solution to reducing the overhead involved we discuss we introduce the concepts of hardware efficient QEC and cite a few examples of the same in Sec. 2.2. A more detailed discussion of a specific hardware efficient encoding, the “cat code”, is included in the next chapter. Although hardware-efficient QEC reduces the overhead associated with quantum systems, there is still a significant ‘software overhead’ resulting from making real-time decisions during the error correction protocol. In Sec. 2.3 we show that every QEC code can be converted

to instead operate in a fully autonomous manner such that no real-time decision making is required. The discussion in this chapter is not a comprehensive review. It is rather a list of concepts that will be useful later in the rest of the thesis. We refer the interested reader to the seminal book by Nielsen and Chuang [2011] for further insights.

2.1 Basic principles

The idea of error correction, by itself, is not new. From ancient pendulum clocks to modern telecommunication, there are multiple examples of error correction in the classical domain. As a specific example, let us consider the protection of a single classical bit. We add some redundancy to the encoding of the bit by employing three bits with $0_L \rightarrow 000$ and $1_L \rightarrow 111$. Here subscript L indicates logical 0 or logical 1. Let us consider what happens when errors occur on the individual bits. Suppose, after sending the information through a noisy channel, we receive an output of 001. In this case, the most likely input of the channel was $0_L = 000$ corresponding to an error on a single bit. Hence, by considering a majority vote on these bits, we recover the initial information.

The picture does not appear to be so straightforward in the case of quantum systems. To begin with, the no cloning theorem prevents the duplication of a qubit. Moreover, QIP requires superposition of quantum states. Therefore, straightforward measurement of qubits is not permissible since that will destroy the superposition. Finally, quantum errors are continuous. As an example, it is possible to partially rotate a qubit around say X -axis, resulting in an erroneous superposition of the form $c_g|g\rangle + c_e|e\rangle$. This makes the task of QEC **seem** insurmountable. However, it turns out, these difficulties do **not** make QEC impossible. In fact, it is possible to utilize the notion of redundant encoding in quantum systems as well. The schemes for encoding quantum information in error resilient manner are called QEC codes. In this section we provide a brief introduction to

the theory of QEC codes along with some examples and pitfalls associated with QEC.

2.1.1 The Knill-Laflamme conditions

We start our discussion by introducing the general conditions under which QEC is possible. The material presented here is simplified for the purpose of this thesis. A more detailed discussion is available in [Nielsen and Chuang, 2011].

Formally, a QEC code is defined as a subspace \mathcal{C}_0 of a larger Hilbert space \mathcal{H} . For simplicity we will assume that \mathcal{C}_0 has a dimension of 2 and is spanned by orthonormal code words $|0_L\rangle, |1_L\rangle$, the 0 and 1 of our ‘logical qubit’. A compact notation for denoting this is given by

$$\mathcal{C}_0 = \text{Span}\{|0_L\rangle, |1_L\rangle\} \quad (2.1)$$

We also define the errors acting on the whole system described by \mathcal{H} as a set of error operators $\mathcal{E} = \{\hat{E}_0 = \hat{I}, \hat{E}_1, \hat{E}_2, \dots, \hat{E}_m\}$. Under the action of these errors, a state $|\psi\rangle \in \mathcal{H}$ evolves as $\hat{E}_k|\psi\rangle$ and the evolution of the system density matrix is given by $\hat{E}_k\rho\hat{E}_k^\dagger$. Note that, since we are describing errors, \hat{E}_k do not have to be unitary operators.

What are the conditions for recovering the information stored in our ‘logical qubit’ in spite of these errors? The necessary and sufficient conditions on \mathcal{C}_0 for recovering from a given set of errors \mathcal{E} are known as the Knill-Laflamme conditions. These are given by

$$\langle u_L | \hat{E}_k^\dagger \hat{E}_l | v_L \rangle = \alpha_{l,k} \delta_{uv}, \quad (2.2)$$

for every $\hat{E}_k, \hat{E}_l \in \mathcal{E}$ and $u, v \in \{0, 1\}$. Here $\alpha_{l,k}$ are entries of a Hermitian matrix α and are independent of the state vectors in \mathcal{C}_0 . δ_{uv} is the Kronecker-delta function. Intuitively, the Knill-Laflamme conditions convey the following:

1. Orthogonal state vectors in \mathcal{C}_0 should remain orthogonal under the action of **all** the

errors in a correctable error-set \mathcal{E} . This is enforced by the Kronecker-delta function.

2. The superpositions in \mathcal{C}_0 should not be distorted under the action of the correctable errors. This is enforced by the condition that $\alpha_{l,k}$ is independent of the state vectors.

In addition, it is easy to verify that any linear combination of the correctable errors also satisfies the Knill-Laflamme conditions and therefore, is a correctable error. On the other hand, products of two operators in \mathcal{E} may not satisfy the above conditions. Therefore, if two correctable errors occur simultaneously, or one after the other such that the first error is not corrected before the second error occurs, then the system may develop an uncorrectable error.

We now outline an explicit construction for recovering from the errors. First, by taking a linear combinations of the operators in \mathcal{E} , we construct a set of operators $\{\hat{F}_0 = \hat{I}, \hat{F}_1, \hat{F}_2, \dots, \hat{F}_M\}$ which diagonalize the Hermitian matrix α . In terms of the orthogonal error operators \hat{F}_k the Knill-Laflamme conditions are now stated as

$$\langle u_L | \hat{F}_k^\dagger \hat{F}_l | v_L \rangle = d_{k,k} \delta_{lk} \delta_{uv}, \quad (2.3)$$

where $d_{k,k}$ are the eigenvalues of α . This implies that each error operator \hat{F}_k acting on the code space \mathcal{C}_0 takes the code space to an orthogonal subspace \mathcal{C}_k when $k \neq 0$. We call $\mathcal{C}_{k \neq 0}$ as error spaces. A short hand notation for representing this is given by

$$\hat{F}_k \mathcal{C}_0 = \mathcal{C}_k = \text{Span} \left\{ \frac{\hat{F}_k}{\sqrt{d_{kk}}} |0_L\rangle, \frac{\hat{F}_k}{\sqrt{d_{kk}}} |1_L\rangle \right\} = \text{Span} \{|0_L^k\rangle, |1_L^k\rangle\}. \quad (2.4)$$

Here $\sqrt{d_{kk}}$ is used in the denominator to make sure that the $|0_L^k\rangle, |1_L^k\rangle$ are normalized. We also construct unitary operators that map the code space to the error spaces.

These are given by

$$\hat{U}_k = |0_L^k\rangle\langle 0_L| + |1_L^k\rangle\langle 1_L| + |0_L\rangle\langle 0_L^k| + |1_L\rangle\langle 1_L^k| + \hat{I}_{\mathcal{H}-\mathcal{C}_0-\mathcal{C}_1}, \quad (2.5)$$

where a projector on the rest of the Hilbert space is added to make sure that \hat{U}_k is a unitary operator on the full Hilbert space \mathcal{H} . Now, error detection and correction can be accomplished in the following manner. First, perform a set of syndrome measurements which measure the projectors on \mathcal{C}_k given by

$$\hat{P}_{\mathcal{C}_k} = |0_L^k\rangle\langle 0_L^k| + |1_L^k\rangle\langle 1_L^k|. \quad (2.6)$$

Note that the projectors are Hermitian operators and hence can be used as observables. This will tell us which of the errors, say \hat{F}_K , has occurred and the system will be left in the corresponding error space \mathcal{C}_K without destroying the underlying superpositions, therefore keeping the information intact. The original state of system can be recovered by the application of the unitary \hat{U}_K^\dagger thus recovering from the error.

A critical reader might object at this point that decoherence is described by a ‘continuous’ Kraus map given by $\mathcal{M}(\rho) = \sum_k \hat{M}_k \rho \hat{M}_k^\dagger$ as we discussed in Sec. 1.1.3 and not by a ‘discrete’ set of operators as we have considered in this section. For simplicity, let us assume that the Kraus operators satisfy the Knill-Laflamme conditions in the form described in Eq. 2.3, i.e. $\hat{M}_k = \hat{F}_k$. Under the action of these operators $\rho \rightarrow \sum_k \hat{F}_k \rho \hat{F}_k^\dagger$. After we perform the syndrome measurement, however, the map will still be projected on one of the error spaces, say $F_K \mathcal{C}_0 = \mathcal{C}_K$. In other words, measurement of the error syndrome effectively discretizes the errors. Hence, a continuous error on the system can be corrected by accounting for a discrete set of error operators.

As a word of caution, although the construction presented here works, it is not very

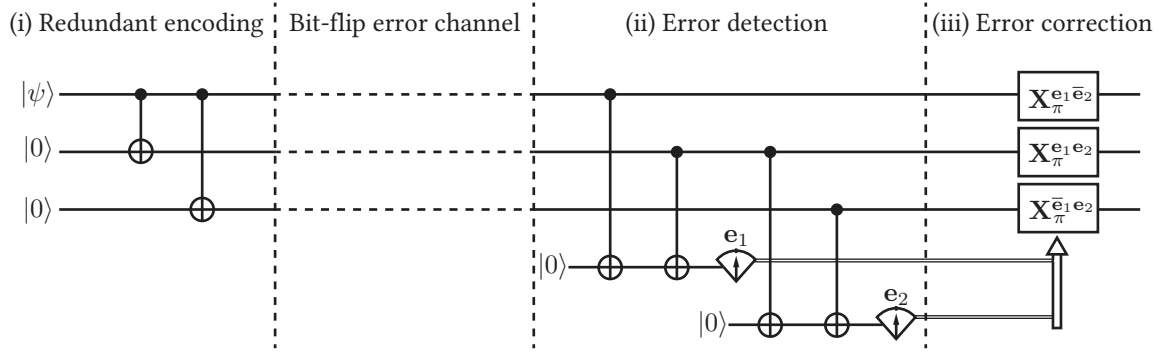


Figure 2.1: Three qubit bit flip code. Before passing through a noisy channel, the initial state $|\psi\rangle = c_0|0\rangle + c_1|1\rangle$ of a qubit is redundantly encoded, with the help of two additional qubits and CNOT gates, to get $|\Psi\rangle = c_0|0, 0, 0\rangle + c_1|1, 1, 1\rangle$. The error channel flips each bit with a probability p . Assuming at most one bit-flip, the goal is to detect which qubit has flipped without measuring the individual qubits. This is accomplished by adding two ancillary qubits and applying appropriate CNOT gates to map the error syndrome $\hat{\sigma}_{z,1}\hat{\sigma}_{z,2}$ on the first ancillary qubit and $\hat{\sigma}_{z,1}\hat{\sigma}_{z,2}$ on the second ancillary qubit. The measurement outcomes e_1, e_2 reveal which qubit has flipped (see table 2.1). The bit flip error is corrected by processing the measurement record classically and applying an X_π rotation on the qubits, conditioned on e_1 and e_2 . We depict the classical decision making by employing e_1, e_2, \bar{e}_1 and \bar{e}_2 as powers of the X_π rotations.

efficient to implement. Typically, while constructing QEC codes, one needs to take advantage of some clever underlying structure of the code to identify and correct for the errors more efficiently. Moreover, especially in infinite dimensional systems, some of the errors only approximately satisfy the Knill-Laflamme conditions. Care has to be taken while constructing recovery operations for such errors.

Armed with this general framework, we now consider some examples of quantum error correction codes.

2.1.2 Examples of QEC codes

One of the easiest examples of QEC is the three-qubit bit-flip code. This code is essentially the quantum counterpart of the classical 3-bit majority vote code that we discussed in the

beginning of this section. Suppose our initial qubit is in a state given by

$$|\psi\rangle = c_0|0\rangle + c_1|1\rangle. \quad (2.7)$$

We encode this information with the help of two additional qubits into an entangled state given by

$$|\Psi\rangle = c_0|0, 0, 0\rangle + c_1|1, 1, 1\rangle. \quad (2.8)$$

Note that this encoding cleverly sidesteps the no-cloning theorem by using entanglement. Such a state can be created with the help of two CNOT gates as shown in Fig. 2.1 under the title of redundant encoding. More formally, the code space \mathcal{C}_0 for the bit-flip code is defined as

$$\mathcal{C}_0 = \text{Span}\{|0_L\rangle = |0, 0, 0\rangle, |1_L\rangle = |1, 1, 1\rangle\} \quad (2.9)$$

Now let us study the effects of single qubit bit-flip errors on this code-space. The effect of the bit-flip $\sigma_{x,k}$ on \mathcal{C}_0 is given by

$$\begin{aligned} \sigma_{x,1}\mathcal{C}_0 &= \mathcal{C}_1 = \text{Span}\{|1, 0, 0\rangle, |0, 1, 1\rangle\}, \\ \sigma_{x,2}\mathcal{C}_0 &= \mathcal{C}_2 = \text{Span}\{|0, 1, 0\rangle, |1, 0, 1\rangle\}, \\ \sigma_{x,3}\mathcal{C}_0 &= \mathcal{C}_3 = \text{Span}\{|0, 0, 1\rangle, |1, 1, 0\rangle\}. \end{aligned} \quad (2.10)$$

It is easy to verify that all the basis states of $\mathcal{C}_0, \mathcal{C}_1, \mathcal{C}_2, \mathcal{C}_3$ are orthogonal to each other. As a result, the bit-flip code satisfies the Knill-Laflamme conditions for $\mathcal{E} = \{\hat{I}, \hat{\sigma}_{x,1}, \hat{\sigma}_{x,2}, \hat{\sigma}_{x,3}\}$ with $\alpha_{l,k} = \delta_{lk}$. In other words, all the single qubit bit-flip errors are a correctable and orthogonal set of errors for this code.

Now the question becomes, how do we detect which error has occurred and how do we correct that error? As we discussed in the last section, this could be accomplished by

Subspace	Subspace basis	Eigenvalue of $\hat{\sigma}_{z,1}\hat{\sigma}_{z,2}$	Eigenvalue of $\hat{\sigma}_{z,2}\hat{\sigma}_{z,3}$	\mathbf{e}_1	\mathbf{e}_2
\mathcal{C}_0	$ 0, 0, 0\rangle, 1, 1, 1\rangle$	+1	+1	0	0
\mathcal{C}_1	$ 1, 0, 0\rangle, 0, 1, 1\rangle$	-1	+1	1	0
\mathcal{C}_2	$ 0, 1, 0\rangle, 1, 0, 1\rangle$	-1	-1	1	1
\mathcal{C}_3	$ 0, 0, 1\rangle, 1, 1, 0\rangle$	+1	-1	0	1

Table 2.1: Outcome of the error syndrome measurements for the bit-flip code.

measuring the projectors $\hat{P}_{\mathcal{C}_k}$ on \mathcal{C}_k . However, there is a more efficient way of accomplishing the same thing. The syndromes that we utilize for detecting the errors are given by $\hat{\sigma}_{z,1}\hat{\sigma}_{z,2}$ and $\hat{\sigma}_{z,2}\hat{\sigma}_{z,3}$. The states in each of the subspaces mentioned earlier are eigenstates of the syndrome operators with different combinations of eigenvalues as summarized in table 2.1. Thus, performing a measurement of the syndrome operators indicates which of the three bits has flipped, if any. A quantum circuit in terms of CNOT gates and two ancillary qubits is shown in error detection part of Fig. 2.1. The first ancillary qubit is flipped if the eigenvalue for $\hat{\sigma}_{z,1}\hat{\sigma}_{z,2}$ is -1 , otherwise the qubit remains in the initial state $|0\rangle$. By measuring the state of this qubit, a classical entity can infer the eigenvalue to be $+1$ if the measurement outcome \mathbf{e}_1 is 0 and -1 if the measurement outcome is 1. Similarly, the measurement outcome \mathbf{e}_2 for the second qubit indicates the eigenvalue for $\hat{\sigma}_{z,2}\hat{\sigma}_{z,3}$. Note that these measurements do not destroy the superpositions since both the basis states in any of the subspaces lead to the same measurement outcome. In other words, the measurements do not distinguish between 0 and 1 of our logical qubit thus preserving the superpositions. Finally the correction is accomplished by classical processing of the measurement record and applying a \mathbf{X}_π rotation on the appropriate qubit thus accomplishing the error correction.

It is instructive to elaborate some important concepts with the help of this example. Firstly, as we discussed in Sec. 1.2.1, the bit flip error channel introduces random rotations around the X -axis. Let us assume, for the purpose of illustration, the first bit undergoes a random rotation through $\mathbf{X}_{\varphi,1} = \cos(\varphi/2)\hat{I} + i\sin(\varphi/2)\hat{\sigma}_{x,1}$. Under the action of such

a rotation, the encoded state $|\Psi\rangle$ evolves as

$$\mathbf{X}_{\varphi,1}|\Psi\rangle = \cos\left(\frac{\varphi}{2}\right)|\Psi\rangle + i\sin\left(\frac{\varphi}{2}\right)|\Psi_1\rangle, \quad (2.11)$$

where $|\Psi_1\rangle = c_0|1, 0, 0\rangle + c_1|0, 1, 1\rangle \in \mathcal{C}_1$. After the application of CNOT gates between the encoding qubits and the first ancilla qubits, the combined state of the system is given by $\cos(\varphi)|\Psi, 0\rangle + i\sin(\varphi)|\Psi_1, 1\rangle$. The measurement of this qubit then projects the encoding qubits in $|\Psi\rangle$ if $e_1 = 0$ and $|\Psi_1\rangle$ if $e_1 = 1$. Thus, a seemingly continuous error is projected to either no error or a bit-flip on the first qubit. This is called discretization of quantum errors and reduces the seemingly intractable problem of QEC to correcting for a discrete set of errors. Moreover, this is consistent with our discussion about Knill-Laflamme conditions in the last sub-section. $\mathbf{X}_{\varphi,1}$ is nothing but a linear combination of \hat{I} and $\hat{\sigma}_{x,1}$ error and is therefore correctable for the three-qubit bit-flip code.

Next, let us consider products of two correctable errors. Of course, the products given by $\hat{\sigma}_{x,k}\hat{I}$ or $\hat{\sigma}_{x,k}^2 = \hat{I}$ are still correctable. However, what happens when there are bit-flip errors on two qubits? Let us suppose there are simultaneous bit-flip errors on qubit 1 and 2 described by $\hat{\sigma}_{x,1}\hat{\sigma}_{x,2}$. Under the action of these errors, the code space \mathcal{C}_0 evolves as

$$\hat{\sigma}_{x,1}\hat{\sigma}_{x,2}\mathcal{C}_0 = \text{Span}\{|0, 0, 1\rangle, |1, 1, 0\rangle\} = \mathcal{C}_3. \quad (2.12)$$

This implies that the error syndrome measurement will detect $e_1 = 0$ and $e_2 = 1$. As a result the correction will flip the third qubit as well. This causes complete loss of information since $|0_L\rangle$ maps to $|1_L\rangle$ and vice versa, a ‘logical bit-flip’. In the case where there are bit-flip errors on all the qubits, the error syndrome is same as that in the case of no errors and therefore results in a complete loss of information. Hence, bit-flip errors on multiple qubits are not correctable with the three-qubit bit-flip code. Of course, one only needs to

check the Knill-Laflamme conditions to assert this. In order to gain an insight into when it is beneficial to use the bit flip code in spite of the possibility of multi-qubit errors, let us perform a crude calculation. Let p be the probability of bit flip for every qubit. Then, an un-encoded qubit returns the correct information with the probability $(1 - p)$. In case of the bit-flip code, the information is conveyed correctly when there are no errors, or only single qubit errors. Hence the probability of faithful information recovery is given by $(1 - p)^3 + 3p(1 - p)^2$. Comparing the two probabilities, it turns out the bit-flip code is advantageous as long as $p < 1/2$. Keep in mind this calculation assumes perfect gates, state preparation and measurement. We will consider the effect of imperfect components in the next sub-section.

More advanced codes have been constructed for protecting against multiple bit-flips and other kinds of errors. Accomplishing this requires larger Hilbert space. It is possible to address all the single qubit error channels with the help of the nine-qubit Shor code or seven-qubit Steane code or a five qubit code which is the minimum required size of the Hilbert space. As an example, we present the error detection and correction steps for the seven-qubit Steane code in Fig. 2.2. The code requires seven encoding qubits and six ancillary qubits for error syndrome measurement. The code space of the Steane code is spanned by

$$|0_L\rangle = \frac{1}{\sqrt{8}} (|0000000\rangle + |1010101\rangle + |0110011\rangle + |1100110\rangle \\ + |0001111\rangle + |1011010\rangle + |0111100\rangle + |1101001\rangle)$$

and

$$|1_L\rangle = \frac{1}{\sqrt{8}} (|1111111\rangle + |0101010\rangle + |1001100\rangle + |0011001\rangle)$$

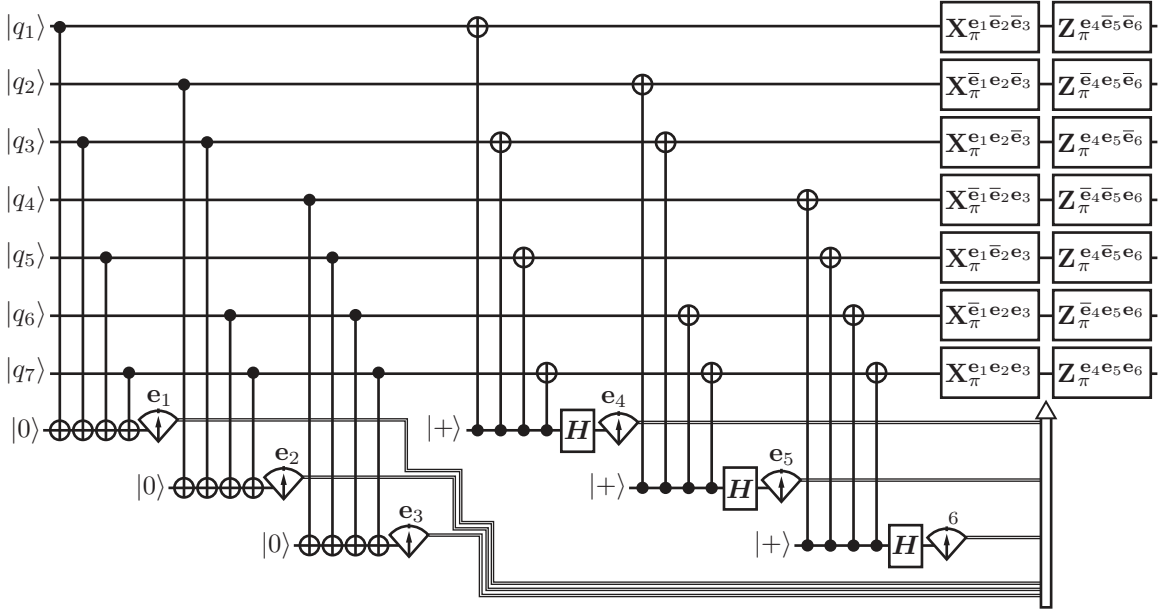


Figure 2.2: Error detection and correction for the Steane code. One logical qubit is encoded by utilizing seven physical qubits. In order to measure the error syndromes for this code, one requires six ancillary qubits, and multiple CNOT gates as shown. This adds to the overhead associated with the code. The first three ancillary qubits measure the error syndrome associated with the bit-flip error while the next three qubits measure the error syndrome for the phase-flip error. In addition, a random rotation of a qubit around the Y -axis can be expressed as a product of bit-flip and phase-flip errors on the same qubit. The Steane code also protects against such a product. Therefore, any arbitrary error is corrected, as long as it affects only one qubit.

$$+|1110000\rangle + |0100101\rangle + |1000011\rangle + |0010110\rangle).$$

The set of correctable errors is given by

$$\mathcal{E} = \{\hat{I}, \hat{\sigma}_{x,k}, \hat{\sigma}_{y,k}, \hat{\sigma}_{z,k} | k \in \{1, 2, 3, 4, 5, 6, 7\}\}. \quad (2.13)$$

It is time consuming to verify the Knill-Laflamme conditions for such a code. However, it is clear from this set that all the single-qubit errors are correctable since they can be expressed as linear combination of the operators in \mathcal{E} . The first three ancillary qubits in

Fig. 2.2 measure the error syndrome for the bit-flip error on any of the qubits. Due to the clever structure of the Steane code, the location of the bit-flip can be inferred by treating e_3, e_2, e_1 as a binary number. For example an error syndrome of $e_3 = 1, e_2 = 0, e_1 = 1$ is a bit-flip error on the 5th qubit. Similarly, the next three ancillary qubits measure the error syndrome for the pure-dephasing error on the qubits. Here the location of the error is read by treating e_6, e_5, e_4 as a binary number. Since the error syndromes for bit-flip and phase-flip are independent, in this special case, the product of the two errors $\hat{\sigma}_{z,k}\hat{\sigma}_{x,k} = i\hat{\sigma}_{y,k}$ is also a correctable error.

The two codes presented here along with the Shor code and the five-qubit code mentioned above are examples of a broad class of QEC codes called the Stabilizer codes. The Stabilizer formalism provides a tractable way to deal with Knill-Laflamme conditions, error syndromes and even gates on the logical qubits in a compact notation. However, in this brief introduction, we will not delve into a discussion of this formalism. Instead, we move on to some of the pitfalls associated with QEC codes.

2.1.3 Failure modes of QEC and fault tolerance

This sub-section is dedicated to the discussion of the failure modes associated with QEC codes. We study these issues with the example of the Steane code in mind. As stated in the last sub-section, the Steane code requires seven encoding qubits and six ancillary qubits, i.e. a total of 13 qubits, for realizing a **single** logical qubit. The state of the art programmable quantum processors, as of writing of this thesis, have a maximum of 53 qubits [Arute *et al.*, 2019]. Moreover, as shown in Fig. 2.3, there are multiple sources of errors that the code cannot address. For example, especially in superconducting circuits, it is very common to have spurious interactions between various qubits of a quantum processor. This would lead to uncorrectable two-qubit errors. Additionally, since qubits are

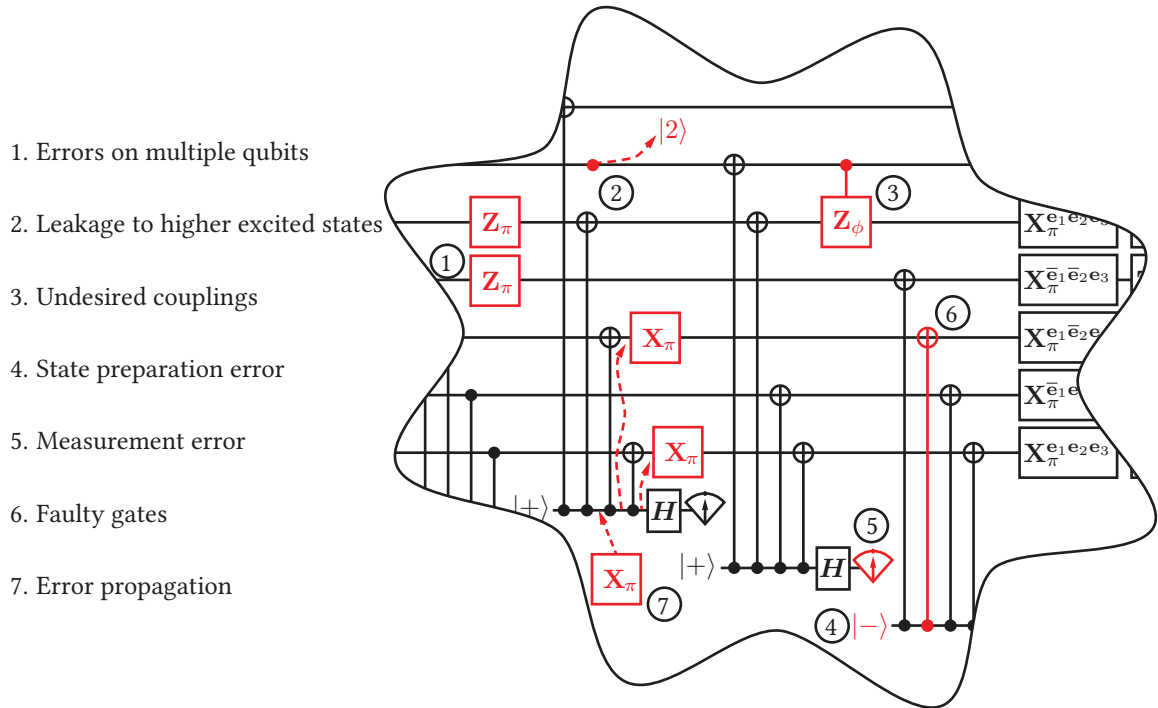


Figure 2.3: Zoomed in portion of Fig. 2.2 with different failure modes marked in red. These failure modes affect any QEC code in general and get worse with increasing hardware overhead. For example, having more encoding qubits leads to a higher probability of failure modes 1, 2 and 3. More ancillary qubits lead to higher probability of failure modes 4, 5 and 6. Moreover, entanglement between the encoding qubits and an ancillary qubit may result in errors on the ancillary qubit converting to added errors on the encoding qubit. This is called error propagation (failure mode 7). These failure modes need to be carefully considered before attempting to implement QEC. Figure inspired from [Petrenko, 2016].

typically implemented as two-level approximation of a multi-level system e.g. transmon, there is some probability associated with the qubits leaking out of the $|0\rangle, |1\rangle$ manifold. Moreover state preparation and measurement (SPAM) errors and erroneous gates also degrade the fidelity of real-world implementations. Apart from these errors affecting individual qubits, one also has to be careful about error propagation. An error on a single qubit is copied over to other qubits when we apply multi-qubit gates. These issues are listed pictorially in Fig. 2.3.

In presence of these issues, how does one ensure reliable storage and processing for

quantum information? The answer to this question is explored through the concept of fault-tolerant quantum computation (FTQC). The first step behind FTQC is to perform computation directly on the error corrected logical qubits with the help of the, so called, fault-tolerant operations. These operations are designed to limit the spread of the errors through the system. As a simplified definition, an operation is called fault-tolerant if failure of a single component of the operation leads to only a correctable error on the system. For a broad class of codes which correct all the errors on a single qubit, this essentially means that the failure of single component should cause an error on at-most one qubit. With such fault-tolerant operations, the probability of lowest order uncorrectable error, i.e. an error on two-qubits, is given by cp^2 where p is the probability of failure for each component and c is essentially the number of pairs of points where failure may occur. The next step for FTQC is to use these error-corrected logical qubits and operations, as individual components for another level of error correction. This is called concatenation of the QEC codes. Concatenation is beneficial only if the probability of uncorrectable errors cp^2 in the first layer is less than the probability p of faults in non error corrected components, i.e. $p < p_{\text{threshold}} = 1/c$. Under such conditions, the successive levels of concatenation allow one to perform a given computation with better and better accuracy i.e. in a fault-tolerant manner.

As a particular example, the error threshold for the Steane code is typically estimated to be $p_{\text{threshold}} \approx 10^{-4}$ [Nielsen and Chuang, 2011], i.e. every component of the code should have at least 99.99% accuracy. Considering today's noisy implementation this seems far fetched. The main reason for such a low threshold is the high number of points where the implementation could go wrong. Better codes have been constructed, for example the Surface code [Kitaev, 2003], which execute FTQC without the need of additional concatenation. For superconducting qubits, the error threshold for the Surface code is still around 10^{-2} , i.e. 99% fidelity for every component [Fowler *et al.*, 2012].

In the next section we will study a completely different approach to QEC which minimizes the required hardware, thus reducing the number of points where things could go wrong.

2.2 Hardware efficient encoding

As we discussed in the previous sub-section, the hardware overhead associated with traditional QEC adds many potential failure points, thus leading to very low error thresholds. Moreover, manipulating such a high number of qubits simultaneously is extremely hard in practice. In this section we briefly discuss a few examples of hardware efficient QEC. A more detailed study of one of these codes, the cat code, is undertaken in the next chapter along with the considerations for autonomous error correction.

The immediate goal of hardware efficient QEC is to minimize the hardware required for information encoding as well as error detection and correction. How could we obtain the large Hilbert spaces required for redundant encoding with the minimum hardware? The answer lies with the use of infinite dimensional systems. Many examples of such systems are available. For example, a rigid quantum rotor, a particle in a box, a harmonic oscillator, all have infinitely many energy-eigenstates. In the case of superconducting circuits, the most easily available infinite Hilbert space is that of the harmonic oscillators. Moreover, these oscillators can be engineered with very low error rates in the domain of superconducting circuits. Therefore, here we will focus on QEC codes called bosonic codes which encode information in the Hilbert space of a harmonic oscillators.

Coming from the perspective of traditional QEC, the binomial codes are perhaps the most straight forward class of Bosonic codes [Michael *et al.*, 2016]. These codes encode information in superpositions of Fock states. The most basic example is a code spanned

by

$$|0_L\rangle = \frac{|0\rangle + |4\rangle}{\sqrt{2}} \text{ and } |1_L\rangle = |2\rangle. \quad (2.14)$$

It corrects a set of errors given by $\mathcal{E} = \{\hat{I}, \hat{a}\}$ thus protecting against stochastic photon loss events. More generalized binomial codes can be constructed by utilizing higher Fock states which correct for up to P photon-losses, Q photon gains and dephasing errors to the R^{th} order, an error set given by

$$\mathcal{E} = \{\hat{I}, \hat{a}, \hat{a}^2, \dots, \hat{a}^P, \hat{a}^\dagger, \hat{a}^{\dagger 2}, \dots, \hat{a}^{\dagger Q}, \hat{n}_a, \hat{n}_a^2, \dots, \hat{n}^R\}. \quad (2.15)$$

Moreover, such higher order codes do not require additional harmonic oscillators. This is the power of infinite dimensional Hilbert space. On the other hand, with this encoding, each of the errors in \mathcal{E} requires its own error syndrome measurement. Moreover, utilizing higher and higher Fock states to correct more errors brings with it the higher error rates associated with occupying these Fock states, since the rate of amplitude damping for the n^{th} Fock state is n times higher. This increase in error probability is the overhead associated with these harmonic oscillator. In addition, the operators in \mathcal{E} are not the Kraus operators describing the amplitude-damping error channel which also includes the energy relaxation given by $e^{-\kappa_{1\text{ph}}\tau\hat{a}^\dagger\hat{a}}$. The Binomial codes approximately protect against this energy relaxation error up to the same order in $\kappa_{1\text{ph}}\tau$ as the number of stochastic-photon jumps. However, a unitary operation required for countering the effects of this additional evolution is hard to realize using a Hamiltonian with low-powers of \hat{a} (i.e. lower order in nonlinearity).

Another major class of bosonic codes is the cat codes [Mirrahimi *et al.*, 2014]. Here, information is stored in the superpositions of coherent states distributed symmetrically around the origin of the phase space. For example, a four-component cat code utilizes

$|\pm\alpha\rangle$ and $|\pm i\alpha\rangle$. In order to protect against P photon losses and Q photon gains, one requires a basis of $2(P + Q + 1)$ coherent states. Thus the four-component cat code protects against a single photon loss. The more interesting feature of this code emerges when one considers energy relaxation and dephasing. It turns out, cat codes exponentially suppress these errors as the amplitude $|\alpha|$ of the coherent states increases. It is this property of exponential suppression which makes cat-codes very interesting. The next chapter discusses these codes in much more detail, since they are the central focus of this thesis. In addition, we also develop a two-cavity cousin of the cat codes, called the pair-cat codes. Although these codes increase the hardware complexity slightly, they have some significant advantages over the cat codes.

The final class of bosonic codes that we mention are the Gottesman-Kitaev-Preskill (GKP) codes. These codes are optimized for protection against small displacements in position and momentum of a harmonic oscillator. The information is stored using a periodic lattice formed by the eigenstates of the position operator. The spacing is cleverly chosen such that taking the Fourier transform results in a periodic lattice of momentum eigenstates with the same spacing. Any error that can be expressed as combination of displacements is protected in the case of GKP codes. However, we will not go in further details of these codes in this thesis. An interested reader should refer to the original article [Gottesman *et al.*, 2001] for a detailed introduction. These codes have been recently implemented with ion-trap [Flühmann *et al.*, 2019] and superconducting circuit [Campagne-Ibarcq *et al.*, 2019] architectures.

2.3 Autonomous Quantum Error Correction (AQEC)

Apart from the overhead associated with using multiple quantum systems, measurement based QEC also requires real-time decision making in order to record and process the

measurement outcomes, as well as to apply appropriate feedback on the quantum systems. Moreover, the duty cycle of such a feedback needs to be much shorter than the lifetimes of the quantum systems for the error correction to be effective. As an example, for superconducting quantum systems, this translates to a duty cycle of a few microseconds. Accomplishing such a feat entails a significant overhead in terms of specialized room temperature hardware. The question naturally arises, can this overhead be eliminated? Could the quantum systems correct errors autonomously without the need of real-time decision making? This is the topic of concern for the current section, and, as we mentioned previously, for this whole thesis.

Before discussing AQEC, let us first look at some simple examples of autonomous feedback in the classical domain. Figure 2.4a depicts a finite state machine used for regulating the temperature in a water heater. The action here is similar to the general notion of error correction that we have studied. The controller actively measures temperature, decides on a course of action i.e. to turn the heater on or not, and then feeds back on the system. There is a finite duty cycle associated with such feedback which is set by the wait time in the controller. We call this ‘discrete feedback’. On the other hand, the centrifugal governor shown in Fig. 2.4b autonomously regulates the speed of an engine under variable load. When the speed of the engine is increased, the rotating spherical weights move outward, raising a movable sleeve with them. The movement of the sleeve feeds-back on the engine by closing the fuel supply valve, resulting in decreased speed. If the speed is decreased below the set value then all weights move inwards which lowers the sleeve, and, as a result, the fuel supply and thus the engine speed is increased. We call such a real-time feedback as the ‘continuous feedback’. The example of the centrifugal governor also illustrates one of essential requirements behind continuous feedback. If there is very little friction in the system, then the weights tend to oscillate resulting in unstable feedback. Therefore, friction, in many examples, holds a key to continuous

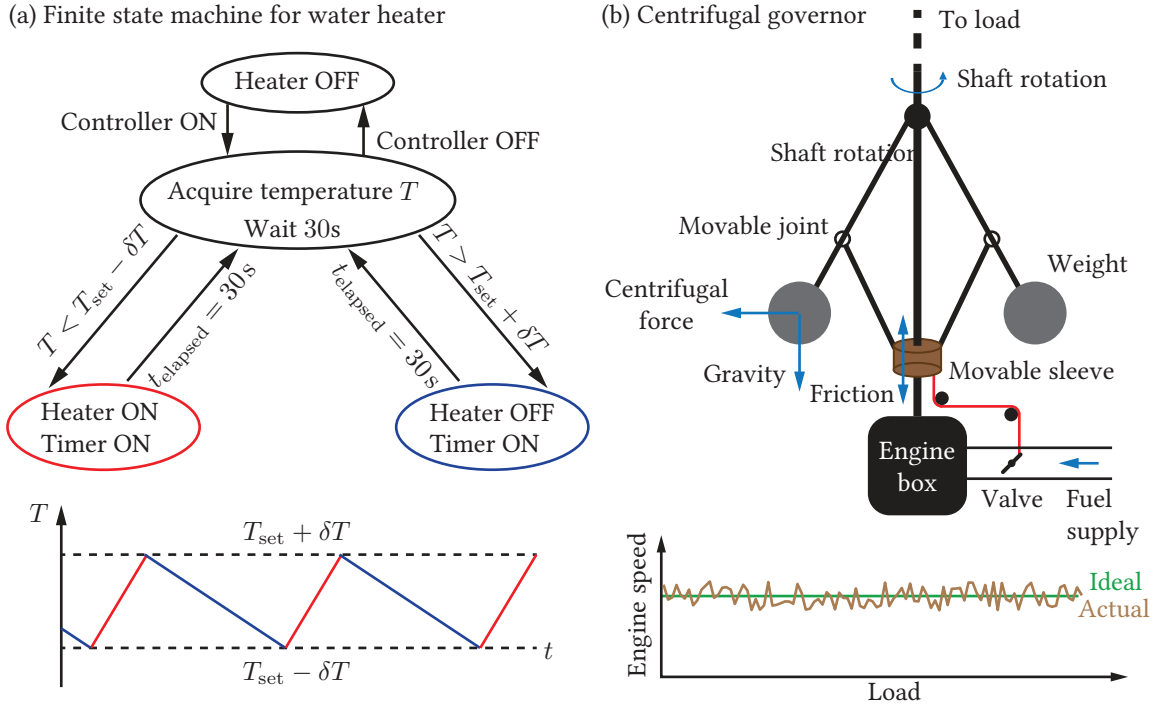


Figure 2.4: Examples of autonomous feedback in classical systems. (a) Stabilization of water temperature with a finite state machine. A sensor records the temperature of the water, a controller processes this data by comparing it with $T_{\text{set}} \pm \delta T$. If $T < T_{\text{set}}$ ($T > T_{\text{set}}$) then the heater is turned ON (OFF) for a specific amount of time before measuring the temperature again. Such a feedback, where measurement, data processing and correction are implemented through separate mechanisms, is called a discrete feedback. (b) Regulation of engine speed in presence of variable load using a centrifugal governor. The two spherical weights rotate with the engine shaft. When the engine speed is increased, the spheres move outward, which moves the attached sleeve upwards. As a result of the sleeve movement, the fuel supply valve is automatically closed, resulting in lesser fuel supply to the engine. The drop in fuel supply results in lower speed of the engine thus resulting regulation of the speed. In case the speed of the engine is lower than the set value, then the whole chain of event reverses, resulting in higher fuel supply, and hence increase in speed. Therefore, the centrifugal governor autonomously controls the engine speed. An additional requirement for this autonomous feedback to work properly is the presence of sufficient friction in the system. In absence of friction, the massive spheres will start oscillating when the engine speed is changed, resulting in an unstable feedback.

feedback mechanisms.

Taking inspiration from these classical feedback mechanisms, let us turn our attention to building such discrete and continuous autonomous feedback for QEC.

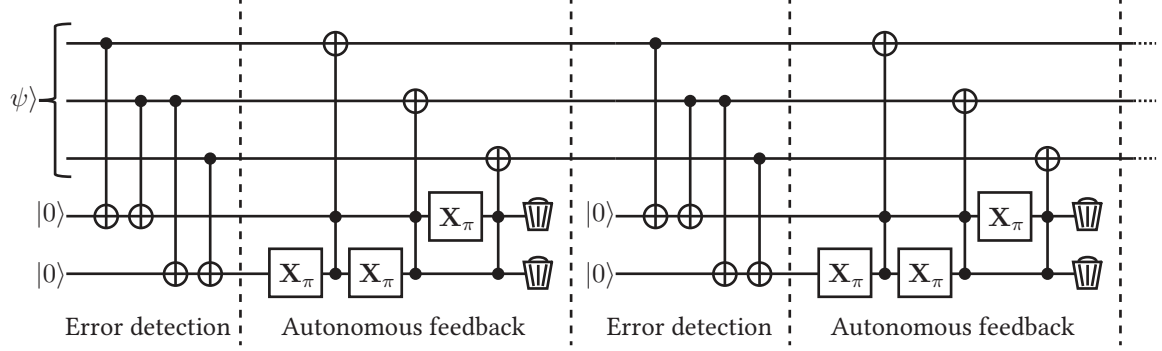


Figure 2.5: Discrete autonomous feedback for the bit-flip code. The error syndrome is mapped on to the ancilla using the same protocol as previously presented in Fig. 2.1. However, instead of measuring the ancillary qubits, the feedback is executed in an autonomous fashion, by applying ancilla rotations and the Toffoli gates. Following the feedback, the ancillary qubits are discarded.

Discrete AQEC

We first give a simplified picture for building discrete AQEC. In Sec. 2.1.1 we provided an explicit construction of a two-step error detection and recovery mechanism for a set of errors \mathcal{E} on a QEC code \mathcal{C}_0 . This was accomplished by measuring the projectors $\hat{P}_{\mathcal{C}_k}$ on the orthogonal error spaces \mathcal{C}_k as error syndromes, followed by a unitary operation \hat{U}_K^\dagger which corrects for the detected K^{th} error. However, it is possible to accomplish the error correction without first knowing the outcome of the measurement. Imagine an ancillary system with Hilbert space \mathcal{H}_A such that $\dim(\mathcal{H}_A) \geq$ the number of error operators \hat{F}_k . Now the error correction can be accomplished in the following manner. Step 1: Apply a unitary operation \hat{U}_{map} to map the errors on the ancillary system

$$\hat{U}_{\text{map}} = \sum_k \hat{P}_{\mathcal{C}_k} \otimes \left(|k\rangle\langle 0| + |0\rangle\langle k| + \sum_{l \neq \{0, k\}} |l\rangle\langle l| \right) + \hat{I}_{\mathcal{H} - \sum_k \mathcal{C}_k} \otimes \hat{I}_{\mathcal{H}_A} \quad (2.16)$$

which will entangle the k^{th} excited state $|k\rangle$ of the ancillary system with the k^{th} error space \mathcal{C}_k . In a measurement based feedback scheme, one would measure the state of the

system at this point to project on to a single error K and then apply the feedback unitary \hat{U}_K^\dagger . However, here we will take a different route. Step 2: Apply a feedback unitary of the form

$$\hat{U}_{\text{feedback}} = \sum_k U_k^\dagger \otimes |k\rangle\langle k|, \quad (2.17)$$

without performing any measurement. Under the action of this unitary, the states in error spaces \mathcal{C}_k will revert back to the original code space \mathcal{C}_0 . Additionally the principal system will disentangle from the ancillary system leaving it in a random superposition state depending on which errors occurred. Therefore, in order to begin another round of error correction, we undertake Step 3: Reset the ancillary system to its ground state i.e. dump the entropy created in the ancilla. This approach detects and corrects the errors on the system without having the necessity of real-time classical feedback. Of-course one might object that resetting the ancillary system still needs measurement and feedback. However, it is possible to reset the ancillary system with the help of an engineered dissipation instead as we see later. Moreover, step 1 and 2 need not be separate. A single unitary given by $\hat{U}_{\text{feedback}}\hat{U}_{\text{map}}$ is enough. An example of discrete autonomous feedback in case of the bit-flip code is presented in Fig. 2.5. The error detection step is the same as the one we studied previously. However, the correction is implemented with the help of a feedback unitary in an autonomous fashion as shown. After the feedback is finished the entropy of the ancillary qubits is dumped as shown by the dustbin symbol.

Continuous AQEC

Next, we discuss how to build continuous feedback mechanisms for AQEC. This discussion is a simplified version of a formal construction by Lihm *et al.* [2018]. The task of continuous protection is accomplished by engineering additional dissipation on the system. At first glance, adding dissipation to the system seems counter intuitive since that

might increase the errors on the system. However, such dissipation, if appropriately engineered, can effectively suppress errors on the system. The Lindblad jump operators $\hat{L}_{k,\text{eng}}$ for such engineered dissipation are given by

$$\hat{L}_{k,\text{eng}} = \sqrt{\Gamma_{k,\text{eng}}} (|0_L\rangle\langle 0_L^k| + |1_L\rangle\langle 1_L^k|), \quad (2.18)$$

where $\Gamma_{k,\text{eng}}$ is the rate of the k^{th} engineered dissipation. The express purpose of this operator is to dissipate all the error spaces \mathcal{C}_k to the original code space \mathcal{C}_0 in a coherent manner. The complete Lindblad master equation of the system in presence of the engineered dissipation is then given by

$$\dot{\rho} = -\frac{i}{\hbar}[\hat{H} + \hat{H}_{\text{eng}}, \rho] + \sum_j \mathcal{D}[\hat{L}_j]\rho + \sum_k \mathcal{D}[\hat{L}_{k,\text{eng}}]\rho. \quad (2.19)$$

Here \mathcal{H} is the intrinsic Hamiltonian and \hat{L}_j are the Lindblad jump operators corresponding to the intrinsic dissipation. We have also added an engineered Hamiltonian \hat{H}_{eng} in order to cancel the effect of any spurious evolution under the intrinsic Hamiltonian. If the Kraus operators describing the evolution under the intrinsic dissipation satisfy the Knill-Laflamme for our QEC code and all the rates of intrinsic dissipation $\Gamma \ll \Gamma_{\text{eng}}$, the rates of engineered dissipation, then it is possible to show that the errors on the system are effectively suppressed. We refer the interested reader to [Lihm *et al.*, 2018] for a more formal discussion and a proof.

In many cases, the Kraus operators describing the density matrix evolution only approximately satisfy the Knill-Laflamme conditions. This is especially true for the bosonic codes like the binomial codes and the cat codes. In those cases additional dissipation operators are needed in order to make sure that the system does not leak to the rest of the Hilbert space, i.e. to $\mathcal{H} - \sum_k \mathcal{C}_k$. Lihm *et al.* also indicate how to construct these additional

dissipation operators. In this thesis, however, we will not go in the details of this general construction. Instead, we focus on the particular example of the cat codes and the pair-cat codes.

Being able to find out the dissipation operators, required for protecting against the errors affecting a system, is very encouraging towards our goal of realizing the error protected logical qubit. At the same time, writing such operators is just the first step. The more challenging part is to engineer the required dissipation operators from using the set of interactions that are naturally available in a system. For example, the dissipation operators needed for the bit-flip code are given by

$$\hat{L}_{1,\text{eng}} = \sqrt{\Gamma_{1,\text{eng}}} (|0, 0, 0\rangle\langle 1, 0, 0| + |1, 1, 1\rangle\langle 0, 1, 1|) \quad (2.20)$$

$$\hat{L}_{2,\text{eng}} = \sqrt{\Gamma_{2,\text{eng}}} (|0, 0, 0\rangle\langle 0, 1, 0| + |1, 1, 1\rangle\langle 1, 0, 1|) \quad (2.21)$$

$$\hat{L}_{3,\text{eng}} = \sqrt{\Gamma_{3,\text{eng}}} (|0, 0, 0\rangle\langle 0, 0, 1| + |1, 1, 1\rangle\langle 1, 1, 0|). \quad (2.22)$$

A scheme for implementing the bit-flip code dissipation operators shown above is presented in [Cohen and Mirrahimi, 2014]. It requires three transmon qubit modes, one low- Q oscillator mode and four off-resonant pumps. In addition, careful tuning of the parameters is required for the scheme to not introduce any additional dephasing errors on the system since those errors are not corrected by the code. This highlights some of the difficulties encountered while implementing continuous AQEC. The Steane code required for correcting all the single-qubit errors, requires even more engineered dissipation operators to account for all the error spaces. As a result, it is immediately clear that the hardware efficient QEC codes are better suited for continuous error correction. However, even such codes often require highly nonlinear interactions for implementing the corrective dissipation. Therefore, our attempts to implement the continuous codes focus on two aspects: (i) obtaining higher-order nonlinear interaction from easily available lower-

order interactions and (ii) proposal for a new code, the pair-cat code, which allows us to implement the required dissipation operators using the technology developed in this thesis.

2.4 Summary and prelude to the next chapter

This chapter has provided an introduction to QEC along with a discussion about FTQC, hardware efficient encoding and most importantly, autonomous QEC. Some of the key concepts from this chapter are as follows:

- (i) The Knill-Laflamme conditions state that, an error on an encoding is correctable, if and only if, the error maps the code space to itself or an orthogonal sub-space without any distortions. Moreover, if a code space satisfies the Knill-Laflamme conditions for a given set of error operators, then an explicit recovery mechanism can be constructed. That Knill-Laflamme conditions are necessary and sufficient for QEC.
- (ii) If a set of error operators are correctable, then all the superpositions of those operators are correctable. As a result, quantum errors, in many cases, can be treated as discrete.
- (iii) Redundantly encoding information using multiple qubits results in a significant hardware overhead. This hardware overhead can be minimized by utilizing infinite dimensional Hilbert space of the harmonic oscillators to encode information with the help of bosonic QEC codes.
- (iv) Every measurement based quantum error correction process can be converted to discrete AQEC given the availability of necessary unitary operations and the reset of the ancillary qubits.

- (v) Errors can be suppressed in a continuous fashion by engineering specific dissipation operators that map the error spaces back to the code space and prevent the leakage to the rest of the Hilbert space. Such continuous error correction can be especially powerful since only always-on continuous wave tones are required for protecting against errors. This is expected to result in many hardware simplifications.

With our goal of autonomous error correction in mind, the next chapter (Ch. 3) presents an introduction to the hardware efficient cat codes, with a special emphasis on the autonomous protection of these states against energy relaxation and dephasing errors. Chapters 4 to 6 cover the requisite Hamiltonian engineering techniques for this autonomous correction. The pair-cat code, which is our candidate for implementing the fully autonomous correction against all the errors to the first order, is introduced in the final chapter (Ch. 7). Building on the Hamiltonian engineering techniques developed in the rest of the thesis, we provide an explicit experimental proposal for implementation of this code.

Chapter 3

Cat codes: Hardware efficiency and autonomous error correction

The last chapter explained the basic principles of QEC along with some examples of QEC codes and their limitations. As a result, it emerged that hardware-efficient encoding and autonomous error correction present significant benefits over traditional QEC codes. In this chapter, we study a family of codes, called the cat codes, which store information in the Hilbert space of a harmonic oscillator and allow for protection against photon loss errors (Sec. 3.1). Through our discussion, it becomes clear that the protection of this code against other errors, e.g. the energy relaxation and dephasing, will greatly benefit from an autonomous driven-dissipative stabilization approach. A detailed explanation of such driven-dissipative stabilization is provided in Sec. 3.2. This is followed by Sec. 3.3 which briefly considers some recent developments that show where the cat codes fit into the big picture of FTQC. Finally Sec. 3.4 provides a summary of this chapter and a prelude to the next chapter.

3.1 The cat codes

The cat codes store information in the superpositions of the coherent states of a single harmonic oscillator. As we discussed in Sec. 1.2.2, the coherent states are eigenstates of the destruction operator with $\hat{a}|\alpha\rangle = \alpha|\alpha\rangle$ where $\alpha \in \mathbb{C}$ is the complex amplitude characterizing the coherent state. In the Fock basis, these states are represented as

$$|\alpha\rangle = e^{-\frac{|\alpha|^2}{2}} \sum_{n=0}^{\infty} \frac{\alpha^n}{\sqrt{n!}} |n\rangle. \quad (3.1)$$

In order to store information with these states we first need to check if they are orthogonal to each other. The overlap of two coherent states can be obtained using the Fock-basis representation, and is given by

$$\langle\beta|\alpha\rangle = e^{-\frac{1}{2}(|\alpha|^2+|\beta|^2-2\beta^*\alpha)} \Rightarrow |\langle\beta|\alpha\rangle|^2 = e^{-|\alpha-\beta|^2}. \quad (3.2)$$

It is clear that two coherent states are never orthogonal to each other. However, as $|\alpha - \beta|$ increases, the overlap between the coherent states exponentially decreases. As an example, for $|\alpha - \beta| = 3$, the overlap is $|\langle\beta|\alpha\rangle|^2$ is around 0.012%. Therefore, it should be possible to utilize well-separated coherent states for storing quantum information. The cat-code in particular utilizes coherent states that are placed in a circle around the origin of the phase space. In the next sub-section we study the two-component cat states which store one-bit worth of information. This is followed by a discussion of four-component cat states and the protection against the photon loss errors in a hardware efficient manner using such states. We also discuss the effect of energy relaxation and dephasing errors on these states.

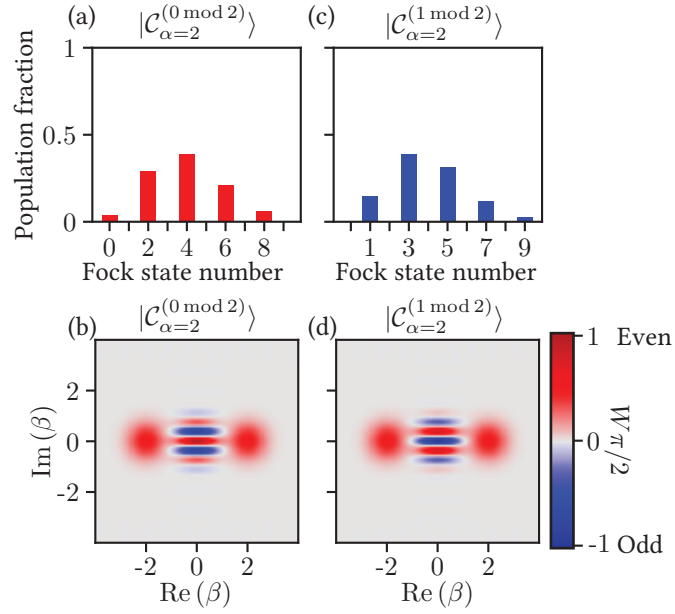


Figure 3.1: Panels (a) and (b) show the Fock state population distribution and the ideal Wigner function of the two-component cat state $|\mathcal{C}_{\alpha=2}^{(0 \bmod 2)}\rangle$. The bars in panel (a) are colored red to indicate that only even states participate in a $(0 \bmod 2)$ cat state. The distributions are centered around the average photon-number $\bar{n} = |\alpha|^2 = 4$ which essentially the size of constituent coherent states. Panels (c) and (d) show the Fock state population distribution and the ideal Wigner function of the two-component cat state $|\mathcal{C}_{\alpha=2}^{(1 \bmod 2)}\rangle$. The bars in panel (c) are colored blue to indicate that only odd states participate in a $(1 \bmod 2)$ cat state. The photon-number parity of the respective states is also inferred from the value of the Wigner function at $\beta = 0$.

3.1.1 Two-component cats

Two-component cat states store information in the superpositions of two coherent states $|\pm \alpha\rangle$. We define the even and odd superpositions of these coherent states as

$$\begin{aligned} |\mathcal{C}_{\alpha}^{(0 \bmod 2)}\rangle &= N_{\alpha}^{(0 \bmod 2)} (|\alpha\rangle + |-\alpha\rangle), \\ |\mathcal{C}_{\alpha}^{(1 \bmod 2)}\rangle &= N_{\alpha}^{(1 \bmod 2)} (|\alpha\rangle - |-\alpha\rangle), \end{aligned} \quad (3.3)$$

respectively with the letter \mathcal{C} in this notation indicating a cat-state. The significance of $(0 \bmod 2)$ and $(1 \bmod 2)$ will be clear once we expand these states in terms of the con-

tributing Fock states. The normalization constants $N_\alpha^{(p \bmod 2)}$ are given by

$$N_\alpha^{(p \bmod 2)} = \frac{1}{\sqrt{2(1 + (-1)^p \times e^{-2|\alpha|^2})}}. \quad (3.4)$$

The $\pm 2e^{-2|\alpha|^2}$ term in the denominator is the consequence of the nonzero overlap of the coherent states, and, for a reasonably large $|\alpha|$, $N_\alpha^{(p \bmod 2)} \approx 1/\sqrt{2}$. Now, let us represent these two-component cat states in terms of the contributing Fock states. We obtain

$$|\mathcal{C}_\alpha^{(0 \bmod 2)}\rangle = 2N_\alpha^{(0 \bmod 2)} e^{-\frac{|\alpha|^2}{2}} \sum_{n=0}^{\infty} \frac{\alpha^{2n}}{\sqrt{(2n)!}} |2n\rangle \quad (3.5)$$

$$|\mathcal{C}_\alpha^{(1 \bmod 2)}\rangle = 2N_\alpha^{(1 \bmod 2)} e^{-\frac{|\alpha|^2}{2}} \sum_{n=0}^{\infty} \frac{\alpha^{2n+1}}{\sqrt{(2n+1)!}} |2n+1\rangle. \quad (3.6)$$

Therefore, $|\mathcal{C}_\alpha^{(0 \bmod 2)}\rangle$ is a superposition of the even Fock states and $|\mathcal{C}_\alpha^{(1 \bmod 2)}\rangle$ is a superposition of the odd Fock states. The notation $(k \bmod 2)$ implies that only the Fock states corresponding to the k^{th} residual class of 2 contribute. Finally, it should be noted that these cat states are the eigenstates of the parity operator $\hat{\Pi} = e^{i\pi\hat{a}^\dagger\hat{a}}$ with

$$\begin{aligned} \hat{\Pi}|\mathcal{C}_\alpha^{(0 \bmod 2)}\rangle &= +1|\mathcal{C}_\alpha^{(0 \bmod 2)}\rangle, \\ \hat{\Pi}|\mathcal{C}_\alpha^{(1 \bmod 2)}\rangle &= -1|\mathcal{C}_\alpha^{(1 \bmod 2)}\rangle. \end{aligned} \quad (3.7)$$

We have provided a pictorial representation of the Fock-state populations and Wigner functions of these states in Fig. 3.1 assuming $\alpha = 2$. The Fock-state distributions have an average photon-number (center of the distribution) of $\bar{n} = |\alpha|^2 = 4$. The parameter $\bar{n} = |\alpha|^2$ is often regarded as the size of the coherent states and, by extension, the cat states, for this reason.

It is possible to store information in the manifold spanned by the two-component cat states. We declare our logical 0 and logical 1 as $|0_L\rangle = |\mathcal{C}_\alpha^{(0 \bmod 2)}\rangle$ and $|1_L\rangle = |\mathcal{C}_\alpha^{(1 \bmod 2)}\rangle$.

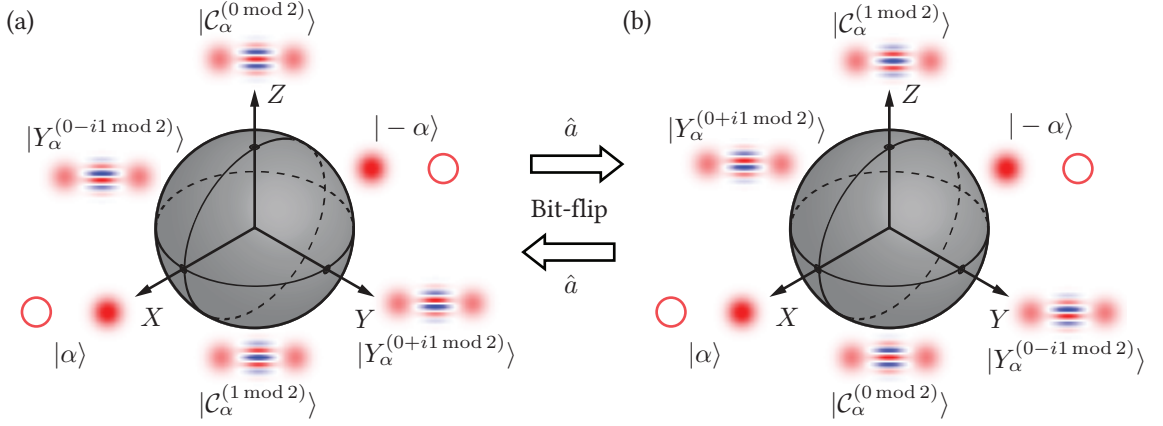


Figure 3.2: Information encoding and the effect of a photon loss for two-component cat states. (a) $|\mathcal{C}_\alpha^{(0 \bmod 2)}\rangle$ is taken to be $|0_L\rangle$ and $|\mathcal{C}_\alpha^{(1 \bmod 2)}\rangle$ is taken as $|1_L\rangle$ for the purpose of encoding. The eigenstates of the logical $\hat{\sigma}_x$ operator for this encoding are simply the individual coherent states with $|\pm_L\rangle = |+\alpha\rangle$. The eigenstates of the logical $\hat{\sigma}_y$ are the parity less Yurke-Stoler cats, here denoted by $|Y_\alpha^{(0\pm i1 \bmod 2)}\rangle$. (b) The effect of a single photon loss on the encoding presented in panel (a). As shown, the eigenstates of $\hat{\sigma}_z$ and $\hat{\sigma}_y$ of the logical qubit are flipped, however, the eigenstates of $\hat{\sigma}_x$ remain unaffected since coherent states are immune to photon loss. As a result, photon loss events create a logical bit-flip which is random 180° rotation around the x -axis of the Bloch sphere. A photon loss error also leads some distortion of the cat state manifold. However, such distortion is suppressed for a large enough $|\alpha|$ (see text).

Note that choosing such a basis has an advantage of making the two logical states completely orthogonal to each other. This logical encoding is represented in panel (a) of Fig. 3.2. As shown in the figure, the eigenstates of the logical $\hat{\sigma}_x$ operator are

$$|\pm_L\rangle = \frac{|\mathcal{C}_\alpha^{(0 \bmod 2)}\rangle \pm |\mathcal{C}_\alpha^{(1 \bmod 2)}\rangle}{\sqrt{2}} \approx |\pm\alpha\rangle \text{ for } e^{-2|\alpha|^2} \ll 1. \quad (3.8)$$

Similarly, the eigenstates of the logical $\hat{\sigma}_y$ operator are the so called Yurke-Stoler cats [Yurke and Stoler, 1986] which we here denote as $|Y_\alpha^{(0\pm i1 \bmod 2)}\rangle$. The notation $(0 \pm i1 \bmod 2)$ implies a superposition of a $(0 \bmod 2)$ and $\pm i$ times the $(1 \bmod 2)$ cat, i.e.

$$|Y_\alpha^{(0\pm i1 \bmod 2)}\rangle = \frac{|\mathcal{C}_\alpha^{(0 \bmod 2)}\rangle \pm i|\mathcal{C}_\alpha^{(1 \bmod 2)}\rangle}{\sqrt{2}} \approx \frac{|\alpha\rangle \mp i|-\alpha\rangle}{\sqrt{2}} \text{ for } e^{-2|\alpha|^2} \ll 1. \quad (3.9)$$

Here we have ignored a global phase while representing in terms of $|\pm\alpha\rangle$. An expansion of the $|Y_\alpha^{(0\pm i1 \bmod 2)}\rangle$ cats in terms of the contributing Fock states shows that both even and odd Fock states contribute. Therefore, these are not the eigenstates of the parity operator. As a result, these states are sometimes termed as the parity-less cats.

Figure 3.2b shows the effect of losing a single-photon on our code space. We model this error by acting the destruction operator \hat{a} on the states in the code space. As one would expect a single photon loss takes an even state into an odd state and vice versa. That is

$$\begin{aligned}\hat{a}|\mathcal{C}_\alpha^{(0 \bmod 2)}\rangle &= \frac{\alpha N_\alpha^{(0 \bmod 2)}}{N_\alpha^{(1 \bmod 2)}} |\mathcal{C}_\alpha^{(1 \bmod 2)}\rangle \\ \text{and } \hat{a}|\mathcal{C}_\alpha^{(1 \bmod 2)}\rangle &= \frac{\alpha N_\alpha^{(1 \bmod 2)}}{N_\alpha^{(0 \bmod 2)}} |\mathcal{C}_\alpha^{(0 \bmod 2)}\rangle.\end{aligned}\quad (3.10)$$

The photon loss also flips the eigenstates of logical $\hat{\sigma}_y$ operator as shown in the figure. Only the coherent states, which are approximately the eigenstates of the logical $\hat{\sigma}_x$ operator ($\hat{a}^\dagger + \hat{a}$) for a large enough α , remain unchanged. Therefore, the loss of a single photon is essentially a logical bit-flip error in the code space of the two-component cat states, and we are not protected from such error. In addition, there is a slight distortion of the code-space since the constants $\frac{\alpha N_\alpha^{(0 \bmod 2)}}{N_\alpha^{(1 \bmod 2)}}$ and $\frac{\alpha N_\alpha^{(1 \bmod 2)}}{N_\alpha^{(0 \bmod 2)}}$ are not equal to each other. For large cat sizes, the difference is exponentially suppressed and, thus, we ignore such distortion. Moreover, the rate of this bit-flip error is amplified since the occupation of higher Fock states results in faster photon losses. Formally, the bit flip rate is given by

$$\begin{aligned}\Gamma_{\text{L-flip}} &= \left| \langle \mathcal{C}_\alpha^{(0 \bmod 2)} | \sqrt{\kappa_{1\text{ph}}} \hat{a} | \mathcal{C}_\alpha^{(1 \bmod 2)} \rangle \right|^2 + \left| \langle \mathcal{C}_\alpha^{(1 \bmod 2)} | \sqrt{\kappa_{1\text{ph}}} \hat{a} | \mathcal{C}_\alpha^{(0 \bmod 2)} \rangle \right|^2 \\ &\approx 2|\alpha|^2 \kappa_{1\text{ph}} \text{ for } e^{-2|\alpha|^2} \ll 1.\end{aligned}\quad (3.11)$$

Here we have used $\Gamma_{\text{L-flip}}$ to denote the rate of logical bit-flip error and $\kappa_{1\text{ph}}$ is the rate

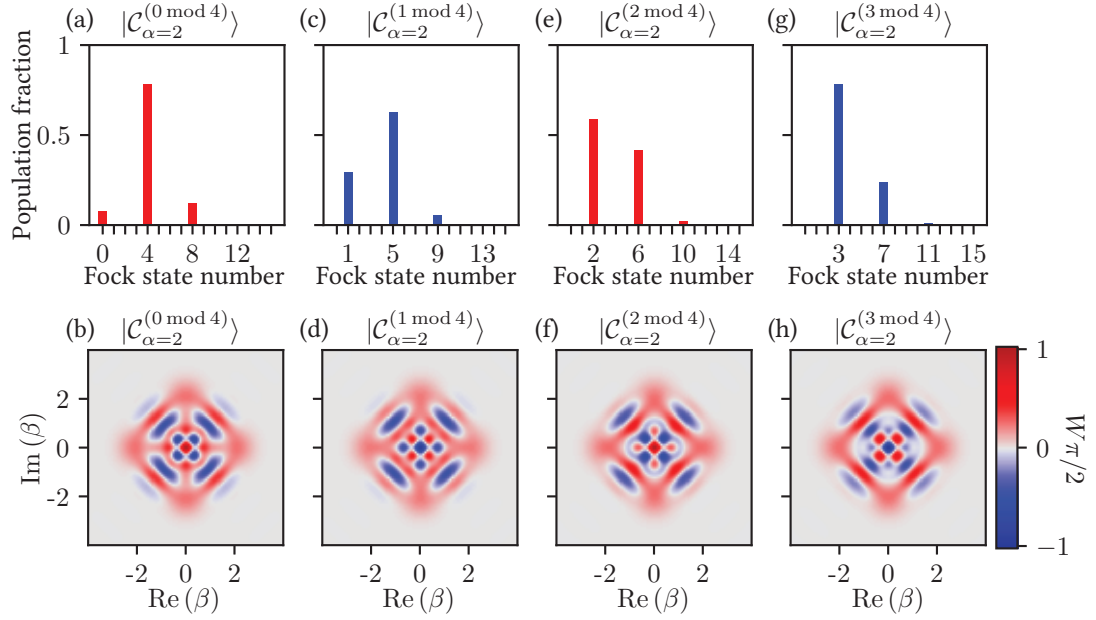


Figure 3.3: Fock state population fractions and ideal Wigner functions of four-component cat states. Panels (a), (b) correspond to the $|\mathcal{C}_{\alpha=2}^{(0 \bmod 4)}\rangle$ where only $(4n)^{\text{th}}$ Fock states are occupied. Panels (c), (d) correspond to $|\mathcal{C}_{\alpha=2}^{(1 \bmod 4)}\rangle$ cat states with $(4n + 1)^{\text{th}}$ Fock states occupied. Similarly, panels (e), (f) and (g), (h) correspond to $|\mathcal{C}_{\alpha=2}^{(2 \bmod 4)}\rangle$ and $|\mathcal{C}_{\alpha=2}^{(3 \bmod 4)}\rangle$ cat states respectively, with $(4n + 2)^{\text{th}}$ and $(4n + 3)^{\text{th}}$ Fock states occupied. The Fock state distributions are again centered around average photon-number $\bar{n} = 4$.

of photon loss for the harmonic oscillator. Therefore, the rate of bit-flips increases with the increasing size ($|\alpha|^2$) of the cat-states. In the next sub-section, we discuss the four-component cat states which offer protection against the photon loss error as well.

3.1.2 Four-component cats and protection against photon loss

The four-component cat states are equal superpositions of four-coherent states $|\pm\alpha\rangle$ and $|\pm i\alpha\rangle$ given by

$$|\mathcal{C}_{\alpha}^{(k \bmod 4)}\rangle = N_{\alpha}^{(k \bmod 4)} [|\alpha\rangle + (-1)^k |-\alpha\rangle + (-i)^k |i\alpha\rangle + (i)^k | -i\alpha\rangle], \quad (3.12)$$

where $k \in \mathbb{W}$. Note that there are four such states since $(k \bmod 4) \in \{0, 1, 2, 3\}$. The normalization constants $N^{(k \bmod 4)}$ are

$$N_{\alpha}^{(k \bmod 4)} = \frac{1}{2\sqrt{1 + (-1)^k e^{-2|\alpha|^2} + 2e^{-|\alpha|^2} \operatorname{Re}(i^k e^{-i|\alpha|^2})}} \approx \frac{1}{2} \text{ for } e^{-2|\alpha|^2} \ll 1. \quad (3.13)$$

In order to keep our expressions simple, we will repeatedly make use of the $N_{\alpha}^{(k \bmod 4)} \approx 1/2$ approximation. The expansion of four-component cat states in terms of the Fock states is

$$|\mathcal{C}_{\alpha}^{(k \bmod 4)}\rangle = 4N_{\alpha}^{(k \bmod 4)} e^{-\frac{|\alpha|^2}{2}} \sum_{n=0}^{\infty} \frac{\alpha^{4n+k}}{\sqrt{(4n+k)!}} |4n+k\rangle. \quad (3.14)$$

It is clear from these expressions that only the $(4n+k)^{\text{th}}$ Fock states participate in a $(k \bmod 4)$ cat state. The Fock state population distribution and the Wigner functions of the four-component cat states are plotted in Fig. 3.3 assuming $\alpha = 2$. Along with the photon-number parity $\hat{\Pi}$, these states are also the eigenstates of the, so-called, super-parity $\sqrt{\hat{\Pi}} = e^{i\pi\hat{a}^{\dagger}\hat{a}/2}$ with $\sqrt{\hat{\Pi}}|\mathcal{C}_{\alpha}^{(k \bmod 4)}\rangle = i^k |\mathcal{C}_{\alpha}^{(k \bmod 4)}\rangle$. Note that there are four distinct eigenvalues of the super-parity operator.

The availability of two even-parity and two odd-parity states allows us to engineer protection against the photon loss errors. Let us first discuss the effect of losing a single photon on the four-component cat states. We again utilize the destruction operator \hat{a} to model the loss. Action of \hat{a} on the cat state $|\mathcal{C}_{\alpha}^{(k \bmod 4)}\rangle$ is given by

$$\hat{a}|\mathcal{C}_{\alpha}^{(k \bmod 4)}\rangle = \alpha \frac{N_{\alpha}^{(k \bmod 4)}}{N_{\alpha}^{(k-1 \bmod 4)}} |\mathcal{C}_{\alpha}^{(k-1 \bmod 4)}\rangle \approx \alpha |\mathcal{C}_{\alpha}^{(k-1 \bmod 4)}\rangle. \quad (3.15)$$

This implies that the cat states are connected to each other in a cycle with

$$(3 \bmod 4) \rightarrow (2 \bmod 4) \rightarrow (1 \bmod 4) \rightarrow (0 \bmod 4) \rightarrow (-1 \bmod 4) = (3 \bmod 4)$$

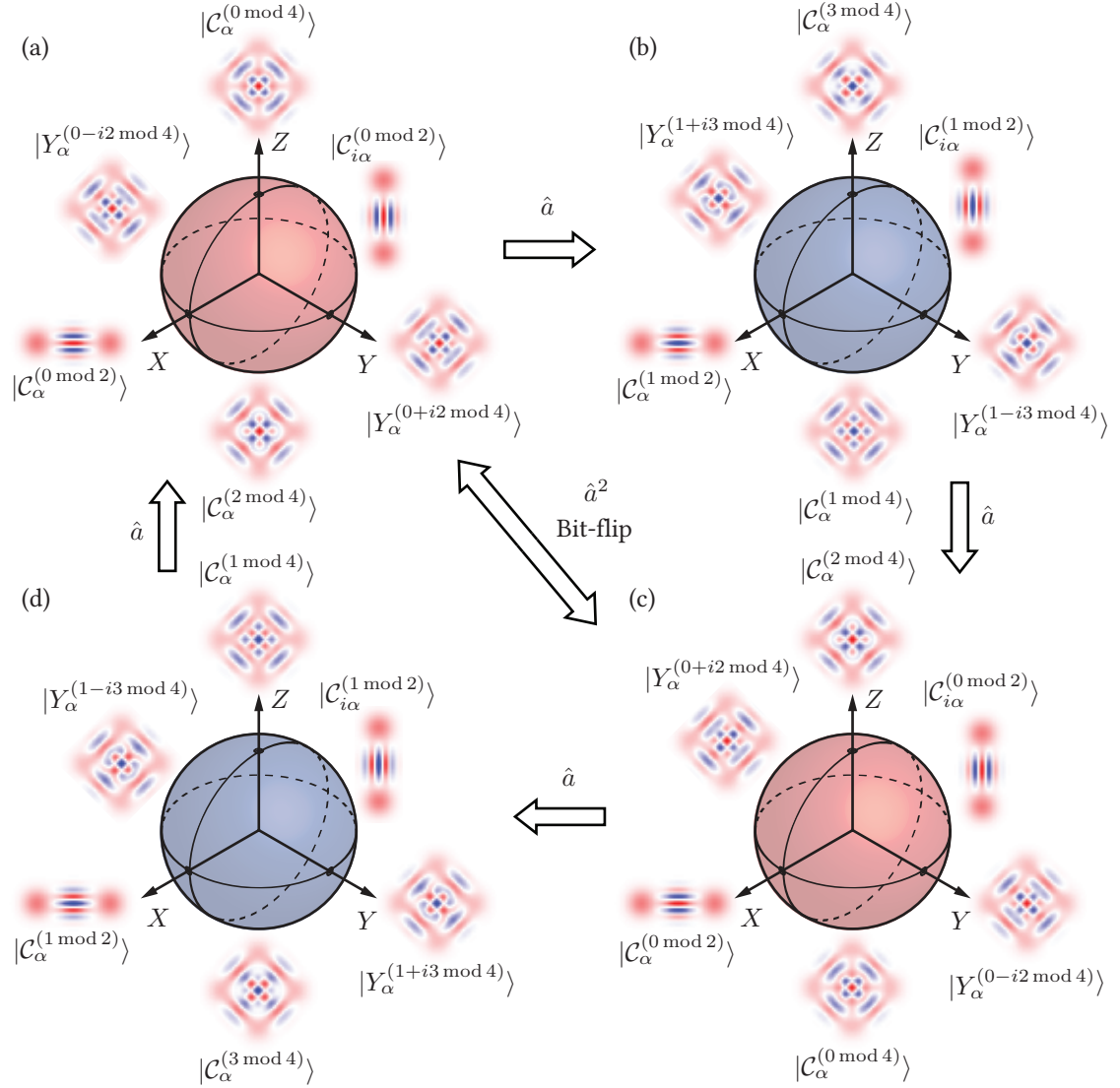


Figure 3.4: Four-component cat state encoding and effect of photon loss. (a) Encoding in an even manifold with the six cardinal states and their ideal Wigner functions as shown. (b) Effect of a photon loss on the encoding manifold. The system shifts to an orthogonal odd-manifold. (c) Effect of a second photon loss. The system reverts back to an even manifold, however, undergoes an effective Bit-flip compared to the original encoding manifold. (d) A third photon loss results in an odd manifold. The encoding here has undergone a bit-flip when compared to the encoding in panel (b). A further photon loss brings the system back to the original manifold. It is possible to retrieve the stored information as long as each of the photon-jumps are tracked. Missing a photon-jump, i.e. loss of two-photons, results in a bit-flip error. Every photon loss event also leads to an additional distortion of the code space which is suppressed for large enough $|\alpha|$ (see Sec. 3.1.3).

under the action of successive photon losses. Therefore, if we encode the information in the even manifold, spanned by $|\mathcal{C}_\alpha^{(0 \bmod 4)}\rangle$ and $|\mathcal{C}_\alpha^{(2 \bmod 4)}\rangle$, then loss of a single photon results in the system going to a completely orthogonal manifold, spanned by $|\mathcal{C}_\alpha^{(3 \bmod 4)}\rangle$ and $|\mathcal{C}_\alpha^{(1 \bmod 4)}\rangle$, leading to a correctable error. In the language of the last chapter (Ch. 2), the code-space

$$\mathcal{C}_\alpha^{\text{even}} = \text{Span}\{|0_L\rangle = |\mathcal{C}_\alpha^{(0 \bmod 4)}\rangle, |1_L\rangle = |\mathcal{C}_\alpha^{(2 \bmod 4)}\rangle\} \quad (3.16)$$

satisfies the Knill-Laflamme conditions in the diagonal form for the set of error operators $\mathcal{E} = \{\hat{F}_0 = \hat{I}, \hat{F}_1 = \hat{a}\}^1$. We denote the error space $\hat{a}\mathcal{C}_\alpha^{\text{even}}$ as $\mathcal{C}_\alpha^{\text{odd}}$. The Bloch-sphere corresponding to $\mathcal{C}_\alpha^{\text{even}}$ and $\mathcal{C}_\alpha^{\text{odd}}$ are depicted in Fig. 3.4, panel a and b respectively. The Bloch spheres in those panels are given red and blue colors in order to associate them with the parity of the respective sub-spaces. In addition, the figure shows the eigenstates of logical $\hat{\sigma}_x$ and $\hat{\sigma}_y$ operators. The $|\pm_L\rangle$ states are two-component cat states which are rotated by $\pi/2$ with respect to each other. The eigenstates of logical $\hat{\sigma}_y$ are denoted as $|Y_\alpha^{(p+iq \bmod 4)}\rangle$ where

$$|Y_\alpha^{(p+iq \bmod 4)}\rangle = \frac{1}{\sqrt{2}} (|\mathcal{C}_\alpha^{(p \bmod 4)}\rangle + i|\mathcal{C}_\alpha^{(q \bmod 4)}\rangle). \quad (3.17)$$

The effects of two and three photon loss events are also depicted in the figure. Two-photon losses, i.e. $\hat{a}^2\mathcal{C}_\alpha^{\text{even}}$, results in a transition to the even parity space, however, the definition of the logical 0 and 1 states is flipped as shown in Fig. 3.4c. This implies that the loss of two consecutive photons from the code-space is a logical bit-flip error. Moreover, such an error cannot be detected, since the error space $\hat{a}^2\mathcal{C}_\alpha^{\text{even}}$ overlaps with original code-

¹There is a caveat here. Due to slightly different normalization factors, $\langle\mathcal{C}_\alpha^{(0 \bmod 4)}|\hat{a}^\dagger\hat{a}|\mathcal{C}_\alpha^{(0 \bmod 4)}\rangle$ and $\langle\mathcal{C}_\alpha^{(2 \bmod 4)}|\hat{a}^\dagger\hat{a}|\mathcal{C}_\alpha^{(2 \bmod 4)}\rangle$ are different from each other by $\mathcal{O}(|\alpha|^2 e^{-2|\alpha|^2})$. This leads to a distortion of the of the cat state manifold. See Sec. 3.1.3 for further details.

space. Similarly, losing three consecutive photons gives the encoding shown in Fig. 3.4d. This sub-space overlaps with the single photon loss subspace $\mathcal{C}_\alpha^{\text{odd}}$. A further photon loss results in the system going back to the original code-space. Since every photon loss event causes a jump in the parity of the system, it is possible to track exactly which manifold the system ends up in, as long as all the parity-jumps can be observed. Since the Kraus operator describing l photon jumps in a time interval τ is given by

$$\hat{M}_{l,\text{photon-loss}} = \sqrt{\frac{(1 - e^{-\kappa_{1\text{ph}}\tau})^l}{l!}} \hat{a}^l, \quad (3.18)$$

the probability of l photon jumps from a cat state with coherent state amplitude α is given by

$$p_{l\text{-jumps}} = \frac{|\alpha|^{2l}(1 - e^{-\kappa_{1\text{ph}}\tau})^l}{l!} \approx \frac{(|\alpha|^2\kappa_{1\text{ph}}\tau)^l}{l!} \text{ for } \tau \ll \kappa_{1\text{ph}}. \quad (3.19)$$

Therefore, if the time interval between two parity measurements is much smaller than $1/(|\alpha|^2\kappa_{1\text{ph}})$, only a single photon jump occurs with the highest probability. Hence, by measuring the photon-number parity $\hat{\Pi}$ in quick succession, the four-component cat code can be protected against the photon loss error to the first order.

One possible pulse-sequence for monitoring photon-number parity is depicted in Fig. 3.5. The idea is to map the parity on an ancillary qubit with unitary gate of the form

$$\hat{U}_{\text{map}} = (\hat{\Pi} + 1)\hat{\sigma}_x/2 \quad (3.20)$$

on the joint oscillator-qubit system. Such a gate is typically engineered by utilizing the readily available dispersive interaction of the form

$$\hat{H}_{\text{dispersive}} = -\chi_{aq}\hat{n}|e\rangle\langle e| \quad (3.21)$$

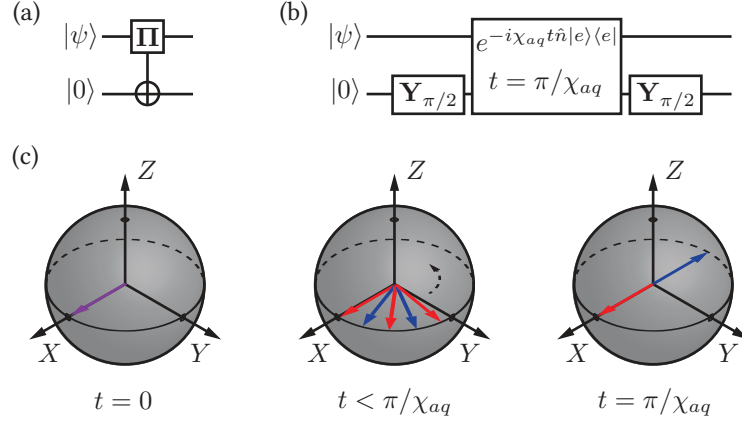


Figure 3.5: (a) Symbol of the $\hat{U}_{\text{map}} = (\hat{\Pi} + 1)\hat{\sigma}_x/2$ gate which maps the photon-number parity of the harmonic oscillator to the state of the qubit. (b) Pulse sequence for implementing the \hat{U}_{map} gate with the help of the dispersive Hamiltonian $\hat{H}_{\text{dispersive}} = -\chi_{aq}\hat{n}\hat{\sigma}_z$. The qubit is first put in the $|+\rangle$ state with the help of a $\mathbf{Y}_{\pi/2}$ rotation. The system is allowed to evolve under the dispersive interaction for $t = \pi/\chi_{aq}$. Finally another $\mathbf{Y}_{\pi/2}$ rotation is applied. Both $\mathbf{Y}_{\pi/2}$ rotations are required to be successful irrespective of the state of the oscillator. (c) The evolution of the oscillator-qubit system under the action of the dispersive interaction. The first $\mathbf{Y}_{\pi/2}$ rotation initiates the qubit in $|+\rangle$ state irrespective of the state of the oscillator. The dispersive interaction entangles the qubit with the oscillator, since the Bloch-vector of the qubit rotates at the rate of $n\chi_{aq}$ when the oscillator is in n^{th} Fock state. At time $t = \pi/\chi_{aq}$ all the Bloch vectors corresponding to even Fock states converge to $|+\rangle$ (red arrows) and those corresponding to the odd Fock states converge to $|-\rangle$ (blue arrows). The following $\mathbf{Y}_{\pi/2}$ rotation then maps the even states to $|1\rangle$ of the qubit and the odd states to $|0\rangle$.

between the oscillator and the qubit (see Sec. 4.1.2). Panels (b) and (c) of Fig. 3.5 illustrate how the dispersive interaction is converted to the required \hat{U}_{map} gate. The parity of the oscillator is then inferred by measuring the state of the qubit. A seminal experiment by N. Ofek and A. Petrenko *et al.* [Ofek *et al.*, 2016] has demonstrated the use of such parity measurement to track the photon jumps thus protecting the cat code from the photon loss error to the first order. In their case, a break-even with the single-photon life-time $1/\kappa_{1\text{ph}}$ was achieved, in spite of the utilized cat size of $|\alpha|^2 = 3$. This is one of the first examples of a QEC code achieving break-even.

It is also possible to correct for the loss of a single photon instead of simply monitoring

the photon-jumps. Such a correction process is proposed in [Leghtas *et al.*, 2013b]. It involves converting the dispersive interaction to a correction unitary of the form

$$\hat{U}_{\text{correction}} = |\mathcal{C}_\alpha^{(0 \bmod 4)}\rangle\langle\mathcal{C}_\alpha^{(3 \bmod 4)}| + |\mathcal{C}_\alpha^{(2 \bmod 4)}\rangle\langle\mathcal{C}_\alpha^{(1 \bmod 4)}| + \hat{U}_{\text{rest}} \quad (3.22)$$

once a photon-jump is detected. Here \hat{U}_{rest} is added to make sure that $\hat{U}_{\text{correction}}$ is a unitary on the joint Hilbert-space of the oscillator-qubit system. It is essentially an identity on the rest of the Hilbert space of the harmonic oscillator. Moreover, the dispersive interaction can also be utilized for building a discrete-autonomous feedback that we considered in Sec. 2.3. Instead of measuring the ancillary qubit after the \hat{U}_{map} gate, a unitary of the form

$$U_{\text{auto-correction}} = \left(|\mathcal{C}_\alpha^{(0 \bmod 4)}\rangle\langle\mathcal{C}_\alpha^{(3 \bmod 4)}| + |\mathcal{C}_\alpha^{(2 \bmod 4)}\rangle\langle\mathcal{C}_\alpha^{(1 \bmod 4)}| + \hat{U}_{\text{rest}} \right) \otimes |0\rangle\langle 0| + \hat{I}_a \otimes |1\rangle\langle 1| \quad (3.23)$$

applies the correction to the oscillator without the need of knowing the qubit state. Here we have used ‘ \otimes ’ to avoid confusion between the oscillator states and the qubit states. Post correction, the qubit needs to be reset by any means available before repeating the same sequence. The continuous-autonomous correction against photon loss errors requires an always-on dissipator of the form

$$\kappa_{\text{correction}} \mathcal{D} \left[\left(|\mathcal{C}_\alpha^{(0 \bmod 4)}\rangle\langle\mathcal{C}_\alpha^{(3 \bmod 4)}| + |\mathcal{C}_\alpha^{(2 \bmod 4)}\rangle\langle\mathcal{C}_\alpha^{(1 \bmod 4)}| \right) \right]. \quad (3.24)$$

However, to the best of our knowledge, such a dissipator cannot be built using the dispersive interaction. Instead an element which includes an interaction of the form $\hat{\Pi} \otimes \hat{\sigma}_z$ in the Hamiltonian is needed. Such an element, in the realm of superconducting circuits, is proposed by [Cohen *et al.*, 2017].

As we have seen earlier, the photon losses are not the only errors that affect harmonic oscillators. We also have to deal with the energy relaxation and the dephasing errors. The effect of these errors is discussed in the next section.

3.1.3 Effect of energy relaxation and dephasing

In this sub-section we study the effect of energy relaxation and dephasing errors on the cat code encoding. As we discussed in Sec. 1.2.2, the Kraus operator describing the energy relaxation in a time step τ is

$$\hat{M}_{\text{relaxation}} = e^{-\frac{1}{2}\kappa_{1\text{ph}}\tau\hat{n}}. \quad (3.25)$$

The Kraus operators describing the dephasing error channel are given by

$$\hat{M}_{l,\text{dephasing}} = \sqrt{\frac{(\kappa_{\phi}t)^l}{l!}} e^{-\frac{1}{2}\kappa_{\phi}\tau\hat{n}^2} \hat{n}^l \text{ for } l \in \mathbb{N}. \quad (3.26)$$

Therefore, the combined effect of one photon loss event, the energy relaxation error and the dephasing error can be modeled by extending our set of error operators to

$$\mathcal{E} = \{\hat{I}, \hat{a}\} \cup \{\hat{n}^l\}_{l=1}^{\infty} \quad (3.27)$$

However, since the operators \hat{n}^l can be normal ordered to linear combinations of $\hat{a}^{\dagger l}\hat{a}^l$, it is equivalent to use

$$\mathcal{E} = \{\hat{I}, \hat{a}\} \cup \{\hat{a}^{\dagger l}\hat{a}^l\}_{l=1}^{\infty} \quad (3.28)$$

We further extend this set to include operators of the form $\hat{a}^{\dagger l}\hat{a}^{l+1}$ which, for $l > 0$, combine the effect of energy relaxation and dephasing with a single photon loss. Thus, the

complete error set that we would like to analyze is

$$\mathcal{E} = \{\hat{I}, \hat{a}\} \cup \{\hat{a}^{\dagger l} \hat{a}^l, \hat{a}^{\dagger l} \hat{a}^{l+1}\}_{l=1}^{\infty} \quad (3.29)$$

Now, first note that any operator of the form $\hat{a}^{\dagger l} \hat{a}^l$ does not change the parity $\hat{\Pi}$ or the super-parity $\sqrt{\hat{\Pi}}$ of the cat states. It is, therefore, straightforward to verify that

$$\langle \mathcal{C}_{\alpha}^{(k \bmod 4)} | \hat{a}^{\dagger l} \hat{a}^l | \mathcal{C}_{\alpha}^{(m \bmod 4)} \rangle = 0 \text{ for } k \neq m. \quad (3.30)$$

Moreover the code-space and the error-spaces for the four-component cat code satisfy

$$\langle \mathcal{C}_{\alpha}^{(k \bmod 4)} | \hat{a}^{\dagger l} \hat{a}^{l+1} | \mathcal{C}_{\alpha}^{(k \bmod 4)} \rangle = \langle \mathcal{C}_{\alpha}^{(k \bmod 4)} | \hat{a}^{\dagger l} \hat{a}^{l+1} | \mathcal{C}_{\alpha}^{(k-2 \bmod 4)} \rangle = 0. \quad (3.31)$$

Therefore, all the off diagonal elements and many of the diagonal elements in the Knill-Laflamme conditions are zero. The issue arises when we have a closer look at the non-zero diagonal elements. As we discussed in Sec. 2.1.1, for the superpositions in the code-space to remain un-distorted, the value of these elements should be independent of the individual states. However, for $l \neq 0$

$$\langle \mathcal{C}_{\alpha}^{(k \bmod 4)} | \hat{a}^{\dagger l} \hat{a}^l | \mathcal{C}_{\alpha}^{(k \bmod 4)} \rangle - \langle \mathcal{C}_{\alpha}^{(k-2 \bmod 4)} | \hat{a}^{\dagger l} \hat{a}^l | \mathcal{C}_{\alpha}^{(k-2 \bmod 4)} \rangle = \mathcal{O}(|\alpha|^{2l} e^{-2|\alpha|^2}), \quad (3.32)$$

owing to the difference in normalization constants $N^{(k \bmod 4)}$ for the different cat states. This discrepancy results in continuous distortion of the code space over the period of time. As an example, Fig. 3.6c shows the effect of energy relaxation acting in isolation for $t = 1/2\kappa_{1\text{ph}}$. Due to this error the constituent coherent states are effectively pulled towards the center of the phase-space, as the coherent state amplitudes change from α to $\alpha e^{-\frac{1}{2}\kappa_{1\text{ph}}t}$. Similarly, Fig. 3.6d shows the effect of dephasing error acting in isolation for

$t = 1/2\kappa_\phi$. The states here are a mixture of multiple mutually rotated cat states. Note that although the parity of the depicted states remains unchanged, the errors lead to increase in overlap for the states on the equator thus decreasing their information content. In general, the energy relaxation and dephasing errors cause the logical Bloch vectors to shrink towards the Z -axis of the sphere thus causing a logical dephasing error. Moreover, the photon loss events also give rise to such distortion along with changing the parity, since the diagonal elements of the Knill-Laflamme conditions for this error are given by $l = 1$ in Eq. (3.32).

Now the question naturally arises, is it possible to protect against these errors? Upfront, they don't satisfy the Knill-Laflamme conditions. On the other hand, the discrepancy in Eq. (3.32) is highly suppressed when $2l \ll |\alpha|^2$. Moreover, as indicated by equations (3.30) and (3.31), the distortion induced by these errors leads to leakage out of the space spanned by the $|\mathcal{C}_\alpha^{(k \bmod 4)}\rangle$ cat states. As a result, it turns out, protecting against these errors is indeed possible. One way to accomplish this correction is illustrated in [Leghtas *et al.*, 2013b]. The underlying principle behind that scheme is to repeatedly decode the information stored in the cat-qubit on to an ancilla qubit and then re-encode in the original cat basis. If such a process is repeated faster than the rate of logical dephasing, which is suppressed exponentially in cat size, then the accumulation of errors is prevented, thus protecting the cat qubit. At the same time, since the ancillary qubit holds the information for some stretches of time, the scheme is sensitive to the decoherence rate of the ancillary qubit as well. Instead, there exists a more elegant continuous and autonomous procedure to protect against these and any other errors that are polynomial in $\hat{a}^\dagger \hat{a}$. We discuss such autonomous stabilization in the next section.

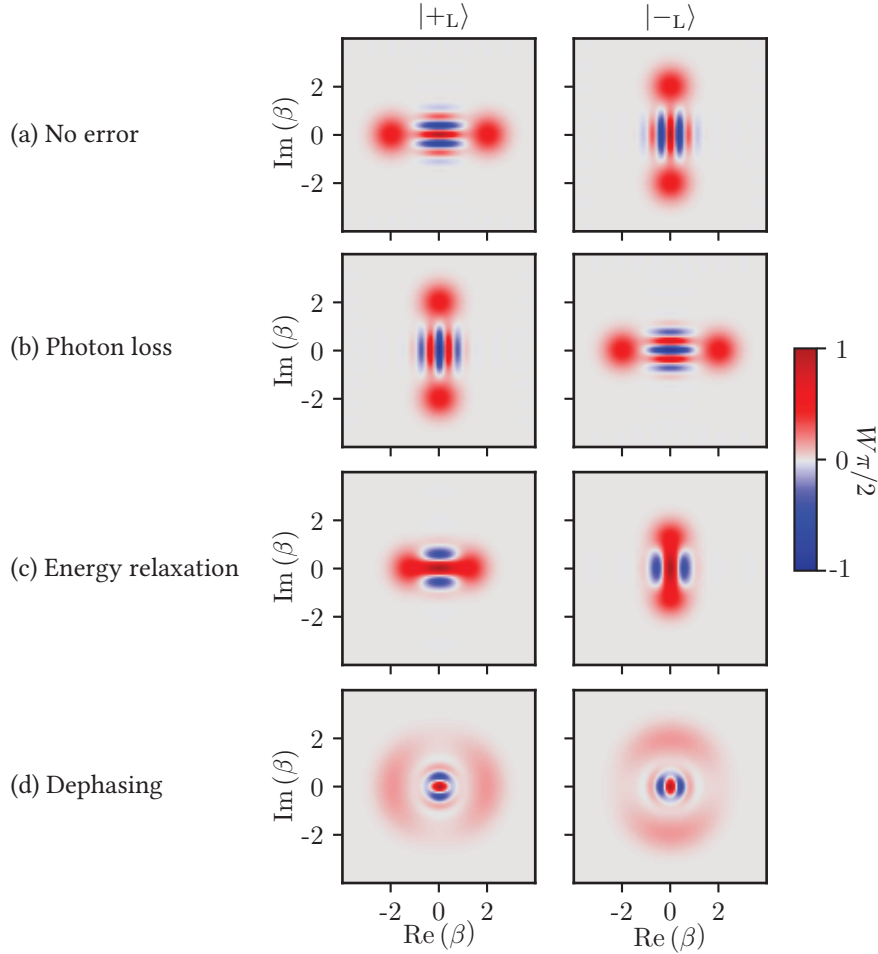


Figure 3.6: (a) Wigner functions of the logical $|+_{\text{L}}\rangle = |\mathcal{C}_{\alpha}^{(0 \bmod 2)}\rangle$ and $|-_{\text{L}}\rangle = |\mathcal{C}_{\alpha}^{(0 \bmod 2)}\rangle$ for a four-component cat-state encoding. (b) Effect of losing a single photon. The parity of the states changes from even to odd as we have already discussed earlier. (c) Effect of energy relaxation on $|\pm_{\text{L}}\rangle$. Under the action of this error the constituent coherent states shrink towards the ground state, thus making smaller cats as shown. Although the parity of the cats is unchanged, their orthogonality decreases resulting in eventual loss of information. (d) Effect of dephasing error on $|\pm_{\text{L}}\rangle$. Again, the parity of the states is unchanged. However, due to random rotations in the phase space, the constituent coherent states have increased overlap with each other, resulting in loss of information. Both energy relaxation and dephasing errors cause an effective dephasing error in the logical qubit.

3.2 Autonomously stabilizing coherent state manifolds

The last section illustrated the use of coherent state superpositions for storing information.

From our discussion about energy relaxation and dephasing errors, it emerged that such

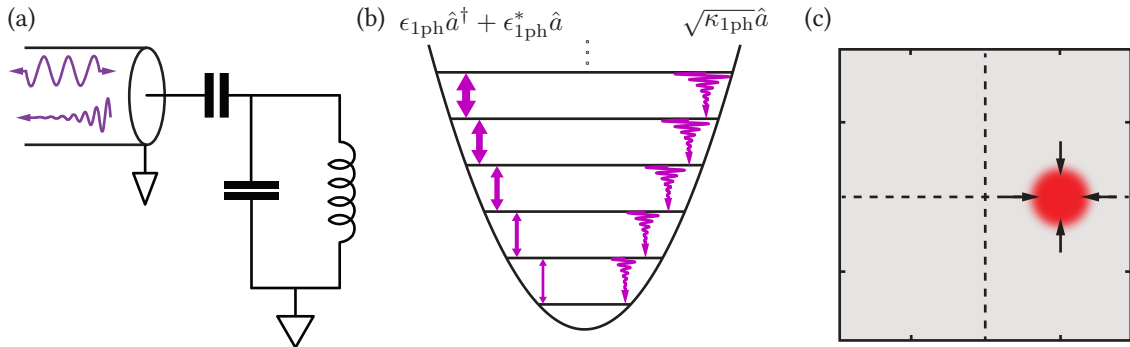


Figure 3.7: (a) An LC circuit coupled to a transmission line. The transmission line can be utilized to drive the circuit by sending tones down the line. At the same time, coupling with the transmission line also leads to amplitude damping since the signal leaked to the line is irreversibly lost. (b) Cartoon representing a single-photon drive and dissipation on harmonic oscillator. The drive connects the nearest neighbor levels in a reversible manner as indicated by the double-arrows. The width of the double arrows is increased to indicate that the matrix elements of the drive get stronger up the ladder. The dissipation is indicated by the wavy decaying arrows connecting nearest levels. The width of the arrows increase going up the ladder. (c) The attractive potential created by the driven-dissipative process pulls all the states in the phase-space towards the stabilized coherent state.

errors result in a leakage out of the manifold spanned by the utilized coherent states. Here we focus on the stabilization of the coherent state manifolds against these leakages by employing autonomous feedback in the form of driven-dissipative processes on the harmonic oscillators. It is also possible to stabilize single coherent states and a manifold of two-component cat states by utilizing clever Hamiltonian terms only [Puri *et al.*, 2017, Grimm *et al.*, 2019]. However, such scheme for four-component cat states is extremely hard to implement. Therefore, we solely focus on the driven-dissipative stabilization. Let us start our discussion with driven-dissipative stabilization of a single coherent state.

3.2.1 Single-photon driven-dissipative process

Let us consider a harmonic oscillator with a Hamiltonian given by

$$\frac{\hat{H}}{\hbar} = \omega_a \hat{a}^\dagger \hat{a} + \cos(\omega_a t + \phi) (\epsilon_{1\text{ph}} \hat{a}^\dagger + \epsilon_{1\text{ph}}^* \hat{a}) \quad (3.33)$$

where the first term describes the energy levels of the harmonic oscillator and the second term is a drive. The frequency of the drive is ω_a which is the resonant frequency of the oscillator and ϵ_a accounts for the strength and phase of the drive. We work in an interaction picture with respect to $\hat{H}_0 = \hbar\omega_a \hat{a}^\dagger \hat{a}$ in order to eliminate the fast rotations in the phase space of the harmonic oscillator. In this rotating frame the Hamiltonian is given by

$$\frac{\hat{H}_{1\text{ph}}}{\hbar} = \epsilon_{1\text{ph}} \hat{a}^\dagger + \epsilon_{1\text{ph}}^* \hat{a}. \quad (3.34)$$

Here we have also performed the rotating wave approximation (RWA) to drop the fast rotating terms of the form $e^{2i\omega_a t} \epsilon_{1\text{ph}} \hat{a}^\dagger + e^{-2i\omega_a t} \epsilon_{1\text{ph}}^* \hat{a}$. In addition to this Hamiltonian we also consider a single-photon dissipation on the harmonic oscillator given by the Lindblad term $\mathcal{D}[\sqrt{\kappa_{1\text{ph}}} \hat{a}]$. In practice such single-photon drive and dissipation can be engineered by hooking up the harmonic oscillator to a transmission line as shown in Fig. 3.7a. The drive is applied by sending a tone at the frequency of the oscillator down the transmission line. The transmission line also causes dissipation since the signal leaked through the transmission line to the environment is irreversibly lost. Another cartoon depicting the single-photon drive and dissipation with the help of harmonic oscillator energy levels is shown in Fig. 3.7b.

The master equation for modeling the dynamics of the harmonic oscillator in the pres-

ence of this drive and dissipation is given by

$$\dot{\rho} = -\frac{i}{\hbar} \left[\hat{H}_{1\text{ph}}, \rho \right] + \mathcal{D}[\sqrt{\kappa_{1\text{ph}}}\hat{a}]\rho. \quad (3.35)$$

So far, we have only studied the deleterious effects of the single photon dissipation which leads to photon loss and energy relaxation errors. However, in presence of the drive, the steady state of the system turns out to be the coherent state. In order to prove this, let us perform a little bit of algebra on our master-equation as follows:

$$\begin{aligned} \dot{\rho} &= -\frac{i}{\hbar} \left[\hat{H}_{1\text{ph}}, \rho \right] + \mathcal{D}[\sqrt{\kappa_{1\text{ph}}}\hat{a}]\rho \\ &= -i \left[(\epsilon_{1\text{ph}}\hat{a}^\dagger + \epsilon_{1\text{ph}}^*\hat{a}), \rho \right] + \kappa_{1\text{ph}}\hat{a}\rho\hat{a}^\dagger - \frac{\kappa_{1\text{ph}}}{2} \left\{ \hat{a}^\dagger\hat{a}, \rho \right\} \\ &= \kappa_{1\text{ph}} \left(\hat{a} + \frac{2i\epsilon_{1\text{ph}}}{\kappa_{1\text{ph}}} \right) \rho \left(\hat{a} + \frac{2i\epsilon_{1\text{ph}}}{\kappa_{1\text{ph}}} \right)^\dagger - \frac{\kappa_{1\text{ph}}}{2} \left\{ \left(\hat{a} + \frac{2i\epsilon_{1\text{ph}}}{\kappa_{1\text{ph}}} \right)^\dagger \left(\hat{a} + \frac{2i\epsilon_{1\text{ph}}}{\kappa_{1\text{ph}}} \right), \rho \right\} \\ &= \kappa_{1\text{ph}} \mathcal{D} \left[\hat{a} + \frac{2i\epsilon_{1\text{ph}}}{\kappa_{1\text{ph}}} \right] \rho \\ &= \kappa_{1\text{ph}} \mathcal{D} [\hat{a} - \alpha] \rho. \end{aligned} \quad (3.36)$$

Here we have used $\alpha = -\frac{2i\epsilon_{1\text{ph}}}{\kappa_{1\text{ph}}}$ in the last step. Now, if $\rho = |\alpha\rangle\langle\alpha|$ then

$$\dot{\rho} = \kappa_{1\text{ph}} \mathcal{D} [\hat{a} - \alpha] |\alpha\rangle\langle\alpha| = 0, \quad (3.37)$$

since $|\alpha\rangle$ has an eigenstate of $\hat{a} - \alpha$ with an eigenvalue of 0. In other words $|\alpha\rangle$ is in the Kernel of the $\hat{a} - \alpha$ operator. Hence, the coherent state $|\alpha\rangle$, which is a pure state, is stabilized by the single-photon driven-dissipative process.

It is clear that the drive in the single photon-driven-dissipative process constantly provides energy to counter the effect of energy relaxation error. However, the driven-dissipative process also protects against the effect of dephasing error when $\kappa_{1\text{ph}} \gg \kappa_\phi$.

The dephasing error results into random rotation of coherent state $|\alpha\rangle$ to $|\alpha e^{i\phi}\rangle$. However, the driven-dissipative process results in a ‘well’ that attracts all the other coherent states in the phase space towards the stabilized coherent state $|\alpha\rangle$ as shown in Fig. 3.7c. This well prevents the coherent state from leaking to any other states in the phase space as long as $\kappa_{1\text{ph}}$ is much stronger than the rate of the errors. Moreover, such protection is autonomous since no real time decision making is required. Instead a strong dissipation and an always on drive are sufficient to protect against errors. Hence, it is interesting to see if this trick of driven-dissipative processes could be utilized for stabilizing multiple coherent states and all of their superpositions simultaneously.

3.2.2 Multi-photon driven-dissipative processes

The last sub-section showed that a single-photon driven-dissipative process stabilizes a coherent state. However, in order to store information with the help of cat codes, we need to stabilize a manifold spanned by multiple coherent states and all their superpositions. In this sub-section we discuss the multi-photon driven-dissipative processes required for such manifold stabilization. The focus here is on the error correction properties of these processes. The question of how to implement such highly nonlinear interactions is the topic of the next chapter (Ch. 4).

An N -photon drive is expressed in the rotating frame of $H_0 = \hbar\omega_a\hat{a}^\dagger\hat{a}$, as

$$\frac{\hat{H}_{N\text{ph}}}{\hbar} = \epsilon_{N\text{ph}}\hat{a}^{\dagger N} + \epsilon_{N\text{ph}}\hat{a}^{\dagger N}. \quad (3.38)$$

Similarly, the required N -photon dissipation is modeled by $\mathcal{D}[\hat{a}^N]$ which results in the master equation

$$\dot{\rho} = -\frac{i}{\hbar} \left[\hat{H}_{N\text{ph}}, \rho \right] + \kappa_{N\text{ph}} \mathcal{D}[\hat{a}^N] \rho. \quad (3.39)$$

With the help of some algebra, the master equation can again be expressed in a compact form given by

$$\dot{\rho} = \kappa_{N\text{ph}} \mathcal{D}[\hat{a}^N - \alpha^N] \rho. \quad (3.40)$$

where

$$\alpha = \left(-\frac{2i\epsilon_{N\text{ph}}}{\kappa_{N\text{ph}}} \right)^{\frac{1}{N}}. \quad (3.41)$$

Note that this equation has multiple solutions. If we take α_0 to be one such solution then $\alpha_0 e^{\frac{im\pi}{N}}$ is also a solution for $m \in \mathbb{Z}$. In total there are N unique solutions. As a result, any coherent state $|\alpha_0 e^{\frac{im\pi}{N}}\rangle$ for $m \in [0, N)$ is in the Kernel of the $\hat{a}^N - \alpha^N$ operator and is stabilized by the N -photon driven-dissipative process. Moreover, any superpositions of these coherent states given by

$$|\psi\rangle = \sum_{m=0}^N c_m |\alpha_0 e^{\frac{im\pi}{N}}\rangle \quad (3.42)$$

are also in the Kernel of the $\hat{a}^N - \alpha^N$ and, hence, are also stabilized. Therefore, the N -photon driven-dissipative process stabilizes the entire manifold spanned by these states.

The specific examples of two- and four-photon driven-dissipative processes are illustrated in Fig. 3.8. The cartoons in panel (a) and (c) of the figure show that the two-photon driven-dissipative process connects alternate levels and four-photon driven-dissipative process connects $n, n \pm 4$ levels with each other. This serves to illustrate that both the processes conserve the parity of the system and the four-photon driven-dissipative process conserves the super-parity as well. Formally, this can be verified by checking

$$[\hat{\Pi}, \hat{a}^2] = [\hat{\Pi}, \hat{a}^4] = [\sqrt{\hat{\Pi}}, \hat{a}^4] = 0. \quad (3.43)$$

Thus parity (and super-parity) are good quantum numbers for two-photon (four-photon)

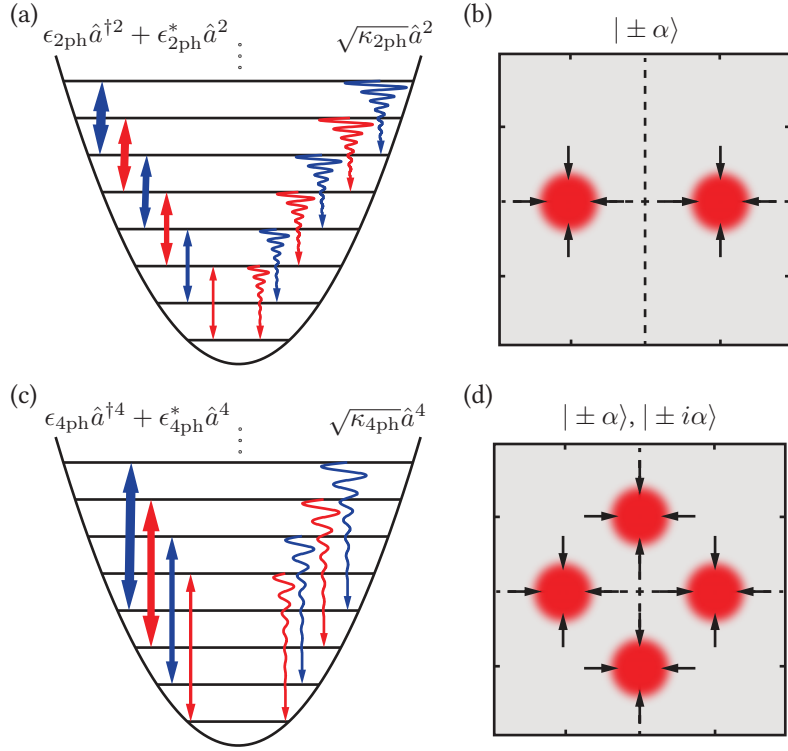


Figure 3.8: (a) Cartoon representing two-photon drive (double-sided arrows) and dissipation (decaying wavy arrows). The drive and dissipation connect the alternate states with each other and are color coded so that the red-arrows only connect the even states while blue-arrows only connect the odd states. (b) The potential created by the two-photon driven-dissipative process attracts the coherent states towards one of the two steady states $|\pm\alpha\rangle$ as shown. (c) Cartoon representing four-photon drive (double-sided arrows) and dissipation (decaying wavy arrows). The arrows connect the n^{th} Fock state to $(n\pm 4)^{\text{th}}$ Fock states and the dissipation connects the n^{th} Fock state with the $(n-4)^{\text{th}}$ Fock state. (d) All the coherent states are attracted towards the four steady states $|\pm\alpha\rangle$ and $|\pm i\alpha\rangle$.

driven-dissipative processes.

The coherent states stabilized by the two-photon driven-dissipative process are $|\pm\alpha\rangle$ and that by the four-photon driven-dissipative process are $|\pm\alpha\rangle$ as well as $|\pm i\alpha\rangle$. Under the action of the driven-dissipative processes, all the other states in the phase space are attracted towards these coherent states as shown in panels (b) and (d) of Fig. 3.8. This restoration towards the constituent coherent states allows autonomous correction against any error that can be modeled as a small displacement in the phase space. Especially, the

energy relaxation and dephasing errors are suppressed exponentially due to such a correction. Similar to the case of single-photon driven-dissipative process, the multi-photon drive continuously provides energy to the system thus the energy relaxation error is not an issue. In the case of the dephasing error, as long as the rate of stabilization is much greater than the rate of the dephasing error, i.e. $\kappa_{N\text{ph}} \gg \kappa_\phi$, the distortion of the individual coherent states is suppressed. Moreover, since making the coherent states further apart leads to less overlap in spite of the distortions, the rate of logical-dephasing is exponentially suppressed as the size of coherent states $|\alpha|^2$ is increased. In the case of four-component cat states, the effective rate of dephasing error for $e^{-2|\alpha|^2} \ll 1$ can be approximated by

$$\begin{aligned}
\Gamma_{\phi,\text{cat-qubit}} &= 2|\langle +_L | \sqrt{\kappa_\phi} \hat{a}^\dagger \hat{a} | -_L \rangle|^2 \\
&= \left| \langle \mathcal{C}_\alpha^{(0 \bmod 2)} | \sqrt{\kappa_\phi} \hat{a}^\dagger \hat{a} | \mathcal{C}_{i\alpha}^{(0 \bmod 2)} \rangle \right|^2 \\
&= \kappa_\phi |\alpha|^2 \left| \langle \mathcal{C}_\alpha^{(1 \bmod 2)} | \mathcal{C}_{i\alpha}^{(1 \bmod 2)} \rangle \right|^2 \\
&\approx 4|\alpha|^2 e^{-2|\alpha|^2} \sin^2(|\alpha|^2) \kappa_\phi.
\end{aligned} \tag{3.44}$$

This exponential protection against the dephasing error is a very useful feature of the cat-code. Also note that there is some interesting value of $|\alpha|$ where the dephasing is further suppressed.

In addition to autonomous protection against errors, the confinement to the cat state manifold also allows us to simplify the operations on the cat state. When a process acting on the harmonic oscillator is slower than the ‘rate of confinement’ given by $\kappa_{N\text{ph}}|\alpha|^{2N}$, the process can be projected on to the cat manifold to analyze its effect. As an example, the unitary required for introducing a change in the parity could be implemented by a Hamiltonian of the form $(\epsilon \hat{a}^\dagger + \epsilon^* \hat{a})$ as long the rate $|\epsilon| \ll \kappa_{N\text{ph}}$. Such a Hamiltonian term has been utilized for performing the logical \mathbf{X}_φ rotation in the two-component cat-

space [Touzard *et al.*, 2018]. Similarly, the dissipator for autonomously correcting photon loss errors that we discussed in Eq. (3.24) can be simplified to $\mathcal{D}[\sqrt{\kappa_{\text{correction}}}a^\dagger(\hat{\Pi} - 1)]$ in presence of a strong four-photon driven-dissipative process.

On the flip side, the confinement to the cat state manifold implies that the discrete parity measurement using dispersive readout does not work in the presence of the driven-dissipative stabilization. The evolution of the oscillator-qubit system under the dispersive interaction can be seen as the different Fock states gaining different phases as function of time if the qubit is in $|1\rangle$. However, the driven-dissipative process will oppose such phase gain. Therefore, if the rate of confinement $|\alpha|^4\kappa_{4\text{ph}}$ is stronger than the strength of the dispersive interaction χ_{aq} , then the parity measurement will not work. On the other hand a strong χ_{aq} implies that any spurious excitation of the qubit leads to complete dephasing of the oscillator. To put this more succinctly, since the $e^{i\phi\hat{a}^\dagger\hat{a}}$ operator does not commute with $\hat{a}^4 - \alpha^4$ at arbitrary values of ϕ , the discrete parity measurement is not compatible with the driven-dissipative process. Hence, the stabilization needs to be turned off in order to measure the parity as outlined. Of course, if the device for continuous parity measurement outlined by [Cohen *et al.*, 2017] is implemented then the stabilization and the parity measurement are compatible, since $\hat{\Pi} = e^{i\pi\hat{a}^\dagger\hat{a}}$ commutes with $\hat{a}^4 - \alpha^4$. In Ch. 7 we study another code which simplifies the photon loss monitoring considerably, thus allowing stabilization and photon loss error correction simultaneously without needing the added complication of continuous parity measurement.

3.3 Fault tolerance and cat codes

Let us briefly discuss the bigger picture of fault tolerance in regards to the cat codes. As mentioned in Sec. 2.1, along with error correction, one requires the ability to perform fault-tolerant operations on the logical qubits. Such fault-tolerant operations in the case

of stabilized two-component cat codes have been proposed recently by [Guillaud and Mirrahimi, 2019] and [Puri *et al.*, 2019]. In these proposals, the stabilized two-component cat qubits are termed as ‘biased noise qubits’, since all except the bit-flip error channel are exponentially suppressed. In such a scenario, one requires a universal set of gates which preserve the bias of the logical qubit in order to perform FTQC. The two quoted references develop bias-preserving CNOT gate between two-component cat qubits. Such a CNOT gate is made possible by the ability to continuously and adiabatically distort the cat states by slowly changing α of the constituent coherent states. In other words, the bias preserving CNOT gate is facilitated by the infinite dimensional Hilbert space of the harmonic oscillator. Moreover, the references show that, by concatenating multiple cat qubits, a completely error protected universal FTQC can be performed. In addition, the bias of the noise processes gives rise to higher error thresholds on individual components compared to that needed for QEC codes on unbiased qubits. Such universal set of fault-tolerant gates have not been developed in the case of four-component cat states as yet. Since the four-component cat states offer intrinsic protection against stochastic photon loss errors, it might be exceptionally beneficial to develop such operations.

All of these considerations are valid only when we have access to continuous stabilization of the cat code. Therefore, in this thesis we concern ourselves with the implementation of the required driven-dissipative processes, and the possibility of building continuous and autonomous error correction stochastic photon loss.

3.4 Summary and prelude to the next chapter

We summarize some of the important points that are central to the understanding of the rest of this thesis:

- (i) Four-component cat states can be utilized for encoding a logical qubit which is pro-

tected from errors on the harmonic oscillator to the first order.

- (ii) The photon loss error is monitored by repeatedly measuring the parity of the harmonic oscillator. As long as the parity jumps are not missed, the stored information remains intact.
- (iii) Discrete monitoring of the parity is accomplished by a utilizing an ancillary qubit which is dispersively coupled to the oscillator.
- (iv) Implementing protection against photon loss in continuous and autonomous manner requires a specially built circuit which measures the parity directly as proposed in [Cohen *et al.*, 2017].
- (v) The protection against the energy relaxation and dephasing errors in the case of four-component cat states is best accomplished by a four-photon driven-dissipative process of the form $\mathcal{D}[\hat{a}^4 - \alpha^4]$

As mentioned, the protection against the photon loss error by discrete parity monitoring has already been accomplished [Ofek *et al.*, 2016]. The continuous parity measurement, autonomous protection against photon loss and the implementation of four-photon driven-dissipative process are still open challenges. In this thesis, we focus on how to engineer the highly nonlinear four-photon driven-dissipative process required for autonomous stabilization of four-component cat states. Moreover, in the final chapter of this thesis, we propose a new code, namely the pair-cat code, which simplifies the detection of photon loss error. This simplification brings the continuous and autonomous protection against photon loss errors, while simultaneously stabilizing the encoding manifold, within the realm of currently available cQED technology.

Chapter 4

Engineering nonlinear driven-dissipative processes

The multi-photon driven-dissipative processes that we studied in the last chapter play an important role of stabilizing the cat state manifolds. The question naturally arises, how does one realize these processes in practice? The current chapter is aimed at answering this question. As we mentioned in Sec. 3.2.1 it is possible to implement a single-photon driven-dissipative process by coupling the harmonic oscillator to a transmission line which acts as an environment to which the oscillator dissipates as well as allows driving of the oscillator. However, the nonlinear drives and dissipation required for implementing multi-photon driven-dissipative processes are not possible with the help of this limited toolbox. Instead, we need to introduce some form of nonlinearity in the system. The following section (Sec. 4.1) focuses on the Josephson junction transmons, the nonlinear elements of choice in the domain of superconducting circuits. We also discuss the coupling of transmons to the harmonic oscillator modes here. Sec. 4.2 illustrates the realization of two-photon driven-dissipative process with the help of this nonlinearity. In Sec. 4.3 we move on to the implementation of four-photon driven-dissipative processes.

First, the underlying difficulties behind implementing this higher-order nonlinear process is discussed. In order to overcome this challenge, we propose and analyze a scheme for obtaining the required nonlinearity by cascading readily available lower-order nonlinear processes.

4.1 Nonlinearity in cQED

The nonlinearity in cQED is provided by the Josephson junctions. In this section we provide the Hamiltonian for this circuit element and discuss the transmon qubit which will be the qubit of choice in our case. We also describe the Hamiltonian of a coupled transmon-oscillator systems and learn how to model the off-resonant drives on this system which play an important role in implementing multi-photon driven-dissipative processes.

4.1.1 Josephson junction and transmon

Josephson-junctions are superconducting-insulator-superconducting junctions. The implementations considered in this thesis, utilize aluminum as the superconductor and aluminum oxide as the insulating layer. A cartoon and circuit symbol of a Josephson junction is shown in Fig. 4.1a. The Cooper pairs in the superconducting region tunneling across the insulating layer in a Josephson junction give rise to a potential of the form

$$U = -E_J \cos\left(\frac{\hat{\Phi}}{\phi_0}\right) = -E_J \cos(\hat{\varphi}) \quad (4.1)$$

where E_J is the Josephson tunneling energy and $\hat{\Phi}$ is the branch flux through the junction. We also define $\hat{\varphi} = \hat{\Phi}/\phi_0$ to be the superconducting phase across the junction where $\phi_0 = \hbar/2e$ is the reduced magnetic flux quantum. Here e is the charge of an electron. Another quantity that is used to characterize Josephson junction is the Josephson inductor

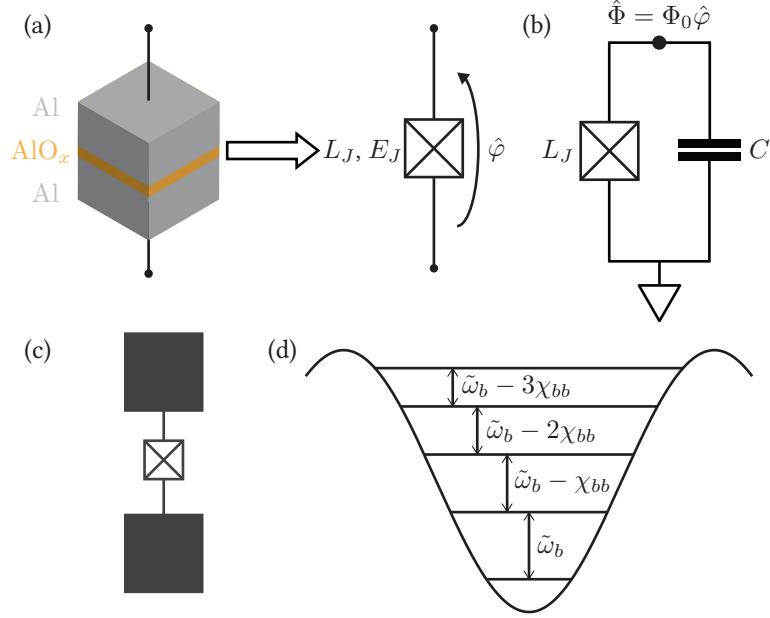


Figure 4.1: (a) Cartoon and symbol of a Josephson junction. A Josephson junction is a superconducting-insulator-superconducting (SIS) junction. In cQED implementation aluminum is used as the superconductor and aluminum-oxide is used as the insulating layer as shown. The circuit symbol of a Josephson junction is shown to the right of the cartoon. The Josephson energy E_J or the inductance L_J is used for characterizing the junction. (b) Circuit of a transmon which is essentially a Josephson junction shunted by a large capacitance. (c) Cartoon of a typical implementation of a transmon. The two big pads are made out of aluminum or niobium and they provide the shunting capacitance. These pads also act like antennas which facilitate capacitive coupling with the transmon mode. (d) The nonlinear potential and energy-levels of a transmon. Due to the nonlinearity offered by the Josephson junction, the energy eigenstates of the transmon are unequally spaced. Here $\tilde{\omega}_b$ denotes the renormalized frequency of the b mode and χ_{bb} denotes the anharmonicity of the transmon.

$$L_J = \phi_0^2 / E_J \text{ where } \phi_0 = \Phi_0 / 2\pi \text{ is the reduced flux quantum.}$$

With the Josephson junction as the source of nonlinearity, many circuits that take on the role of qubits, amplifiers, frequency-converters etc., have been designed. A recent review and further references on such circuits can be found in [Krantz *et al.*, 2019, Vool, 2017]. Here, we utilize the transmon circuit, originally proposed by [Koch *et al.*, 2007, Schreier *et al.*, 2008], as our qubit as well as source of nonlinearity. The circuit diagram of a transmon, in its simplest form, is shown in Fig. 4.1b. It consists of a single junction shunted

by a capacitance. Let the Josephson inductance of the junction be L_J and the capacitance of the capacitor be C as shown in the figure. We also define the charging energy of the capacitor as $E_C = e^2/2C$ where e is again the charge of an electron. In case of transmon the ratio of the Josephson energy to the charging energy of the capacitor E_J/E_C should be greater than 50. This suppresses the sensitivity of the energy eigenstates of transmon to the charge fluctuations on the capacitor. Under such circumstances, the Hamiltonian of the transmon is expressed as

$$\hat{H} = 4E_C \hat{N}^2 - E_J \cos(\hat{\varphi}) = \frac{\hat{Q}^2}{2C} - E_J \cos(\hat{\varphi}) \quad (4.2)$$

where $E_C = e^2/2C$ is the charging energy of the capacitor, \hat{N} is the Cooper pair number operator and $\hat{Q} = 2e\hat{N}$ is the charge operator on the capacitor. In case of the low energy eigenstates of this Hamiltonian (energy $\ll E_J$), the potential can be expanded around the minimum at $\varphi_{\min} = 0$ to give

$$\hat{H} = \frac{\hat{Q}^2}{2C} - E_J + E_J \frac{\hat{\varphi}^2}{2!} - E_J \frac{\hat{\varphi}^4}{4!} + \dots \quad (4.3)$$

Note that we ignore the constant term $-E_J$ while expanding the cosine. It is simply an energy offset. Substituting $\hat{\varphi} = \hat{\Phi}/\phi_0$ in the quadratic-term, we get

$$\hat{H} = \frac{\hat{Q}^2}{2C} + \frac{\hat{\Phi}^2}{2L_J} - E_J - \frac{E_J}{4!} \hat{\varphi}^4 + \dots \quad (4.4)$$

The first two terms here look like the Hamiltonian of the harmonic oscillator. Indeed, it is useful to express this Hamiltonian in terms of the creation and destruction operators as in the case of the harmonic oscillators. We use

$$\hat{Q} = iQ_{\text{ZPF}}(\hat{b}^\dagger - \hat{b})$$

$$\hat{\varphi} = \frac{\hat{\Phi}}{\phi_0} = \frac{\Phi_{\text{ZPF}}}{\phi_0} (\hat{b}^\dagger + \hat{b}) = \varphi_{\text{ZPF}} (\hat{b}^\dagger + \hat{b}) \quad (4.5)$$

where \hat{b}^\dagger and \hat{b} are the creation and destruction operator of the transmon mode and

$$\begin{aligned} \Phi_{\text{ZPF}} &= \sqrt{\frac{\hbar Z_J}{2}} \\ Q_{\text{ZPF}} &= \sqrt{\frac{\hbar}{2Z_J}}. \end{aligned} \quad (4.6)$$

with $Z_J = \sqrt{\frac{L_J}{C}}$. In terms of these \hat{b}^\dagger and \hat{b} the Hamiltonian of the transmon is given by

$$\begin{aligned} \hat{H} &= \hbar\omega_b \left(\hat{b}^\dagger \hat{b} + \frac{1}{2} \right) - E_J - \frac{E_J}{4!} \left(\varphi_{\text{ZPF}} (\hat{b} + \hat{b}^\dagger) \right)^4 + \dots \\ &= \hbar\omega_b \left(\hat{b}^\dagger \hat{b} + \frac{1}{2} \right) - E_J \left[\cos \left(\varphi_{\text{ZPF}} (\hat{b} + \hat{b}^\dagger) \right) + \frac{\varphi_{\text{ZPF}}^2}{2} (\hat{b} + \hat{b}^\dagger)^2 \right] \end{aligned} \quad (4.7)$$

with $\omega_b = 1/\sqrt{L_J C}$. In the second row, we have taken the full cosine into account with an added quadratic term which compensates for the absorption of the quadratic part of the cosine in $\hbar\omega_b \hat{b}^\dagger \hat{b}$. Going forward we ignore the zero point energy $\omega_b/2$ and the constant term $-E_J$ in the cosine expansion since they do not contribute to the energy difference between any two eigenstates.

In order to understand the energy levels of the transmon it is helpful to collect the energy conserving diagonal terms from the fourth-order expansion of the cosine to get

$$\frac{\hat{H}_{b,\text{diag}}}{\hbar} = \tilde{\omega}_b \hat{b}^\dagger \hat{b} - \frac{\chi_{bb}}{2} \hat{b}^{\dagger 2} \hat{b}^2 \quad (4.8)$$

where $\chi_{bb} = \frac{E_J}{2\hbar} \varphi_{\text{ZPF}}^4 = \frac{E_C}{\hbar}$ is called the anharmonicity and $\tilde{\omega}_b = \omega_b - \chi_{bb}$ is the effective resonant frequency of the transmon. Note that this procedure of collecting the diagonal terms is equivalent to quoting the Hamiltonian up to the first order in perturbation theory. The energy-eigenstates of the transmon are shown as a cartoon in Fig. 4.1d. Due to the

anharmonicity term, the energy eigenstates are no longer equally spaced as is clear from the figure. In order to avoid confusing the transmon eigenstates with the Fock states of a harmonic oscillator, hereon we name the lowest four states, $|0\rangle$ to $|3\rangle$, of the transmon as $|g\rangle$, $|e\rangle$, $|f\rangle$ and $|h\rangle$ respectively. Typically for the transmons that we utilize in this thesis, Josephson energy $E_J/h = 15$ to 100 GHz, charging energy $E_C/h \approx$ the anharmonicity $\alpha/2\pi = 50$ to 250 MHz, the frequency $\omega_b/2\pi = 4$ to 9 GHz and $\varphi_{\text{ZPF}} = 0.15$ to 0.45 .

The transmons constitute the most widely used qubits in cQED. Since the energy levels are un-equally spaced, the transitions between two levels of the transmon can be selectively addressed. Specifically, the ground $|g\rangle$ and the first excited state $|e\rangle$ of the transmon are used as the $|0\rangle$ and $|1\rangle$ state of the qubit. In the $g - e$ manifold of the transmons the correspondence between the transmon operators and the Pauli-operators is as follows:

$$\begin{aligned}
\hat{\sigma}_- &\leftrightarrow \hat{b} \\
\hat{\sigma}_+ &\leftrightarrow \hat{b}^\dagger \\
\hat{\sigma}_x &\leftrightarrow (\hat{b} + \hat{b}^\dagger) \\
\hat{\sigma}_y &\leftrightarrow i(\hat{b} - \hat{b}^\dagger) \\
\frac{(\hat{\sigma}_z + 1)}{2} &\leftrightarrow \hat{b}^\dagger \hat{b}
\end{aligned} \tag{4.9}$$

The \mathbf{X}_φ and \mathbf{Y}_φ rotations on the transmon qubit are implemented by activating a drive term of them form

$$\hat{H}_{\text{drive}} = \hbar\epsilon(t) \cos(\omega_d t + \phi) (\hat{b} + \hat{b}^\dagger). \tag{4.10}$$

Here ω_d is the frequency of the drive and, for the rotations on the $g - e$ transition, it is taken to be $\omega_d = \tilde{\omega}_b$. The phase ϕ decides the axis of rotation. The \mathbf{Z}_φ rotations are implemented in software by updating the phase ϕ for all of the following pulses. $\epsilon(t)$ is a

slowly varying envelope which is typically selected to be a truncated Gaussian given by

$$\epsilon(t) = A \operatorname{rect}\left(\frac{t-t_0}{T}\right) e^{-\frac{(t-t_0)^2}{2\sigma^2}} \quad (4.11)$$

where A is the amplitude, $T \geq 4\sigma$ is total duration, t_0 is the center of the pulse and σ is the standard deviation of the Gaussian. In order to rotate by angle φ we select $\int_{t_0-T/2}^{t_0+T/2} dt \epsilon(t) = \varphi$. Since the transmon is a multi-level system, one has to be careful while performing these rotations so that the leakage to the $|f\rangle$ or higher states does not occur. If the frequency spread of the pulse given by $1/\sigma$ is much less than the anharmonicity α then, to the first order, leakage to higher excited state is suppressed. More sophisticated pulse shapes have been developed to further suppress such leakage. We refer an interested reader to [Motzoi *et al.*, 2009, Reed, 2013] for understanding those techniques and experimental tuning of the single-qubit rotations. We will assume the availability of these pulses in our future theoretical as well as experimental discussion. Similarly, the multi-qubit gates between transmon qubits has also been an area of intense research. This thesis does not require such gates and as a result we do not venture into that discussion. The review article by [Krantz *et al.*, 2019] is an excellent place for finding further references on those topics.

Finally, the errors that affect transmons are similar to those discussed in the 1.2.1. The amplitude damping for a transmon is given by $\mathcal{D}[\sqrt{\Gamma_\downarrow} \hat{b}]$, heating is given by $\mathcal{D}[\sqrt{\Gamma_\uparrow} \hat{b}^\dagger]$ and dephasing is given by $\mathcal{D}[\sqrt{\Gamma_\phi} \hat{b}^\dagger \hat{b}]$. We typically quote the error rates on the transmon as the rate of relaxation given by $\Gamma_1 = \Gamma_\uparrow + \Gamma_\downarrow$ and the rate of total dephasing $\Gamma_2 = \Gamma_\phi + \Gamma_1/2$.

4.1.2 Transmon-cavity system

In this sub-section we focus on coupling the transmon to a harmonic oscillator. Since our discussions come from the perspective of storing information on harmonic oscillator and using the transmon as an ancilla for realizing engineered dissipation, we assume that

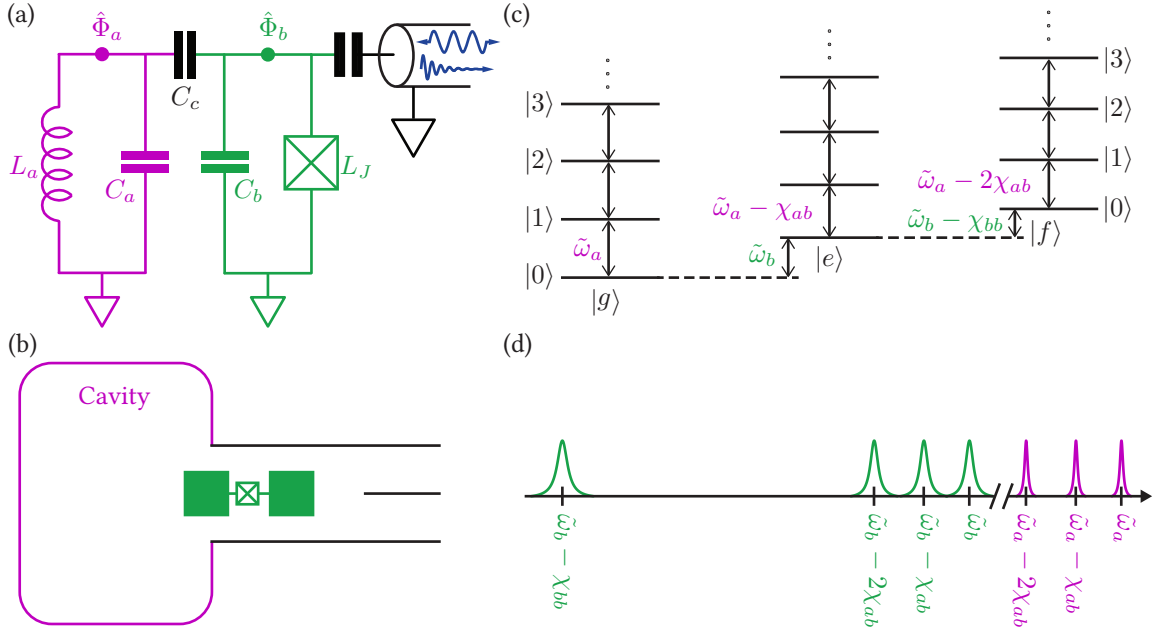


Figure 4.2: (a) Circuit diagram of a transmon (green) coupled to a harmonic oscillator (purple). For our purposes the harmonic oscillator is taken to be high- Q ($Q \approx 10^7$) and denoted by letter a in subscripts. The transmon is denoted by the letter b and is taken to be relatively lower- Q ($Q \approx 10^4 - 10^6$) as indicated by coupling to transmission line. The transmission line also serves the purpose of driving the transmon. In most of the application a second low- Q harmonic oscillator ($Q \approx 10^3$) is connected is coupled to the transmon which serves as readout resonator r (Not shown). (b) Cartoon representing the transmon-oscillator system. The harmonic oscillator is implemented as a simple metallic enclosure, i.e. a cavity, which is here represented as an empty box. The transmon is represented by two antenna pads and a Josephson junction as discussed previously. (c) The energy-level diagram of the joint transmon-oscillator system. Here $\tilde{\omega}_a$ is the renormalized frequency of the oscillator, $\tilde{\omega}_b$ is the renormalized frequency of the transmon, χ_{ab} is the cross-Kerr between transmon and the oscillator and χ_{bb} is the anharmonicity of the transmon. The anharmonicity inherited by the oscillator χ_{aa} is too small to be represented at this scale. (d) Relevant transition frequencies of the system.

the harmonic oscillator is high- Q and the transmon is low- Q . The circuit diagram of such transmon-oscillator system is depicted in Fig. 4.2a. In the figure and throughout this thesis, a is used for denoting the high- Q oscillator and b for denoting the transmon. In order to derive the Hamiltonian of this circuit, one first writes the Lagrangian with the Kinetic-energy and potential-energy terms of various circuit elements and then takes

the Legendre transform. We do not carry out this procedure here explicitly and instead refer a reader to [Vool, 2017] for further reading. The Hamiltonian of the circuit after the Legendre transform and quantization is as follows:

$$\hat{H} = \frac{\hat{Q}_a^2}{2\tilde{C}_a} + \frac{\hat{\Phi}_a^2}{2L_a} + \frac{\hat{Q}_b^2}{2\tilde{C}_b} - E_J \left[\cos \left(\frac{\hat{\Phi}_b}{\Phi_0} \right) + \frac{1}{2} \left(\frac{\hat{\Phi}_b}{\Phi_0} \right)^2 \right] + \frac{\hat{Q}_a \hat{Q}_b}{2\tilde{C}_c}. \quad (4.12)$$

Here the \tilde{C} s indicate the re-normalized capacitances that are obtained after the Legendre transform. The last term $\frac{\hat{Q}_a \hat{Q}_b}{2\tilde{C}_c}$ is essentially the energy stored in the coupling capacitance and describes the oscillator-transmon coupling. In terms of the creation-destruction operators this Hamiltonian is then written as

$$\begin{aligned} \frac{\hat{H}}{\hbar} = & \omega_a \hat{a}^\dagger \hat{a} + \omega_b \hat{b}^\dagger \hat{b} - g(\hat{a} - \hat{a}^\dagger)(\hat{b} - \hat{b}^\dagger) \\ & - \frac{E_J}{\hbar} \left[\cos \left(\varphi_{\text{ZPF},b}(\hat{b} + \hat{b}^\dagger) \right) + \frac{\left(\varphi_{\text{ZPF},b}(\hat{b} + \hat{b}^\dagger) \right)^2}{2} \right]. \end{aligned} \quad (4.13)$$

The new quantity introduced here is the coupling strength g which is defined as

$$g = \frac{Q_{\text{ZPF},a} Q_{\text{ZPF},b}}{2\hbar \tilde{C}_c}. \quad (4.14)$$

The first three terms in the transmon-oscillator Hamiltonian are bi-linear. The nonlinearity is completely captured by the cosine terms. In order to simplify this Hamiltonian, we first deal with the bi-linear part

$$\begin{aligned} \frac{\hat{H}_{\text{bi-linear}}}{\hbar} = & \omega_a \hat{a}^\dagger \hat{a} + \omega_b \hat{b}^\dagger \hat{b} - g(\hat{a} - \hat{a}^\dagger)(\hat{b} - \hat{b}^\dagger) \\ \approx & \omega_a \hat{a}^\dagger \hat{a} + \omega_b \hat{b}^\dagger \hat{b} + g(\hat{a}^\dagger \hat{b} + \hat{a} \hat{b}^\dagger). \end{aligned} \quad (4.15)$$

In the second row, we have ignored the $\hat{a}^\dagger \hat{b}^\dagger + \hat{a} \hat{b}$ terms since they don't conserve the excitation number and, as a result, don't contribute significantly to the dynamics of the system. This can be made clearer by going into an interaction picture with respect to $\frac{\hat{H}_0}{\hbar} = \omega_a \hat{a}^\dagger \hat{a} + \omega_b \hat{b}^\dagger \hat{b}$. The ignored terms each oscillate at $\omega_a + \omega_b$ which is much faster than the time scales of interest, and thus, the effect of these terms essentially averages to zero on those time scales. This is called rotating wave approximation (RWA). Going further, it is beneficial to diagonalize this bi-linear part of the Hamiltonian. This is accomplished by performing the Bogoliubov transformation which changes the operator \hat{a} and \hat{b} as follows:

$$\begin{aligned}\hat{a} &= \cos(\theta)\hat{A} - \sin(\theta)\hat{B} \\ \hat{b} &= \sin(\theta)\hat{A} + \cos(\theta)\hat{B}\end{aligned}\tag{4.16}$$

The angle θ is given by

$$\theta = \frac{1}{2} \arctan\left(\frac{2g}{\omega_a - \omega_b}\right),\tag{4.17}$$

which is chosen such that the term $g(\hat{a}^\dagger \hat{b} + \hat{a} \hat{b}^\dagger)$ in Eq. 4.15 is canceled. In terms of these new hybridized operators, the full Hamiltonian is given by

$$\frac{\hat{H}}{\hbar} = \omega_A \hat{A}^\dagger \hat{A} + \omega_B \hat{B}^\dagger \hat{B} - \frac{E_J}{\hbar} \left[\cos(\hat{\varphi}_{AB}) + \frac{1}{2} \hat{\varphi}_{AB}^2 \right],\tag{4.18}$$

where

$$\begin{aligned}\omega_A &= \frac{1}{2} \left(\omega_a + \omega_b - \text{sign}(\omega_a - \omega_b) \sqrt{4g^2 + (\omega_a - \omega_b)^2} \right) \\ \omega_B &= \frac{1}{2} \left(\omega_a + \omega_b + \text{sign}(\omega_a - \omega_b) \sqrt{4g^2 + (\omega_a - \omega_b)^2} \right)\end{aligned}\tag{4.19}$$

are the frequencies of the hybridized modes, and

$$\hat{\varphi}_{AB} = \varphi_{\text{ZPF},b} \sin(\theta) \hat{A} + \varphi_{\text{ZPF},b} \cos(\theta) \hat{B} = \varphi_A \hat{A} + \varphi_B \hat{B}. \quad (4.20)$$

For the vast majority of transmon-oscillator systems, $|\omega_a - \omega_b| \gg g$. This is called the dispersive regime. In the dispersive regime the frequencies of the hybridized modes are not much different from original frequencies. Moreover, the participation of mode A in the cosine is much smaller than that of mode B since $\varphi_A \ll \varphi_B$. In other words, modes are not much perturbed due to the hybridization with each other. In addition, we only have to deal with the diagonalized version of the Hamiltonian in this thesis. Therefore, in order to keep the notation simple, we hereon replace the uppercase letters A, B by the original small case letters a, b . Repeating the above Hamiltonian in this updated notation, we have

$$\frac{\hat{H}_{ab}}{\hbar} = \omega_a \hat{a}^\dagger \hat{a} + \omega_b \hat{b}^\dagger \hat{b} - \frac{E_J}{\hbar} \left[\cos(\hat{\varphi}_{ab}) + \frac{1}{2} \hat{\varphi}_{ab}^2 \right], \quad (4.21)$$

with

$$\hat{\varphi}_{ab} = \varphi_a \hat{a} + \varphi_b \hat{b}. \quad (4.22)$$

In order to understand the energy eigenstates of the Hamiltonian, we again collect the diagonal terms up to the fourth-order in the cosine. This gives

$$\frac{\hat{H}_{ab,\text{diag}}}{\hbar} = \tilde{\omega}_a \hat{a}^\dagger \hat{a} + \tilde{\omega}_b \hat{b}^\dagger \hat{b} - \chi_{ab} \hat{a}^\dagger \hat{a} \hat{b}^\dagger \hat{b} - \frac{\chi_{aa}}{2} \hat{a}^{\dagger 2} \hat{a}^2 - \frac{\chi_{bb}}{2} \hat{b}^{\dagger 2} \hat{b}^2 \quad (4.23)$$

where $\tilde{\omega}_a, \tilde{\omega}_b$ are the effective resonant frequencies of the modes, χ_{ab} is the cross-Kerr between the two modes and χ_{aa}, χ_{bb} are the self-Kerrs of the respective modes. The renor-

malized resonant frequencies are now given by

$$\begin{aligned}\tilde{\omega}_a &= \omega_a - \chi_{aa} - \frac{\chi_{ab}}{2} \\ \tilde{\omega}_b &= \omega_b - \chi_{bb} - \frac{\chi_{ab}}{2}\end{aligned}\tag{4.24}$$

The expressions for ‘Kerrs’ are

$$\begin{aligned}\chi_{ab} &= E_J \varphi_a^2 \varphi_b^2 \\ \chi_{aa} &= \frac{E_J}{2} \varphi_a^4 \\ \chi_{bb} &= \frac{E_J}{2} \varphi_b^4.\end{aligned}\tag{4.25}$$

It is also useful to note that $\chi_{ab} = \sqrt{4\chi_{aa}\chi_{bb}}$ and, in the dispersive regime, $\chi_{bb} \gg \chi_{ab} \gg \chi_{aa}$. The level structure of such dispersive Hamiltonian is illustrated in panel (c) and (d) of Fig. 4.2.

Typically, the systems that we will be dealing with have $\omega_a/2\pi = 5 - 8$ GHz, $\varphi_a = 0.01 - 0.05$, $\varphi_b = 0.15 - 0.45$, $\chi_{ab}/2\pi = 0.2 - 5$ MHz and $\chi_{aa}/2\pi = 1 - 100$ kHz in addition to the transmon parameters mentioned in the previous section. In our experimental implementations, an additional low- Q ($Q = 1000$ to 8000) harmonic oscillator is also coupled to the transmon. Such an oscillator is denoted by letter r and is utilized for performing readout or evacuating entropy of the transmon. The Hamiltonian of such multi-mode system is similar to those quoted in Eq. (4.21) and Eq. (4.23).

4.1.3 Modeling off-resonant drives and dissipation

The Hamiltonian of the systems in presence of drives is given by

$$\frac{\hat{H}_{\text{driven}}}{\hbar} = \frac{\hat{H}_{ab}}{\hbar} + \sum_{k=0}^N (\epsilon_k e^{i\omega_k t} \hat{b}^\dagger + \epsilon_k^* e^{-i\omega_k t} \hat{b}), \quad (4.26)$$

where \hat{H}_{ab} is the transmon-oscillator Hamiltonian quoted in Eq. (4.21), ω_k are the frequencies of the drives, ϵ_k are the complex amplitudes of the drives and a total of N drives are applied. Additionally, we have assumed that the drive amplitudes are constant and the only couple to the transmon mode. These assumptions are somewhat relaxed later. We also assume that the dominant dissipation in the system is due to the amplitude damping and, for the purpose of analysis, ignore the dephasing errors. Therefore, the master equation governing the evolution of the system is

$$\dot{\rho} = -\frac{i}{\hbar} [\hat{H}_{\text{driven}}, \rho] + \kappa_{1\text{ph}} \mathcal{D}[\hat{a}] \rho + \Gamma_{\downarrow} \mathcal{D}[\hat{b}] \rho. \quad (4.27)$$

We now show a series of transformations on the system that simplify the modeling of nonlinear processes. Let us consider the first transformation to be under the Unitary

$$\hat{U}_l = e^{i\omega_l \hat{b}^\dagger \hat{b}} \hat{D}_b[\xi_l] e^{-i\omega_l \hat{b}^\dagger \hat{b}} \quad (4.28)$$

where l indicates one of the drives, \hat{D}_b denotes displacement on the transmon mode and

$$\xi_l = \frac{-i\epsilon_l}{\frac{\Gamma_{\downarrow}}{2} + i(\omega_l - \omega_b)}. \quad (4.29)$$

Under the action of this unitary, the density matrix $\rho_l = \hat{U}_l \rho \hat{U}_l^\dagger$ evolves as

$$\dot{\rho}_l = \dot{\hat{U}}_l \hat{U}_l^\dagger \rho_l + \rho_l \hat{U}_l \dot{\hat{U}}_l^\dagger - \frac{i}{\hbar} \left[\hat{H}_{\text{driven},l}, \rho_l \right] + \kappa_{1\text{ph}} \mathcal{D}[\hat{a}] \rho_l + \Gamma_\downarrow \mathcal{D}[\hat{b}_l] \rho_l. \quad (4.30)$$

where

$$\hat{b}_l = \hat{U}_l \hat{b} \hat{U}_l^\dagger = \hat{b} + \xi_l e^{-i\omega_l t} \quad (4.31)$$

and

$$\hat{H}_{\text{driven},l} = \hat{U}_l \hat{H}_{\text{driven}} \hat{U}_l^\dagger. \quad (4.32)$$

It is easy to derive the full expression for $\hat{H}_{\text{driven},l}$ by replacing $\hat{b} \rightarrow \hat{b}_l$ everywhere. The derivative of the unitary \hat{U}_l is given by

$$\dot{\hat{U}}_l = i\omega_l \hat{b}^\dagger \hat{b} \hat{U}_l + \hat{U}_l (-i\omega_l \hat{b}^\dagger \hat{b}). \quad (4.33)$$

Substituting Eq. (4.31) to Eq. (4.33) in Eq. (4.30), and simplifying, we get

$$\dot{\rho}_l = -\frac{i}{\hbar} \left[\hat{H}_{\text{disp},l}, \rho_l \right] + \kappa_{1\text{ph}} \mathcal{D}[\hat{a}] \rho_l + \Gamma_\downarrow \mathcal{D}[\hat{b}] \rho_l \quad (4.34)$$

with

$$\frac{\hat{H}_{\text{disp},l}}{\hbar} = \omega_a \hat{a}^\dagger \hat{a} + \omega_b \hat{b}^\dagger \hat{b} - \frac{E_J}{\hbar} \left[\cos(\hat{\varphi}_l(t)) + \frac{\hat{\varphi}_l^2(t)}{2} \right] + \sum_{k \neq l} \left(\epsilon_k e^{-i\omega_k t} \hat{b}^\dagger + \epsilon_k^* e^{i\omega_k t} \hat{b} \right) \quad (4.35)$$

where

$$\hat{\varphi}_l(t) = \varphi_a \hat{a}^\dagger \hat{a} + \varphi_b \hat{b}^\dagger \hat{b} + \varphi_b (\xi_l e^{-i\omega_l t} + \xi_l^* e^{i\omega_l t}). \quad (4.36)$$

It is clear from the last three equations that the transformation in Eq. 4.28 has the effect displacing the Hamiltonian (hence the subscript disp) such that the l^{th} drive is absorbed inside the cosine. We typically use such transformation for drives where $|\omega_l - \omega_b|/\Gamma_\downarrow \gg 1$.

There is no formal restriction on ϵ_l , however, experimentally speaking $|\varphi_b \xi_l|$ approaching 1 tends to create chaotic processes [Lescanne *et al.*, 2019a] and hence, we strive to design systems where such a limit is not reached.

Now, as promised, let us reconsider the assumptions about drives being constant amplitudes and only coupling to the transmon. If the time dependence of the amplitude of the l^{th} drive is much slower than $\left| \frac{\Gamma_l}{2} + i(\omega_l - \omega_b) \right|$ then our analysis remains valid and the displacement ξ_l simply inherits the time dependence from ϵ_l according to Eq. (4.29). A faster time dependence leads to distortion of the pulse-shape. Next, the situation in which the l^{th} drive is coupled to the oscillator instead of the transmon, our effective Hamiltonian $\hat{H}_{\text{eff},l}$ from Eq. (4.35) remains the same except for re-normalization of the coupling displaced drive strength $\varphi_b \xi_l$. Hence, our assumption of coupling the drives exclusively to the transmon does not limit our analysis. In fact, experimentally speaking, under most circumstances, drives couple through all the modes of the system. However, without loss of generality we assume them to be coupling to one mode or the other according to the convenience of the analysis at hand.

It is possible to repeat the above analysis for multiple drives. Say, we want to absorb the effect of three drives, denoted by subscripts l, m, n , into the cosine, then we apply three successive transformations \hat{U}_l, \hat{U}_m and \hat{U}_n to get

$$\dot{\rho} = -\frac{i}{\hbar} \left[\hat{H}_{\text{disp}}, \rho \right] + \kappa_{\text{1ph}} \mathcal{D}[\hat{a}] \rho + \Gamma_{\downarrow} \mathcal{D}[\hat{b}] \rho \quad (4.37)$$

with

$$\frac{\hat{H}_{\text{disp}}}{\hbar} = \omega_a \hat{a}^\dagger \hat{a} + \omega_b \hat{b}^\dagger \hat{b} - \frac{E_J}{\hbar} \left[\cos(\hat{\varphi}(t)) + \frac{\hat{\varphi}^2(t)}{2} \right] + \sum_{k \neq l, m, n} \left(\epsilon_k e^{-i\omega_k t} \hat{b}^\dagger + \epsilon_k^* e^{i\omega_k t} \hat{b} \right) \quad (4.38)$$

where

$$\hat{\varphi}(t) = \varphi_a \hat{a}^\dagger \hat{a} + \varphi_b \hat{b}^\dagger \hat{b} + \varphi_b \sum_{j=l,m,n} (\xi_j e^{-i\omega_j t} + \xi_j^* e^{i\omega_j t}). \quad (4.39)$$

Note that we have not added subscripts lmn to ρ , \hat{H}_{disp} and $\hat{\varphi}(t)$ in last three equations to keep the notation simple. An observant reader might object to the notation since the transformed density matrix $\rho_{lmn} \neq \rho$, the density matrix in the original frame. However, we treat these density matrices on the same footing due to the following considerations. If the drives are always on, then the system density matrix is indeed ρ_{lmn} . On the other hand, if the drives are turned on and off, then, by keeping the ramp-up and ramp-down of the drives slow compared to $\left| \frac{\Gamma_\perp}{2} + i(\omega_l - \omega_b) \right|$ one allows for adiabatic evolution between the un-displaced and the displaced frame, thereby permitting us to treat the un-displaced and the displaced density matrix on the same footing.

While analyzing driven nonlinear processes, we typically expand the cosine in the effective Hamiltonian with the assumption of $\|\varphi(t)\| \ll 1$. This gives

$$\frac{\hat{H}_{\text{eff}}}{\hbar} = \omega_a \hat{a}^\dagger \hat{a} + \omega_b \hat{b}^\dagger \hat{b} - \frac{E_J}{\hbar} \left(\frac{\hat{\varphi}(t)^4}{4!} - \frac{\hat{\varphi}(t)^6}{6!} + \dots \right) + \sum_{k \neq l,m,n} (\epsilon_k e^{-i\omega_k t} \hat{b}^\dagger + \epsilon_k^* e^{i\omega_k t} \hat{b}). \quad (4.40)$$

The $\hat{\varphi}(t)^{2p}$ terms in the Hamiltonian are called p -wave mixing terms (four-wave, six-wave etc.). The four-wave mixing term is the strongest in the transmon-cavity Hamiltonian and we typically only consider the expansion of the cosine upto the fourth order. It is helpful, towards our latter discussion, to isolate the time-independent and diagonal fourth-order terms and show them explicitly in the rest of the Hamiltonian. We call this diagonal part \hat{H}_{diag} which is

$$\frac{\hat{H}_{\text{diag}}}{\hbar} = \tilde{\omega}_a \hat{a}^\dagger \hat{a} + \tilde{\omega}_b \hat{b}^\dagger \hat{b} - \chi_{ab} \hat{a}^\dagger \hat{a} \hat{b}^\dagger \hat{b} - \frac{\chi_{aa}}{2} \hat{a}^{\dagger 2} \hat{a}^2 - \frac{\chi_{bb}}{2} \hat{b}^{\dagger 2} \hat{b}^2. \quad (4.41)$$

Although this part looks exactly like the Hamiltonian in Eq. (4.23), the effective resonant frequencies $\tilde{\omega}_a$ and $\tilde{\omega}_b$ are now modified due to the Stark-shift generated by the lmn drives in addition to the previous renormalization. The expressions for $\tilde{\omega}_a$ and $\tilde{\omega}_b$ are

$$\begin{aligned}\tilde{\omega}_a &= \omega_a - \chi_{aa} - \frac{\chi_{ab}}{2} - \sum_{j=l,m,n} \chi_{ab} |\xi_j|^2 \\ \tilde{\omega}_b &= \omega_b - \chi_{bb} - \frac{\chi_{ab}}{2} - \sum_{j=l,m,n} 2\chi_{aa} |\xi_j|^2.\end{aligned}\tag{4.42}$$

The expressions for the Kerrs are the same as those in Eq. 4.25.

As a final remark, let us discuss the pure dephasing of the transmon mode, modeled by $\mathcal{D}[\hat{b}^\dagger \hat{b}]$, in this displaced frame. It can be shown that the dephasing noise is converted to additional single amplitude damping and heating of the transmon mode [Boissonneault *et al.*, 2009]. However, this effect is typically weak and for the purpose of this thesis dephasing is ignored.

4.2 Engineering two-photon drive and dissipation

The nonlinearity present in the transmon-oscillator system combined with off-resonant drives allows us to engineer a plethora of nonlinear processes. Here, the focus is on the engineering of multi-photon drives and dissipation. In particular, this section talks about the two-photon driven-dissipative process.

Let us first discuss an intuitive picture for how two-photon driven-dissipative process is engineered. The system that we imagine is a high- Q oscillator coupled to a very low- Q transmon. Now, if we could exchange two-photons of the oscillator with a single excitation of the transmon, then the loss of the transmon excitation results in an effective loss of two-photons of the oscillator. Similarly, if we first put an excitation in the transmon and exchange it for two photons in the oscillator, then the oscillator will gain two photons

simultaneously thus realizing a two-photon drive. Therefore, exchanging two oscillator photons with single transmon excitation and vice versa, an interaction between three photons, is the key to realizing the two-photon driven-dissipative process. However, typically, such an interaction does not conserve energy, since two oscillator photons might have a different energy compared to the transmon excitation. How does one bridge the energy gap? This is where the four-wave mixing property of the Josephson junction comes in handy. If an additional ‘pump’ tone is applied, which provides photons that bridge the energy difference, then such a process becomes energy-conserving. Cartoons in Fig. 4.3a depict such four-wave mixing between two oscillator photons, one transmon excitation and a pump-photon. We hereby assume that the Stark shifted frequency of the transmon, $\tilde{\omega}_b$, is less than that of the oscillator, $\tilde{\omega}_a$. As indicated by the cartoon, exchanging transmon excitation for two oscillator photons requires an additional $\omega_{p,2ph} = 2\tilde{\omega}_a - \tilde{\omega}_b$ energy obtained from the pump. The other way round, when two oscillator photons are exchanged for an excitation in the transmon, a pump photon at the same frequency is released. The entire two-photon driven-dissipative process engineered with the help of such two-photon exchange is illustrated using a level diagram in Fig. 4.3b and the involved frequencies are depicted in Fig. 4.3c.

Having described an intuitive picture for engineering two-photon driven-dissipative process, let us now show a formal derivation of the two-photon exchange Hamiltonian and the effective master equation of the system. This derivation is instructive towards our latter discussion of four-photon driven-dissipative process.

4.2.1 Effective equation of motion of the oscillator

Here we formally show that the combination of two-photon exchange process combined with a drive and dissipation on the transmon mode give rise to a two-photon driven-

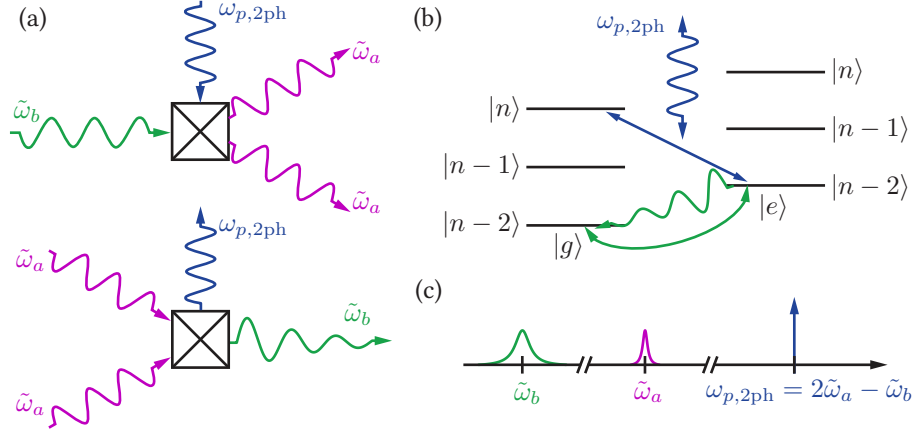


Figure 4.3: (a) Utilization of four-wave mixing for exchanging a transmon excitation for two photons of the harmonic oscillator and vice versa. Under the assumption that the effective transmon frequency $\tilde{\omega}_b$ is less than the effective oscillator frequency $\tilde{\omega}_a$, an additional pump photon at $\omega_{p,2ph}$ is required for transmon to oscillator exchange. In the reverse process, an additional pump photon is released along with the transmon excitation. (b) Representation of the two-photon driven-dissipative process with the help of a Fock-state ladder. Imagine that the system is in the $|g, n\rangle$ state. The two-photon exchange (straight blue arrow) connects $|g, n\rangle$ to $|e, n-2\rangle$ with the help of a pump photon (wave blue arrow) at $\omega_{p,2ph}$. The $|e, n-2\rangle$ then decays to $|g, n-2\rangle$ due to the transmon dissipation (decaying wavy green arrow), thus resetting the transmon and implementing two-photon dissipation. Similarly, the system can start in $|g, n-2\rangle$, excite to $|e, n-2\rangle$ due to transmon drive (double sided green arrow) and then connect to $|g, n\rangle$ with the help of two-photon exchange process, effectively adding two-photons on the oscillator. (c) Frequencies involved in two-photon exchange process.

dissipative process on the harmonic oscillator. As discussed previously, the two-photon exchange is engineered by adding a pump tone at $\omega_{p,2ph} = 2\tilde{\omega}_a - \tilde{\omega}_b$. The Hamiltonian of the transmon-oscillator system in presence of this pump tone and the transmon drive is given by

$$\frac{\hat{H}}{\hbar} = \omega_a \hat{a}^\dagger \hat{a} + \omega_b \hat{b}^\dagger \hat{b} - \frac{E_J}{\hbar} \left[\cos(\hat{\varphi}(t)) + \frac{(\hat{\varphi}(t))^2}{2} \right] + \left(\epsilon_d e^{-i\omega t} \hat{b}^\dagger + \epsilon_d^* e^{i\omega t} \hat{b} \right) \quad (4.43)$$

where

$$\hat{\varphi}(t) = \varphi_a (\hat{a} + \hat{a}^\dagger) + \varphi_b (\hat{b} + \hat{b}^\dagger) + \varphi_p (\xi_p e^{-i\omega_{p,2ph} t} + \xi_p^* e^{i\omega_{p,2ph} t}), \quad (4.44)$$

and $\omega_d = \tilde{\omega}_b$. We have absorbed the off resonant pump-tone into the cosine, while keeping the resonant drive on the transmon outside the cosine. Additionally, the effective frequencies $\tilde{\omega}_{a,b}$ are utilized while defining the pump and drive frequencies in anticipation of the renormalization to the nonlinearity and the pump-induced Stark-shifts. We expand the cosine up to the fourth order to get

$$\begin{aligned} \frac{\hat{H}}{\hbar} = & \tilde{\omega}_a \hat{a}^\dagger \hat{a} + \tilde{\omega}_b \hat{b}^\dagger \hat{b} - \chi_{ab} \hat{a}^\dagger \hat{a} \hat{b}^\dagger \hat{b} - \frac{\chi_{aa}}{2} \hat{a}^{\dagger 2} \hat{a}^2 - \frac{\chi_{bb}}{2} \hat{b}^{\dagger 2} \hat{b}^2 \\ & + \left(g_{2\text{ph}} e^{-i\omega_p, 2\text{ph}t} \hat{a}^{\dagger 2} \hat{b} + g_{2\text{ph}}^* e^{i\omega_p, 2\text{ph}t} \hat{a}^2 \hat{b}^\dagger \right) + \left(\epsilon_d e^{-i\omega_d t} \hat{b}^\dagger + \epsilon_d^* e^{i\omega_d t} \hat{b} \right) + \frac{\hat{H}_{\text{rest}}}{\hbar}. \end{aligned} \quad (4.45)$$

The terms in the first row are simply the effective frequencies and the Kerrs with the expressions for the effective frequencies given by

$$\begin{aligned} \tilde{\omega}_a &= \omega_a - \chi_{aa} - \frac{\chi_{ab}}{2} - \chi_{ab} |\xi_p|^2 \\ \tilde{\omega}_b &= \omega_b - \chi_{bb} - \frac{\chi_{ab}}{2} - 2\chi_{aa} |\xi_p|^2. \end{aligned} \quad (4.46)$$

The first term in the second row is the two-photon exchange term with

$$g_{2\text{ph}} = -\frac{\chi_{ab}}{2} \xi_p. \quad (4.47)$$

and the second term is the drive on the transmon. \hat{H}_{rest} represents rest of the terms in the Hamiltonian. We isolate the two-photon exchange and the transmon drive in this manner since they conserve energy in spite of not being diagonal. This becomes clear by going into the rotating frame with respect to

$$\frac{\hat{H}_0}{\hbar} = \tilde{\omega}_a \hat{a}^\dagger \hat{a} + \tilde{\omega}_b \hat{b}^\dagger \hat{b} \quad (4.48)$$

and keeping only the non-rotating terms. In other words, performing an RWA to the first order. Under such RWA, our Hamiltonian becomes

$$\begin{aligned} \frac{\hat{H}_{\text{RWA}}}{\hbar} = & -\chi_{ab}\hat{a}^\dagger\hat{a}\hat{b}^\dagger\hat{b} - \frac{\chi_{aa}}{2}\hat{a}^{\dagger 2}\hat{a}^2 - \frac{\chi_{bb}}{2}\hat{b}^{\dagger 2}\hat{b}^2 \\ & + \left(g_{2\text{ph}}\hat{a}^2\hat{b} + g_{2\text{ph}}^*\hat{a}^2\hat{b}^\dagger\right) + \left(\epsilon_d\hat{b}^\dagger + \epsilon_d^*\hat{b}\right). \end{aligned} \quad (4.49)$$

It is clear from inspecting this Hamiltonian that we indeed have a resonant two-photon exchange process as well as a resonant drive on the transmon.

The equation of motion of the complete transmon-resonator system is given by

$$\dot{\rho} = -\frac{i}{\hbar} \left[\hat{H}_{\text{RWA}}, \rho \right] + \kappa_{1\text{ph}} \mathcal{D}[\hat{a}]\rho + \Gamma_{\downarrow} \mathcal{D}[\hat{b}]\rho. \quad (4.50)$$

In the regime where $\frac{\chi_{ab}}{\Gamma_{\downarrow}}, \frac{|g_{2\text{ph}}|}{\Gamma_{\downarrow}}, \frac{|\epsilon_d|}{\Gamma_{\downarrow}} \sim \delta \ll 1$ and $\frac{\chi_{aa}}{\Gamma_{\downarrow}}, \frac{\kappa_{1\text{ph}}}{\Gamma_{\downarrow}} \sim \delta^2$, it is possible to perform the so called adiabatic elimination [Wiseman and Milburn, 1993, 1994] of the transmon degree of freedom to get the effective master equation of the oscillator. Such an elimination, in our context, is explained in the supplementary material of [Leghtas *et al.*, 2015]. We repeat the derivation here for the sake of completeness. Such adiabatic elimination will be repeatedly utilized in this thesis. The elimination is carried out by looking for a solution to the master equation of the form

$$\rho = \rho_{gg}|g\rangle\langle g| + \delta\rho_{ge}|g\rangle\langle e| + \delta\rho_{eg}|e\rangle\langle g| + \delta^2\rho_{ee}|e\rangle\langle e|. \quad (4.51)$$

Note that we have limited the system to the $g - e$ manifold of the transmon since none of our drives lead to a leakage out of this manifold. The effective density matrix of the oscillator is given by $\text{Tr}_b(\rho) = \rho_{gg} + \delta^2\rho_{ee}$. We derive the dynamics of this effective density

matrix up to the second order in δ . The equation of motion for ρ_{gg} is given by

$$\frac{1}{\Gamma_{\downarrow}} \dot{\rho}_{gg} = -i \left[-\frac{\chi_{aa}}{2\Gamma_{\downarrow}} \hat{a}^{\dagger 2} \hat{a}^2, \rho_{gg} \right] + \frac{\kappa_{1\text{ph}}}{\Gamma_{\downarrow}} \mathcal{D}[\hat{a}] \rho_{gg} - i\delta^2 \left(\hat{\mathbf{A}}^{\dagger} \rho_{eg} - \rho_{ge} \hat{\mathbf{A}} \right) + \delta^2 \rho_{ee} \quad (4.52)$$

where $\hat{\mathbf{A}} = \frac{1}{\delta\Gamma_{\downarrow}} (g_{2\text{ph}}^* \hat{a}^2 + \epsilon_d)$ is zeroth order in δ . We now need to find expressions for ρ_{ge} , ρ_{eg} and ρ_{ee} to the zeroth order in δ . The equation of motion for these are

$$\frac{1}{\Gamma_{\downarrow}} \dot{\rho}_{eg} = -i \hat{\mathbf{A}} \rho_{gg} - \frac{1}{2} \rho_{eg} + \mathcal{O}(\delta), \quad (4.53)$$

$$\frac{1}{\Gamma_{\downarrow}} \dot{\rho}_{ee} = -i \left(\hat{\mathbf{A}} \rho_{ge} + \rho_{eg} \hat{\mathbf{A}}^{\dagger} \right) - \rho_{ee} + \mathcal{O}(\delta), \quad (4.54)$$

Now, since ρ_{gg} only varies as $\mathcal{O}(\delta^2)$ compared to the damping rate which is $\mathcal{O}(1)$, we assume that $\dot{\rho}_{ee} = \dot{\rho}_{ge} = 0$. This is called the adiabatic approximation which essentially assumes that these quantities are continuously in the steady states. This leads to

$$\begin{aligned} \rho_{eg} &= -2i \hat{\mathbf{A}} \rho_{gg} + \mathcal{O}(\delta) \\ \rho_{ee} &= 4 \hat{\mathbf{A}} \rho_{gg} \hat{\mathbf{A}}^{\dagger} + \mathcal{O}(\delta). \end{aligned} \quad (4.55)$$

Finally, using Eq. (4.52), Eq. (4.55), and the assumption that $\dot{\rho}_{ee} = 0$, we get the effective master equation of the oscillator mode as

$$\dot{\rho}_a = \dot{\rho}_{gg} = -i \left[\epsilon_{2\text{ph}} \hat{a}^{\dagger 2} + \epsilon_{2\text{ph}}^* \hat{a}^2 - \frac{\chi_{aa}}{2}, \rho_a \right] + \kappa_{2\text{ph}} \mathcal{D}[\hat{a}^2] \rho_a + \kappa_{1\text{ph}} \mathcal{D}[\hat{a}] \rho_a \quad (4.56)$$

where

$$\epsilon_{2\text{ph}} = -\frac{2ig_{2\text{ph}}\epsilon_d}{\Gamma_{\downarrow}} \quad \text{and} \quad \kappa_{2\text{ph}} = \frac{4|g_{2\text{ph}}|^2}{\Gamma_{\downarrow}}. \quad (4.57)$$

Therefore, we indeed get an effective two-photon driven-dissipative process on the oscillator by activating two-photon exchange along with a drive and strong dissipation on

transmon-oscillator system. This technique has been utilized to engineer two-photon driven-dissipative process in three different experiments [Leghtas *et al.*, 2015, Touzard *et al.*, 2018, Lescanne *et al.*, 2019b]. Therefore, we do not dwell further on this topic and move onto our discussion on engineering four-photon driven-dissipative process.

4.3 Engineering four-photon driven-dissipative process

The four-component cat states require a four-photon driven-dissipative process on the harmonic oscillator in order to stabilize the manifold spanned by these states. The basic principle behind engineering such a processes is similar to the one we studied in the last section for engineering a two-photon driven-dissipative process. The idea is to enable a parametric interaction which exchanges four-photons of the oscillator mode with some excitation of an auxiliary transmon mode. Combining this exchange interaction with a dissipation and drive on the transmon mode should then results in a four-photon driven-dissipative process. The bottleneck, as it turns out, is the engineering of four-photon exchange process. In the next two sub-sections, we focus on this problem and come up with a feasible way for implementing four-photon exchange. This is followed by a discussion on converting this four-photon exchange into a four-photon driven-dissipative process.

4.3.1 Four-photon exchange using six-wave mixing

While implementing two-photon exchange process we utilized the four-wave mixing property of the Josephson junction, giving us an effective interaction of the form $\hat{a}^2\hat{b}^\dagger + \hat{a}^{\dagger 2}\hat{b}$. As a straightforward extension of this, one could envision implementing a four-photon exchange of the form $\hat{a}^4\hat{b}^\dagger + \hat{a}^{\dagger 4}\hat{b}$. This interaction involves four oscillator photons and one transmon excitation. Moreover, in order to bridge the energy gap between the four photons of the oscillator and one excitation of the transmon, that is to make this process

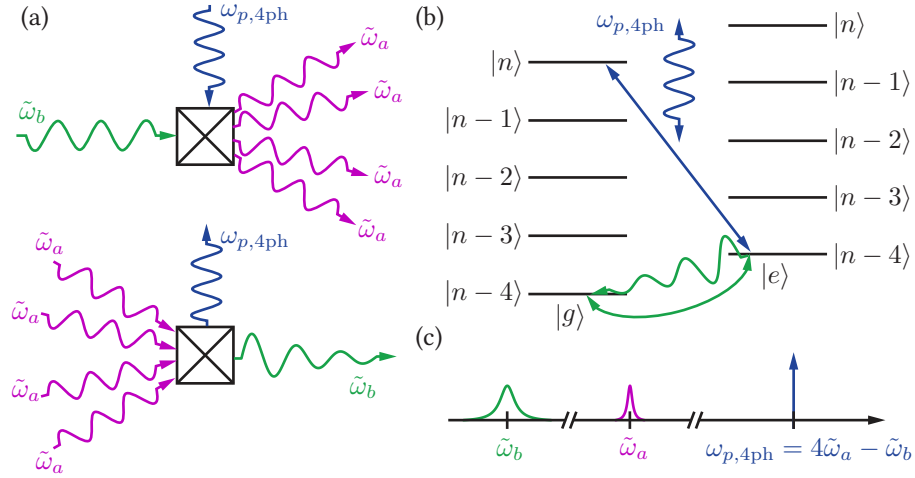


Figure 4.4: (a) Cartoon of a four-photon exchange performed using the six-wave mixing property of the Josephson junction. An excitation of the transmon and a pump photon at $\omega_{p,4ph} = 4\tilde{\omega}_a - \tilde{\omega}_b$ are converted to four-photons of the harmonic oscillator and vice-versa. (b) Explanation of the four-photon exchange and four-photon driven-dissipative process using the energy levels of the system. Suppose the system starts in the $|g, n\rangle$ state of the oscillator. The four-photon exchange (indicated by straight blue arrow) takes the system to $|e, n - 4\rangle$ state. A strong $|e\rangle$ to $|g\rangle$ dissipation on the transmon (decaying wavy green arrow) will then take the system to $|g, n - 4\rangle$ state thus resetting the transmon and effectively losing four-photon on the oscillator. Similarly, if the system starts in $|g, n - 4\rangle$ then the drive on transmon (double-sided green arrow) excites the system to $|e, n - 4\rangle$ state and then the four-photon exchange takes the system to the $|g, n\rangle$ state thus adding four-photons to the oscillator resulting in the four-photon drive. (c) Frequencies involved in the four-photon exchange process.

resonant / energy conserving, we require at least a single pump-photon at an appropriate frequency. Therefore, one could envision implementing the four-photon exchange with the help of the six-wave mixing property of the Josephson junction as depicted in the cartoons of Fig. 4.4a. As shown, a pump-photon at $\omega_{p,4ph} = 4\tilde{\omega}_a - \tilde{\omega}_b$ and a single transmon excitation can be destroyed to create four-photons of the resonator and vice versa. Panel (b) of the same figure shows how this process can be converted into a four-photon driven-dissipative process and panel (c) shows the frequencies involved in engineering such interaction. However, even though this implementation seems plausible, the problem with such an approach becomes clear once we take a closer look at the achievable

magnitudes of the four-photon exchange process.

In order to estimate the magnitude of this process let us start with the pumped Hamiltonian of the system

$$\frac{\hat{H}}{\hbar} = \omega_a \hat{a}^\dagger \hat{a} + \omega_b \hat{b}^\dagger \hat{b} - \frac{E_J}{\hbar} \left[\frac{(\hat{\varphi}(t))^4}{4!} - \frac{(\hat{\varphi}(t))^6}{6!} + \dots \right] \quad (4.58)$$

with

$$\hat{\varphi}(t) = \varphi_a (\hat{a} + \hat{a}^\dagger) + \varphi_b (\hat{b} + \hat{b}^\dagger) + \varphi_b (\xi_p e^{-i\omega_p, 4\text{ph}t} + \xi_p^* e^{i\omega_p, 4\text{ph}t}). \quad (4.59)$$

The magnitude of the six-wave mixing term which performs the four-photon exchange is then given by

$$|g_{4\text{ph}, 6\text{-wave}}| = \frac{E_J}{6!} \times \binom{6}{4} \times 2 \times \varphi_a^4 \varphi_b^2 |\xi_p| = \frac{\chi_{aa}}{12} \varphi_b^2 |\xi_p| \quad (4.60)$$

Here, $\binom{6}{4} \times 2 = \frac{6!}{4!2!} \times 2$ is the combinatorial factor for the four-photon exchange interaction and we have utilized $\chi_{aa} = \frac{E_J}{2} \varphi_a^4$. As we have discussed previously φ_b is in the range 0.15 – 0.45 for most of our systems and $|\xi_p|$ is $\mathcal{O}(1)$. Therefore, typically, the four-photon exchange obtained through six-wave mixing is at least an order of magnitude weaker than the anharmonicity of the oscillator. The other four-wave mixing terms, like the cross-Kerr χ_{ab} completely dominate the six-wave mixing interaction. As a result, naively utilizing the six-wave mixing property of the transmon mode does not work. There could be two approaches to making the six-wave mixing four-photon exchange usable. The first one is to replace transmon with circuits that cancel the four-wave mixing terms while keeping the required six-wave mixing terms. One such circuit has been proposed in [Mirrahimi *et al.*, 2014]. In fact, a different circuit discussed in Ch. 6 of this thesis and another circuit proposed and implemented in [Lescanne *et al.*, 2019b] could be adopted to perform such six-wave mixing process. However, in spite of these improvements, the achievable

magnitude of six-wave mixing is still comparable to single-photon dissipation rates, thus hampering the prospect of implementing four-photon driven-dissipative process. Therefore, the second step necessary for utilizing six-wave mixing is to increase the permissible pump strengths $|\xi_p|$. This task is complicated by the presence of chaotic processes at higher pump strengths [Sank *et al.*, 2016, Lescanne *et al.*, 2019a]. Work is in progress to alleviate these issues.

In the next sub-section, we propose a completely different approach to engineering four-photon exchange process. It turns out, this new approach allows for much stronger interactions even after the circuit and pump-strength improvements that we mentioned in the last paragraph. Such an approach brings four-photon driven-dissipative processes squarely into the realm of currently achievable technology.

4.3.2 Four-photon exchange with Raman-assisted cascading

In this sub-section, we propose an alternate method for implementing the four-photon exchange process which achieves a much higher interaction strength than the six-wave mixing approach. The overarching idea is to achieve this higher-order interaction by cascading readily available, lower-order parametric processes. In particular, we cascade two four-wave mixing processes to achieve the exchange of four oscillator photons with two excitations of a transmon mode and two pump photons, and vice versa. We have already seen in Sec. 4.2, that a four-wave mixing process enabled by a pump at frequency $2\tilde{\omega}_a - \tilde{\omega}_b$ can be employed to exchange two-photons of the oscillator with a single g to e excitation of the transmon mode. If this exchange is followed by another pump at frequency $2\tilde{\omega}_a - \tilde{\omega}_b + \chi_{bb}$, which exchanges two more photons of the oscillator with an e to f excitation of the transmon, then we would have exchanged four-photons of the oscillator with two excitations of the transmon. However, in this format, such a pro-

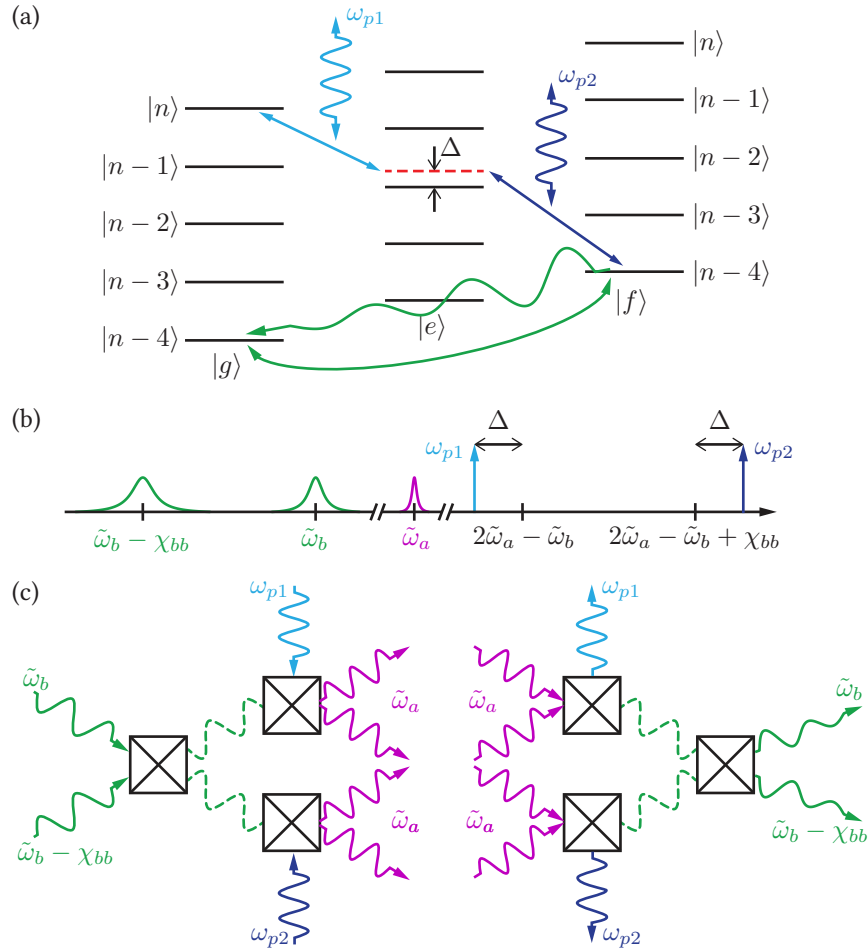


Figure 4.5: (a) Explanation of Raman-assisted cascading with the help of energy level diagram. Suppose the system starts in the $|g, n\rangle$ state. A four wave mixing process (straight light-blue arrow), enabled by a pump at frequency $\omega_{p1} = 2\tilde{\omega}_a - \tilde{\omega}_b - \Delta$, connects $|g, n\rangle$ to a virtual state (dashed red line) which is detuned from $|e, n-2\rangle$ by the detuning Δ . Another four wave-mixing process (dark-blue straight arrow), enabled by pump at $\omega_{p2} = 2\tilde{\omega}_a - \tilde{\omega}_b + \chi_{bb} + \Delta$ connects the virtual state to the $|f, n-4\rangle$ state, thus exchanging four-photons of the oscillator for two excitations in the transmon. An $f \rightarrow g$ dissipation on the transmon (decaying wavy green arrow) and a $f \leftrightarrow g$ drive (double sided green arrow) allow for converting the cascaded four-photon exchange into a four-photon driven-dissipative process. (b) Relevant frequencies involved in Raman-assisted cascading process. Note the key-role played by the anharmonicity of the transmon χ_{bb} in determining the pump frequencies. (c) Representation of the cascading process in terms of four-wave mixing diagrams. The dashed green lines indicate a virtual excitation.

cess only works stroboscopically since we have to let one exchange finish before starting the next one. There is no higher-order process generated and we inherit a strong sensitivity to dissipation of the transmon since a relaxation of the transmon after the first two-photon exchange will cause an effective two-photon loss on the oscillator. Instead, it is possible to cascade these process in a Raman-like transition in order to achieve an effective higher-order process. This is accomplished by shifting both the pumps from their respective resonant frequencies with equal and opposite detuning Δ . An energy level diagram explaining the resultant Raman-assisted cascaded process is depicted in Fig. 4.5a and Fig. 4.5c. The first two-photon exchange process now connects the initial $|g, n\rangle$ state of the transmon to a virtual state detuned from $|e, n - 2\rangle$ by a detuning Δ . At the same time, the second two-photon exchange process connects the virtual state to the $|f, n - 4\rangle$ state. This combination, in effect, connects the $|g, n\rangle$ directly to the $|f, n - 4\rangle$ state. To make this claim more intuitive, note that the individual two-photon exchange processes do not work, since the pumps do not provide enough energy for completing these processes. However, the combination of the two pumps provides the exact energy required for the $|g, n\rangle \leftrightarrow |f, n - 4\rangle$ transition. We give a formal analysis of such cascading process in this sub-section and show how to convert this four-photon exchange into a four-photon driven-dissipative process in the next sub-section. It is worth mentioning here that the conversion to four-photon driven-dissipative process now requires an $f \leftrightarrow g$ drive and an $f \rightarrow g$ dissipation. We also include the analysis of the $f \leftrightarrow g$ drive in this section since it requires many of the same techniques that we discuss here.

We start our analysis from the pumped Hamiltonian of the system given by

$$\frac{\hat{H}}{\hbar} = \omega_a \hat{a}^\dagger \hat{a} + \omega_b \hat{b}^\dagger \hat{b} - \frac{E_J}{\hbar} \left[\cos(\hat{\varphi}(t)) + \frac{(\hat{\varphi}(t))^2}{2} \right] \quad (4.61)$$

with

$$\hat{\varphi}(t) = \varphi_a (\hat{a} + \hat{a}^\dagger) + \varphi_b (\hat{b} + \hat{b}^\dagger) + \varphi_b \left(\sum_{k=1}^3 \xi_k e^{-i\omega_{pk}t} + \xi_k^* e^{i\omega_{pk}t} \right). \quad (4.62)$$

The first two pumps are used for addressing the cascaded four-photon exchange. The third pump is utilized for performing the $g \leftrightarrow f$ drive. The frequencies of the pumps are given by

$$\begin{aligned} \omega_{p1} &= 2\tilde{\omega}_a - \tilde{\omega}_b - \Delta + \delta \\ \omega_{p2} &= 2\tilde{\omega}_a - (\tilde{\omega}_b - \chi_{bb}) + \Delta + \delta \\ \omega_{p3} &= \tilde{\omega}_b - \frac{\chi_{bb}}{2} - \frac{\delta}{2}, \end{aligned} \quad (4.63)$$

where the renormalized and Stark-shifted frequencies $\tilde{\omega}_a$ and $\tilde{\omega}_b$ are

$$\begin{aligned} \tilde{\omega}_a &= \omega_a - \chi_{aa} - \frac{\chi_{ab}}{2} - \chi_{ab} \sum_{k=1}^3 |\xi_k|^2 \\ \tilde{\omega}_b &= \omega_b - \chi_{bb} - \frac{\chi_{ab}}{2} - 2\chi_{bb} \sum_{k=1}^3 |\xi_k|^2. \end{aligned} \quad (4.64)$$

As expected, the first pump is detuned from the $|g, n\rangle \leftrightarrow |e, n-2\rangle$ transition by $-\Delta$ and the second pump is detuned from the $|e, n-2\rangle \leftrightarrow |f, n-4\rangle$ transition with a detuning $+\Delta$. The additional detuning δ is small compared Δ and is added in order to compensate for higher-order frequency shifts. The expression for this compensation becomes clear later in the analysis. Developing the cosine up to fourth-order terms and keeping only the diagonal and the two-photon exchange terms, we get a Hamiltonian of

the form

$$\begin{aligned} \frac{\hat{H}_{\text{sys}}}{\hbar} = & \tilde{\omega}_a \hat{a}^\dagger \hat{a} + \tilde{\omega}_b \hat{b}^\dagger \hat{b} - \frac{\chi_{aa}}{2} \hat{a}^{\dagger 2} \hat{a}^2 - \frac{\chi_{bb}}{2} \hat{b}^{\dagger 2} \hat{b}^2 - \chi_{ab} \hat{b}^\dagger \hat{a} \hat{b}^\dagger \hat{b} \\ & + \sum_{k=1,2} \left(g_k e^{-i\omega_{pk}t} \hat{a}^{\dagger 2} \hat{b} + g_k^* e^{i\omega_{pk}t} \hat{a}^2 \hat{b}^\dagger \right) + \left(g_3 e^{-2i\omega_{p3}t} \hat{b}^{\dagger 2} + g_3^* e^{2i\omega_{p3}t} \hat{b}^2 \right). \end{aligned} \quad (4.65)$$

Here we have ignored all the other terms assuming a sufficiently large frequency difference, $|\tilde{\omega}_a - \tilde{\omega}_b|$, between the two modes. In the rotating frame with respect to the stationary part of the Hamiltonian, those terms oscillate much faster than Δ and hence don't contribute significantly to the dynamics of the system. Finally, the amplitudes of the nonlinear processes, g_k , are expressed as

$$g_{1/2} = -\frac{\chi_{ab}}{2} \xi_{1/2} \quad \text{and} \quad g_3 = -\frac{\chi_{bb}}{2} \xi_3^2. \quad (4.66)$$

In order to extract the effective dynamics of the system we go into a rotating frame with respect to

$$\frac{\hat{H}_0}{\hbar} = \tilde{\omega}_a \hat{a}^\dagger \hat{a} + (\tilde{\omega}_b - \delta) \hat{b}^\dagger \hat{b} - \frac{\chi_{bb}}{2} \hat{b}^{\dagger 2} \hat{b}^2 \quad (4.67)$$

The Hamiltonian in this interaction picture is given by

$$\begin{aligned} \frac{\hat{H}_1}{\hbar} = & \delta \hat{b}^\dagger \hat{b} - \frac{\chi_{aa}}{2} \hat{a}^{\dagger 2} \hat{a}^2 - \chi_{ab} \hat{a}^\dagger \hat{a} \hat{b}^\dagger \hat{b} \\ & + g_1 \exp \left[i \left(\chi_{bb} \hat{b}^\dagger \hat{b} + \Delta \right) t \right] \hat{a}^{\dagger 2} \hat{b} + \text{h.c.} \\ & + g_2 \exp \left[i \left(\chi_{bb} \left(\hat{b}^\dagger \hat{b} - 1 \right) - \Delta \right) t \right] \hat{a}^{\dagger 2} \hat{b} + \text{h.c.} \\ & + g_3 \exp \left[-2i \chi_{bb} \left(\hat{b}^\dagger \hat{b} - 2 \right) \right] \hat{b}^{\dagger 2} + \text{h.c.} \end{aligned} \quad (4.68)$$

Here *h.c.* denotes Hermitian conjugate. Note the presence of $\hat{b}^\dagger \hat{b}$ in the exponents which appears due the addition of qubit anharmonicity in \hat{H}_0 (Eq. 4.67). It turns out, to the first

order in RWA only the terms in first row and some part of the term in the last row survives. The two-photon exchange terms do not contribute to the first order in RWA at all, since we detuned the pumps from their respective resonant frequencies. The higher order process resulting from the two-photon exchange can be made apparent by performing RWA to the second order. The theory behind second order RWA is developed in [Mirrahimi and Rouchon, 2015]. Here, however, we simply use the results. The Hamiltonian to the second order in RWA is given by

$$H_{\text{eff}} = \overline{\hat{H}_1} - i \overline{\left(\hat{H}_1 - \overline{\hat{H}_1} \right) \int dt \left(\hat{H}_1 - \overline{\hat{H}_1} \right)} \quad (4.69)$$

where $\overline{\hat{A}} = \lim_{T \rightarrow \infty} \frac{1}{T} \int_0^T \hat{A}(t) dt$. Substituting for \hat{H}_1 and evaluating we get

$$\frac{\hat{H}_{\text{eff}}}{\hbar} = (g_{4\text{ph}} \hat{a}^{\dagger 4} - \epsilon_{fg}^*) \hat{\sigma}_{fg} + (g_{4\text{ph}}^* \hat{a}^4 - \epsilon_{fg}) \hat{\sigma}_{fg}^\dagger \quad (4.70)$$

$$+ \left(\zeta_{gaa} \hat{\sigma}_{gg} + \zeta_{eaa} \hat{\sigma}_{ee} + \zeta_{faa} \hat{\sigma}_{ff} - \frac{\chi_{aa}}{2} \right) \hat{a}^{\dagger 2} \hat{a}^2 \quad (4.71)$$

$$+ ((\chi_{ea} - \chi_{ab}) \hat{\sigma}_{ee} + (\chi_{fa} - 2\chi_{ab}) \hat{\sigma}_{ff}) \hat{a}^\dagger \hat{a} \quad (4.72)$$

$$+ \left(\delta + \frac{\chi_{ea}}{2} - \frac{3|g_3|^2}{\chi_{bb}} \right) \hat{\sigma}_{ee} + \left(2\delta + \frac{\chi_{fa}}{2} \right) \hat{\sigma}_{ff} \quad (4.73)$$

where we have only considered the first three energy levels g , e and f of the junction mode. The other energy levels of this mode are never populated in this scheme. The transition operators $\hat{\sigma}_{jk}$ are given by $|k\rangle\langle j|$. The first row of (4.73) is the four-photon exchange term and the two-photon $g \leftrightarrow f$ drive on the junction mode with

$$g_{4\text{ph}} = \sqrt{2} g_1 g_2 \left(\frac{1}{\Delta} - \frac{1}{\chi_{bb} + \Delta} \right) \text{ and } \epsilon_{fg} = \sqrt{2} g_3. \quad (4.74)$$

Note the importance of the transmon anharmonicity in this expression. If $\chi_{bb} = 0$ then the $g_{4\text{ph}}$ term vanishes. Therefore the b mode cannot be a harmonic oscillator. In fact $\chi_{bb} \gg \Delta$

regime is the most beneficial since the $g_{4\text{ph}}$ asymptotically approaches the maximum as χ_{bb} increases. In addition to the desired four-photon exchange term, the pumping also modifies the cross-Kerr terms by

$$\begin{aligned}\chi_{ea} &= \frac{4|g_2|^2}{\chi_{bb} - \Delta} - \frac{4|g_1|^2}{\Delta}, \\ \chi_{fa} &= \frac{8|g_2|^2}{\Delta} - \frac{8|g_1|^2}{\chi_{bb} + \Delta}\end{aligned}\quad (4.75)$$

and produces higher order interactions

$$\begin{aligned}\zeta_{gaa} &= \left(\frac{|g_1|^2}{\Delta} - \frac{|g_2|^2}{\chi_{bb} + \Delta} \right), \\ \zeta_{eaa} &= \left(-\frac{|g_1|^2(\chi_{bb} - \Delta)}{\Delta(\chi_{bb} + \Delta)} - \frac{|g_2|^2(2\chi_{bb} + \Delta)}{\Delta(\chi_{bb} + \Delta)} \right), \\ \zeta_{faa} &= \left(\frac{|g_2|^2(2\chi_{bb} + \Delta)}{\Delta(\chi_{bb} - \Delta)} - \frac{|g_1|^2}{2\chi_{bb} + \Delta} \right).\end{aligned}\quad (4.76)$$

Although these frequency changes tend to modify the frequency matching conditions, the discussion in the next sub-section shows that, in presence of dissipation, only a few of these higher-order frequency shifts are important.

In order to show the correctness of the effective dynamics, let us consider the oscillations between the states $|f, 0\rangle$ and $|g, 4\rangle$. The terms $(\zeta_{gaa}\hat{\sigma}_{gg} - \chi_{aa}/2)\hat{a}^{\dagger 2}\hat{a}^2$ and $(2\delta + \chi_{fa}/2)\hat{\sigma}_{ff}$ produce additional frequency shifts between $|g, 4\rangle$ and $|f, 0\rangle$, thus hindering the oscillations. We counter the effect of these terms by selecting parameters such that

$$\zeta_{gaa} = \frac{\chi_{aa}}{2} \text{ and } \delta = -\frac{\chi_{fa}}{4}.\quad (4.77)$$

The numerically obtained results for the dynamics given by Hamiltonian (4.65) (simulated in the rotating frame of $\tilde{\omega}_a\hat{a}^\dagger\hat{a} + \tilde{\omega}_b\hat{b}^\dagger\hat{b}$) is compared with the effective dynamics given by Hamiltonian (4.73) in Fig. 4.6a. The system parameters are $\chi_{aa}/(2\pi) = 312$ Hz,

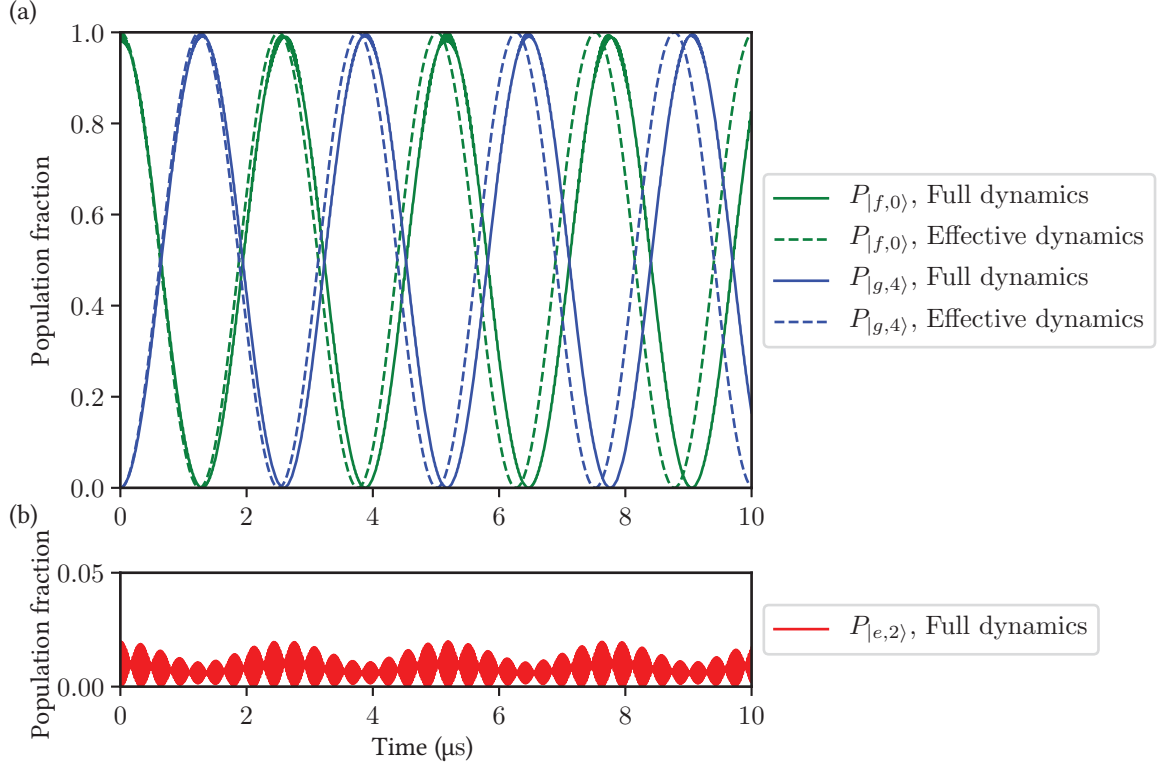


Figure 4.6: Numerical simulations of $|g, 4\rangle \leftrightarrow |f, 0\rangle$ oscillations. Panel (a) compares the effective dynamics given by the Hamiltonian (4.73) with the full dynamics corresponding to Eq. (4.65). For the four-photon exchange we do not need the $g \leftrightarrow f$ Rabi drive (see text). Consequently we set $g_3 = 0$. We start in the state $|f, 0\rangle$ and monitor the population of $|g, 4\rangle$ (blue) and $|f, 0\rangle$ (green). (b) Population leakage to the state $|e, 2\rangle$. The system parameters are $\chi_{aa}/(2\pi) = 312$ Hz, $\chi_{bb}/(2\pi) = 200$ MHz, $\chi_{ab}/(2\pi) = 0.5$ MHz. We choose $\delta = 153$ kHz, $\Delta = 50$ MHz, $g_1/(2\pi) = 899$ kHz, $g_2/(2\pi) = 2$ MHz in order to satisfy Eq. (4.77). No dissipation is added to the system.

$\chi_{bb}/(2\pi) = 200$ MHz, $\chi_{ab}/(2\pi) = 0.5$ MHz. The values $\Delta/(2\pi) = 50$ MHz, $\delta/(2\pi) = 153$ kHz, $g_1/(2\pi) = 899$ kHz and $g_2/(2\pi) = 2$ MHz are selected to satisfy Eq. (4.77). The third drive g_3 is set to zero in this simulation. Note that the strengths of the two-photon exchange processes $|g_1|$ and $|g_2|$ are chosen to be stronger than χ_{ab} . This turns out to be necessary for the four-photon exchange as well as the four-photon driven-dissipative process to work well. We will consider the effect of different magnitudes of $|g_{1,2}|/\chi_{ab}$ in a latter section. Dynamics given by both, (4.65) and (4.73), show the required oscillations.

The slight mismatch between the oscillation frequencies is due to a higher order effect induced by the occupation of the state $|e, 2\rangle$. Figure 4.6b shows the population leakage to the $|e, 2\rangle$ state. This leakage leads to an important limitation of the protocol as we will see in the next sub-section.

As a final point, let us compare the strength of four-photon exchange obtained from cascading to the one obtained from the six-wave mixing process. The four-photon exchange rate for $\Delta/2\pi = 50$ MHz, $\chi_{ab}/2\pi = 0.5$ MHz and $\chi_{bb}/2\pi = 200$ MHz and $g_{1,2} = \xi_{1,2}\chi_{ab}/2$ is $g_{4ph}/2\pi = |\xi_1\xi_2| \times 5.6$ kHz. For the same system parameters, and assuming a reasonable $E_J \approx 25$ GHz, we get the rate of six-wave mixing process to be around $|\xi_p| \times 3.3$ Hz where $|\xi_p|$ is the strength of the pump used to address the six-wave mixing process. It is clear that the six-wave mixing process is at-least three orders of magnitude weaker than the cascaded four-wave mixing process. Therefore, exploring the Raman-assisted cascading is crucial for implementation of four-photon driven-dissipative process.

4.3.3 Including dissipation on the transmon

As we have mentioned previously, along with the four-photon exchange process, we need an $g \leftrightarrow f$ drive and an $f \leftrightarrow g$ dissipation in order to get the full four-photon driven-dissipative process. We have also studied the implementation of the $g \leftrightarrow f$ drive in the last sub-section along with the four-photon exchange. Let us now focus on adding strong $f \rightarrow g$ dissipation to the system so that the transmon degree of freedom can be adiabatically eliminated (similar to Sec. 4.2). We consider two different ways of adding such dissipation.

The first is by utilizing the amplitude damping channel of the transmon mode. Under this channel the transmon dissipates from $|f\rangle$ to $|e\rangle$ followed by another relaxation from

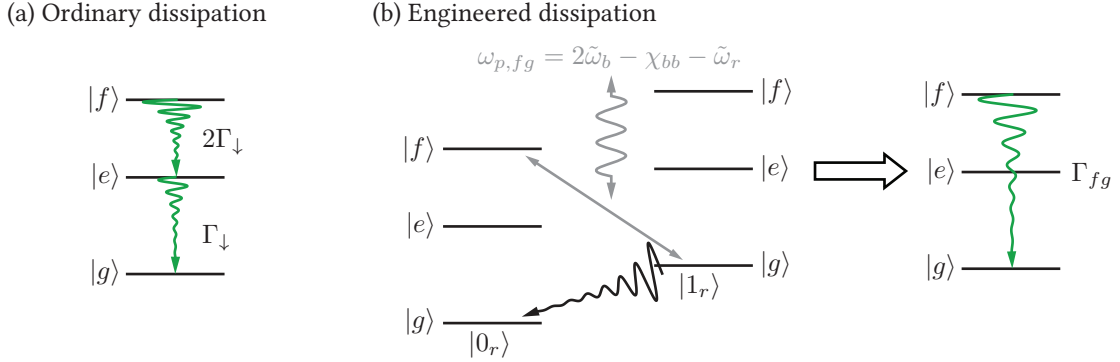


Figure 4.7: (a) The required $f \rightarrow g$ dissipation through the amplitude damping channel. The f state dissipates to e at the rate $2\Gamma_{\downarrow}$ and the e state to g at the rate Γ_{\downarrow} . (b) Engineered direct $f \rightarrow g$ dissipation. A two-photon exchange between the transmon and an auxiliary low- Q system r is enabled by a pump at $\omega_{p,fg} = 2\tilde{\omega}_b - \chi_{bb} - \tilde{\omega}_r$. This exchanges two transmon excitations in the $|f, 0_r\rangle$ state with a single excitation in the low- Q mode r , taking the system to $|g, 1_r\rangle$ state. Loss of this excitation in r results in system going to $|g, 0_r\rangle$ an effective $f \rightarrow g$ dissipation for the qubit.

$|e\rangle$ to $|g\rangle$ as indicated in Fig. 4.7a. It is possible to accomplish our goal of strong $f \rightarrow g$ dissipation by making the rate of amplitude damping Γ_{\downarrow} stronger than all the other rates in \hat{H}_{eff} of Eq. (4.73). Although this accomplishes our goal of having an $f \rightarrow g$ dissipation, it also leads to an unintended and fatal consequence for the four-component cat code. As we have discussed in the last section, the Raman-assisted cascading also leads to some leakage into the intermediate $|e, n-2\rangle$ state. A strong Γ_{\downarrow} then implies that this leaked population of the $|e, n-2\rangle$ state will then dissipate to the $|g, n-2\rangle$ state leading to a two-photon dissipation on the system which is a logical bit-flip error for the four-component cat states. Although the leakage can be suppressed by making the detuning Δ larger, a strong $e \rightarrow g$ dissipation is not ideal for the system.

The second way of achieving the required dissipation is by engineering a direct process which selectively dissipates from f to g without adding any dissipation from e to g . This can be achieved by making the transmon mode high- Q (small Γ_{\downarrow}) to suppress the e to g dissipation and engineering the direct $f \rightarrow g$ process with the help of an additional

auxiliary low- Q mode. Let us assume, for the sake of discussion, this low- Q mode is a readout mode r coupled to the transmon. Then, by enabling a process of the form $\hat{\sigma}_{fg}\hat{r}^\dagger + \hat{\sigma}_{gf}\hat{r}$ with the help of a pump at $2\tilde{\omega}_b - \chi_{bb} - \tilde{\omega}_r$, one could engineer an effective $f \rightarrow g$ dissipation on the transmon as shown in Fig. 4.7. Note that this is very similar to a two-photon driven-dissipative process, except the role of the oscillator is taken up by the transmon and the dissipation is provided by an auxiliary low- Q oscillator.

The master equation of the system in presence of ordinary amplitude damping channel and the engineered $f \rightarrow g$ dissipation is

$$\dot{\rho} = -\frac{i}{\hbar} \left[\hat{H}_{\text{sys}}, \rho \right] + \kappa_{1\text{ph}} \mathcal{D}[\hat{a}] \rho + \Gamma_{\downarrow} \mathcal{D}[\hat{b}] \rho + \Gamma_{fg} \mathcal{D}[\hat{\sigma}_{fg}] \rho. \quad (4.78)$$

where \hat{H}_{sys} is the system Hamiltonian before second order RWA mentioned in Eq. (4.65). In order to correctly model the effective dynamics of the system when dissipation is present, one has to perform the second order RWA in presence of the dissipation. Appendix A illustrates a way to accomplish this. The overall idea is to model dissipation using a Hamiltonian which includes the coupling of the transmon to many low- Q ‘bath’ oscillators. Adiabatic elimination of the bath oscillators then leads to the master equation in Eq. (4.78). However, in order to obtain the effective dynamics, one first performs the second order RWA on the system-bath Hamiltonian and then performs the adiabatic elimination of the bath degrees of freedom. Going further, under the assumption $2\Gamma_{\downarrow} + \Gamma_{fg} \gg \left\| \frac{\hat{H}_{\text{eff}}}{\hbar} \right\|$, where \hat{H}_{eff} is given in Eq. 4.73, it is possible to eliminate the transmon degree of freedom as well to get the effective dynamics of the high- Q oscillator mode. We quote the result for this oscillator dynamics over here and refer the interested reader to [Mundhada *et al.*, 2017] or appendix A for a complete derivation. The dynamics of the

oscillator is approximated by

$$\dot{\rho}_a = -\frac{i}{\hbar} \left[\hat{H}_{\text{eff},a}, \rho_a \right] + \kappa_{1\text{ph}} \mathcal{D}[\hat{a}] \rho_a + \kappa_{2\text{ph}} \mathcal{D}[\hat{a}^2] \rho_a + \kappa_{4\text{ph}} \mathcal{D}[\hat{a}^4] \rho_a. \quad (4.79)$$

with

$$\frac{\hat{H}_{\text{eff},a}}{\hbar} = \epsilon_{4\text{ph}} \hat{a}^{\dagger 4} + \epsilon_{4\text{ph}} \hat{a}^4 + \left(\zeta_{gaa} - \frac{\chi_{aa}}{2} \right) \hat{a}^{\dagger 2} \hat{a}^2 \quad (4.80)$$

and

$$\epsilon_{4\text{ph}} = -\frac{2ig_{4\text{ph}}\epsilon_{fg}}{\Gamma_{fg} + 2\Gamma_{\downarrow}} \quad (4.81)$$

$$\kappa_{2\text{ph}} = \left(\left| \frac{g_1}{\Delta} \right|^2 + \left| \frac{g_2}{\Delta + \chi_{bb}} \right|^2 \right) \Gamma_{\downarrow} \quad (4.82)$$

$$\kappa_{4\text{ph}} = \frac{4|g_{4\text{ph}}|^2}{\Gamma_{fg} + 2\Gamma_{\downarrow}}. \quad (4.83)$$

It is clear from the effective dynamics of the oscillator that we have a four-photon driven-dissipative process. The term that is worrying is the two-photon dissipation $\kappa_{2\text{ph}} \mathcal{D}[\hat{a}^2]$. As we mentioned earlier, this term is arising due to the leakage to the intermediate $|e, 2\rangle$ state in the Raman transition. From the expression for $\kappa_{2\text{ph}}$ it is clear that such a term could be minimized by either increasing Δ and χ_{bb} or by minimizing Γ_{\downarrow} . However, since the Γ_{\downarrow} can never be made zero, there is always some amount of logical bit-flip error introduced by our protocol. How useful is this protocol in that scenario? The answer comes from comparing the additional two-photon loss introduced by the protocol to the one inherited from losing single-photon twice in a given time interval τ . The probability of losing two-photons due to $\kappa_{1\text{ph}}$ is given by $(|\alpha|^2 \kappa_{1\text{ph}} \tau)^2 / 2$. The probability of losing two-photons in the same time interval due to the presence of $\kappa_{2\text{ph}}$ is given by $|\alpha|^4 \kappa_{2\text{ph}} \tau$. Therefore, if $\kappa_{2\text{ph}} \ll \kappa_{1\text{ph}}^2 \tau / 2$, then the added two-photon loss due to the protocol is much smaller than the probability of losing two-photons due to the natural means. In such a

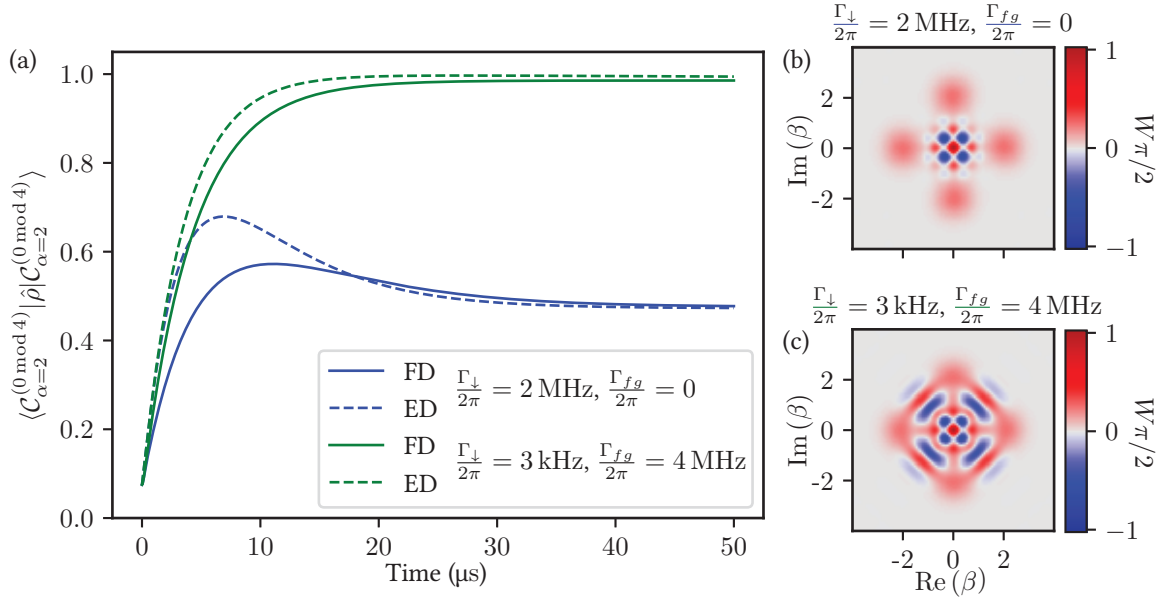


Figure 4.8: (a) Comparison between the numerical simulation of the full dynamics (FD, solid lines) given by Eq. (4.78) and the effective dynamics (ED, dashed lines) given by Eq. (4.79) for different values of Γ_{\perp} and Γ_{fg} . The blue curves have $\Gamma_{\perp}/2\pi = 2 \text{ MHz}$ and $\Gamma_{fg} = 0$. The green curves have $\Gamma_{\perp}/2\pi = 3 \text{ kHz}$ and $\Gamma_{fg}/2\pi = 4 \text{ MHz}$. Although the resulting $\kappa_{4\text{ph}}/2\pi = 1.65 \text{ kHz}$ is the same in both the cases, the rate of two-photon dissipation error $\kappa_{2\text{ph}}$ is suppressed by almost three orders of magnitude when engineered dissipation is dominant. The mismatch between effective dynamics and the full dynamics is due to the breakdown of the adiabatic approximation. We discuss this in more detail in appendix B. See text for other parameters. (b) Wigner function at $t = 50 \mu\text{s}$ for the $\Gamma_{\perp} = 2 \text{ MHz}$, $\Gamma_{fg} = 0$, case. The resultant state is a mixture of $|\mathcal{C}_{\alpha=2}^{(0 \bmod 4)}\rangle$ and $|\mathcal{C}_{\alpha=2}^{(2 \bmod 4)}\rangle$ as a result of the induced two-photon dissipation. (c) Wigner function at $t = 50 \mu\text{s}$ for the $\Gamma_{\perp} = 3 \text{ kHz}$, $\Gamma_{fg} = 4 \text{ MHz}$ case. The suppression of two-photon dissipation leads to high-fidelity preparation of $|\mathcal{C}_{\alpha=2}^{(0 \bmod 4)}\rangle$.

scenario, this protocol is useful since the four-photon driven-dissipative process protects against all the other errors present on the system. Going further, in Ch. 7 we propose a new encoding scheme which uses a similar protocol for manifold stabilization, however, is insensitive to the leakage losses.

In order to establish the validity of the effective dynamics, we compare the numerical simulation of the full dynamics given by Eq. 4.78 with those of effective dynamics in

Eq. 4.79 (see Fig. 4.8a). The system is started in the ground state and the overlap with the expected $|\mathcal{C}_\alpha^{(0 \bmod 4)}\rangle$ state is plotted as function of time. The evolution under the full master equation is represented by solid lines and that under the effective master equation is represented by the dashed lines. The Hamiltonian parameters are $\chi_{bb}/(2\pi) = 200$ MHz, $\chi_{aa}/(2\pi) = 312$ Hz, $\chi_{ab}/(2\pi) = 0.5$ MHz, $\Delta/(2\pi) = 50$ MHz, $\delta/(2\pi) = 153$ kHz, $g_2/(2\pi) = 2$ MHz and $g_1/(2\pi) = 899$ kHz. The parameters satisfy $\zeta_{gaa} = \chi_{aa}/2$. The four-photon exchange rate for these parameters $g_{4\text{ph}}/(2\pi) = 41$ kHz and the amplitude of the coherent states in the stabilized cat is given by $\alpha = \left(\frac{\epsilon_{fg}^*}{g_{4\text{ph}}}\right) = 2$. The single-photon dissipation rate of the oscillator $\kappa_{1\text{ph}}$ is set to zero. In the blue curves $\Gamma_\downarrow/(2\pi) = 2$ MHz and $\Gamma_{fg}/(2\pi) = 0$ giving $1/\kappa_{4\text{ph}} = 96 \mu\text{s}$ and $1/\kappa_{2\text{ph}} = 205 \mu\text{s}$. The full-dynamics (solid lines) and effective dynamics (dashed lines) converge to the same steady state. The differences at the short time scales arise due to breakdown of adiabatic approximation which has been elaborated in appendix B. The inherited two-photon dissipation in this case severely limits the fidelity of the $|\mathcal{C}_{\alpha=2}^{(0 \bmod 4)}\rangle$ state preparation. The Wigner function of the resulting state is shown in Fig. 4.8b. It is a mixture of the $|\mathcal{C}_{\alpha=2}^{(0 \bmod 4)}\rangle$ and $|\mathcal{C}_{\alpha=2}^{(2 \bmod 4)}\rangle$ state. On the other hand, the green curves show the simulation results where $\Gamma_\downarrow/(2\pi) = 3$ kHz and $\Gamma_{fg}/(2\pi) = 4$ MHz. The full dynamics and effective dynamics show better matching in this case. Additionally, although $\kappa_{4\text{ph}}$ is maintained to be around the same value as in the case of blue curves ($1/\kappa_{4\text{ph}} = 96 \mu\text{s}$), the two-photon error rate $\kappa_{2\text{ph}}$ is suppressed such that $1/\kappa_{2\text{ph}} = 136$ ms. It is clear from the achieved overlap for the green curves and the Wigner function in Fig. 4.8c that the protocol works much better in this case. Moreover, for the typical values of $1/\kappa_{1\text{ph}} \sim 0.1 - 1$ ms we have a two to three orders of magnitude separation between $\kappa_{2\text{ph}}$ and $\kappa_{1\text{ph}}$. Therefore, for a reasonable value of a time step $\tau \sim 10 \mu\text{s}$, which is determined by the frequency of parity measurements, the probability of two-photon loss due to $\kappa_{2\text{ph}}$ should be less than the probability of two-photon loss due to $\kappa_{1\text{ph}}$ thus making the added error tolerable.

4.3.4 Required pump strengths to overcome Cross-Kerr

In the last sub-section we showed through analysis and simulations that the cascaded four-photon exchange process indeed produces the required four-photon driven-dissipative process. However, while selecting the parameters for the simulation, we have always selected the strengths of the two-photon exchange process, $g_{1,2} > \chi_{ab}$ the cross-Kerr between the oscillator and the transmon mode. Experimentally speaking, this is not always possible since the pump strengths required to achieve such high two-photon exchange rates result into other spurious processes as well. What happens if we increase the magnitude of the cross-Kerr? We examine the effect of the increasing values of cross-Kerr on the dynamics of the system in Fig. 4.9. All the other parameters are kept the same as the previous section. It is clear from this simulation that as the magnitude of χ_{ab} increases, the fidelity of the process decreases. The strong cross-Kerr completely distorts the state of the oscillator which leads to the decrease in fidelity. In fact, through many more numerical simulations, we have figured out, as a rule of thumb, we require $g_2 \geq 2\chi_{ab}$ for the process to work.

The reason behind the deleterious effect of the cross-Kerr is the following. The resonant frequencies of the $|g, n\rangle \leftrightarrow |e, n-2\rangle$ and $|e, n-2\rangle \leftrightarrow |f, n-4\rangle$ transitions depend on n due to the presence of cross-Kerr. Therefore, the pumps have different detuning Δ from each of these resonances. This leads to a complete breakdown of the four-photon exchange process. Moreover, the leakage population in the $|e, n-2\rangle$ state also leads to continuous entanglement between the transmon and the oscillator in the presence of the cross-Kerr which adds to the distortion. Therefore, in order for the four-photon driven-dissipative process to work, it is mandatory to either achieve strong two-photon exchange rates or cancel out the cross-Kerr. We provide an improved circuit which allows for such canceling of the cross-Kerr in Ch. 6.

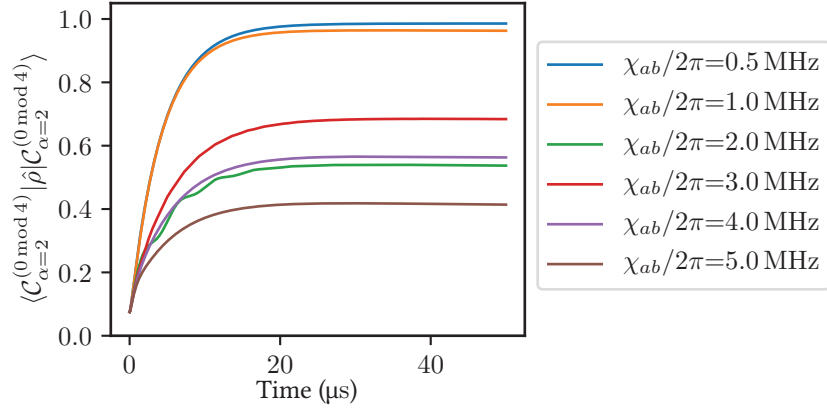


Figure 4.9: Simulation of the full dynamics, Eq. (4.78), for different values of the cross-Kerr. All the other parameters are maintained constant at the values specified in the last section. The system is started in the ground state and the overlap with the $|\mathcal{C}_{\alpha=2}^{(0 \bmod 4)}\rangle$ is plotted as function of time. It is clear that the increase in cross-Kerr results in lower fidelity of the process.

4.4 Summary and prelude to the next chapter

We summarize some of the important points of this chapter in the following list:

- (i) Josephson junction based circuits provide the required nonlinearity in cQED.
- (ii) Specifically, we utilize the transmon for providing nonlinearity as well as realizing qubits in our systems.
- (iii) The off-resonant drives on a transmon-oscillator system enables nonlinear processes. Such drives can be modeled by absorbing them in the cosine of transmon potential.
- (iv) Two-photon driven-dissipative process can be realized by utilizing the four-wave mixing property of the transmon along with an off-resonant pump.
- (v) A similar realization of four-photon driven-dissipative process using the six-wave mixing property of the Josephson junction results in a weak interaction.

- (vi) A stronger interaction for implementing four-photon driven-dissipative process can be obtained by cascading two four-wave mixing processes.
- (vii) Combining the cascaded interaction with $f \rightarrow g$ direct dissipation on the transmon and $f \leftrightarrow g$ drive results in a four-photon driven-dissipative process.
- (viii) The amplitude damping of the transmon in presence of cascading results in two-photon loss on the harmonic oscillator which is a bit-flip error on the four-component cat code. Two-photon loss can be suppressed by suppressing amplitude damping and increasing the detuning in the cascading process.
- (ix) For the cascading to work, the two-photon exchange rate needs to be higher than the cross-Kerr interaction between the transmon and the oscillator.

The technique of Raman-assisted cascading of lower-order nonlinear processes to obtain a higher-order nonlinearity is the new, relatively unexplored concept that we have introduced in this chapter. Such cascading can be utilized for engineering a plethora of nonlinear processes. In Ch. 7 we utilize cascading for modifying cross-Kerr between two modes and also for engineering the driven-dissipative process for stabilizing the pair-cat code. However, to the best of our knowledge, such cascading of two nonlinear processes has not been implemented before. Hence, in the next chapter (Ch. 5), we focus on experimentally verifying the feasibility of cascading nonlinear processes in this manner. Ch. 6 develops a new four-wave mixing elements which allows for two-photon exchange while completely canceling the cross-Kerr interaction thereby addressing the issue in point (ix). Furthermore, in Ch. 7 we show that the pair cat-code can tolerate multiple photon losses on a single mode and is therefore immune to the two-photon dissipation error, thus providing a viable solution for the issue in point (vii).

Chapter 5

Demonstration of a cascaded process

From our previous discussion, it is clear that four-photon driven-dissipative process plays an important role in stabilization of four-component cat states. The implementation of such highly nonlinear drive and dissipation requires a four-photon exchange interaction which swaps four photons of the oscillator with some excitations in a nonlinear transmon mode. In the last chapter we established that the best way to achieve this interaction is through Raman-assisted cascading of two four-wave mixing processes that each exchange two photons of the oscillator for an excitation of the transmon. In fact, we later show that such Raman-assisted cascading of lower-order processes enables the engineering many other nonlinear interactions that are useful towards autonomous error correction. Therefore, keeping these applications in mind, here we focus on experimentally verifying the feasibility of such cascading.

The specific process that we demonstrate is a transition between $|f, 0\rangle$ and $|g, 4\rangle$ states of the transmon-oscillator system. This transition is a precursor to the $\hat{a}^{\dagger 4}|g\rangle\langle f| + \hat{a}^4|f\rangle\langle g|$ process which requires all the $|f, n\rangle \leftrightarrow |g, n + 4\rangle$ transitions to occur simultaneously. Nonetheless, our implementation of $|f, 0\rangle \leftrightarrow |g, 4\rangle$ transition serves as a proof of principle for the feasibility of the Raman-assisted cascaded processes. The next section

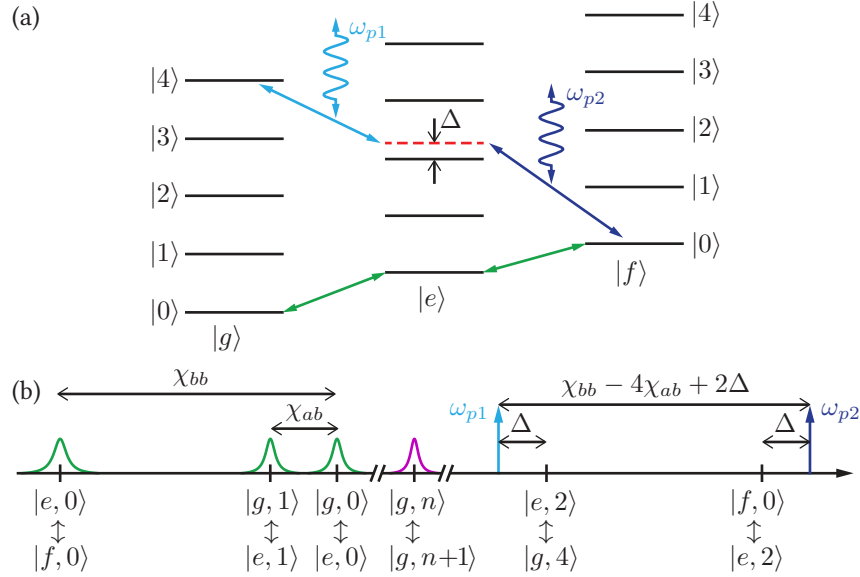


Figure 5.1: (a) Explanation of $|f, 0\rangle \leftrightarrow |g, 4\rangle$ oscillation with the help of energy level diagram of a high- Q harmonic oscillator (hereby called high- Q resonator or storage resonator) and a transmon mode (hereby called conversion transmon). Starting in $|g, 0\rangle$, the system is prepared in $|f, 0\rangle$ by applying $|g\rangle \rightarrow |e\rangle$ and $|e\rangle \rightarrow |f\rangle$ Rabi pulses (green arrows). A pump at frequency ω_{p2} (dark blue) connects $|f, 0\rangle$ to a virtual state, represented by the dashed red line, detuned from $|e, 2\rangle$ with a detuning Δ . A second pump at frequency ω_{p1} (light blue) connects the virtual state to $|g, 4\rangle$, thus converting the two transmon excitations into four resonator excitations. (b) Frequency distribution of the pumps and the transitions involved in the scheme.

(Sec. 5.1) quickly recaps some of the theory required for understanding the work in this chapter. Sec. 5.2 introduces our experimental setup for demonstrating this process. The tuneup and characterization of the pumped transition is undertaken in Sec.s 5.3 and 5.4 respectively. Our data from these sections proves that the Raman-assisted $|f, 0\rangle \leftrightarrow |g, 4\rangle$ transition indeed works as expected. A summary of the current chapter, along with some future directions are presented in the final section (Sec. 5.5).

5.1 Theory of $|f, 0\rangle \leftrightarrow |g, 4\rangle$ transition

As mentioned in Sec. 4.3.4, the cascaded four-photon exchange between transmon and a harmonic oscillator requires the strength of the individual four-wave mixing processes to be stronger than the cross-Kerr interaction between the two modes. Here we get around this issue by explicitly taking the frequency shifts due to cross-Kerr into account, which allows us to demonstrate $|f, 0\rangle \leftrightarrow |g, 4\rangle$ transition without any constraint on the pump strengths. As a downside, our system cannot show the full four-photon exchange involving all the $|f, n\rangle \leftrightarrow |g, n+4\rangle$ transitions since the frequency matching condition depends on n . We address this issue in the next chapter by building a cross-Kerr-free four-wave mixing device.

In this section we develop the theory of $|f, 0\rangle \leftrightarrow |g, 4\rangle$ transition in presence of strong cross-Kerr interaction. This transition is realized by cascading off-resonant $|f, 0\rangle \leftrightarrow |e, 2\rangle$ enabled by pump at frequency ω_{p2} and $|e, 2\rangle \leftrightarrow |g, 4\rangle$ enabled by a pump at frequency ω_{p1} as shown in Fig. 5.1a. The Hamiltonian of the system in presence of the pumps is given by

$$\frac{\hat{H}_{\text{sys}}}{\hbar} = \frac{\hat{H}_{ab}}{\hbar} + \left[(g_1 e^{-i\omega_{p1}t} + g_2 e^{-i\omega_{p2}t}) \hat{a}^{\dagger 2} \hat{b} + \text{h.c.} \right] \quad (5.1)$$

where g_1 and g_2 are amplitudes of the pumped processes and h.c. denotes Hermitian conjugate. This Hamiltonian is obtained by setting $g_3 = 0$ in Eq. (4.65) from the last chapter. The first term \hat{H}_{ab} is, as usual, the diagonal part of the Hamiltonian with

$$\frac{\hat{H}_{ab}}{\hbar} = \tilde{\omega}_a \hat{a}^\dagger \hat{a} + \tilde{\omega}_b \hat{b}^\dagger \hat{b} - \chi_{ab} \hat{a}^\dagger \hat{a} \hat{b}^\dagger \hat{b} - \frac{\chi_{aa}}{2} \hat{a}^{\dagger 2} \hat{a}^2 - \frac{\chi_{bb}}{2} \hat{b}^{\dagger 2} \hat{b}^2,$$

By combining the relations in Eq. (4.64) and Eq. (4.66) of the last chapter, we also express

the Stark shifts directly in terms of the g_1 and g_2 as follows:

$$\begin{aligned}\tilde{\omega}_a &= \omega_a - \frac{4}{\chi_{ab}} (|g_1|^2 + |g_2|^2) \\ \tilde{\omega}_b &= \omega_b - \frac{8\chi_{bb}}{\chi_{ab}^2} (|g_1|^2 + |g_2|^2) .\end{aligned}\quad (5.2)$$

In terms of these quantities, the pump frequencies are expressed as

$$\begin{aligned}\omega_{p1} &= 2\tilde{\omega}_a - \tilde{\omega}_b + \chi_{bb} - 2\chi_{ab} + \Delta + \delta \\ \omega_{p2} &= 2\tilde{\omega}_a - \tilde{\omega}_b + 2\chi_{ab} - \Delta + \delta .\end{aligned}\quad (5.3)$$

It is clear from these expressions that the frequency shifts due to cross-Kerr are explicitly taken into account. As expected, these two pumps are equally detuned from the $|f0\rangle \leftrightarrow |e2\rangle$ and $|e2\rangle \leftrightarrow |g4\rangle$ transitions by a detuning Δ (see Fig. 5.1b). The common shift in the pump frequencies, given by δ (not shown in the figure), helps in accounting for the anharmonicity of the storage resonator and higher-order frequency shifts.

In order to derive the effective Hamiltonian of the system we go into a rotating frame with respect to \hat{H}_0 given by

$$\frac{\hat{H}_0}{\hbar} = \tilde{\omega}_a \hat{a}^\dagger \hat{a} + (\tilde{\omega}_b - \delta) \hat{b}^\dagger \hat{b} - \chi_{ab} \hat{a}^\dagger \hat{a} \hat{b}^\dagger \hat{b} - \frac{\chi_{bb}}{2} \hat{b}^{\dagger 2} \hat{b}^2 .$$

As opposed to the last chapter, here we have included the cross-Kerr term explicitly in the rotating frame. Performing RWA to the second order in this rotating frame gives us the effective Hamiltonian

$$\begin{aligned}\frac{\hat{H}_{\text{eff}}}{\hbar} &= (g_{4\text{ph}} |g, 4\rangle \langle f, 0| + g_{4\text{ph}}^* |f, 0\rangle \langle g, 4|) \\ &+ \left(\frac{12|g_2|^2}{\Delta} - \frac{12|g_1|^2}{\chi_{bb} - 4\chi_{ab} + \Delta} - 6\chi_{aa} \right) |g, 4\rangle \langle g, 4|\end{aligned}$$

$$\begin{aligned}
& - \left(\frac{12|g_2|^2 + 4|g_1|^2}{\Delta} - \frac{4|g_2|^2 + 12|g_1|^2}{\chi_{bb} - 4\chi_{ab} + \Delta} + \chi_{aa} + \delta \right) |e, 2\rangle\langle e, 2| \\
& + \left(\frac{4|g_1|^2}{\Delta} - \frac{4|g_2|^2}{\chi_{bb} - 4\chi_{ab} + \Delta} - 2\delta \right) |f, 0\rangle\langle f, 0|. \tag{5.4}
\end{aligned}$$

The first row in the expression for the effective Hamiltonian is indeed the $|f, 0\rangle \leftrightarrow |g, 4\rangle$ transition. The magnitude of $g_{4\text{ph}}$ in this expression is given by

$$g_{4\text{ph}} = \sqrt{48}g_1g_2 \left(\frac{1}{\Delta} - \frac{1}{\chi_{bb} - 4\chi_{ab} + \Delta} \right). \tag{5.5}$$

Here the factor 48 appears due to the \sqrt{n} constants in the Fock state expansion of the destruction operators. All the other terms in the Hamiltonian are the higher-order frequency shifts. In the experiment, these shifts need to be compensated, which is accomplished by sweeping both the pump frequencies while keeping their difference constant at $\chi_{bb} - 4\chi_{ab} + 2\Delta$. Such common shifts of the pump frequencies is modeled by the quantity δ that we added in expressions for the pump frequencies. We select the value of δ to be

$$\delta = 3\chi_{aa} + \left(\frac{2|g_1|^2 - 6|g_2|^2}{\Delta} + \frac{6|g_1|^2 - 2|g_2|^2}{\chi_{bb} - 4\chi_{ab} + \Delta} \right). \tag{5.6}$$

This value is selected to ensure that the constants in front of the $|g, 4\rangle\langle g, 4|$ and $|f, 0\rangle\langle f, 0|$ terms in Eq. (5.4) are equal, making the $|f, 0\rangle \leftrightarrow |g, 4\rangle$ transition completely resonant.

Now that we have all the theory required for modeling the $|f, 0\rangle \leftrightarrow |g, 4\rangle$ transition in place, let us proceed to the experimental implementation of this transition.

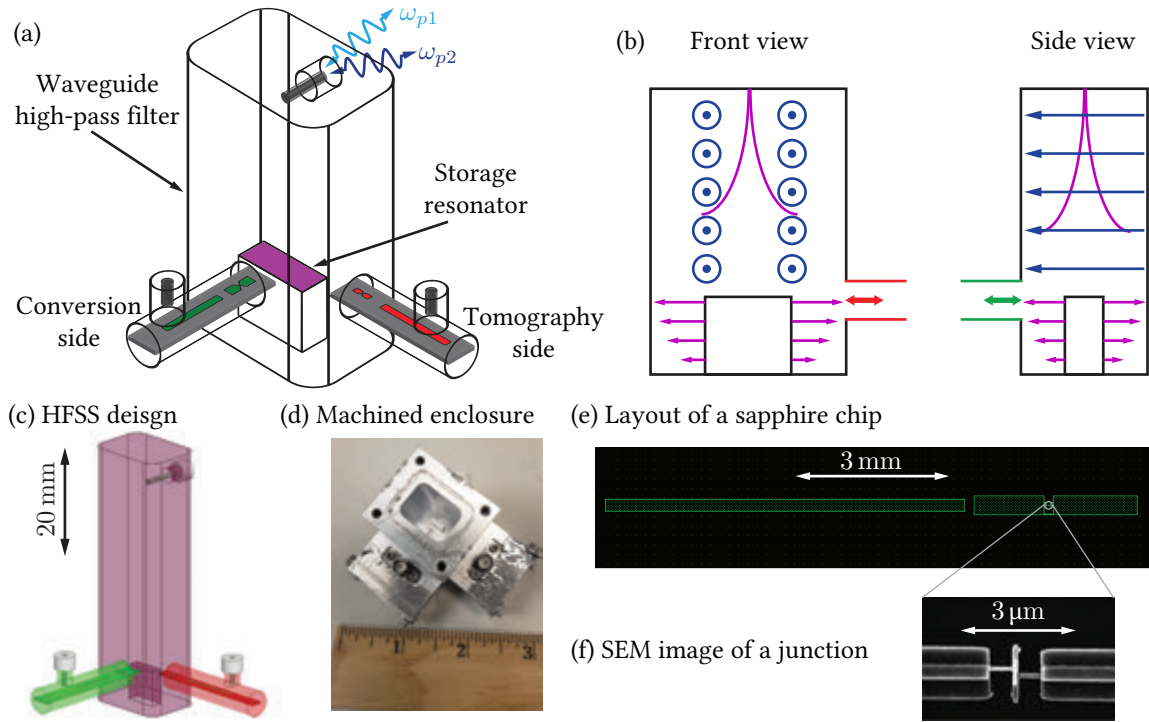


Figure 5.2: (a) Schematic of the implementation. The high- Q resonator is formed by an aluminum $\lambda/4$ -type 3-dimensional superconducting resonator (magenta), which is dispersively coupled to the conversion transmon (green) and the tomography transmon (red). The two $\lambda/2$ stripline resonators coupled to the transmons are used for performing single-shot readout of the respective transmons. The pumps are coupled through a strongly coupled pin at the top of the enclosure which acts as a rectangular waveguide high-pass filter with pump frequencies in the pass-band and the mode frequencies in the stop-band. (b) Cartoon representing the front and side views of the system with the fields of the high- Q resonator mode (purple) and that of the coupled pumps (blue). The red and green arrows represent the dipole moments of the tomography and conversion transmons respectively. The frequency of the high- Q resonator is below the waveguide cutoff and hence the field of this mode decays exponentially towards the top of the waveguide. Near the post, the resonator field extends symmetrically outwards, enabling a coupling to both the transmons. The fields of the pumps on the other hand are parallel to the short edge of the enclosure and therefore only couple to the conversion transmon. (d) Picture of the Ansys HFSS design of the system. (e) The machined system enclosure. (f) An example layout of a sapphire chip containing a transmon and a $\lambda/2$ stripline resonator used as readout mode. Similar chips are utilized as conversion side and the tomography side in the system. (g) Scanning electron microscope (SEM) image of a fabricated Josephson junction.

5.2 Experimental setup

The experimental setup for testing our transition requires (i) a high-Q storage resonator, (ii) a transmon mode for the conversion process, and (iii) a second transmon mode to perform tomography of the storage resonator. In addition, we need to be able to couple pumps strongly with the conversion transmon, while maintaining the quality factor of various modes of the system. A schematic of the system is presented in Fig. 5.2a. As shown, the high-Q storage resonator ($T_1 = 76 \mu\text{s}$)¹ is realized as a high purity aluminum, $\lambda/4$ -type resonator with a frequency of $\omega_a/2\pi = 8.03 \text{ GHz}$. Such resonators have a benefit of being seamless, since the seam is located at the top of the enclosure, while the resonator field decays exponentially towards the top as shown in Fig. 5.2b. The design and development of such high-Q resonators has been explained fully in [Reagor *et al.*, 2013]. The storage resonator is dispersively coupled to two transmons (Fig. 5.2a). The transmon indicated by green color is used for the conversion process and is therefore called the conversion transmon. This transmon has a frequency of $\omega_b/(2\pi) = 5.78 \text{ GHz}$, self-Kerr $\chi_{bb}/(2\pi) = 122.6 \text{ MHz}$ and a cross-Kerr of $\chi_{ab}/(2\pi) = 7.4 \text{ MHz}$ with the storage resonator. The T_1 and T_2 of this mode are $50 \mu\text{s}$ and $7.6 \mu\text{s}$ respectively. The second transmon is employed to perform Wigner tomography on the storage resonator and has a cross-Kerr of 1.1 MHz with it. Both transmons are coupled to low-Q resonators through which we perform single-shot measurements of the transmon state. In the case of the conversion transmon, the measurement distinguishes, in single-shot, between the first three states $|g\rangle$, $|e\rangle$ and $|f\rangle$. The remaining system parameters are quoted in table 5.1.

The enclosure of the system acts as a rectangular wave-guide high-pass filter with a cutoff at $\sim 9.5 \text{ GHz}$. Since the two pump frequencies, $\omega_{p1}/(2\pi) = 10.294 \text{ GHz}$ and $\omega_{p2}/(2\pi) = 10.397 \text{ GHz}$, are above the cutoff, they are applied through the strongly cou-

¹ T_1 of this cavity is Purcell limited by the other low-Q modes in the system

pled (waveguide mode $Q \leq 100$) pin at the top. In addition, the low- Q resonator utilized for measuring the transmon mode is approximately at 9.93 GHz which is also above the waveguide cutoff. Therefore, this mode primarily couples to the external circuitry through the strongly coupled pin. The storage resonator and the transmon modes are below the cutoff, and are thus protected from relaxation through this pin. These modes are driven by other weakly coupled pins present in the system. The wave-guide also acts as a polarization filter. The orientation of the strongly coupled pin with respect to the wave-guide forces the pump fields to be parallel to the shorter edge of the enclosure as shown in Fig. 5.2b. These fields then preferentially couple to the conversion transmon since the dipole moment of the conversion transmon is parallel to the field. On the other hand, the high- Q resonator and the tomography qubit are protected from the pumps due to the respective field orientations.

The entire system is designed using high frequency finite element simulations with ANSYS HFSS package and the Hamiltonian of the system is inferred using energy participation ratio black-box quantization technique [Nigg *et al.*, 2012]. A picture of the HFSS design is shown in Fig. 5.2c. The system enclosure is machined into a single block of high purity aluminum as shown in Fig. 5.2d. The central hollow structure contains the post for realizing the high- Q resonator. This part is later closed with an aluminum lid. The transmons are fabricated as Al/AlO_x/Al Josephson junctions on a c-plane double-side polished sapphire wafer using bridge-free electron beam lithography [Lecocq *et al.*, 2011]. The low- Q resonators are realized as stripline $\lambda/2$ resonators defined lithographically in the same fabrication step as the transmons. A typical layout for the sapphire chip is represented in Fig. 5.2e and a scanning electron microscope (SEM) image of the junction is shown in Fig. 5.2f. The fabricated sapphire chips are inserted into their respective tunnels and are held with the help of aluminum clamps. The coupling pins of the system are coaxial couplers whose coupling strength is tuned by adjusting the length of their exposed pin.

	Conversion resonator	Conversion transmon	Storage resonator	Tomography transmon	Tomography resonator
Conversion resonator	f: 9.93 GHz κ : 5.32 MHz	χ : 5.7 MHz	NA	NA	NA
Conversion transmon	χ : 5.7 MHz	f: 5.78 GHz T_1 : 50 μ s T_2 : 7.6 μ s χ_{self} : 122 MHz	χ : 7.4 MHz	NA	NA
Storage resonator	NA	χ : 7.4 MHz	f: 8.03 GHz T_1 : 72 μ s T_2 : 56 μ s χ_{self} : 122 kHz	χ : 1.1 MHz	NA
Tomography transmon	NA	NA	χ : 1.1 MHz	f: 6.36 GHz T_1 : 38 μ s T_2 : 8.8 μ s χ_{self} : 264 MHz	χ : 0.9 MHz
Tomography resonator	NA	NA	NA	χ : 0.9 MHz	f: 7.53 GHz κ : 0.38 MHz

Table 5.1: System parameters for the experiment. Diagonal elements specify the frequencies (f) and the relaxation rates (T_1) of the respective modes. The dephasing rates (T_2) and the self-Kerrs (χ_{self}) are also specified for the high-Q modes. Off diagonal elements are the cross-Kerrs (χ) between two modes. In particular it is noteworthy that the modes for which the cross-Kerr are listed as NA, are indeed isolated from each other physically, and hence, have negligible cross-Kerr between them.

Figure 5.3 shows a detailed wiring diagram of our measurement setup. The upper half contains the room temperature circuitry (above 300 K dashed line) of the experiment and the lower half shows the wiring inside the dilution refrigerator which is used for cooling the sample to around 20 mK. We describe some highlights of the system starting from the bottom of the diagram and then coming towards the top.

The strongly coupled waveguide pin serves as the pumping pin as well as the readout pin for the conversion transmon. All the tones that need to be applied through this pin are combined with the help of a directional coupler at base. The directional coupler also sends most of the pump signal back to room temperature, hence effectively attenuating

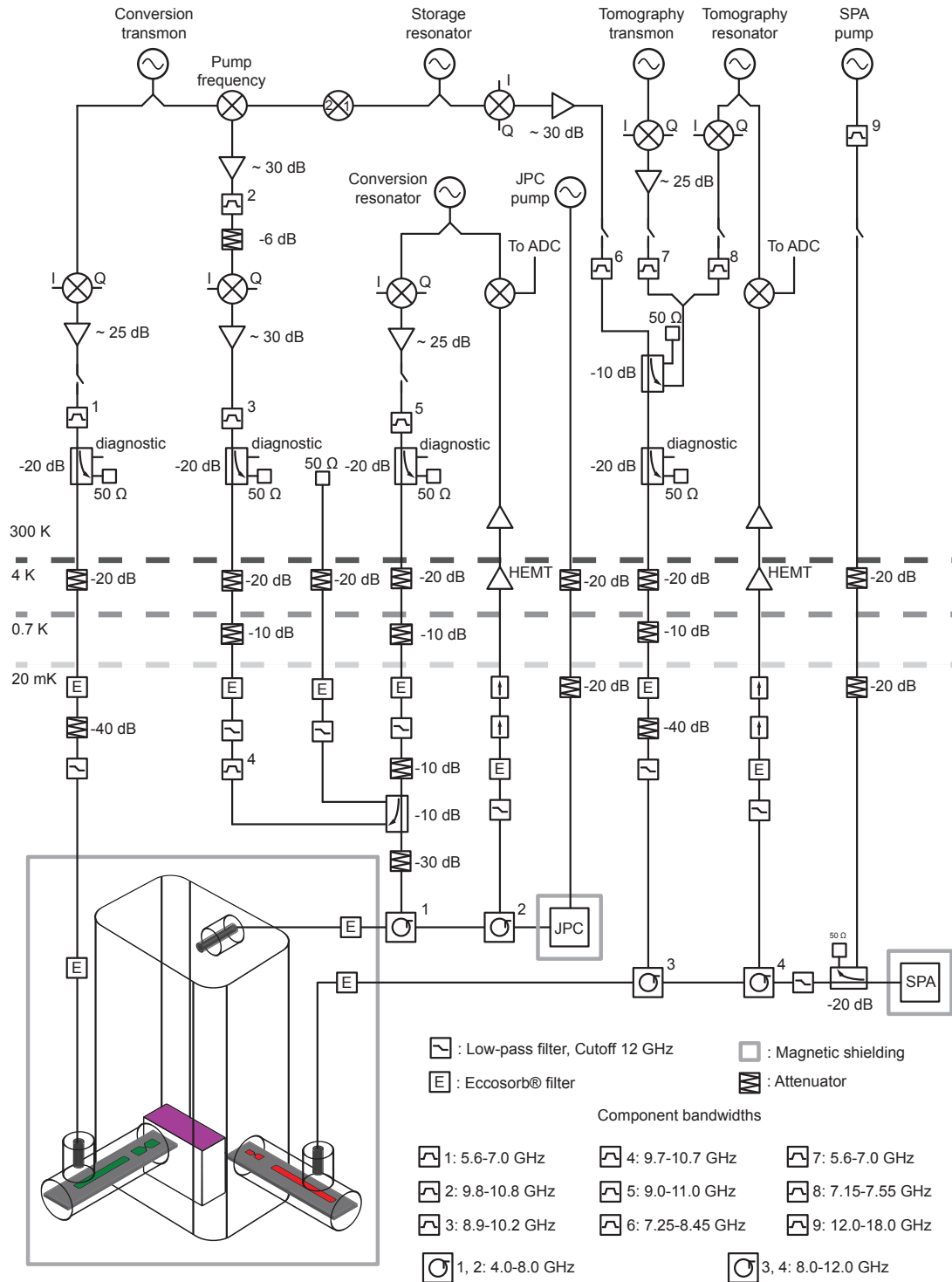


Figure 5.3: Wiring diagram of the measurement setup.

the strong pump tones without heating up the base plate of the dilution refrigerator. The combined signal is further attenuated and fed to a circulator which sends the signal to the waveguide pin. The circulator also directs the reflected signal from the waveguide pin towards a Josephson parametric converter (JPC) [Flurin, 2014] which amplifies the signal at the conversion resonator frequency and sends it back to the room temperature via another circulator, isolators and a high electron mobility transistor (HEMT) amplifier placed at 4K. The coupling pin situated close to the conversion arm is weakly coupled to the system and is used to drive the conversion transmon. The pin situated on the tomography arm, however, is strongly coupled to the tomography resonator and is used for three purposes. Firstly, it is used to readout the tomography resonator in reflection. The signal is routed using two circulators to a SNAIL parametric amplifier (SPA) [Frittini *et al.*, 2018] and the amplified signal is routed through the circulator towards the output chain. The other two purposes of the tomography arm coupling pin are to address the tomography qubit as well as the storage resonator. All the incoming signals on this pin are combined at the room temperature itself. The relaxation time of the storage resonator is limited because of the coupling to the environment via this pin.

At room temperature, we have five generators to address the system and two more for powering the amplifiers. The generators addressing the conversion resonator and the storage resonator are combined to produce a tone close to the frequencies of the pumps thus phase locking the two modes with the pumps. The other three system generators are used to address the conversion resonator, the tomography qubit and the tomography resonator. The frequencies of the five system generators is set slightly (around 50 MHz) away from their required values. The respective generator pulses are then converted to the required frequencies and shaped using IQ-mixers shown in the figure. We also utilize switches on all the lines in order to turn the pulses on and off. The IQ mixers and switches are controlled by a control system consisting of field programmable graphical

array (FPGA) cards and a dedicated computer (not shown in figure). The control system also records the measurement outcome of the system through the interferometric setups built for the readout. In addition the system is capable of making real time decisions conditioned on the measurement records. We employ this feature occasionally for system initialization.

5.3 System tuneup

Having discussed the system and measurement setup used for our experiment let us move on to tune-up of the system. The basic characterization of the system involves locating various modes, tuning up the readout and single-qubit pulses, measuring Hamiltonian parameters and coherence times of various modes, calibrating displacement pulses and parity measurement time for the high- Q resonator mode etc. We refer an interested reader to [Reed, 2013] for qubit characterization, [Narla, 2017] for readout calibration and [Petrenko, 2016] for characterization of the high- Q resonator. Here we assume the availability of this characterization and focus explicitly on tuneup and tomography of the $|f, 0\rangle \leftrightarrow |g, 4\rangle$ transition.

5.3.1 Locating $|f, 0\rangle \leftrightarrow |g, 4\rangle$ transition

In order to locate the correct pump frequencies for the transition of interest, we use the pulse sequence shown in Fig. 5.4a. The system is initialized in $|f0\rangle$ and the two pumps are applied for a variable period of time. For convenience, the pump frequencies are swept such that the frequency difference is maintained constant at $\omega_{p1} - \omega_{p2} = \chi_{aa} - 4\chi_{ab} + 2\Delta$ while sweeping the average frequency of the pumps. We choose $\Delta/2\pi = 5.1$ MHz and $g_{1,2}/2\pi \sim 0.5$ MHz. The rising and falling edges of the pump pulses are smoothed using a hyperbolic tangent function with a smoothing time of 192 ns. These parameters are

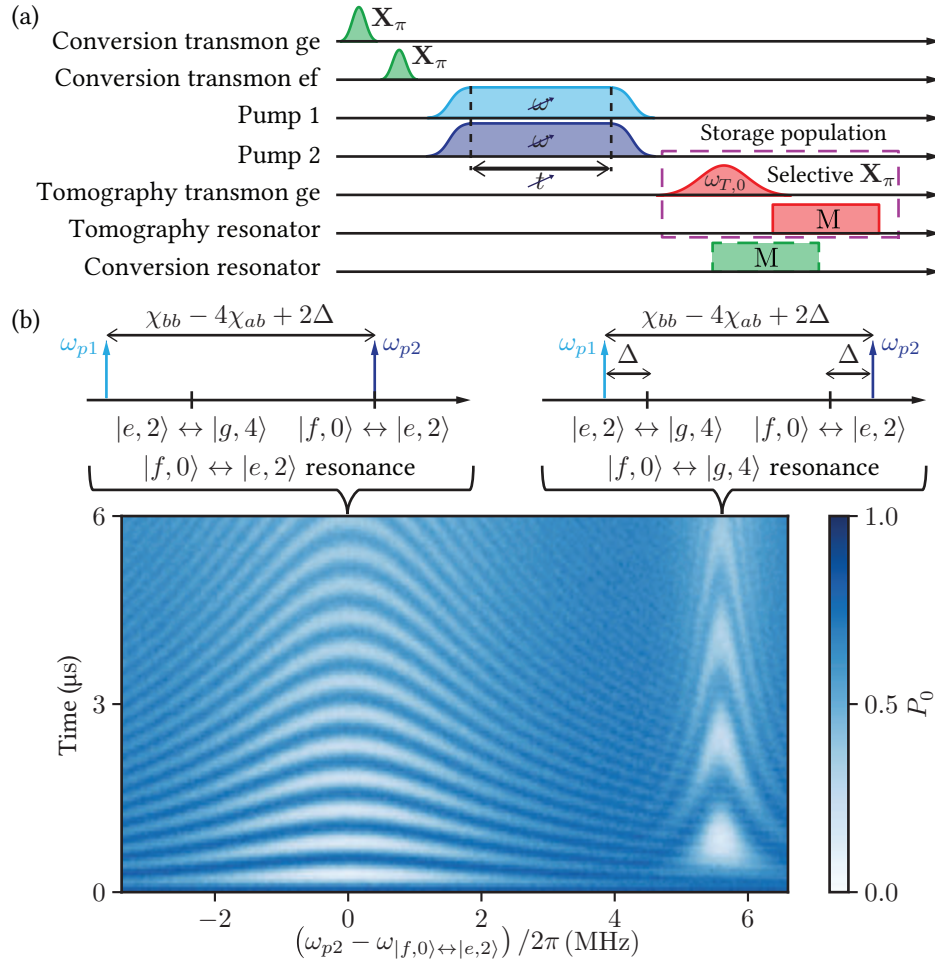


Figure 5.4: (a) Pulse sequence used for locating the $|f, 0\rangle \leftrightarrow |g, 4\rangle$ resonance of the system. The system is initialized in $|f, 0\rangle$ by using π -pulses on $|g\rangle \leftrightarrow |e\rangle$ and $|e\rangle \leftrightarrow |f\rangle$ transitions. Following this, the two pumps are applied with varying frequency and duration. The frequency difference of the two pumps is maintained constant at $\chi_{bb} - 4\chi_{ab} + 2\Delta$ while sweeping the average frequency. Finally an indirect measurement of the storage resonator population is performed using a photon-number selective π -pulse on the tomography transmon and a measurement pulse on the tomography resonator. Optionally, a measurement of the conversion transmon state can also be performed using a measurement pulse on the conversion resonator. (b) Rabi oscillations in the population of Fock state $|0\rangle$ (P_0 color-bar). The x-axis shows the detuning of pump 1 from the $|f, 0\rangle \leftrightarrow |e, 2\rangle$ transition, the y-axis shows the duration for which the two pumps are applied and the color is P_0 . The frequency landscape above the data explains the origin of the two chevron like features.

empirically optimized to reduce the leakage to the $|e2\rangle$ state while achieving a $g_{4\text{ph}}$ that is an order of magnitude faster than the decoherence rates of the system. The resulting resonator state is characterized by applying a photon-number selective π -pulse [Leghtas *et al.*, 2013a] on the tomography transmon. The pulse has a gaussian envelope of width $\sigma_{\text{sel}} = 480$ ns (total length $4\sigma_{\text{sel}}$), resulting in a pulse bandwidth of ~ 332 kHz, which is less than the cross-Kerr between the tomography transmon and the high-Q resonator. As a result the tomography transmon is excited only when the storage resonator is in $|0\rangle$. Finally, the state of the tomography transmon is measured. An optional single-shot measurement of the conversion transmon can also be performed as indicated by the dashed green measurement pulse in Fig. 5.4a.

The outcome of the described measurement is shown in Fig. 5.4b. The population fraction of the Fock state $|0\rangle$ is plotted as a function of the duration for which the pump pulses are applied and the detuning of the first pump ω_{p1} from the $|f0\rangle \leftrightarrow |e2\rangle$ transition. The data displays Rabi oscillations arising from two processes. The one on the left occurs when pump 2 is resonant with the $|f0\rangle \leftrightarrow |e2\rangle$ transition. The one on the right corresponds to the two pumps being equally detuned from the $|f0\rangle \leftrightarrow |g2\rangle$ and $|e2\rangle \leftrightarrow |g4\rangle$ transitions. This is the Raman-assisted $|f0\rangle \leftrightarrow |g4\rangle$ process of our interest. The resulting chevron pattern for this transition is narrower since the cascaded transition occurs at a slower rate than the $|f0\rangle \leftrightarrow |g2\rangle$ transition. From the frequency of the oscillations we extract $g_{4\text{ph}}/2\pi = 0.32$ MHz.

5.3.2 Pump-strength calibration

In order to compare the experimental results with theory, accurate measurements of the pump strengths $g_{1,2}$ are necessary. However, the pumps experience frequency dependent attenuation due to the dispersion in the input lines. Moreover, the coupling strengths

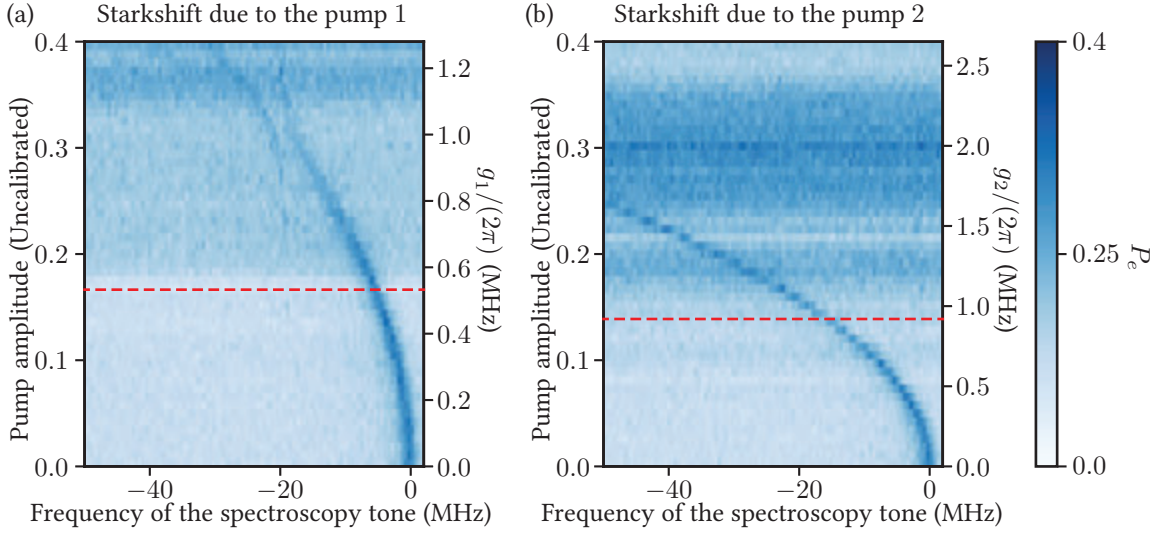


Figure 5.5: Results of the conversion transmon spectroscopy in presence of the pump tones. The pump tones are kept at a fixed frequency and their amplitude is varied. Another weak tone with variable frequency is applied near the $g \leftrightarrow e$ transition of the conversion transmon. Finally the excited state population P_e of the conversion transmon is measured. The result of the spectroscopy experiment can be fitted to obtain the Stark shift of the conversion transmon as function of the pump powers. (a) Spectroscopy of the conversion transmon as function pump 1 amplitude. The second pump is turned off for this experiment and the frequency of the first pump is selected to be the same as that used for the $|f, 0\rangle \leftrightarrow |g, 4\rangle$ transition. (b) Spectroscopy of the conversion transmon as function pump 2 amplitude when the second pump is turned off and the pump 1 frequency is the same as that used for the $|f, 0\rangle \leftrightarrow |g, 4\rangle$ transition. In both the cases, at low pump powers, the Stark-shift is proportional to the mod-square of the amplitude, as predicted by Eq. (5.2). We utilize the data below the dashed red lines to calibrate $|g_1|/(2\pi)$ and $|g_2|/(2\pi)$ as shown in the respective alternate y -axes. Above the red lines, spurious effects induced by higher pump strengths excite the system to higher states. This is reflected by the darker background observed in the data.

of the pumps are also frequency dependent, since the pumps are effectively filtered by the resonant modes of the system. In order to eliminate these effects, we calibrate the pump amplitudes in separate experiments, by measuring the Stark shift of the conversion transmon in presence of individual pumps (with the other pump turned off). The pump frequencies in these measurements are the same as those used for addressing the $|f, 0\rangle \leftrightarrow |g, 4\rangle$ transition. Such Stark shift, as function of the respective pump amplitudes can be

inferred from the data shown in Fig. 5.5. Using Eq. (5.2) we can relate the measured Stark shift, to the pump amplitudes $g_{1,2}$. The Stark shift of the conversion transmon, due to pump 1 and pump 2, at the amplitudes utilized in the rest of experiments, is 4.26 MHz and 5.15 MHz respectively. This results in $g_1/(2\pi) = 0.48$ MHz and $g_2/(2\pi) = 0.53$ MHz. For these parameters, Eq. (5.5) predicts a $g_{4\text{ph}}/(2\pi)$ of 0.33 MHz, in close agreement with the measured value of $g_{4\text{ph}}/2\pi = 0.32$ MHz.

The data shown in Fig. 5.5, along with being useful for pump strength calibration, also shows one of the major limitations of our current setup. At higher pump strengths, a change in the background of the plots can be observed. This change is induced due to the spurious excitations of the system caused by higher pump strengths. These spurious processes have been a topic of intense theoretical and experimental research, and have been explored thoroughly by [Sank *et al.*, 2016, Lescanne *et al.*, 2019a, Verney *et al.*, 2019]. Such spurious processes, in our system, are neither desirable nor controllable. Therefore, we avoid this region by deliberately keeping our pump powers lower than the those indicated by the dashed red lines. On the flip-side, this prevents us from demonstrating the complete $\hat{a}^4|f\rangle\langle g| + \hat{a}^{\dagger 4}|g\rangle\langle f|$ process since, as mentioned before, it requires $|g_1|, |g_2| \geq 2\chi_{ab}$. A solution to this problem is proposed in the next chapter.

5.4 Characterization of four-photon exchange

In order to prove that we have indeed found the $|f, 0\rangle \leftrightarrow |g, 4\rangle$ transition, we perform two tomography experiments. In the next sub-section we show the results for a partial tomography where only the populations of various eigenstates of the transmon and storage resonator are measured. This is followed by conditional Wigner-tomography of the storage resonator which allows us to prove that the oscillations are indeed coherent.

5.4.1 Partial tomography and comparison with simulations

Here, we fix our pump frequencies to be resonant with the $|f, 0\rangle \leftrightarrow |g, 4\rangle$ transition and characterize the populations of various transmon and storage resonator eigenstates. First, we obtain the populations of different Fock states of the storage resonator, by employing a pulse sequence similar to the one presented in Fig. 5.4a. Here, however, the frequency of the photon-number selective pulse on the tomography transmon is varied, whereas the pumps are applied at a constant frequency. The result of this measurement is plotted in Fig. 5.6a. The population fractions of various Fock states are inferred by taking cross-sections at the resonance frequency of the tomography transmon conditioned on the number of photons in the resonator. The resonator oscillates between $|0\rangle$ and $|4\rangle$ with some leakage to $|2\rangle$ due to the finite detuning Δ from $|e, 2\rangle$ (see the $\omega_{T0/2/4}$ lines in Fig. 5.6a). The population appearing in $|1\rangle$ and $|3\rangle$ is due to finite energy relaxation time of the resonator mode. Next, we independently measure the populations of $|f\rangle$, $|e\rangle$ and $|g\rangle$ states of the conversion transmon using the dashed-green measurement pulse shown in Fig. 5.4a. The evolution of the $|0\rangle$, $|2\rangle$ and $|4\rangle$ state populations of the storage resonator and the corresponding evolution of $|f\rangle$, $|e\rangle$, $|g\rangle$ state populations of the conversion transmon are plotted respectively in the left and right columns of Fig. 5.6b. As expected, the $f - 0$, $e - 2$, and $g - 4$ populations oscillate in phase with each other. The amplitude of the oscillations is limited by the T_2 of the conversion qubit and the measurement contrast. We are also able to resolve an envelope of fast oscillations in the populations of $|e\rangle$, $|g\rangle$ and $|2\rangle$, $|4\rangle$ states. These are expected for a Raman transition and occur at a rate given by the detuning Δ .

The black lines in the plots of Fig. 5.6b show the results of a numerical simulation of the Lindblad master equation of the conversion transmon plus resonator system. The

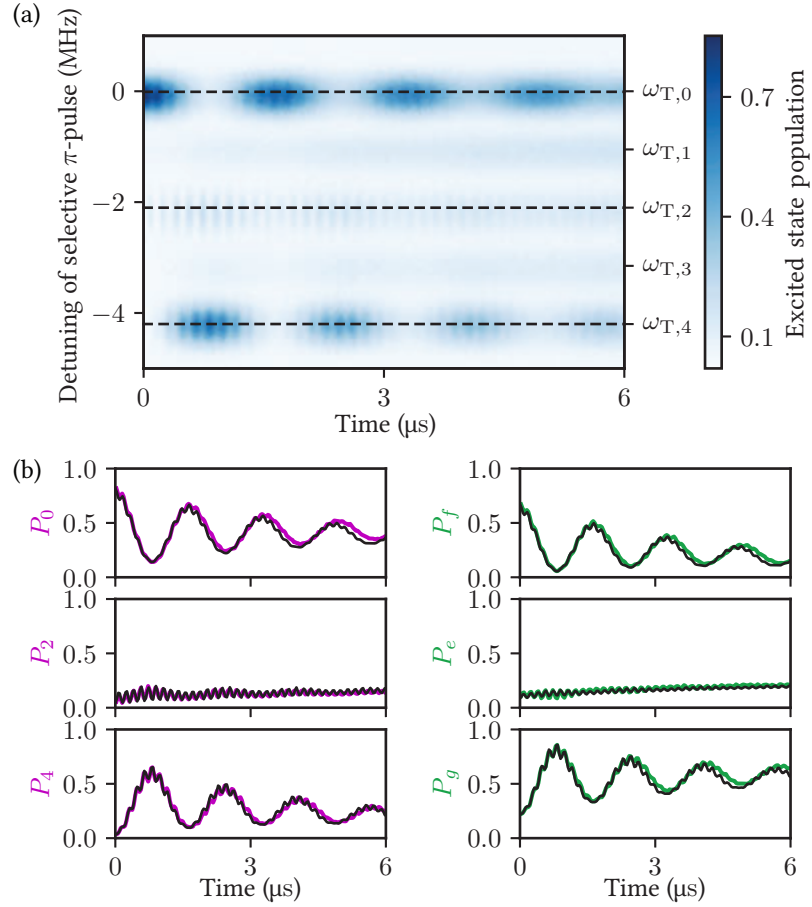


Figure 5.6: Partial tomography of $|f, 0\rangle \leftrightarrow |g, 4\rangle$ oscillations as a function of time. The system is prepared in $|f, 0\rangle$ and the two pumps are applied for a variable period of time on resonance with the $|f, 0\rangle \leftrightarrow |g, 4\rangle$ transition. Following this, a selective pulse with a variable frequency is applied on the tomography transmon enabling an indirect measurement of various Fock state populations of the storage resonator. (a) Excited state population of the tomography transmon (colorbar) versus pump duration (x-axis) and the detuning of the selective π -pulse on the tomography transmon (y-axis). The y-axis on the right shows the frequency of the tomography transmon ($\omega_{T,n}$) conditioned on the number of photons n in the storage mode. The oscillations between the states $|0\rangle$ and $|4\rangle$ are clear from the ω_{T0} and ω_{T4} lines with some leakage to the state $|2\rangle$ (ω_{T2} line) due to finite detuning Δ . A small population is seen in the $|1\rangle$ and $|3\rangle$ lines due to the finite coherence time of the storage resonator. (b) Left column from top to bottom, $|0\rangle$, $|2\rangle$ and $|4\rangle$ Fock state populations (magenta), measured along the dashed lines shown in panel (a). Independently measured populations in $|f\rangle$, $|e\rangle$ and $|g\rangle$ states of the conversion mode (green) are plotted in the right column, respectively, from top to bottom. The black lines show the populations obtained from numerical simulation of the system (see text).

master equation is given by

$$\dot{\rho} = -\frac{i}{\hbar} \left[\hat{H}_{\text{sys}}, \rho \right] + \kappa_{1\text{ph}} \mathcal{D}[\hat{a}] \rho + \kappa_{\phi} \mathcal{D}[\hat{a}^{\dagger} \hat{a}] \rho + \Gamma_{\downarrow} \mathcal{D}[\hat{b}] \rho + \Gamma_{\phi} \mathcal{D}[\hat{b}^{\dagger} \hat{b}] \rho. \quad (5.7)$$

Here is the system Hamiltonian \hat{H}_{sys} is the one mentioned in Eq. 5.1. The decoherence rates have the same definition as before. However, while evaluating the amplitude damping rates for both the modes we simply assume them to be the inverse of T_1 of the respective modes, i.e. we ignore heating rates of the modes. All parameters used in the simulation are previously known and no fitting parameters are required. We set the initial state of the system as $|f0\rangle\langle f0|$ and simulate the master equation with the pump tones on for a variable amount of time. The smoothed edges of the pump tones are taken into account by inducing the same time dependence on $g_{1,2}$, and adding a time dependent Stark-shift. From the resulting density matrix we find the populations of the various Fock states and the $|g\rangle, |e\rangle, |f\rangle$ states of the transmon. The obtained populations are scaled such that the maximum and minimum of each trace, matches with the maximum and minimum of the corresponding experimental data, in order to account for the measurement contrast. The simulation reproduces the experimental results well, including the fast oscillations found in the data.

5.4.2 Coherence of the oscillations

Finally, in order to demonstrate that the oscillations are coherent, we stop the $|f, 0\rangle \leftrightarrow |g, 4\rangle$ process after a quarter of a period (372 ns). This is expected to prepare a coherent superposition of $|f, 0\rangle, |g, 4\rangle$ given by $(|f, 0\rangle + |g, 4\rangle) / \sqrt{2}$. We experimentally characterize the state of the system by performing Wigner tomography of the resonator, conditioned on conversion transmon states. A pulse sequence for such conditioned tomography is shown in Fig. 5.7. The essential idea is to measure the state of the conversion trans-

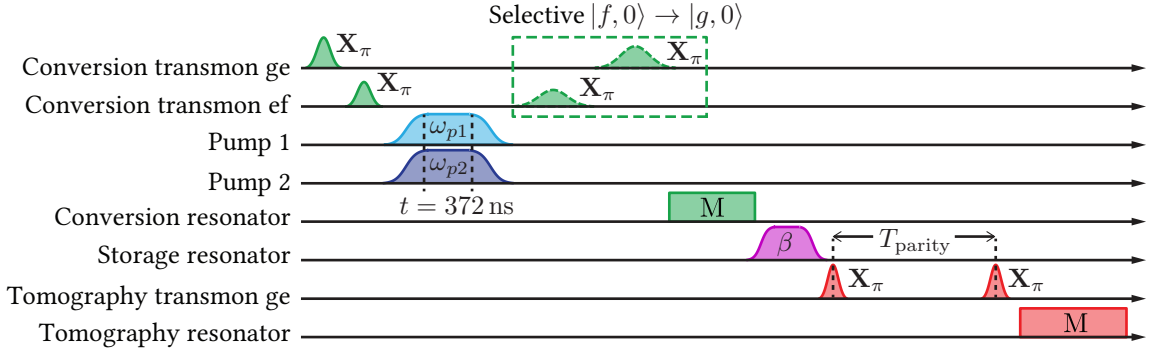


Figure 5.7: Pulse sequence for preparing the system in $(|f, 0\rangle + |g, 4\rangle)/\sqrt{2}$ and performing the tomography of the storage resonator conditioned on the state of the conversion resonator. The system is first prepared in $|f, 0\rangle$ by applying π -pulses on ge and ef transitions. The pumps are then applied at the $|f, 0\rangle \leftrightarrow |g, 4\rangle$ resonance frequency, however, the oscillations are stopped after a quarter period (372 ns). The expected state of the system at this point is $(|f, 0\rangle + |g, 4\rangle)/\sqrt{2}$. This is followed by inferring the state of the conversion transmon by applying a measurement pulse on the conversion resonator. Post this, the Wigner tomography of the resonator is performed by first displacing the storage resonator through a displacement β and then measuring the photon-number parity of the resonator by mapping it onto the tomography transmon with a pulse sequence similar to that described in Fig. 3.5. In post processing, the Wigner tomography data is averaged conditioned on the state of the conversion transmon. In a separate experiment, a photon-number selective $|f, 0\rangle \rightarrow |g, 0\rangle$ transition is applied before measuring the conversion transmon, in order to disentangle the storage resonator and the transmon. This is expected to prepare the storage resonator in $(|0\rangle + |4\rangle)/\sqrt{2}$.

mon before performing the Wigner tomography. This allows one to average the tomography data conditioned on the state of the conversion transmon in post-processing. As expected, the resonator ends up in Fock state $|4\rangle$ ($|0\rangle$) when the conversion transmon is post-selected in $|g\rangle$ ($|f\rangle$) as shown by Fig. 5.8a (b). Moreover, applying a photon-number selective $f \rightarrow g$ pulse on the conversion transmon, conditioned on zero photons in the storage resonator, can be applied to disentangles the transmon from the resonator, leaving the system in $|g\rangle \otimes (|0\rangle + |4\rangle)/\sqrt{2}$. The Wigner function of the resonator after applying this $|f, 0\rangle \rightarrow |g, 0\rangle$ pulse and post-selecting the conversion transmon in $|g\rangle$ is shown by Fig. 5.8c. The Wigner function shows that the resonator is indeed in the $(|0\rangle + |4\rangle)/\sqrt{2}$

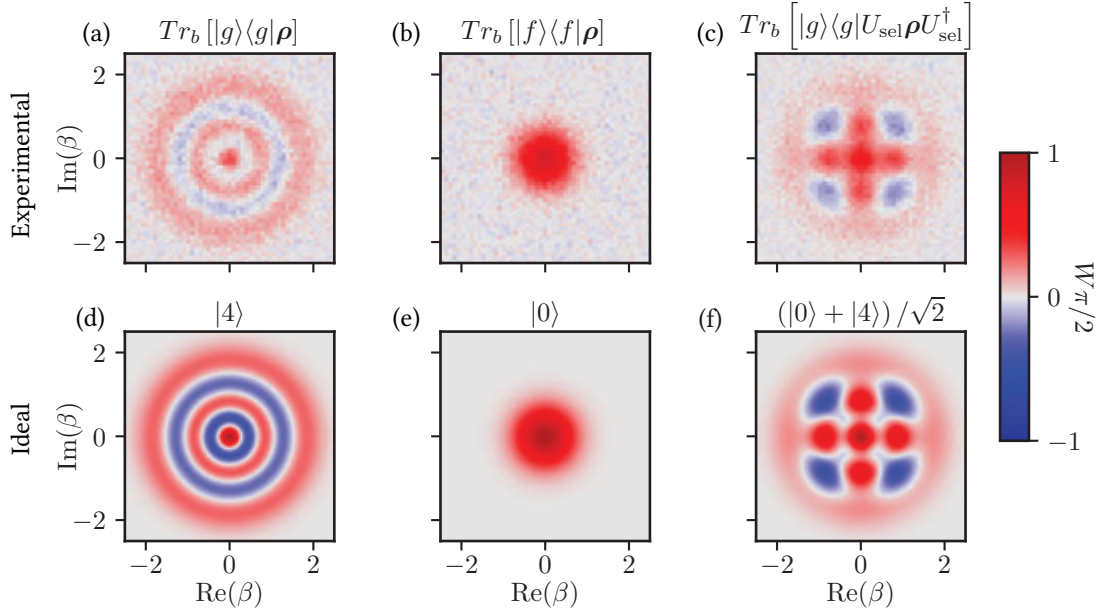


Figure 5.8: Outcome of the conditional Wigner function measurement. Panels (a, b) show experimental Wigner function of the storage resonator after post-selecting the conversion transmon in the $|g\rangle$ and $|e\rangle$ states. This leaves the storage resonator in Fock states $|4\rangle$, $|0\rangle$ respectively. (d, e) show the ideal Wigner functions of Fock states $|4\rangle$, $|0\rangle$ for comparison. Panel (c) shows the Wigner function of the resonator after photon-number selective $|f, 0\rangle$ to $|g, 0\rangle$ transition (indicated by U_{sel}) and post-selecting the conversion transmon in $|g\rangle$. Comparing (c) with the ideal Wigner function of $(|0\rangle + |4\rangle)/\sqrt{2}$ state in (f), shows that the storage resonator is in a coherent superposition of $|0\rangle$ and $|4\rangle$, thus indicating that the $|f, 0\rangle \leftrightarrow |g, 4\rangle$ oscillations are coherent.

state, thus proving that the oscillations are coherent. For comparison, the ideal Wigner functions of $|4\rangle$, $|0\rangle$ and $(|0\rangle + |4\rangle)/\sqrt{2}$ are shown in panels d, e and f of Fig. 5.8 respectively. It is also interesting to note that $(|0\rangle + |4\rangle)/\sqrt{2}$ is one of the logical states of the simplest binomial QEC code [Michael *et al.*, 2016].

5.5 Summary and prelude to the next chapter

In this chapter, we have accomplished an important task of verifying that lower-order nonlinear processes can indeed be cascaded to engineer higher-order nonlinear interac-

tion. More importantly, the rate of this highly nonlinear transition is faster than the decoherence rates, the oscillations are coherent and follow the theoretical predictions closely. Such cascading technique can now be utilized as a Hamiltonian engineering tool in a plethora of applications. We elaborate a few such applications in Ch. 7. The chapter also highlights the two limitations of the cascading process that we discussed previously.

- (i) We have managed to implement a specific transition instead of the entire $\hat{a}^4|f\rangle\langle g| + \hat{a}^{\dagger 4}|g\rangle\langle f|$ process, where all of the $|f, n\rangle \leftrightarrow |g, (n + 4)\rangle$ transitions are resonant simultaneously. For such transition we require the strength of the pumped processes ($|g_{1,2}|$) higher than the cross-Kerr terms χ_{ab} between the storage resonator and the conversion transmon. However, this is not possible in our current setup since stronger pumps tend to heat up the conversion transmon to highly excited states. In the next chapter, we propose a new circuit design which cancels the cross-Kerr interaction while preserving the the four-wave mixing two-photon exchange term, thus offering a way to achieve $|g_{1,2}| > \chi_{ab}$ while using similar pump strengths.
- (ii) A significant leakage to the intermediate state, $|e, 2\rangle$, is observed in our experiment. As discussed in previous chapter, such leakage is fatal for four-component cat states. Although this a leakage can be minimized by increasing Δ , it comes at the cost of slowing the entire process. We get around this limitation in Ch. 7 by proposing to use the pair-cat code, which needs a similar cascading process, however, is immune to the two-photon loss error inherited from the leakage.

Chapter 6

Cross-Kerr-free four-wave mixing

Previously, we have studied that four-wave mixing property of a Josephson junction is extremely useful towards building multi-photon driven-dissipative processes. The diagonal terms like Kerrs and cross-Kerr which always accompany the fourth order nonlinearity are also useful for a plethora of applications. However, for the off-resonant processes of our interest, the cross-Kerr term tends to be harmful. In the specific example of cascaded four-photon exchange, the presence of cross-Kerr results in a requirement of seemingly unachievable pump strengths. Even for two-component cat codes, where cascading is not required for engineering the driven-dissipative process, the cross-Kerr leads to severe limitations. If the cross-Kerr between the storage resonator and any other mode is stronger than the rate of confinement $|\alpha|^2 \kappa_{2\text{ph}}$, then any spurious excitation in the coupled mode translates to a complete dephasing of the cat states. Until recently, this limitation prevented the observation of exponential suppression in logical dephasing rates for these cats [Touzard *et al.*, 2018]. Furthermore, the storage resonator modes also inherit some anharmonicity (self-Kerr) due to coupling with transmon mode. This self-Kerr also leads to unwanted deterministic evolution of the stored states, which, under many circumstances, contributes to logical dephasing. Therefore, although four-wave mixing is beneficial, the

always on diagonal interactions inherited from four-wave mixing can, in many applications, create severe limitation. In this chapter, we discuss design and implementation of a novel circuit that allows certain four-wave mixing interactions, while canceling cross-Kerr and other diagonal terms in the Hamiltonian. The next section (Sec. 6.1) discusses two superconducting circuit elements that will be utilized to engineer the ‘cancellation circuit’. We explain the design of the circuit in Sec. 6.2 along with an explanation of why diagonal four-wave mixing terms are cancelled while some of the other processes survive. Sec. 6.3 explains the design of the system in which we measure the cancellation circuit. Since the circuit requires magnetic flux bias, the major part of this section is focused on devising a novel way to introduce magnetic flux in a superconducting enclosure. This is followed by some preliminary measurement results in Sec. 6.4. Sec. 6.5 compares our circuit with an alternate design recently demonstrated by [Lescanne *et al.*, 2019b]. The similarities and differences in these circuits are extremely interesting to explore. The results of this chapter are summarized in the final section (Sec. 6.6).

6.1 Required circuit elements

In this section we introduce two flux-tunable superconducting circuit elements. The first one is the Superconducting Quantum Interference Device (SQUID) which essentially acts as a Josephson junction with a tunable inductance. Going beyond SQUID, we study a second element, called Superconducting Nonlinear Asymmetric Inductive eLement (SNAIL). This new element offers a fundamentally different potential than a single Josephson junction and, as a result, is useful towards our goal of building the cancellation circuit. This section is focused on analyzing the potential energy terms of these circuit elements classically. The quantization can be carried out at a later stage when the elements are inserted into circuits with respective shunting capacitance.

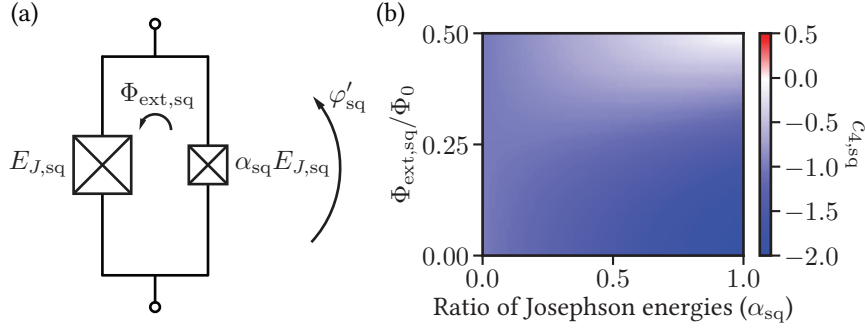


Figure 6.1: (a) Circuit diagram of a SQUID. Two junctions are connected in parallel configuration with $E_{J,sq}$ denoting the Josephson energy of the bigger junction and α_{sq} denoting the ratio of two Josephson energies. The flux through the loop formed by two junctions is denoted as $\Phi_{ext,sq}$ and the superconducting phase across the larger junction is denoted by the phase operator φ'_{sq} . (b) Four-wave mixing coefficient ($c_{4,sq}$) of a SQUID, as function of α_{sq} and $\Phi_{ext,sq}$. It is clear that $c_{4,sq}$ is always less than or equal to zero.

6.1.1 SQUID

The circuit diagram of a SQUID is shown in Fig. 6.1a. It is essentially formed by two Josephson junction connected in a parallel configuration. The two junctions need not have equal Josephson energies. We parameterize a SQUID by the Josephson energy of the larger junction ($E_{J,sq}$), and the ratio of the Josephson energy of the smaller junction to that of the larger junction (α_{sq})¹. In addition we denote the external magnetic flux, applied to the loop formed by the junctions, by $\Phi_{ext,sq}$. For the sake of our discussion we have denoted anti-clockwise as the positive direction of the flux. With this notation, let us discuss the classical potential of the SQUID as function of $\Phi_{ext,sq}$ and α_{sq} . This potential is give by

$$U_{sq} = -\alpha_{sq} E_{J,sq} \cos(\varphi'_{sq}) - E_{J,sq} \cos(\phi_{ext,sq} - \varphi'_{sq}) \quad (6.1)$$

where φ'_{sq} is the superconducting phase across the smaller junction and $\phi_{ext,sq} = 2\pi \frac{\Phi_{ext,sq}}{\Phi_0}$ is an angle in radian².

¹Not to be confused with coherent state amplitude α

²Remember that $\Phi_0 = h/2e$ is the single flux quantum and $\phi_0 = \Phi_0/2\pi$ is the reduced flux quantum

In order to better understand this potential, we simplify it as follows:

$$\begin{aligned}
U_{\text{sq}} &= -\alpha_{\text{sq}} E_{J,\text{sq}} \cos(\varphi'_{\text{sq}}) - E_{J,\text{sq}} \cos(\phi_{\text{ext},\text{sq}} - \varphi'_{\text{sq}}) \\
&= -\alpha_{\text{sq}} E_{J,\text{sq}} \cos(\varphi'_{\text{sq}}) - E_{J,\text{sq}} \cos(\phi_{\text{ext},\text{sq}}) \cos(\varphi'_{\text{sq}}) - E_{J,\text{sq}} \sin(\phi_{\text{ext},\text{sq}}) \sin(\varphi'_{\text{sq}}) \\
&= -E_{J,\text{sq}} [(\alpha_{\text{sq}} + \cos(\phi_{\text{ext},\text{sq}})) \cos(\varphi'_{\text{sq}}) + \sin(\phi_{\text{ext},\text{sq}}) \sin(\varphi'_{\text{sq}})] \\
&= -E_{J,\text{sq}} \sqrt{(\alpha_{\text{sq}} + \cos(\phi_{\text{ext},\text{sq}}))^2 + \sin(\phi_{\text{ext},\text{sq}})^2} \cos(\theta - \varphi'_{\text{sq}}) \\
&= -E_{J,\text{sq}} \sqrt{1 + \alpha_{\text{sq}}^2 + 2\alpha_{\text{sq}} \cos(\phi_{\text{ext},\text{sq}})} \cos(\theta - \varphi'_{\text{sq}}) \\
&= -E_{J,\text{sq}} \sqrt{1 + \alpha_{\text{sq}}^2 + 2\alpha_{\text{sq}} \cos(\phi_{\text{ext},\text{sq}})} \cos(\varphi_{\text{sq}})
\end{aligned} \tag{6.2}$$

where $\theta = \arctan\left(\frac{\sin(\phi_{\text{ext},\text{sq}})}{\alpha_{\text{sq}} + \cos(\phi_{\text{ext},\text{sq}})}\right)$. We have also substituted $\theta - \varphi'_{\text{sq}} = \varphi_{\text{sq}}$ which is equivalent to performing a gauge transformation. In this new gauge, φ_{sq} can simply be assumed as the phase across SQUID element. From this simplified expression, it is clear that we have a potential similar to a single Josephson junction with an effective Josephson energy

$$E_{J,\text{sq,eff}} = E_{J,\text{sq}} \sqrt{1 + \alpha_{\text{sq}}^2 + 2\alpha_{\text{sq}} \cos(\phi_{\text{ext},\text{sq}})}, \tag{6.3}$$

which can be tuned, in situ, by changing the magnetic flux threading through the loop. To infer the four-wave mixing coefficient, we expand the potential around its minimum at $\theta - \varphi'_{\text{sq}} = 0 \Rightarrow \varphi_{\text{sq}} = 0$. We express this expansion in the following form:

$$\frac{U_{\text{sq}}}{E_{J,\text{sq}}} = c_0 + \frac{c_{1,\text{sq}}}{1!} \varphi_{\text{sq}} + \frac{c_{2,\text{sq}}}{2!} \varphi_{\text{sq}}^2 + \frac{c_{3,\text{sq}}}{3!} \varphi_{\text{sq}}^3 + \frac{c_{4,\text{sq}}}{4!} \varphi_{\text{sq}}^4 + \dots, \tag{6.4}$$

where $c_{k,\text{sq}}$ are the expansion coefficients which depend on ϕ_{sq} , and α_{sq} . For a SQUID, all the odd coefficients are zero, i.e. $c_{2k+1,\text{sq}} = 0$, since the potential is essentially a cosine.

On the other hand, all the even ordered coefficients are given by

$$c_{2k,\text{sq}} = (-1)^{k+1} \sqrt{1 + \alpha_{\text{sq}} + 2\alpha_{\text{sq}} \cos(\phi_{\text{ext},\text{sq}})}. \quad (6.5)$$

Note that these even coefficients are equal to each other in absolute value. Due to the presence of $\cos(\phi_{\text{ext},\text{sq}})$ term, the coefficients are periodic in the applied flux with a periodicity of one flux quantum. All the coefficient monotonically decrease from 0 to 0.5 flux quantum and then come back to the original value from 0.5 to 1 flux quantum without ever changing sign.

Since we are specifically interested in the four-wave mixing coefficient, we plot the $c_{4,\text{sq}}$ as a function of α_{sq} and $\Phi_{\text{ext},\text{sq}}$ in Fig. 6.1. As expected, this coefficient is always negative and approaches zero when $\alpha_{\text{sq}} = 1$ and $\Phi_{\text{ext},\text{sq}}/\Phi_0 = 0.5 \Rightarrow \phi_{\text{ext},\text{sq}} = \pi$. Additionally, for our latter discussions, it is helpful to define the effective inductance of the SQUID given by

$$L_{\text{eff},\text{sq}} = \frac{L_{J,\text{sq}}}{c_{2,\text{sq}}} \quad (6.6)$$

where $L_{J,\text{sq}} = \frac{\phi_0^2}{E_{J,\text{sq}}}$. As the $\Phi_{\text{ext},\text{sq}}/\Phi_0$ increases from 0 to 0.5, the effective inductance monotonically increases (as $c_{2,\text{sq}}$ decreases), and then, from $\Phi_{\text{ext},\text{sq}}/\Phi_0 = 0.5$ to 1, the inductance decreases to its original value.

6.1.2 SNAIL

Having studied SQUID, let us proceed to study a more advanced flux tunable element, the SNAIL [Frattoni *et al.*, 2017, Vool, 2017]. The four-wave mixing coefficient of this element is indeed positive for a certain set of parameters. As mentioned before, this property of the SNAIL is very attractive towards building the cancellation circuit. The SNAIL is essentially a small Josephson junction shunted by $N_{\text{sn}} > 1$ larger junctions, as shown in

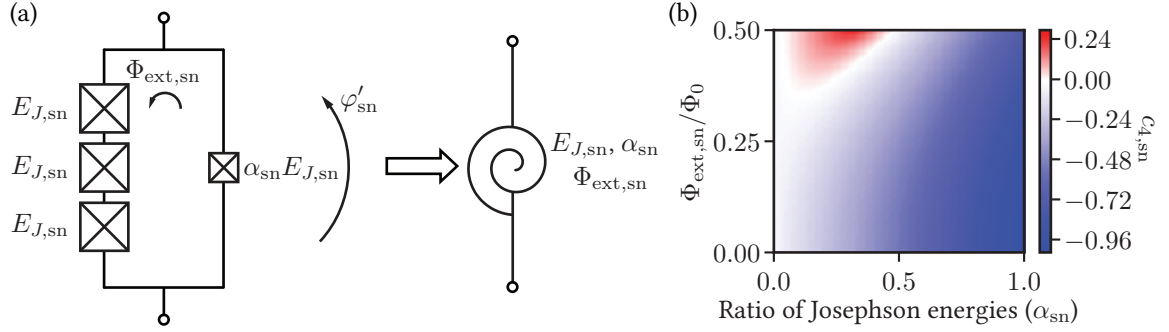


Figure 6.2: (a) Circuit diagram of a SNAIL. It consists of a small junction shunted by multiple larger junction as shown. The SNAIL is characterized by the number of large junctions N_{sn} , the Josephson energy of the large junctions $E_{J,\text{sn}}$, ratio of the Josephson energy of the small junction to the large junctions α_{sn} and the external flux $\Phi_{\text{ext,sn}}$ through the loop formed by the junctions. In the figure we have selected $N_{\text{sn}} = 3$. (b) Amplitude of the fourth-order nonlinearity ($c_{4,\text{sn}}$) of a SNAIL, as function of α_{sn} and $\Phi_{\text{ext,sn}}$. There exists a small parameter space near $\Phi_{\text{ext,sn}} = 0.5\Phi_0$ where the fourth order term of the SNAIL is positive in amplitude. This property of the SNAILS plays an important role in realization of cancellation circuit.

Fig. 6.2a. We have selected $N_{\text{sn}} = 3$ in this particular drawing. An expert might recognize this as the circuit for a flux-qubit [Orlando *et al.*, 1999, You *et al.*, 2007]. However, we operate this circuit in a different parameter regime and hence, inspired by [Frattini *et al.*, 2017], utilize the name SNAIL to identify it. Besides, we do need more slimy creatures in the cQED world, don't we?

In addition to N_{sn} , a SNAIL is parameterized by the Josephson energy of the larger junctions ($E_{J,\text{sn}}$), the ratio of Josephson energies of the smaller junction to the larger junction (α_{sn}) and the external flux through the loop of the loop of the SNAIL ($\Phi_{\text{ext,sn}}$). This parameterization is similar to the one we used for the SQUID. The classical potential of the SNAIL in terms of these parameters is written as

$$U_{\text{sn}} = -\alpha_{\text{sn}} E_{J,\text{sn}} \cos(\varphi'_{\text{sn}}) - N_{\text{sn}} E_{J,\text{sn}} \cos\left(\frac{\phi_{\text{ext,sn}} - \varphi'_{\text{sn}}}{N_{\text{sn}}}\right), \quad (6.7)$$

where φ'_{sn} is the phase across the smaller junction. In addition, we have assumed that

the phase across each of the larger junctions is equal. This assumption is valid when the charging energy of the islands forming the junctions is much smaller than the Josephson energy of the junctions. We refer an interested reader to [Vool, 2017] and [Frattini *et al.*, 2017] for further justification of this assumption. The potential of the SNAIL cannot be simplified in analytical manner for arbitrary values of $\phi_{\text{ext,sn}}$. Instead, we analyze the potential by finding the Taylor expansion around its minimum. The minimum is located by setting the first derivative of the potential to zero, i.e.

$$\frac{\partial U_{\text{sn}}}{\partial \varphi'_{\text{sn}}} = \alpha_{\text{sn}} E_{J,\text{sn}} \sin(\varphi'_{\text{sn}}) - E_{J,\text{sn}} \sin\left(\frac{\phi_{\text{ext,sn}} - \varphi'_{\text{sn}}}{N_{\text{sn}}}\right) = 0. \quad (6.8)$$

In general this equation cannot be solved analytically. Therefore, we typically find the location of the minimum, denoted by $\varphi_{\text{min,sn}}$ numerically. The potential can then be written in terms of $\varphi_{\text{sn}} = \varphi'_{\text{sn}} - \varphi_{\text{min,sn}}$ as

$$\frac{U_{\text{sn}}}{E_{J,\text{sn}}} = c_0 + \frac{c_{2,\text{sn}}}{2!} \varphi_{\text{sn}}^2 + \frac{c_{3,\text{sn}}}{3!} \varphi_{\text{sn}}^3 + \frac{c_{4,\text{sn}}}{4!} \varphi_{\text{sn}}^4 + \dots, \quad (6.9)$$

where

$$c_{k,\text{sn}} = \frac{1}{E_{J,\text{sn}}} \left. \frac{\partial^k U_{\text{sn}}}{\partial \varphi_{\text{sn}}'^k} \right|_{\varphi'_{\text{sn}} = \varphi_{\text{min,sn}}}. \quad (6.10)$$

The first order term is not included in the expansion since $c_{1,\text{sn}}$ is given by the first derivative which is zero at the minimum. One should note that the minimum $\varphi_{\text{min,sn}}$, and the coefficients $c_{k,\text{sn}}$ are functions of N_{sn} , α_{sn} and $\Phi_{\text{ext,sn}}$. The entire recipe for the Taylor expansion needs to be repeated at every flux point for a SNAIL. Additionally, the new variable φ_{sn} is related to φ'_{sn} by a gauge change. Therefore, hereon, we simply use φ_{sn} as the phase across the SNAIL.

Now, let us proceed to discuss some important properties of the SNAIL. Firstly, the odd coefficients $c_{2k+1,\text{sn}}$ of a SNAIL are not necessarily zero for $k > 0$. In fact, the ‘three-

wave mixing' enabled by the $\hat{\varphi}_{\text{sn}}^3$ term when $c_{3,\text{sn}} \neq 0$, is extremely useful for building parametric amplifier [Frattoni *et al.*, 2018]. This three wave mixing property was the main motivation behind the development of the SNAIL. In our case, however, we are most interested in the four-wave mixing coefficient $c_{4,\text{sn}}$. This coefficient for $N_{\text{sn}} = 3$ case is plotted in Fig. 6.2b as function of α_{sn} and $\Phi_{\text{ext,sn}}/\Phi_0$. For most of the parameter space, the value of $c_{4,\text{sn}}$ remains less than zero. However, for a small region near $\Phi_{\text{ext,sn}}/\Phi_0 = 0.5$, the four-wave mixing coefficient is indeed greater than zero. It is precisely this property of the SNAIL which is of immense interest for our purposes.

To illustrate the origin of the positive four-wave mixing further, it is instructive to analytically calculate the expansion of the SNAIL potential at $\Phi_{\text{ext,sn}}/\Phi_0 = 0.5 \Rightarrow \phi_{\text{ext,sn}} = \pi$. We also enforce $\alpha_{\text{sn}} < 1/N_{\text{sn}}$ in this analysis. Above this threshold, the potential tends to have double wells at half flux quantum. We avoid this region in our design. By calculating the first derivative of the SNAIL potential, it can be shown that the minimum of the potential is located at $\varphi_{\text{min,sn}} = \pi$ when $\alpha_{\text{sn}} < 1/N_{\text{sn}}$. Therefore we substitute $\varphi_{\text{sn}} = \pi - \hat{\varphi}_{\text{sn}}$ in the Eq. 6.7 to get

$$U_{\text{sn}} = -\alpha_{\text{sn}} E_{J,\text{sn}} \cos(\pi - \varphi_{\text{sn}}) - N_{\text{sn}} E_{J,\text{sn}} \cos\left(\frac{\varphi_{\text{sn}}}{N_{\text{sn}}}\right) \quad (6.11)$$

$$= \alpha_{\text{sn}} E_{J,\text{sn}} \cos(\varphi_{\text{sn}}) - N_{\text{sn}} E_{J,\text{sn}} \cos\left(\frac{\varphi_{\text{sn}}}{N_{\text{sn}}}\right). \quad (6.12)$$

This change in sign of $\alpha_{\text{sn}} E_{J,\text{sn}} \cos(\varphi_{\text{sn}})$ term leads to the positive four-wave mixing coefficient. The coefficients of the expansion can now be found by simply expanding the cosines in terms of φ_{sn} . This gives

$$c_{2,\text{sn}} = \frac{1}{N_{\text{sn}}} - \alpha_{\text{sn}}$$

$$c_{3,\text{sn}} = 0$$

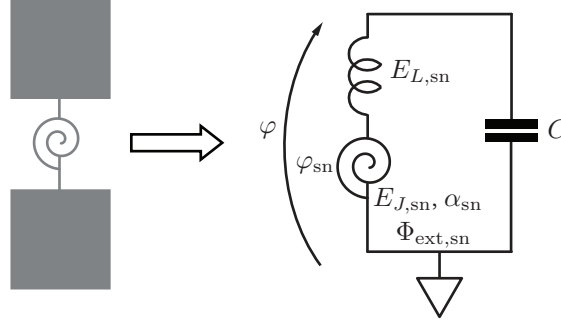


Figure 6.3: Cartoon and circuit diagram of a SNAIL inserted in a transmon-like circuit. The two pads act as antennas which provide the shunting capacitance. The series inductance arising from the geometric and kinetic inductance of the antenna pads and the leads of the device is explicitly shown. Such linear inductance introduces changes in the nonlinear potential of the circuit.

$$c_{4,\text{sn}} = \alpha_{\text{sn}} - \frac{1}{N_{\text{sn}}^3}. \quad (6.13)$$

Judging from the expression for $c_{4,\text{sn}}$, we indeed get positive four-wave mixing coefficient when $\alpha_{\text{sn}} \in \left(\frac{1}{N_{\text{sn}}^3}, \frac{1}{N_{\text{sn}}}\right)$. On the other hand, since we have imposed $\alpha_{\text{sn}} < 1/N_{\text{sn}}$, the coefficient $c_{2,\text{sn}}$ always remains positive. Which in turn allows us to define an effective inductance of the SNAIL $L_{\text{eff,sn}}$ as

$$L_{\text{eff,sn}} = \frac{L_{J,\text{sn}}}{c_{2,\text{sn}}}, \quad (6.14)$$

with $L_{J,\text{sn}} = \phi_0^2/E_{J,\text{sn}}$. Indeed, we utilize the same definition of the effective inductance at all fluxes for $\alpha_{\text{sn}} < 1/N_{\text{sn}}$. Similar to the case of the SQUID, the effective inductance increases as $\Phi_{\text{ext,sn}}/\Phi_0$ increases from 0 to 0.5 and then decreases as $\Phi_{\text{ext,sn}}/\Phi_0$ is varied from 0.5 to 1. Numerical expansion of the SNAIL potential is required to verify this.

6.1.3 Effect of series linear inductance

Fig. 6.3 shows a SNAIL inserted in a transmon like circuit. In such implementations we invariably get a linear inductance in series with the nonlinear device (SNAIL in this case) due to the geometric and the kinetic inductance of the pads and leads of the device. The behavior of the four-wave mixing coefficient of the SNAIL is significantly modified due this inductance as shown in [Fratini *et al.*, 2018, Appendix A]. Here we reproduce the derivations presented in that article, since the modification of fourth-order coefficient is important for our purposes. Although the discussion here is geared towards the SNAIL, the results are equally applicable to SQUIDs and single Junctions, since they can be thought of as special cases of the SNAIL. The potential of the circuit shown in the figure is given by

$$U_{\text{tot}} = \frac{E_{L,\text{sn}}}{2}(\varphi - \varphi_{\text{sn}})^2 + U_{\text{sn}}(\hat{\varphi}_{\text{sn}}) \quad (6.15)$$

where φ is the phase across the entire inductive branch, and $\varphi_{\text{sn}} = \varphi'_{\text{sn}} - \varphi_{\text{min,sn}}$ is the phase across the SNAIL. We have also denoted the inductive energy of the series inductor as $E_L = \phi_0^2/L_{\text{series,sn}}$. The minimum of U_{tot} is simply at $\varphi = \varphi_{\text{sn}} = 0$, since both the terms have simultaneous minimum at that point. The Lagrangian of this circuit is given by

$$\mathcal{L} = \frac{\dot{\varphi}^2}{2C} - U_{\text{tot}}. \quad (6.16)$$

From this Lagrangian, it is clear that φ_{sn} is not a real degree of freedom of the system, since there is no conjugate momentum for this coordinate. This can be clarified by using the Euler-Lagrange relation for φ_{sn} given by

$$\frac{\partial \mathcal{L}}{\partial \varphi_{\text{sn}}} = \frac{d}{dt} \frac{\partial \mathcal{L}}{\partial \dot{\varphi}_{\text{sn}}} = 0, \quad (6.17)$$

which leads us to the so called current conservation relation

$$\frac{\partial U_{\text{tot}}}{\partial \varphi_{\text{sn}}} = -E_{L,\text{sn}}(\varphi - \varphi_{\text{sn}}) + \frac{\partial U_{\text{sn}}}{\partial \varphi_{\text{sn}}} = 0, \forall \varphi. \quad (6.18)$$

The current conservation relation can then be utilized to express φ_{sn} in terms of φ giving us

$$U_{\text{tot}}[\varphi] = \frac{E_{L,\text{sn}}}{2}(\varphi - \varphi_{\text{sn}}[\varphi])^2 + U_{\text{sn}}(\hat{\varphi}_{\text{sn}}[\varphi]). \quad (6.19)$$

Now, we would like to again expand the potential around the minimum at $\varphi = \varphi_{\text{sn}} = 0$ as we did in the previous section. The potential is expressed in the form

$$\frac{U_{\text{tot}}}{E_{J,\text{sn}}} = \tilde{c}_{0,\text{sn}} + \tilde{c}_{2,\text{sn}} \frac{\varphi^2}{2!} + \tilde{c}_{3,\text{sn}} \frac{\varphi^3}{3!} + \tilde{c}_{4,\text{sn}} \frac{\varphi^4}{4!} \quad (6.20)$$

where

$$\tilde{c}_{k,\text{sn}} = \frac{1}{E_{J,\text{sn}}} \left. \frac{\partial^k U_{\text{tot}}}{\partial \varphi^k} \right|_{\varphi=0}. \quad (6.21)$$

These new coefficients can be related to the old $c_{k,\text{sn}}$ coefficients by explicitly calculating the derivatives of U_{tot} . The first derivative of U_{tot} is given by

$$\frac{\partial U_{\text{tot}}}{\partial \varphi} = E_{L,\text{sn}}(\varphi - \varphi_{\text{sn}}) + \frac{\partial U_{\text{tot}}}{\partial \varphi_{\text{sn}}} \frac{\partial \varphi_{\text{sn}}}{\partial \varphi} = E_{L,\text{sn}}(\varphi - \varphi_{\text{sn}}). \quad (6.22)$$

Here we have utilized $\frac{\partial U_{\text{tot}}}{\partial \varphi_{\text{sn}}} = 0$ from the current conservation relation. Note that $\varphi = \varphi_{\text{sn}} = 0$ indeed satisfies $\frac{\partial U_{\text{tot}}}{\partial \varphi} = 0$ as expected from the minimum of the potential. The further derivatives U_{tot} are

$$\begin{aligned} \frac{\partial^2 U_{\text{tot}}}{\partial \varphi^2} &= E_{L,\text{sn}} \left(1 - \frac{\partial \varphi_{\text{sn}}}{\partial \varphi} \right), \\ \frac{\partial^3 U_{\text{tot}}}{\partial \varphi^3} &= -E_{L,\text{sn}} \frac{\partial^2 \varphi_{\text{sn}}}{\partial \varphi^2}, \end{aligned}$$

$$\frac{\partial^4 U_{\text{tot}}}{\partial \varphi^4} = -E_{L,\text{sn}} \frac{\partial^3 \varphi_{\text{sn}}}{\partial \varphi^3}. \quad (6.23)$$

The derivatives of φ_{sn} with respect to φ can be calculated by differentiating the current conservation relation. For example the first derivative is calculated as follows:

$$\begin{aligned} \frac{\partial U_{\text{tot}}}{\partial \varphi_{\text{sn}}} &= -E_{L,\text{sn}}(\varphi - \varphi_{\text{sn}}) + \frac{\partial U_{\text{sn}}}{\partial \varphi_{\text{sn}}} = 0 \\ \Rightarrow -E_{L,\text{sn}} \left(1 - \frac{\partial \varphi_{\text{sn}}}{\partial \varphi}\right) + \frac{\partial^2 U_{\text{sn}}}{\partial \varphi_{\text{sn}}^2} \frac{\partial \varphi_{\text{sn}}}{\partial \varphi} &= 0 \\ \Rightarrow \frac{\partial \varphi_{\text{sn}}}{\partial \varphi} &= \frac{E_{L,\text{sn}}}{E_{L,\text{sn}} + \frac{\partial^2 U_{\text{sn}}}{\partial \varphi_{\text{sn}}^2}} \end{aligned} \quad (6.24)$$

Moreover, since we are only interested in $\frac{\partial^k U_{\text{tot}}}{\partial \varphi^k}$ at the minimum of the potential, we only need to calculate $\frac{\partial^k U_{\text{sn}}}{\partial \varphi_{\text{sn}}^k}$ at the minimum as well. Therefore, we can substitute $\frac{\partial^2 U_{\text{sn}}}{\partial \varphi_{\text{sn}}^2} \Big|_{\varphi_{\text{sn}}=0} = E_{J,\text{sn}} c_{2,\text{sn}}$ in the above relation, giving us

$$\frac{\partial \varphi_{\text{sn}}}{\partial \varphi} \Big|_{\varphi=0} = \frac{E_{L,\text{sn}}}{E_{L,\text{sn}} + E_{J,\text{sn}} c_{2,\text{sn}}}. \quad (6.25)$$

Pulling similar tricks for all the higher derivatives, we get the renormalized coefficients as

$$\begin{aligned} \tilde{c}_{2,\text{sn}} &= p_{\text{sn}} c_{2,\text{sn}} \\ \tilde{c}_{3,\text{sn}} &= p_{\text{sn}}^3 c_{3,\text{sn}} \\ \tilde{c}_{4,\text{sn}} &= p_{\text{sn}}^4 \left[c_{4,\text{sn}} - (1 - p_{\text{sn}}) \frac{3c_{3,\text{sn}}^2}{c_{2,\text{sn}}} \right]. \end{aligned} \quad (6.26)$$

Here

$$p_{\text{sn}} = \frac{E_{L,\text{sn}}}{c_{2,\text{sn}} E_{J,\text{sn}} + E_{L,\text{sn}}} = \frac{L_{\text{eff},\text{sn}}}{L_{s,\text{sn}} + L_{\text{eff},\text{sn}}} \quad (6.27)$$

is called the linear participation ratio of the SNAIL and $c_{k,\text{sn}}$ are as defined in Eq. 6.10. We have also utilized $L_{\text{eff,sn}} = \phi_0^2 / (c_{2,\text{sn}} E_{J,\text{sn}})$ and $L_{\text{s,sn}} = \phi_0^2 / E_{L,\text{sn}}$. It is clear from this expression that for $L_{\text{series,sn}} = 0$ the participation ratio $p_{\text{sn}} = 1$ and, as a result, we recover the original expressions for the nonlinearity coefficients. Moreover, $\tilde{c}_{4,\text{sn}}$ is modified only when the third order coefficient $c_{3,\text{sn}} \neq 0$. For a SQUID, which can be thought of as special case of a SNAIL, the third order coefficient is always zero and therefore, the fourth order coefficient remains unmodified.

From here onwards, we will directly utilize the phase across the entire inductive branch, φ , as the only degree of freedom and rechristen it as $\varphi_{\text{sn/sq}}$ if the branch contains a SNAIL or a SQUID. As a result $\tilde{c}_{k,\text{sn/sq}}$ will be the nonlinearity coefficients utilized for describing this potential. Since there is a single degree of freedom, the quantization of the SNAIL or SQUID inserted in a transmon like circuit proceeds in a similar manner to the single junction transmon. The resulting Hamiltonian of the circuit is therefore given by

$$\begin{aligned} \hat{H}_{\text{sn/sq}} &= \frac{\hat{Q}^2}{2C} + E_{J,\text{sn/sq}} \left(\frac{\tilde{c}_{2,\text{sn/sq}} \hat{\varphi}_{\text{sn/sq}}^2}{2!} + \frac{\tilde{c}_{3,\text{sn/sq}} \hat{\varphi}_{\text{sn/sq}}^3}{3!} + \frac{\tilde{c}_{4,\text{sn/sq}} \hat{\varphi}_{\text{sn/sq}}^4}{4!} + \dots \right) \\ &= \frac{\hat{Q}^2}{2C} + \frac{\hat{\Phi}_{\text{sn/sq}}^2}{L_{\text{s,sn/sq}} + L_{\text{eff,sn/sq}}} + E_{J,\text{sn/sq}} \frac{\tilde{c}_{3,\text{sn/sq}} \hat{\varphi}_{\text{sn/sq}}^3}{3!} + E_{J,\text{sn/sq}} \frac{\tilde{c}_{4,\text{sn/sq}} \hat{\varphi}_{\text{sn/sq}}^4}{4!} + \dots \end{aligned}$$

with $\hat{\Phi}_{\text{sn/sq}} = \phi_0 \varphi_{\text{sn/sq}}$.

6.2 Circuit design

Having studied these flux tunable circuit elements, we are now ready to discuss the design of the cancellation circuit. As mentioned previously, the idea is to combine two circuit elements, one with a positive four-wave mixing coefficient the other with a negative four-wave mixing coefficient. In addition, a specific device geometry is required, in order to cancel undesired terms while making sure that the desired four-wave mixing terms sur-

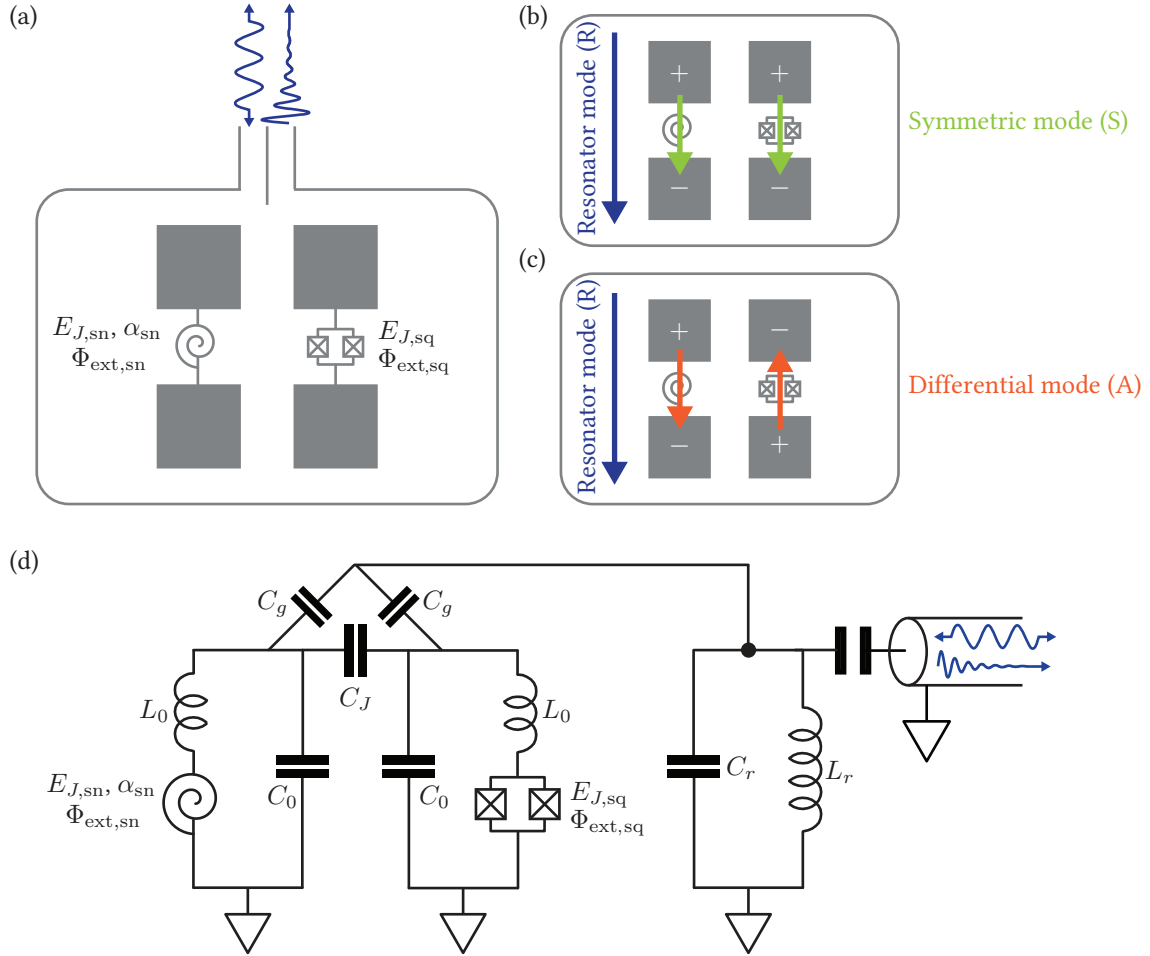


Figure 6.4: (a) Cartoon of the cancellation circuit enclosed in a 3D readout cavity. The circuit consists of two capacitively coupled transmon like modes. The Josephson junction for the first transmon (left) is substituted by a SNAIL and for the second transmon (right) it is substituted by a SQUID. Antenna pads of both the transmon like modes are identical to each other. (b) Symmetric mode (\hat{S}) of the circuit when the effective inductance of the SNAIL ($L_{\text{eff,sn}}$) is equal to the effective inductance of the SQUID ($L_{\text{eff,sq}}$). The field excitation through the SNAIL and SQUID is oriented in the same direction for this mode. (c) Asymmetric mode (\hat{A}) of the circuit when the effective inductance of $L_{\text{eff,sn}} = L_{\text{eff,sq}}$. The field excitation through the SNAIL and the SQUID is oriented in the opposite direction as shown. (d) Circuit diagram of the cancellation circuit coupled to the readout cavity. We have added an inductance L_0 in series with both the SNAIL and the SQUID in order to explicitly model the geometric and kinetic inductance of the antenna pads and the leads of the devices.

vive. We achieve this fine balance by utilizing the circuit design shown in Fig. 6.4a. The essential idea is to utilize two capacitively coupled transmon-like elements with identical antenna pads. The Josephson junction of one transmon is substituted by a SNAIL and that of the other transmon is substituted by a SQUID as shown in the figure. We use the SNAIL as our source of positive four-wave mixing coefficient and the SQUID as a tunable inductance Josephson junction. We have also included a low- Q readout cavity (the rectangular enclosure) so that the coupling of this circuit to a harmonic oscillator mode can be modeled. Changing the Q of this mode does not affect our analysis, and hence, coupling to a high- Q storage mode will behave in a similar manner.

In order to realize the cross-Kerr free four-wave mixing, we enforce two conditions on this circuit. Let us develop an intuitive understanding of the circuit under these conditions. The first condition is

$$L_{\text{eff,sn}} = L_{\text{eff,sq}}. \quad (6.28)$$

This implies that the frequencies of the SQUID and SNAIL mode are equal to each other. Such a condition can be satisfied with ease as long as $L_{J,\text{sq}} < L_{\text{eff,sq}}$. Due to the frequencies being equal, the two modes completely hybridize to form a symmetric mode (denoted by the letter S) and an asymmetric mode (denoted by the letter A). We represent these hybridized modes in Fig. 6.4b and Fig. 6.4c respectively. As shown, the field excitation of the symmetric mode is in the same direction through SNAIL and SQUID. On the other hand the field excitation of the asymmetric mode is in the opposite direction. Moreover, due to the equal hybridization of the modes, the phase drop of the symmetric and asymmetric modes across SNAIL and SQUID are equal. Similarly, since the field of the readout mode is in the vertical direction (Fig. 6.4 b and c), the readout mode also drives the excitation through the SNAIL and SQUID in the symmetric direction with equal participation in the two modes. Using these considerations, we can write down the four-wave mixing

nonlinearity of the system as

$$\frac{\hat{H}_{4\text{wave}}}{\hbar} = g_{4\text{wave},\text{sn}}^{\text{eff}} (\hat{\varphi}_S + \hat{\varphi}_R + \hat{\varphi}_A)^4 + g_{4\text{wave},\text{sq}} (\hat{\varphi}_S + \hat{\varphi}_R - \hat{\varphi}_A)^4. \quad (6.29)$$

Here $g_{4\text{wave},\text{sn}}^{\text{eff}}$ is the effective magnitude of four-wave mixing nonlinearity of the SNAIL and $g_{4\text{wave},\text{sq}}$ is the four-wave mixing amplitude of the SQUID. The reason for the superscript eff in case of SNAIL will be apparent in the next sub-section. The operators $\hat{\varphi}_K = \varphi_K(\hat{K} + \hat{K}^\dagger)$ represent the phase drops of the various hybridized modes across the SNAIL and the SQUID. Note the minus sign in front of $\hat{\varphi}_A$ in the second term. This minus sign will play a crucial role in the next step.

The second condition enforced on the circuit is

$$g_{4\text{wave},\text{sn}}^{\text{eff}} = -g_{4\text{wave},\text{sq}} = g_{4\text{wave}}. \quad (6.30)$$

As a result of this condition the four-wave mixing part of the circuit Hamiltonian becomes

$$\frac{\hat{H}_{4\text{wave}}}{\hbar} = 4g_{4\text{wave}} (\hat{\varphi}_S + \hat{\varphi}_R)^3 \hat{\varphi}_A + 4g_{4\text{wave}} (\hat{\varphi}_S + \hat{\varphi}_R) \hat{\varphi}_A^3, \quad (6.31)$$

where we have performed a binomial expansion of the terms in Eq. (6.29). It is clear from this expression that any of the diagonal four-wave mixing terms, including frequency renormalization, Kerrs and cross-Kerrns, are not present in this Hamiltonian. However, at the same time, we need other four-wave mixing interactions, like the two-photon exchange process to be present in the system. To see if these processes are indeed present, let us analyze the behavior of this system in presence of an off-resonant pump. We assume that this pump couples through the symmetric mode and therefore generates a symmetric excitation through the SNAIL and the SQUID. As usual, we model this pump by adding a time dependent displacement inside the nonlinearity. Therefore, the driven four-wave

mixing term in the Hamiltonian is given by

$$\frac{\hat{H}_{4\text{wave,driven}}}{\hbar} = 4g_{4\text{wave}} (\hat{\varphi}_S + \hat{\varphi}_R + \varphi_S \xi_p(t))^3 \hat{\varphi}_A + 4g_{4\text{wave}} (\hat{\varphi}_S + \hat{\varphi}_R + \varphi_S \xi_p(t)) \hat{\varphi}_A^3, \quad (6.32)$$

where $\xi_p(t) = \xi_p e^{-i\omega_p t} + \xi_p^* e^{i\omega_p t}$. It is clear from this displaced Hamiltonian that off diagonal terms that consist of odd (1 or 3) power of $\hat{\varphi}_A$ can be made resonant by selecting an appropriate pump frequency. For example, by selecting the pump frequency $\omega_p = 2\omega_R - \omega_A$, a two photon-exchange between the resonator and the asymmetric mode can be enabled. Indeed, this is the process that we are looking for. Therefore, we have managed to design a cancellation circuit that allows cross-Kerr free four-wave mixing.

Having developed an intuitive picture, in the next sub-section, we perform a more thorough analysis of the Hamiltonian of the circuit. In addition, we find out the parameter space for the SNAIL which allows for the above conditions to be satisfied.

6.2.1 Formal analysis

A circuit diagram of the cancellation circuit and coupled readout cavity is depicted in Fig. 6.4d. From the circuit diagram, it is clear that both the transmon-like modes have identical shunting capacitance C_0 and they couple to each other through a coupling capacitance C_J . Both the transmon also couple identically with the resonator through coupling capacitors C_g . The SNAIL and the SQUID elements are also shown and they are parameterized in the same manner as the previous section, except, we have assumed $\alpha_{\text{sq}} = 1$ for the sake of simplicity. In addition, the series inductance arising from the pads and leads of the transmon-like modes is assumed to be the same and is denoted by L_0 . In order to write down the Hamiltonian of the circuit, we assume $\hat{\Phi}_{\text{sn}}$ and $\hat{\Phi}_{\text{sq}}$ to be the flux operators for the entire inductive branches of the SNAIL mode and SQUID mode respectively. We

also define the linear participation ratios of both the modes as $p_{\text{sn}} = L_{\text{eff,sn}}/(L_{\text{eff,sn}} + L_0)$ and $p_{\text{sq}} = L_{\text{eff,sq}}/(L_{\text{eff,sq}} + L_0)$. The Hamiltonian of the circuit is then written as

$$\begin{aligned} \hat{H}_{\text{circ}} = & \frac{\hat{Q}_{\text{sn}}^2}{2\tilde{C}_0} + \frac{\hat{\Phi}_{\text{sn}}^2}{2(L_{\text{eff,sn}} + L_0)} + \frac{\hat{Q}_{\text{sq}}^2}{2\tilde{C}_0} + \frac{\hat{\Phi}_{\text{sq}}^2}{2(L_{\text{eff,sq}} + L_0)} + \frac{\hat{Q}_{\text{sn}}\hat{Q}_{\text{sq}}}{2\tilde{C}_J} \\ & + \frac{\hat{Q}_r^2}{2\tilde{C}_r} + \frac{\hat{\Phi}_r^2}{2L_r} + \frac{\hat{Q}_{\text{sn}}\hat{Q}_r}{2\tilde{C}_g} + \frac{\hat{Q}_{\text{sq}}\hat{Q}_r}{2\tilde{C}_g} \\ & + \frac{E_{J,\text{sn}}\tilde{c}_{3,\text{sn}}}{3!} \left(\frac{\hat{\Phi}_{\text{sn}}}{\phi_0} \right)^3 + \frac{E_{J,\text{sn}}\tilde{c}_{4,\text{sn}}}{4!} \left(\frac{\hat{\Phi}_{\text{sn}}}{\phi_0} \right)^4 + \frac{E_{J,\text{sq}}\tilde{c}_{4,\text{sq}}}{4!} \left(\frac{\hat{\Phi}_{\text{sq}}}{\phi_0} \right)^4. \end{aligned} \quad (6.33)$$

Here \tilde{C}_k are the renormalized capacitances and $\tilde{c}_{k,\text{sn/sq}}$ are the renormalized nonlinearity coefficients from Eq. 6.26. We then express the Hamiltonian in terms of creation and destruction operators in a manner similar to Sec. 4.1.2. In our notation \hat{b}_{sq} , \hat{b}_{sn} and \hat{r} are used to denote the SQUID, SNAIL and readout mode destruction operators respectively. Note that the definitions of Φ_{ZPF} and Q_{ZPF} of the SNAIL and SQUID modes now utilize $(L_{J,\text{eff,sn}} + L_0)$ and $(L_{J,\text{eff,sq}} + L_0)$ as the inductances and hence, these quantities are flux dependent. As a result, our Hamiltonian in terms of creation and destruction operators will have hidden flux dependence and hence should be treated with care. This Hamiltonian is given by

$$\begin{aligned} \frac{\hat{H}_{\text{circ}}}{\hbar} = & \omega_{\text{sn}}\hat{b}_{\text{sn}}^\dagger\hat{b}_{\text{sn}} + \omega_{\text{sq}}\hat{b}_{\text{sq}}^\dagger\hat{b}_{\text{sq}} + g_{\text{sq,sn}}(\hat{b}_{\text{sn}}\hat{b}_{\text{sq}}^\dagger + \hat{b}_{\text{sn}}^\dagger\hat{b}_{\text{sq}}) \\ & + \omega_r\hat{r}^\dagger\hat{r} + g_{\text{sn,r}}(\hat{b}_{\text{sn}}\hat{r}^\dagger + \hat{b}_{\text{sn}}^\dagger\hat{r}) + g_{\text{sq,r}}(\hat{b}_{\text{sq}}\hat{r}^\dagger + \hat{b}_{\text{sq}}^\dagger\hat{r}) \\ & + g_{3\text{wave,sn}}(\hat{b}_{\text{sn}} + \hat{b}_{\text{sn}}^\dagger)^3 + g_{4\text{wave,sn}}(\hat{b}_{\text{sn}} + \hat{b}_{\text{sn}}^\dagger)^4 + g_{4\text{wave,sq}}(\hat{b}_{\text{sq}} + \hat{b}_{\text{sq}}^\dagger)^4. \end{aligned} \quad (6.34)$$

where $\omega_{\text{sn/sq}} = 1/\sqrt{\tilde{C}_0(L_0 + L_{\text{eff,sn/sq}})}$, $\omega_r = 1/\sqrt{C_r L_r}$ and $g_{j,k} = Q_{\text{ZPF,j}}Q_{\text{ZPF,k}}/\tilde{C}_{jk}$.

The magnitudes of the nonlinear terms are

$$g_{3\text{wave,sn}} = \frac{E_{J,\text{sn}}\tilde{c}_{3,\text{sn}}}{3!} \left(\frac{\Phi_{\text{ZPF,sn}}}{\phi_0} \right)^3,$$

$$\begin{aligned}
g_{4\text{wave,sn}} &= \frac{E_{J,\text{sn}} \tilde{c}_{4,\text{sn}}}{4!} \left(\frac{\Phi_{\text{ZPF,sn}}}{\phi_0} \right)^4, \\
g_{4\text{wave,sq}} &= \frac{E_{J,\text{sq}} \tilde{c}_{4,\text{sq}}}{4!} \left(\frac{\Phi_{\text{ZPF,sq}}}{\phi_0} \right)^4.
\end{aligned} \tag{6.35}$$

In order keep the math tractable, we analyze the bi-linear part, given by the first two rows, and the four-wave mixing part of the Hamiltonian in Eq. (6.29) separately. The four-wave mixing part, however, needs to be isolated carefully. The presence of three-wave mixing term modifies the four-wave mixing nonlinearity of the SNAIL to the second-order in the perturbation theory. The effective magnitude of the four-wave mixing nonlinearity of the SNAIL due to such perturbative correction is given by

$$g_{4\text{wave,sn}}^{\text{eff}} = g_{4\text{wave,sn}} - \frac{5g_3^2}{\omega_{\text{sn}}} = \frac{E_{J,\text{sn}} \tilde{c}_{4,\text{sn}}^{\text{eff}}}{4!} \left(\frac{\Phi_{\text{ZPF,sn}}}{\phi_0} \right)^4, \tag{6.36}$$

where

$$\tilde{c}_{4,\text{sn}}^{\text{eff}} = p_{\text{sn}}^4 \left[c_4 - (1 - p_{\text{sn}}) \frac{3c_{3,\text{sn}}^2}{c_{2,\text{sn}}} - \frac{5c_3^2}{3c_2} p_{\text{sn}} \right] = p_{\text{sn}}^4 c_{4,\text{sn}}^{\text{eff}}. \tag{6.37}$$

As a result, the four wave mixing part of the Hamiltonian is

$$\frac{\hat{H}_{4\text{wave}}}{\hbar} = g_{4\text{wave,sn}}^{\text{eff}} (\hat{b}_{\text{sn}} + \hat{b}_{\text{sn}}^\dagger)^4 + g_{4\text{wave,sq}} (\hat{b}_{\text{sq}} + \hat{b}_{\text{sq}}^\dagger)^4. \tag{6.38}$$

To further analyze the Hamiltonian we have to first diagonalize the bi-linear part. In general, this diagonalization needs to be performed numerically. However, after imposing the first condition, $L_{\text{eff,sn}} = L_{\text{eff,sq}}$, this diagonalization can be performed using our intuition from the last section. Under this condition, the frequencies, participation ratios, Φ_{ZPFs} and the Q_{ZPFs} of the SNAIL and SQUID modes are equal. Moreover, the coupling strength of these modes with the readout cavity is also equal. We denote $\omega_{\text{sn}} = \omega_{\text{sq}} = \omega_0$, $\Phi_{\text{ZPF,sn}} = \Phi_{\text{ZPF,sq}} = \Phi_{\text{ZPF,0}}$, $p_{\text{sn}} = p_{\text{sq}} = p_0$ and $g_{\text{sn,r}} = g_{\text{sq,r}} = g_0$ under this condi-

tion. Next, the bi-linear part of the Hamiltonian is diagonalized in two steps. First, we substitute

$$\hat{b}_{\text{sn}} = \frac{1}{\sqrt{2}}(\hat{s} + \hat{A}) \quad \text{and} \quad \hat{b}_{\text{sq}} = \frac{1}{\sqrt{2}}(\hat{s} - \hat{A}), \quad (6.39)$$

where \hat{s} and \hat{A} are the creation and destruction operators of the symmetric and asymmetric modes respectively. We deliberately denote the symmetric mode operator using a small case letter since it will undergo further hybridization later. In terms of these operators the bi-linear part becomes,

$$\frac{\hat{H}_{\text{circ,lin}}}{\hbar} = \omega_s \hat{s}^\dagger \hat{s} + \omega_A \hat{A}^\dagger \hat{A} + \omega_r \hat{r}^\dagger \hat{r} + \sqrt{2}g_0(\hat{s}^\dagger \hat{r} + \hat{s} \hat{r}^\dagger) \quad (6.40)$$

with $\omega_s = \omega_0 + g_{\text{sn,sq}}$ and $\omega_A = \omega_0 - g_{\text{sn,sq}}$. Moreover, it is clear from this expression that only the symmetric mode now couples with the readout mode. This is what one would expect from our discussion in the last section. To completely diagonalize the bi-linear part, we substitute

$$\hat{s} = \cos(\theta)\hat{S} + \sin(\theta)\hat{R} \quad \text{and} \quad \hat{r} = \cos(\theta)\hat{R} - \sin(\theta)\hat{S} \quad (6.41)$$

with $\theta = \frac{1}{2} \arctan\left(\frac{2\sqrt{2}g_0}{\omega_r - \omega_s}\right)$. The bi-linear part of the system Hamiltonian then simplifies to

$$\frac{\hat{H}_{\text{circ,lin}}}{\hbar} = \omega_S \hat{S}^\dagger \hat{S} + \omega_A \hat{A}^\dagger \hat{A} + \omega_R \hat{R}^\dagger \hat{R}. \quad (6.42)$$

where

$$\begin{aligned} \omega_S &= \frac{1}{2} \left(\omega_s + \omega_r - \text{sign}(\omega_r - \omega_s) \sqrt{4g^2 + (\omega_r - \omega_s)^2} \right) \\ \omega_R &= \frac{1}{2} \left(\omega_s + \omega_r + \text{sign}(\omega_r - \omega_s) \sqrt{4g^2 + (\omega_r - \omega_s)^2} \right). \end{aligned} \quad (6.43)$$

The effective four-wave mixing part is now give by

$$\frac{\hat{H}_{4\text{wave}}}{\hbar} = g_{4\text{wave,sn}}^{\text{eff}} (\hat{\varphi}_S + \hat{\varphi}_R + \hat{\varphi}_A)^4 + g_{4\text{wave,sq}} (\hat{\varphi}_S + \hat{\varphi}_R - \hat{\varphi}_A)^4, \quad (6.44)$$

with

$$\begin{aligned} \hat{\varphi}_S &= \varphi_S(\hat{S} + \hat{S}^\dagger) = \frac{\cos(\theta)}{\sqrt{2}}(\hat{S} + \hat{S}^\dagger), \\ \hat{\varphi}_R &= \varphi_R(\hat{R} + \hat{R}^\dagger) = \frac{\sin(\theta)}{\sqrt{2}}(\hat{R} + \hat{R}^\dagger), \\ \hat{\varphi}_A &= \varphi_A(\hat{A} + \hat{A}^\dagger) = \frac{1}{\sqrt{2}}(\hat{A} + \hat{A}^\dagger). \end{aligned} \quad (6.45)$$

Note that the $\hat{H}_{4\text{wave}}$ quoted here is the same as the one quoted in the last sub-section (Eq. 6.29). The rest of the analysis performed in the last section by imposing the second condition $g_{4\text{wave,sn}}^{\text{eff}} = g_{4\text{wave,sq}} = g_{4\text{wave}}$ follows in the same manner and we do not repeat it here.

6.2.2 Permissible parameter space

Summarizing from the last sub-section, we have imposed

$$\begin{aligned} \text{Condition 1: } & L_{\text{eff,sn}} = L_{\text{eff,sq}} \\ \text{and Condition 2: } & g_{4\text{wave,sn}}^{\text{eff}} = -g_{4\text{wave,sq}}, \end{aligned} \quad (6.46)$$

along with the specific geometry of the circuit, to engineer a Kerr- and cross-Kerr-free four wave mixing element. The question immediately becomes, can we actually satisfy these conditions? What parameters for the SNAIL and SQUID are required such that a cancellation circuit can indeed be implemented? We now discuss this topic in detail.

As mentioned before $L_{\text{eff,sn/sq}} = L_{J,\text{sn/sq}}/c_{2,\text{sn/sq}}$. Therefore the first condition trans-

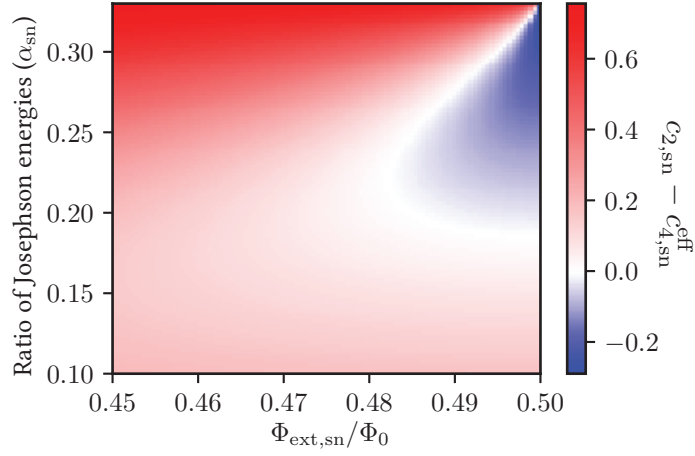


Figure 6.5: $c_{2,\text{sn}} - c_{4,\text{sn}}^{\text{eff}}$ (color) for a SNAIL as function of α_{sn} (y-axis) and $\Phi_{\text{ext,sn}}$ (x-axis). We have assumed $p_{\text{sn}} = 1$ for the purpose of this plot. It is clear that the required condition of $c_{2,\text{sn}} - c_{4,\text{sn}}^{\text{eff}} = 0$ can be satisfied by tuning the flux through the SNAIL, as long as the α_{sn} of the fabricated device is between 0.185 to 0.33. This flexibility in the values of α_{sn} eases the stringent fabrication constraints otherwise required for this circuit.

lates to

$$\frac{L_{J,\text{sn}}}{c_{2,\text{sn}}} = \frac{L_{J,\text{sq}}}{c_{2,\text{sq}}}. \quad (6.47)$$

Satisfying this condition is relatively easy since the SQUID inductance can be tuned over a wide range of values. The design of the circuit, therefore, depends strongly on the second condition. This condition translates to

$$\begin{aligned} \frac{E_{J,\text{sn}} \tilde{c}_{4,\text{sn}}^{\text{eff}}}{4!} \left(\frac{\Phi_{\text{ZPF,sn}}}{\phi_0} \right)^4 &= - \frac{E_{J,\text{sq}} \tilde{c}_{4,\text{sq}}}{4!} \left(\frac{\Phi_{\text{ZPF,sq}}}{\phi_0} \right)^4 \\ \Rightarrow \frac{E_{J,\text{sn}} p_{\text{sn}}^4 c_{4,\text{sn}}^{\text{eff}}}{4!} \left(\frac{\Phi_{\text{ZPF},0}}{\phi_0} \right)^4 &= - \frac{E_{J,\text{sq}} p_{\text{sq}}^4 c_{4,\text{sq}}}{4!} \left(\frac{\Phi_{\text{ZPF},0}}{\phi_0} \right)^4 \\ \Rightarrow E_{J,\text{sn}} p_0^4 c_{4,\text{sn}}^{\text{eff}} &= - E_{J,\text{sq}} p_0^4 c_{4,\text{sq}} \\ \Rightarrow \frac{c_{4,\text{sn}}^{\text{eff}}}{L_{J,\text{sn}}} &= - \frac{c_{4,\text{sq}}}{L_{J,\text{sq}}} = \frac{c_{2,\text{sq}}}{L_{J,\text{sq}}} = \frac{c_{2,\text{sn}}}{L_{J,\text{sn}}} \\ \Rightarrow c_{4,\text{sn}}^{\text{eff}} &= c_{2,\text{sn}} \end{aligned} \quad (6.48)$$

Therefore, $c_{4,\text{sn}}^{\text{eff}} = c_{2,\text{sn}}$ is the condition that the SNAIL needs to satisfy to realize a cancellation circuit. Note that the major reason behind this condition is actually the property of the SQUID which states that $c_{4,\text{sq}} = -c_{2,\text{sq}}$. In the simplest case where $\Phi_{\text{ext,sn}} = 0.5\Phi_0$, i.e. SNAIL biased at half flux, we have $c_{4,\text{sn}}^{\text{eff}} = c_{4,\text{sn}}$ since $c_{3,\text{sn}} = 0$. Therefore, at this flux bias $c_{4,\text{sn}}^{\text{eff}} = c_{2,\text{sn}}$ translates to

$$c_{4,\text{sn}} = c_{2,\text{sn}} \Rightarrow \left(\alpha_{\text{sn}} - \frac{1}{N_{\text{sn}}^3} \right) = \left(\frac{1}{N_{\text{sn}}} - \alpha_{\text{sn}} \right) \Rightarrow \alpha_{\text{sn}} = \frac{1}{2} \left(\frac{1}{N_{\text{sn}}} + \frac{1}{N_{\text{sn}}^3} \right). \quad (6.49)$$

In other words, the SNAIL needs to be designed with a specific value of α_{sn} to ensure that the conditions for the cancellation are satisfied. This, however, is very hard to implement experimentally since a device with such a specific parameter cannot be easily fabricated. Instead, it is more appropriate to design the device with a specific α_{sn} and then tune the flux through the SNAIL to satisfy the second condition. This is accomplished by numerically exploring the behavior of $c_{4,\text{sn}}^{\text{eff}} - c_{2,\text{sn}}$ as function of $\Phi_{\text{ext,sn}}$ and α_{sn} . Fig. 6.5 plots $c_{4,\text{sn}}^{\text{eff}} - c_{2,\text{sn}}$ for $p_{\text{sn}} = 1$ and $N_{\text{sn}} = 3$. It is clear from the figure that for $\alpha_{\text{sn}} \in (\sim 0.185, \sim 0.333)$ it is possible to tune the external flux bias to satisfy $c_{4,\text{sn}}^{\text{eff}} = c_{2,\text{sn}}$. In general, for arbitrary N_{sn} , this condition translates to $\alpha_{\text{sn}} \in \left[\frac{1}{2} \left(\frac{1}{N_{\text{sn}}} + \frac{1}{N_{\text{sn}}^3} \right), \frac{1}{N_{\text{sn}}} \right)$ for all values of p_{sn} , thus offering us a continuous range of α_{sn} in which the cancellation circuit can be realized. This relaxes the constraint on the accuracy of fabrication required for realizing the cancellation circuit.

6.2.3 Numerical simulations

We have checked the conditions under which Kerr- and cross-Kerr cancellation can be realized. In this sub-section we numerically show that for a reasonable set of parameters, we indeed get Kerr and cross-Kerr cancellation while still retaining the ability to perform two-photon exchange between the readout and the asymmetric mode. The uti-

Quantity	Value
\tilde{C}_0	0.12 pF
\tilde{C}_J	0.7 pF
\tilde{C}_g	4 pF
\tilde{C}_r	0.07 pF
L_r	5.475 nH
L_0	1.81 nH
$L_{J,\text{sq}}$	3.68 nH
$L_{J,\text{sn}}$	0.54 nH
α_{sn}	0.2114
α_{sq}	1

Table 6.1: Parameters for the numerical simulations of the cancellation circuit. These parameters are optimized to reproduce the experimental results shown later in the chapter.

lized parameters are specified in table 6.1. These parameters are essentially motivated by the experimental realization that we show in a latter section. The frequencies of the bare SNAIL, SQUID and readout modes as function of the external flux through SNAIL and SQUID are shown in Fig. 6.6a and Fig. 6.6b respectively. The frequency of SNAIL mode intersects both readout and the SQUID mode at certain flux points. The circuit satisfies the first condition $L_{\text{eff,sn}} = L_{\text{eff,sq}}$ at the points where the bare frequency of the SNAIL mode is equal to the bare frequency of the SQUID mode. In fact, by varying the flux through the SQUID mode, such an intersection point can be tuned to a variety of different points. However, both the cancellation conditions are satisfied simultaneously at a single point which is determined by the $\Phi_{\text{ext,sn}}$ at which $c_{4,\text{sn}}^{\text{eff}} = c_{2,\text{sn}}$. For our parameters, that point occurs at $\Phi_{\text{ext,sn}}/\Phi_0 \sim 0.485$. Having found this point, we can simply tune the flux bias of the SQUID to $\Phi_{\text{ext,sq}}/\Phi_0 \sim 0.160$, in order to simultaneously satisfy the first condition. In other words, $\Phi_{\text{ext,sn}}/\Phi_0 \sim 0.485$, $\Phi_{\text{ext,sq}}/\Phi_0 \sim 0.160$ is the unique point at which we get perfect cancellation of all the diagonal terms arising from four-wave mixing.

Although the perfect cancellation point is unique, there are multiple bias points at

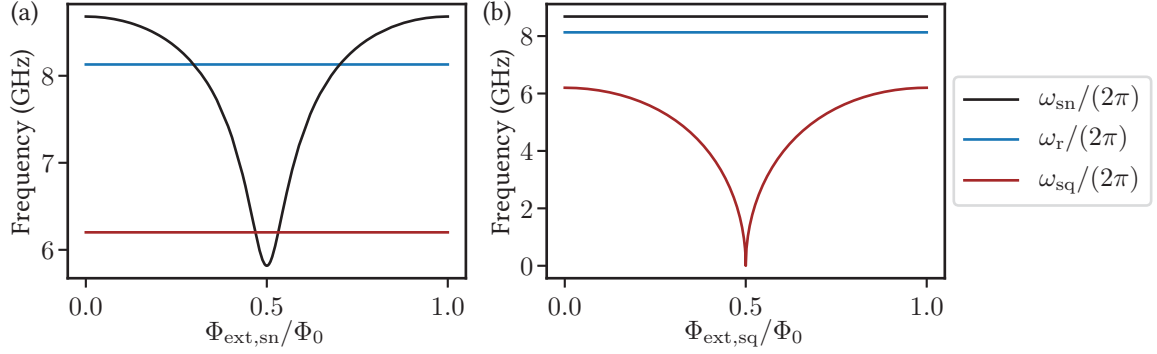


Figure 6.6: (a) Bare frequencies of the SNAIL mode (black), SQUID mode (brown) and the readout mode (blue) as function of the external flux through the SNAIL ($\Phi_{\text{ext,sn}}$) for the parameters mentioned in table 6.1. Only the SNAIL mode changes in frequency while the modes remain constant. Note that the bare SNAIL mode crosses the readout mode and the SQUID mode. (b) Bare frequencies of the aforementioned modes as function of the external flux through the SQUID ($\Phi_{\text{ext,sq}}$) for the same parameters. The frequency of the SQUID mode is tuned to lower values as function of flux, until it approaches 0 at the half flux and then starts increasing again.

which individual diagonal terms vanish. In Fig. 6.7 panels (a) and (b), we illustrate such cancellation by plotting the numerical values of χ_{AA} , χ_{SS} , χ_{AR} and χ_{SR} . We obtain these quantities by isolating the diagonal terms from

$$\frac{\hat{H}_{4\text{wave}}}{\hbar} = g_{4\text{wave,sn}}^{\text{eff}} \left[\varphi_{S,\text{sn}}(\hat{S} + \hat{S}^\dagger) + \varphi_{R,\text{sn}}(\hat{R} + \hat{R}^\dagger) + \varphi_{A,\text{sn}}(\hat{A} + \hat{A}^\dagger) \right]^4 + g_{4\text{wave,sq}} \left[\varphi_{S,\text{sq}}(\hat{S} + \hat{S}^\dagger) + \varphi_{R,\text{sq}}(\hat{R} + \hat{R}^\dagger) + \varphi_{A,\text{sq}}(\hat{A} + \hat{A}^\dagger) \right]^4, \quad (6.50)$$

where $g_{4\text{wave,sn}}^{\text{eff}}$, $g_{4\text{wave,sq}}$ and $\varphi_{K,\text{sn/sq}}$ are calculated separately at every flux bias. The calculations of $\varphi_{K,\text{sn/sq}}$ involves diagonalization of the bi-linear part of the Hamiltonian at every flux point which is accomplished numerically. The analytical diagonalization presented in Sec. 6.2.1 is valid only when $L_{\text{eff,sn}} = L_{\text{eff,sq}}$. It is clear from the plots for χ_{AA} , χ_{SS} , χ_{AR} and χ_{SR} that all the quantities cancel at multiple points. In addition, there is indeed a unique point at the flux bias of $\Phi_{\text{ext,sn}}/\Phi_0 \sim 0.485$, $\Phi_{\text{ext,sq}}/\Phi_0 \sim 0.160$ where the four quantities cancel simultaneously. The perfect cancellation point, although interesting

for some applications, is of limited interest for our goal of cascading nonlinear processes. As discussed in the previous chapters, although cross-Kerr is harmful for cascading, the self-Kerr indeed plays an important role, and the cascading cannot work without the presence of self-Kerr (see Sec. 4.3). This however, is not a problem for our design, since there are multiple points where the cross-Kerr between the asymmetric mode and the readout mode vanishes while the self-Kerr of the asymmetric mode survives.

Going further, we plot the amplitude of the two-photon exchange interactions $g_{2\text{ph},DR}$ and $g_{2\text{ph},SR}$ in Fig. 6.7c. These amplitudes are calculated by isolating the $\hat{R}^2\hat{A}^\dagger + \hat{R}^{\dagger 2}\hat{A}$ and $\hat{R}^2\hat{S}^\dagger + \hat{R}^{\dagger 2}\hat{S}$ terms from

$$\begin{aligned} \frac{\hat{H}_{4\text{wave}}}{\hbar} = & g_{4\text{wave},\text{sn}}^{\text{eff}} \left[\varphi_{S,\text{sn}}(\hat{S} + \hat{S}^\dagger) + \varphi_{R,\text{sn}}(\hat{R} + \hat{R}^\dagger) + \varphi_{A,\text{sn}}(\hat{A} + \hat{A}^\dagger) + \varphi_{S,\text{sn}}\xi_p(t) \right]^4 \\ & + g_{4\text{wave},\text{sq}} \left[\varphi_{S,\text{sq}}(\hat{S} + \hat{S}^\dagger) + \varphi_{R,\text{sq}}(\hat{R} + \hat{R}^\dagger) + \varphi_{A,\text{sn}}(\hat{A} + \hat{A}^\dagger) + \varphi_{S,\text{sq}}\xi_p(t) \right]^4. \end{aligned} \quad (6.51)$$

Here $\xi_p(t) = \xi_p(e^{i\omega_p t} + e^{-i\omega_p t})$ and we have assumed that the pump couples through the symmetric mode. The values of $g_{2\text{ph},AR}$ and $g_{2\text{ph},SR}$ in the figure are for $\xi_p = 1$. As expected, due to the specific symmetry of the circuit, $g_{2\text{ph},SR}$ vanishes at the same location as χ_{SR} , while $g_{2\text{ph},AR}$ is nonzero when $\chi_{AR} = 0$. Therefore, the circuit can be utilized to perform the two-photon exchange process between readout and asymmetric mode while canceling the cross-Kerr between them. Especially the points, where $\chi_{AR} = 0$ and $\chi_{AA} \neq 0$ are particularly useful for cascaded four-photon exchange. Finally, as a word of caution, the cancellation points may change in presence of strong off-resonant pumps as seen in the case of SNAIL parametric amplifiers [Sivak *et al.*, 2019]. However it should be possible to re-tune the circuit to achieve the required cancellation by changing the flux bias as achieved in the same article by Sivak *et al.* [2019].

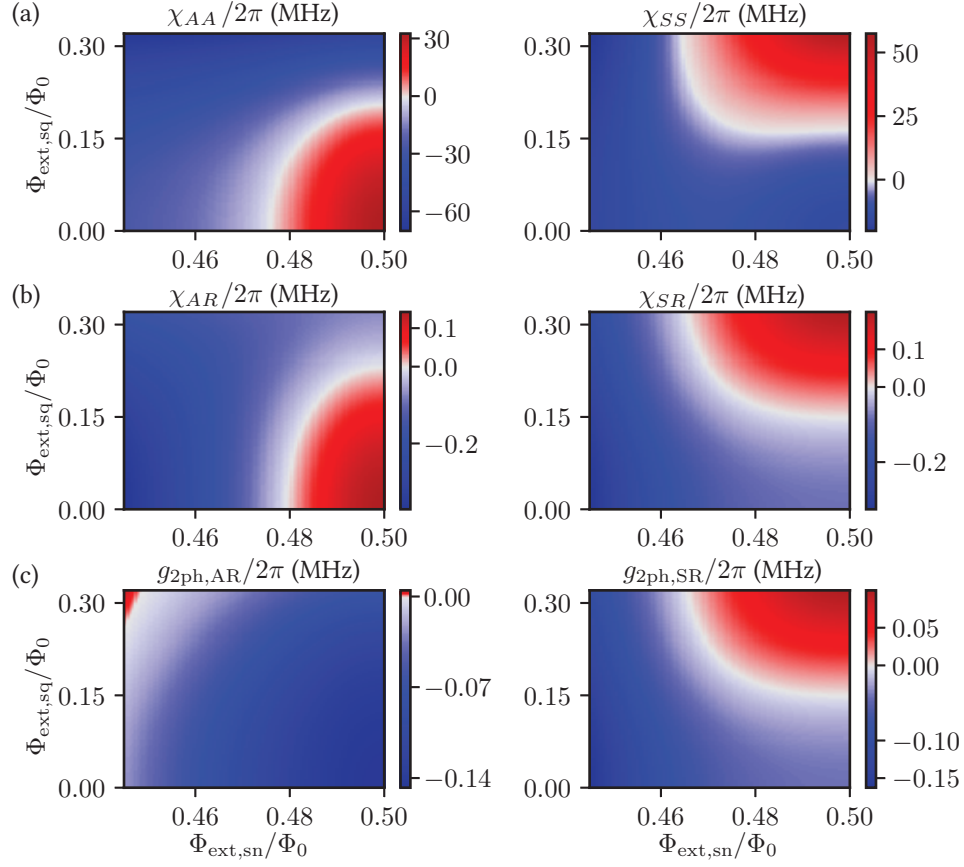


Figure 6.7: (a) Numerically obtained values of self-Kerrs χ_{AA} and χ_{SS} for the parameters specified in table 6.1. (b) Numerically obtained values of the cross-Kerrs with the readout mode χ_{AR} and χ_{SR} for the same set of parameters. Comparing these plots with each other and those in panel (a) it is clear that, each of the depicted Kerrs and cross-Kerrs go through zero and then change sign. However, the contours of cancellation (the white regions) are different for each of these quantities. In fact all the quantities cancel simultaneously only at a unique flux-bias of $\Phi_{ext,sn}/\Phi_0 \sim 0.485$ and $\Phi_{ext,sq} \sim 0.160$. This unique point obeys the relation $c_{4eff,sn} = c_{2sn}$. (c) Amplitude of the two-photon exchange interaction $g_{2ph,AR}$ and $g_{2ph,SR}$ as function of external flux through the SQUID and the SNAIL. These strengths are calculated assuming $\xi_p = 1$. Comparing these plots with those in (b), it is clear that $g_{2ph,AR}$ does not cancel at the same point as χ_{AR} . Therefore, the asymmetric mode can be utilized for performing cross-Kerr free two-photon exchange. On the other hand, as expected, $g_{2ph,SR}$ cancels at the same points as χ_{SR} .

6.3 Experimental design

The positive four-wave mixing coefficient required for engineering the cancellation circuit can only be obtained by utilizing flux biased circuit elements (SNAIL in our case). Moreover, having an independently tunable SQUID adds flexibility in fabrication and tuning of the circuit. Therefore, magnetic flux is one of the central requirements for realizing the cancellation circuit. Many two-dimensional superconducting circuit architectures regularly utilize such flux biased elements [Arute *et al.*, 2019]. In our case, however, high- Q harmonic oscillators, form a central part of the architecture. These high- Q oscillators are realized using aluminum enclosures, since aluminum being a superconductor allows for extremely low conductor losses. On the other hand, due to the Meissner effect, a superconducting aluminum enclosure does not allow any magnetic flux to thread through it. Therefore, in this section we primarily focus on the challenge of integrating magnetic flux with superconducting aluminum enclosures. The following sub-section discusses our relatively simple yet effective method of delivering magnetic flux. This is followed by a discussion of the specific experimental design that we have utilized for measuring the cancellation circuit.

6.3.1 Magnetic field in 3D aluminum cavities

Integrating flux bias into 3D environment is typically accomplished by utilizing a copper enclosure and a solenoid to apply the magnetic field. However, as mentioned before, this method cannot be directly applied to aluminum enclosures. As a superconductor, aluminum does not allow magnetic field to penetrate, as long as the strength of the magnetic field remains below a certain critical strength. Above this critical strength, we get magnetic vortices through the superconductor and eventually, above another critical threshold, the superconductivity breaks down. Such high fields and the resulting breakdown

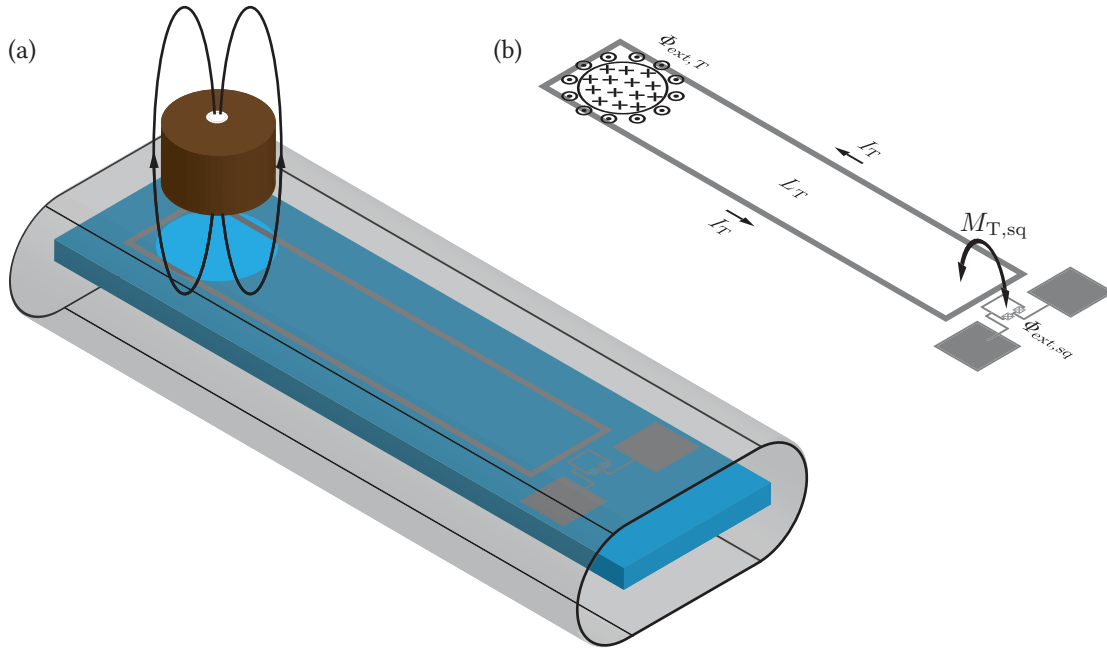


Figure 6.8: (a) Cartoon of a flux-bias compatible 3D aluminum enclosure (translucent grey). The enclosure has a hole through which we apply magnetic field using a solenoid made out of copper (brown). The field lines of the solenoid go into the enclosure and curl back to come out through the same hole. This prevents the threading of any magnetic flux through the superconducting enclosure. The enclosure houses a sapphire chip (blue) with a SQUID mode and a large loop of aluminum. This large loop of aluminum, which we hereby call a flux transformer, separates the SQUID mode from the low- Q copper magnet. Such a separation helps in maintaining the quality factor of the SQUID mode. In addition, the flux-transformer acts as a pickup loop and transports the flux bias of the magnet to the SQUID. (b) Explanation of the working of a flux-transformer. The applied external magnetic field threads a flux ($\Phi_{\text{ext},T}$) through the superconducting aluminum loop constituting the transformer. Due to fluxoid-quantization, the next flux through the loop is maintained at approximately zero by an induced current $I_T = \Phi_{\text{ext},T}/L_T$, where L_T is the self inductance of the transformer loop. The mutual inductance $M_{T,\text{sq}}$ between the flux transformer and the SQUID loop then leads to a flux through the SQUID loop given by $\Phi_{\text{ext},\text{sq}} = M_{T,\text{sq}}I_T$.

of the superconductivity (including vortices) is neither controllable nor desirable for the high- Q applications. Therefore, integrating magnetic flux in superconducting environment has been a widely studied yet the currently available solutions have not yet proven completely satisfactory.

One solution to introduce magnetic flux in aluminum enclosure is discussed in [Reed, 2013]. Here the so called fast-flux lines, commonly utilized in the 2D architecture, are integrated into a 3D aluminum cavity. However, the filtering requirements for the fast flux lines make this integration complicated and a more involved fabrication process is required. More recently, specialized devices called magnetic hoses [Navau *et al.*, 2014, Gargiulo *et al.*, 2018] have been proposed and demonstrated for routing magnetic field at arbitrary distances. These devices also require specialized fabrication and are not yet commercially available. Moreover, the quality factors in presence of these devices are not well studied and both the solutions are strongly geared towards applying time dependent flux bias. Here, we propose a simpler solution for applying a static flux bias that is required for operating our implementation of the cancellation circuit.

The basic idea behind our solution is illustrated in Fig. 6.8. As shown in panel (a) of this figure, we introduce magnetic flux inside an aluminum enclosure by designing a hole through the enclosure. The magnetic field applied with the help of a solenoid can go in through the hole as long as the magnetic field lines come back through the same hole resulting in zero net flux through the hole. Although this solves the issue of introducing magnetic flux into an aluminum enclosure, it is not a complete solution for two reasons: (i) the magnetic field entering the enclosure is greatly attenuated due to the screening action of the superconductor, and (ii) if the copper magnet is placed near a high- Q mode, it limits the Q of the mode since the copper is not a superconductor. We counter both of these issues by utilizing, what we call, a flux-transformer. The flux transformer is essentially a loop made out of aluminum. The flux transformer and the device (a SQUID transmon in the figure) are fabricated on a sapphire chip using the usual single-step e-beam lithography and aluminum deposition. This sapphire chip is then put in the aluminum enclosure with a hole (Fig. 6.8a) and cooled down in zero magnetic field. The working of the flux transformer is illustrated in Fig. 6.8b. Due to the magnetic field applied through the hole

in the aluminum enclosure, the flux transformer receives a flux of $\Phi_{\text{ext},T}$. However, the fluxoid quantization property of the superconductor requires that the total flux through this superconducting loop remains quantized. Moreover, since the initial flux through the loop is zero, this condition translates to

$$\Phi_{\text{tot},T} = \Phi_{\text{ext},T} + I_T L_T = 0, \quad (6.52)$$

where $\Phi_{\text{tot},T}$ is the total flux through the transformer, I_T is the induced current in the loop and L_T is the self-inductance of the loop. In other words, the external magnetic flux induces a current through the superconducting loop of the flux transformer in order to ensure that a net zero flux is threaded through the loop. The resulting current I_T through the loop can then be utilized for applying flux bias on another device, i.e. the SQUID in our case. Given a mutual inductance $M_{T,\text{sq}}$ between the flux transformer and the SQUID, we get a flux bias of

$$\Phi_{\text{ext},\text{sq}} = M_{T,\text{sq}} I_T = \frac{M_{T,\text{sq}}}{L_T} \Phi_{\text{ext},T} \quad (6.53)$$

through the SQUID loop. Thus, a simple loop of superconducting aluminum can be utilized for transporting the flux bias from the solenoid to the device (SQUID) of interest.

While designing flux-transformers, we keep the following principles in mind:

1. Having a large enclosed area near the solenoid is beneficial. The flux received from the solenoid increases with increase in area.
2. The loop of the device to be biased (SQUID in Fig. 6.8) should be placed as close to the flux transformer as possible in order to increase the mutual inductance between the transformer and the loop. In our design, we typically have merely 5 – 10 μm gap between the two loops. In addition, for lithographic convenience, the specialized shape of the SQUID loop shown in the figure is specifically optimized to place the

loop close to the transformer while keeping the junction far away from this large feature.

3. The length of the flux transformer is fixed by considering two important factors. Firstly, the magnet should be far enough away from the high- Q modes of interest to preserve their quality factor. Second, the flux transformer itself acts as a resonator giving rise to multiple harmonic modes. The minimum frequency of these modes is determined by the length of the flux transformer. Since these modes set the Purcell limit of the high- Q modes, it is beneficial to engineer the transformer such that all the additional harmonic modes are higher in frequency compared to the high- Q modes of interest.
4. Above a critical current density, the thin film aluminum loses its superconductivity. As a result, below the minimum trace width (typically around $5\ \mu\text{m}$), the flux transformer cannot carry enough current (I_T) to apply the required flux bias. Therefore, as a rule of thumb, the minimum width of the flux transformer at any point should be at least $5\ \mu\text{m}$.
5. Another important consideration would be the flux noise transferred from the transformer to the device (SQUID). A priori it seems that such flux noise should be suppressed since, typically, $M_{T,\text{sq}}/L_T \ll 1$ (< 0.001 in the design presented subsequently). As a result, only a fraction of the flux noise in the transformer will couple to the device of interest. On the other hand, the flux transformer has a considerably larger area and a careful analysis and measurement of the $1/f$ noise needs to be performed. We leave this as a future direction.

Armed with this understanding, in the next section, describe an enclosure designed for measuring the cancellation circuit.

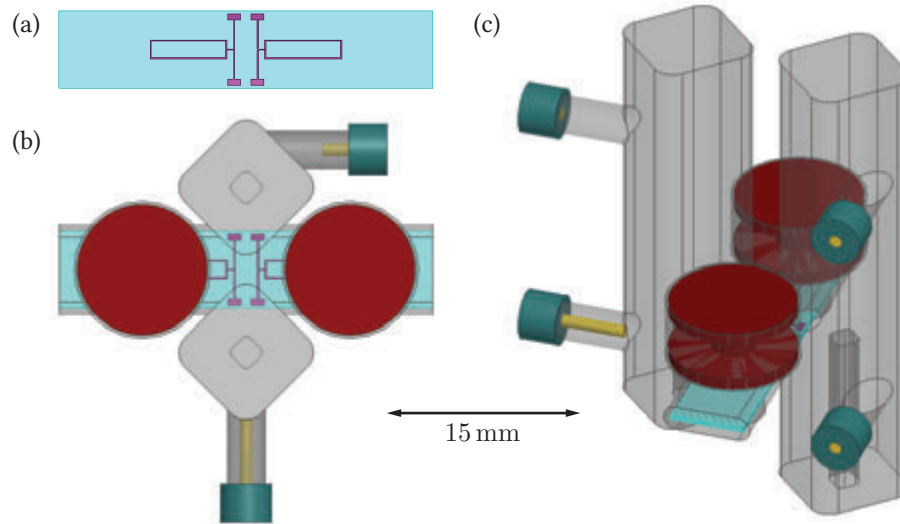


Figure 6.9: (a) HFSS design of a sapphire chip with the cancellation circuit (central vertical features) and two flux transformers (horizontal loops). Two separate flux transformers allow independent flux biasing of the SNAIL and SQUID modes of the cancellation circuit. (b, c) Top and isometric view of the enclosure designed for the preliminary experiments with the cancellation circuit. The sapphire chip shown in panel (a) is placed centrally between two $\lambda/4$ type resonator modes. Either one of these modes can be used as a readout and the other as the high- Q storage resonator. This choice is dictated by the length of the coupling pins utilized for addressing each of the resonators. Two separate magnets are utilized for biasing the flux-transformers. The applied flux of the magnets enters and leaves the enclosure through the corresponding holes below the magnets (not shown).

6.3.2 Enclosure for the cancellation circuit

In order to completely test the cancellation circuit we require an independent flux bias for the SNAIL and the SQUID. In addition a low- Q Readout mode coupled symmetrically to the SNAIL mode and the SQUID mode is also required. The pictures of our design which satisfies this wish list are shown in Fig. 6.9. It consists of a sapphire chip with the cancellation circuit in the center and two flux-transformers, one coupling to the SNAIL mode and the other coupling to the SQUID mode, as shown in Fig. 6.9a. This chip is then placed inside an aluminum enclosure as depicted in Fig. 6.9b and Fig. 6.9c. Two magnets with their respective holes (not shown) are positioned towards the ends of the flux transform-

ers in order to apply the requisite flux bias. The enclosure also consists of two $\lambda/4$ type resonators with different fundamental frequencies. Both the resonators couple symmetrically with the cancellation circuit and either can be used as the readout mode. Specifically, we utilize the higher frequency $\lambda/4$ mode (~ 8.1 GHz) as the readout mode. The lower frequency (~ 5.1 GHz) $\lambda/4$ mode is tuned to be relatively high- Q and is not utilized in our current experiment. This mode could be utilized as the high- Q storage harmonic oscillator for experiments involving cat-state stabilization which we do not explore here. The parameters used for the rest of the system will be clear in the next section where we discuss some of the preliminary experimental results.

6.4 Preliminary experimental results

In this section, we discuss the experimental results for the characterization of the cancellation circuit. The focus here is to prove that cancellation circuit can indeed provide four-wave mixing in absence of cross-Kerr. In order to prove this, we utilize the cancellation circuit and the readout mode of the enclosure discussed in the last section. This system is modeled well by the parameters specified in table 6.1. Indeed these parameters were optimized to reproduce the frequencies of all the involved modes at certain flux points. Therefore, a reader should review the bare frequencies of the SNAIL, SQUID and the readout mode as function of $\Phi_{\text{ext,sn}}$ and $\Phi_{\text{ext,sq}}$ specified in Fig. 6.6 and the behavior of cancellation circuit shown in Fig. 6.7 before attempting to understand the experimental data.

We characterize the system by utilizing two types of experiments. The first experiment is called readout spectroscopy. The idea here is to send a probe tone on the strongly coupled pin of the readout and observe the change in phase of the reflected signal. By sweeping the frequency of the applied tone, one first locates the phase-roll generated by the the

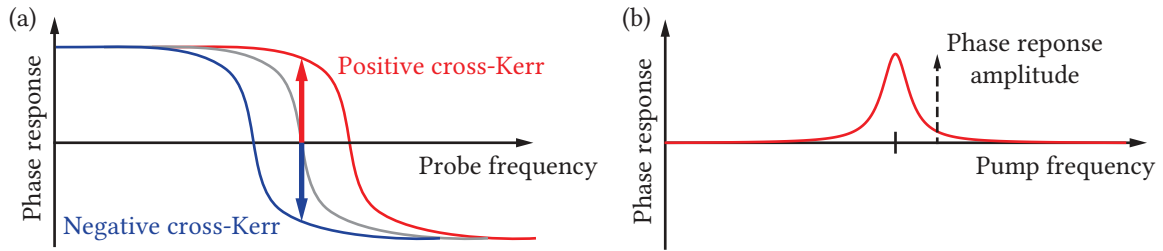


Figure 6.10: (a) Cartoon representing the phase response of the readout mode, measured by observing the reflection of a probe tone. When there is no excitation in the asymmetric or symmetric modes, the phase response of the readout mode is given by the gray line. The frequency where the phase response crosses zero is the resonance frequency of the readout. The two-tone spectroscopy is performed by continuously measuring the phase response at this frequency while applying another pump tone at different frequencies. If the pump tone excites any one of the asymmetric or the symmetric mode, then the readout frequency shifts due to the cross-Kerr interaction. If the cross-Kerr is positive, we get the response marked by the red color, and if the cross-Kerr is negative then we get the response marked by the blue color. As a result, the phase response at the readout resonance frequency is positive or negative depending on sign of the cross-Kerr. (b) Cartoon of the data obtained from a two-tone spectroscopy experiment. The x-axis plots the frequency of the pump and the y-axis plots the phase response at the readout resonance frequency. From this data we infer the resonance frequency of a process that excites one of the modes, and also the sign of the cross-Kerr between the mode and the readout.

readout resonator. A cartoon of this phase roll is shown by the gray line in Fig. 6.10a. The resonant frequency of the readout tone is then obtained by fitting to this phase response using the input-output formalism [Gardiner and Collett, 1985, Clerk *et al.*, 2010]. In our data, the resonant frequency of the readout mode can also be located by finding the probe frequency where the phase response of the probe tone is zero, since the measurement operator is calibrated to cancel the electrical delay induced by the input and output lines. The results of performing the readout spectroscopy as function of the current through the SNAIL magnet is shown in Fig. 6.11a. The current through the SQUID magnet is set to zero for the purpose of this experiment. As the current through the SNAIL magnet increases, the readout moves down in frequency. At the point where the SNAIL mode frequency intersects the readout mode frequency, there is an avoided crossing which manifests as

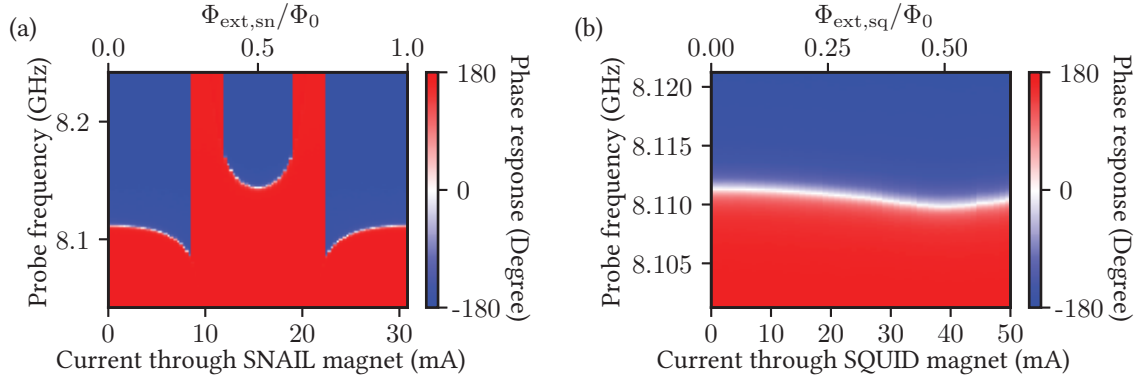


Figure 6.11: (a) Readout spectroscopy as function of the current through the SNAIL magnet. The SNAIL mode is initially above the readout mode. As the current through the SNAIL magnet is changed, the readout frequency moves downward due to the repulsion from the SNAIL mode. At around 10 mA the SNAIL mode crosses the readout mode resulting in an avoided crossing, which here manifests as a jump in the readout frequency. At a current of ~ 15.425 mA, the SNAIL bias reaches half flux quantum and the SNAIL mode reaches the minimum frequency. As the current is further increased, the same effects occur in a reversed fashion. We utilize this data to calibrate $\Phi_{\text{ext,sn}}$ as shown by the alternate x-axis. (b) Spectroscopy of the readout resonator as function of the current through the SQUID magnet. Note that the scale of the y-axis is different from the one in panel (a). The SQUID frequency always remains below the readout frequency and as a result there is no avoided crossing. The minimum in the readout frequency occurs when the SQUID is at half flux. The calibration $\Phi_{\text{ext,sn}}$ is again shown by the alternate x-axis.

a jump of the readout frequency observed in the figure. We use the data to calibrate the relation between $\Phi_{\text{ext,sn}}/\Phi_0$ and the current through the SNAIL magnet. Similarly, the readout spectroscopy as function of the current through the SQUID magnet, while the current through the SNAIL magnet is set to zero, is presented in Fig. 6.11b. We again see the variation in the readout frequency as function of the SQUID current. Since the SQUID mode never crosses the readout mode, we do not see any abrupt jumps. This data is again utilized for finding a relation between the current through SQUID magnet and $\Phi_{\text{ext,sq}}/\Phi_0$ as shown. Moreover, this figures proves that the flux transformers are indeed working correctly for this sample.

The second experiment used for characterizing the sample is the so called two-tone

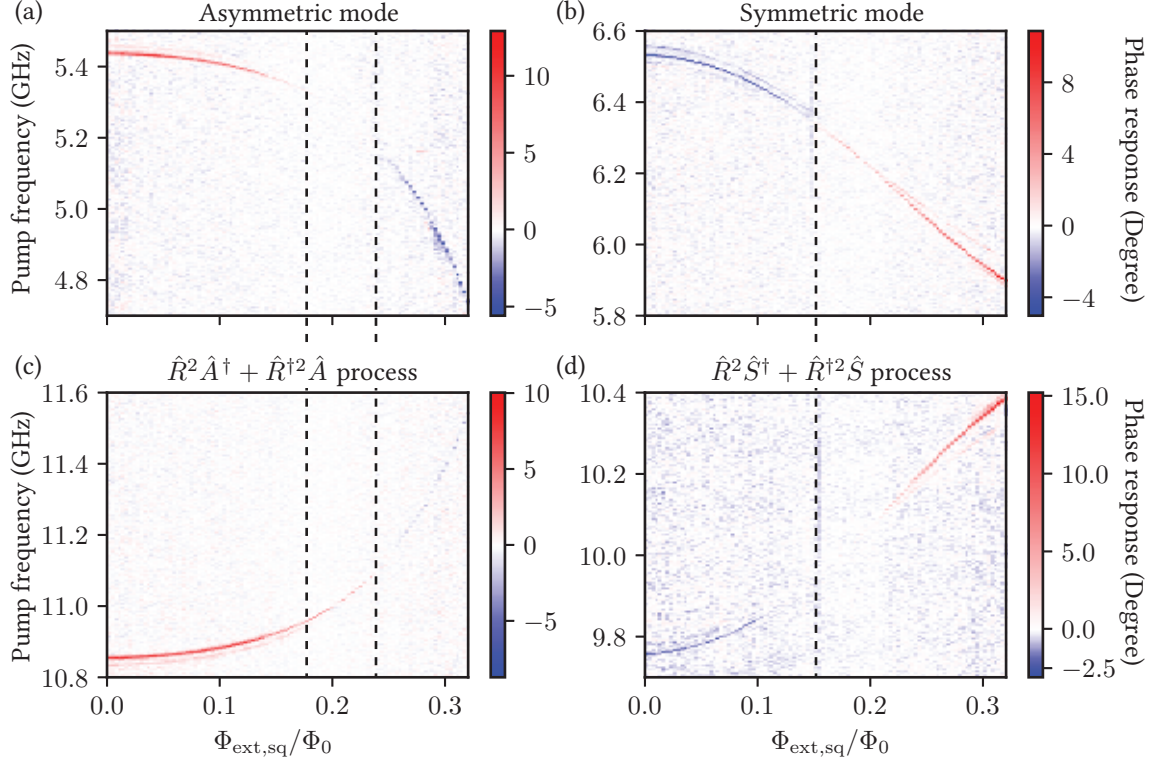


Figure 6.12: Two-tone spectroscopy of the system as a function of $\Phi_{\text{ext,sq}}/\Phi_0$ (x-axis), when the SNAIL is parked at half flux ($\Phi_{\text{ext,sn}}/\Phi_0 = 0.5$). The experiment is performed by identifying readout resonance at each flux point and then applying the pump tone at different frequencies. (b, c) The lines corresponding to the $g - e$ transition of the asymmetric and symmetric modes respectively. Judging from red and blue colors of the lines, χ_{AR} changes from positive to negative, and χ_{SR} changes from negative to positive, when $\Phi_{\text{ext,sq}}$ is increased. Therefore, the cross-Kerrs go through zero at intermediate points. This cross-Kerr cancellation is manifested as vanishing of the respective lines. The vertical black lines are a guide for eye showing the cross-Kerr cancellation. (d,e) The lines corresponding to the two-photon exchange $\hat{R}^2\hat{A}^\dagger + \hat{R}^{\dagger 2}\hat{A}$ and $\hat{R}^2\hat{S}^\dagger + \hat{R}^{\dagger 2}\hat{S}$ processes respectively. Comparing these plots with those in (b,c) it is clear that $\hat{R}^2\hat{A}^\dagger + \hat{R}^{\dagger 2}\hat{A}$ process is present even when χ_{AR} vanishes. On the other hand $\hat{R}^2\hat{S}^\dagger + \hat{R}^{\dagger 2}\hat{S}$ is indeed canceled close to the $\chi_{SR} = 0$ region.

spectroscopy. The idea here is to park the frequency of the probe tone at the resonance frequency of the readout mode. Another tone, which we hereby call the pump tone, is then applied at different frequencies. If the pump tone addresses a transition that puts excitation into either the asymmetric mode or the symmetric mode of the system then,

due to the cross-Kerr interaction between these modes and the readout mode, the effective resonance frequency of the readout mode shifts. As shown in Fig. 6.10a, if the cross-Kerr is positive, then the effective resonance frequency and, hence, the phase-roll of the readout shift to the right (red curve). Similarly, if the cross-Kerr is negative, then the effective frequency and the phase roll shift to the left (blue curve). As a result, the phase response of the probe tone, which is parked at the resonant frequency of the readout mode, is either positive or negative. Thus, by monitoring the phase response at the readout resonance as function of the pump frequency we obtain two vital pieces of information: (i) Location of the different transitions in the system and (ii) sign of the cross-Kerr between the readout mode and the other mode which receives an excitation. Moreover, over short range of pump frequency, this experiment can also be used to get an idea of the relative magnitude of the cross-Kerr interaction. Higher the phase response amplitude (see Fig. 6.10b), the stronger the cross-Kerr interaction.

We first utilize the two-tone spectroscopy experiment to characterize the system as function of $\Phi_{\text{ext,sq}}/\Phi_0$ when the SNAIL is biased at half flux ($\Phi_{\text{ext,sn}}/\Phi_0 = 0.5$). The results of this experiment for four different ranges of pump frequency are shown in Fig. 6.12. The line visible in panel (a) of the figure is the $g - e$ transition of the asymmetric mode which is lower in frequency. The phase response of the readout (color of the line) changes from positive (red) to negative (blue) as $\Phi_{\text{ext,sq}}/\Phi_0$ increases. This is because the cross-Kerr between the asymmetric mode and readout changes from positive to negative over this flux range. Moreover, the region where the line vanishes indicates the cross-Kerr is close to zero, thus providing us a signature of cross-Kerr cancellation. In addition, although not clearly visible, there is also an avoided crossing with the lower frequency $\lambda/4$ mode around ~ 5.14 GHz. Panel (b) of the same figure shows the $g - e$ transition line of the symmetric mode which shows a similar behavior. The cross-Kerr changes from negative to positive and goes through zero at an intermediate flux point. Combined, the data in

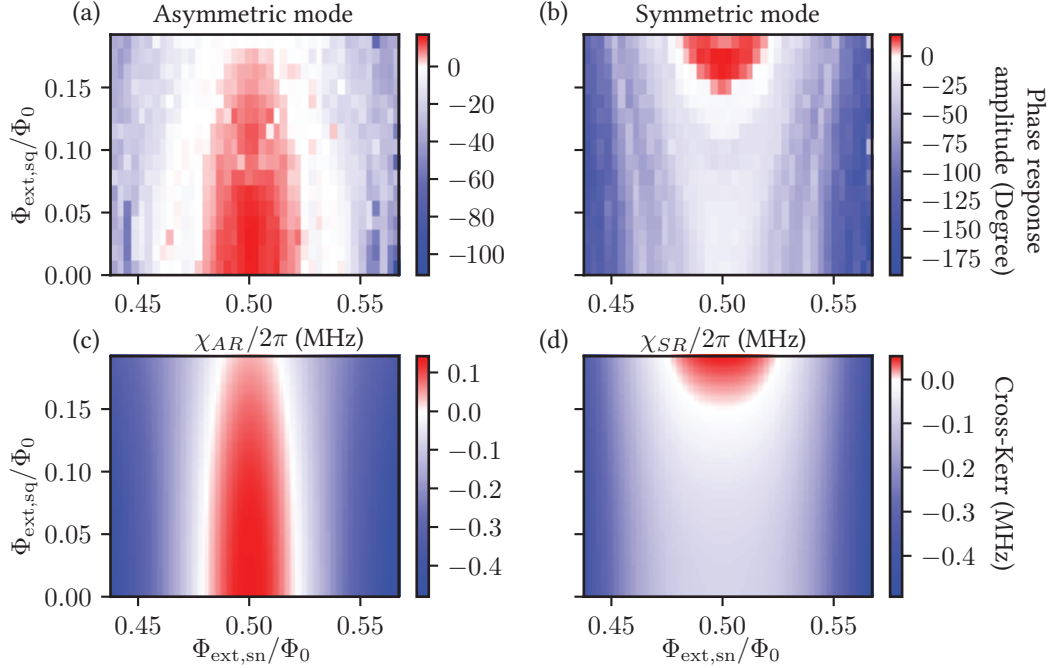


Figure 6.13: (a) Phase response amplitude (color) of the asymmetric mode as function of $\Phi_{\text{ext,sn}}/\Phi_0$ (x-axis) and $\Phi_{\text{ext,sq}}/\Phi_0$ (y-axis). The data allows us to infer the sign and relative magnitude of the cross-Kerr interaction between the asymmetric mode and the readout (χ_{AR}). (b) Phase response amplitude (color) of the symmetric mode as function of external flux-bias. We infer the sign and relative magnitude of the cross-Kerr interaction χ_{SR} from this data. (c, d) Numerical values of χ_{AR} and χ_{SR} obtained from the same simulations that produced the data in Fig. 6.7. By comparing the plots in panels (c) and (d) with this in panels (a) and (b) it is clear that the experimental results match well with the theoretical predictions for the cancellation circuit. We attribute the slight mismatch between theory and experiment to the errors in our circuit parameters.

panel (a) and (b) show that the cross-Kerr with both the modes gets canceled albeit at different flux points (since $\alpha_{\text{sn}} \neq 0.185$). Panels (c) and (d) of the figure show the two tone spectroscopy at higher pump frequencies, where The pump tone addresses the two photon exchange processes with the symmetric and asymmetric modes respectively. It is clear from (c) that the two-photon exchange with the asymmetric mode survives in spite of the cross-Kerr cancellation between asymmetric and the readout mode. On the other hand, the two-photon exchange between the readout mode and the symmetric mode is not present near the cancellation region of this mode as we predicted in our theoretical

analysis. Therefore, we have indeed realized the cancellation circuit.

Finally we perform two-tone spectroscopy experiments as function of both $\Phi_{\text{ext,sn}}$ and $\Phi_{\text{ext,sq}}$, for the $g - e$ transitions of the asymmetric and the symmetric mode. The resultant data at every flux point is then analyzed to obtain the amplitude of the phase response. This amplitude is plotted as function of $\Phi_{\text{ext,sn}}$ and $\Phi_{\text{ext,sq}}$ in Fig. 6.13 panel (a) and panel (b). It shows that the cross-Kerr cancellation happens at multiple points for both the modes. In addition, there are flux points near $\Phi_{\text{ext,sn}}/\Phi_0 \sim 0.48$ and $\Phi_{\text{ext,sn}} \sim 0.16$ where both the cross-Kerrs seem to cancel simultaneously as expected. Panel (c) and (d) of the same figure reproduce the numerically simulated data, previously plotted for different flux ranges in Fig. 6.7b. Qualitatively speaking, the numerical simulations describe the experimental data very well. The small quantitative disagreement between the theory and experiment is most likely due to the errors in our circuit parameters. Nonetheless, this data shows that the cancellation circuit works as expected and can thus be utilized for cross-Kerr free four-wave mixing that is needed in our experiments.

We have not yet studied the two-photon and four-photon driven dissipative processes using the cancellation circuit. This is one of the future directions for this work.

6.5 Comparison with a different implementation

As a final remark on cross-Kerr free four-wave mixing, we compare our circuit with another one recently demonstrated by [Lescanne *et al.*, 2019b]. Although the two circuits are quite different and have different operating constraints, they share very similar underlying principle. The two circuits, in simplified forms, are represented in Fig. 6.14. The circuit by [Lescanne *et al.*, 2019b] is essentially a SQUID shunted by a linear inductance

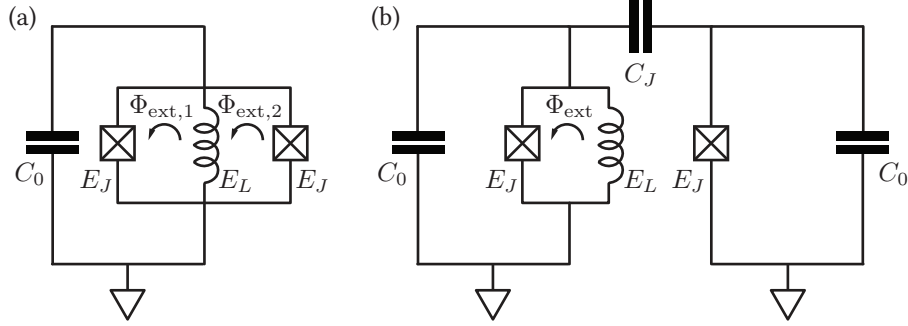


Figure 6.14: (a) Simplified version of a cross-Kerr-free four-wave mixing device demonstrated by [Lescanne *et al.*, 2019b]. It consists of a single dipole element realized as a SQUID shunted by a linear inductance. The junctions have the same Josephson energy E_J and the inductive energy of linear inductor is represented by E_L . The flux through the two loops is denoted by $\Phi_{\text{ext},1}(t)$ and $\Phi_{\text{ext},2}(t)$. As discussed in text, this time dependence of the external flux bias is required for addressing the four-wave mixing processes of interest. (b) Simplified version of the cancellation circuit. We have replaced the SNAIL by an RF-SQUID which is essentially a Josephson junction shunted by a linear inductance. In place of a SQUID we have simply utilized a single Josephson junction. In this simplified implementation, we need both the Josephson junctions to have the same E_J .

as shown in panel (a) of the figure. The Potential of this circuit is given by

$$U = \frac{E_L}{2} \hat{\varphi}^2 - E_J \cos(\phi_{\text{ext},1} - \hat{\varphi}) - E_J \cos(\phi_{\text{ext},2} + \hat{\varphi}), \quad (6.54)$$

where $\hat{\varphi}$ is the phase across the linear inductor, and $\phi_{\text{ext},k} = 2\pi\Phi_{\text{ext},k}/\Phi_0$. Now, if we bias the circuit with $\phi_{\text{ext},1} = \pi + \epsilon(t)$ and $\phi_{\text{ext},2} = \epsilon(t)$ then

$$\begin{aligned} U &= \frac{E_L}{2} \hat{\varphi}^2 + E_J \cos(\hat{\varphi} - \epsilon(t)) - E_J \cos(\hat{\varphi} + \epsilon(t)) \\ &= \frac{E_L}{2} \hat{\varphi}^2 + 2E_J \sin(\hat{\varphi}) \sin(\epsilon(t)). \end{aligned} \quad (6.55)$$

It is clear from this expression that the potential does not contain any diagonal four-wave mixing terms. However, off-diagonal pumped four wave mixing terms, like the two-photon exchange process, can be made resonant by selecting proper time dependence

for $\epsilon(t)$. Note that if the time dependent part of the flux bias, $\epsilon(t)$ is made zero or time independent, then none of the processes will be resonant and circuit will not provide any nonlinear interaction. As a result, fast-flux pumping is a key requirement for this circuit.

Let us now proceed to analyze a simplified version of our circuit shown in Fig. 6.14b. Here we have replaced the SQUID with an inductively shunted Josephson junction (i.e. an RF-SQUID) and the SQUID with a simple Josephson junction. The potential of this simplified version is then given by

$$\frac{\hat{H}}{\hbar} = \frac{E_L}{2} \hat{\varphi}_1^2 - E_J \cos(\phi_{\text{ext}} - \hat{\varphi}_1) - E_J \cos(\hat{\varphi}_2), \quad (6.56)$$

where $\hat{\varphi}_1$ is the phase across inductor of the RF-SQUID and $\hat{\varphi}_2$ is the phase across the single Josephson junction. We consider the case where the RF-SQUID is biased at half flux, i.e. $\phi_{\text{ext}} = 2\pi\Phi_{\text{ext}}/\Phi_0 = \pi$. With this bias the potential becomes

$$\frac{\hat{H}}{\hbar} = \frac{E_L}{2} \hat{\varphi}_1^2 + E_J \cos(\hat{\varphi}_1) - E_J \cos(\hat{\varphi}_2). \quad (6.57)$$

Note the sign change of the first cosine. This sign change is very similar to one that we studied in the other circuit. Now, as we have discussed in previous sections, for the cancellation circuit to operate, we need equal participation of the two hybridized modes in the two cosines. This is achieved by making sure that the effective inductance on both arms of the circuit is equal. For the simplified implementation shown here, such a condition translates to $E_L = 2E_J$. Under this assumption, we again utilize

$$\hat{\varphi}_1 = \hat{\varphi}_S - \hat{\varphi}_A \quad \text{and} \quad \hat{\varphi}_2 = \hat{\varphi}_S + \hat{\varphi}_A, \quad (6.58)$$

where $\hat{\varphi}_S$ and $\hat{\varphi}_A$ are the phase drops of the symmetric and the asymmetric modes re-

spectively. With this substitution, we get

$$\begin{aligned}\frac{\hat{H}}{\hbar} &= E_J(\hat{\varphi}_S - \hat{\varphi}_A)^2 + E_J \cos(\hat{\varphi}_S - \hat{\varphi}_A) - E_J \cos(\hat{\varphi}_S + \hat{\varphi}_A) \\ &= E_J(\hat{\varphi}_S - \hat{\varphi}_A)^2 + 2E_J \sin(\hat{\varphi}_A) \sin(\hat{\varphi}_S)\end{aligned}\quad (6.59)$$

It is clear that the potential of our cancellation circuit is similar to the one of the circuit by [Lescanne *et al.*, 2019b], except, the place of the time dependent flux term is taken by the symmetric mode. As a result, our circuit can operate on static flux bias, and the pump term can couple in through the symmetric mode.

To summarize, the idea of changing the sign of a cosine term from negative to positive in order to cancel the diagonal terms is common to both the circuit. The pumping of the [Lescanne *et al.*, 2019b] circuit is accomplished by adding time dependence to the flux bias. This necessitates integration of fast flux lines with the architecture under consideration. Although this can be accomplished in 2D architectures, performing flux pumping in 3D while maintaining high quality factors has not yet been satisfactorily achieved. On the other hand, the pumping in our implementation is accomplished by introducing an additional mode which allows the pump to couple in. As a result a static flux bias is sufficient for our circuit. This simplification comes at the cost of an additional mode and a somewhat stringent condition ($E_L = 2E_J$) on the parameters of the circuit. Similar to our discussion about the permissible parameter regime for the SNAIL mode, the condition on the circuit parameter can be relaxed by allowing the RF-SQUID to be biased at arbitrary flux points.

6.6 Summary and prelude to the next chapter

This chapter has focused on developing and testing a device which performs four-wave mixing while canceling the always-on diagonal terms like cross-Kerr and self-Kerr. Furthermore, we have also implemented a technique for applying static magnetic flux bias inside aluminum enclosures. The discussions in this chapter give us following takeaway points:

- (i) In order to engineer cross-Kerr-free four wave mixing, one requires a combination of two circuit elements, one with positive four-wave mixing coefficient and the other with a negative four-wave mixing coefficient.
- (ii) The negative four-wave mixing coefficient is more common for Josephson junction based circuit elements. A single junction, a SQUID, and even a SNAIL or RF-SQUID parked near zero flux can provide such a negative four-wave mixing coefficient.
- (iii) The positive four-wave mixing coefficient requires a flux-biased element like a SNAIL or an RF-SQUID biased near half flux.
- (iv) In order to get perfect Kerr and cross-Kerr cancellation for all the modes simultaneously we need to impose two conditions. The first condition is the equal participation of all the modes of the system in the aforementioned nonlinear elements. One way to achieve this is by engineering equal capacitance and equal effective inductance for the two nonlinear elements. The second condition requires the four-wave mixing coefficients of the two modes to be equal and opposite.
- (v) If a SNAIL is utilized for engineering the positive four-wave mixing coefficient, then the permissible range of α_{sn} for perfect cancellation is between $\frac{1}{2} \left(\frac{1}{N_{\text{sn}}} + \frac{1}{N_{\text{sn}}^3} \right)$ and $\frac{1}{N_{\text{sn}}}$, where N_{sn} are the number of shunting junctions.

- (vi) Although the perfect cancellation point is unique, it is possible to cancel a particular cross-Kerr or self-Kerr at multiple bias points. In particular, the points where self-Kerr between the asymmetric mode of the circuit and a harmonic oscillator mode cancels, while the self-Kerr of the asymmetric mode is preserved are of immense interest to us. These are the points where Raman-assisted cascading can be utilized for engineering higher order nonlinear processes.
- (vii) A flux transformer, which is essentially a loop of superconducting aluminum, can be utilized for ‘transporting’ flux bias from one point to another. We utilize this device for independently biasing the SNAIL and SQUID elements of our cancellation circuit.
- (viii) The preliminary experiments show that the cancellation circuit and flux transformers indeed work as advertised. It provides us the possibility of four-wave mixing while canceling the cross-Kerr between the symmetric and asymmetric mode and a readout resonator.

Although we have proven that the cancellation circuit and the flux-transformers work as expected, there is much work to be done in the future. We take this opportunity to highlight three such future directions:

- (i) Maintaining the high quality factors of the storage resonator modes is a key to storing information using the bosonic codes. Therefore, a thorough study of the quality factors of various modes in presence of flux-transformers is a requirement before such devices can be widely utilized.
- (ii) Implementation of two-photon driven-dissipative process with the help of the cancellation circuit biased at the perfect cancellation point. This experiment will be

similar to the one performed by [Lescanne *et al.*, 2019b] and will serve as a benchmark for comparing the two circuits.

- (iii) Implementation of cascaded four-photon exchange and four-photon driven-dissipative process with the help of the cancellation circuit. This is indeed the main motivation behind us developing the cancellation circuit in the first place.

Having studied the Raman assisted cascading and the cancellation circuit, we are now ready to discuss fully autonomous and continuous first order error correction against all the errors using the pair-cat codes. We take up this topic in the next and final chapter of the thesis.

Chapter 7

Fully autonomous QEC with pair cat code

In Ch. 3 we introduced the four-component cat codes which allow first-order protection against photon loss events. Moreover, a four-photon driven-dissipative process allows us to autonomously and continuously stabilize these states by exponentially suppressing the dephasing and energy relaxation errors as the size ($|\alpha|^2$) of the states increases. Ch. 4 and Ch. 5 focused on theoretical and experimental work geared towards implementing this four-photon driven-dissipative process. Such process requires an interaction between at least six or more photons. We showed a way to obtain such higher-order interaction by cascading the readily available lower-order four-wave mixing interactions. In addition, we introduced and demonstrated a new device which further tames the four-wave mixing nonlinearity to suit the needs of our proposal. This brings the autonomous protection against energy relaxation and dephasing, squarely within the grasp of available superconducting technology. The continuous protection against the photon loss errors, on the other hand, requires direct monitoring of the parity operator by engineering an interaction of the form $e^{i\pi\hat{a}^\dagger\hat{a}}\sigma_z$ in the Hamiltonian of the system. Such interaction, due to the

presence of an exponent, is of infinite-order in nonlinearity, and cannot be achieved with the superconducting circuit elements that we have studied in this thesis. Indeed, a new, and yet unimplemented circuit element proposed by [Cohen *et al.*, 2017] is required for engineering such an interaction. However, it is possible to simplify the design of a hardware efficient autonomous logical qubit, by utilizing a two-oscillator cousin of the cat codes, called the pair-cat code [Albert *et al.*, 2019]. This particular code offers a protection which is comparable, or even slightly better than the four-component cat code, while completely circumventing the need for continuous parity measurements.

The pair-cat code allows for the correction against photon loss events, as long as they affect only one of the oscillators. Such photon loss events can be monitored by observing the photon number difference between the oscillators, an error syndrome of the form $\hat{a}_2^\dagger \hat{a}_2 - \hat{a}_1^\dagger \hat{a}_1$. Here \hat{a}_1 and \hat{a}_2 are destruction operators of the two oscillator modes. It is clear that the error syndrome, in this case, is bi-linear, as opposed to the exponential parity operator in the case of four-component cat code. We later show that such an error syndrome can be continuously monitored by utilizing four-wave mixing and the circuit elements that we have already developed. Furthermore, a driven-dissipative process which forces simultaneous loss or gain of two photons in each of the oscillators, described by $\mathcal{D}[\hat{a}_2^2 \hat{a}_1^2 - \gamma^4]$, allows the stabilization of this code against energy relaxation and dephasing errors present in both the oscillator. Notice that, this driven-dissipative process is the same order of nonlinearity as the four-photon driven-dissipative process studied previously. Indeed, we show that the cascading technique developed in earlier chapters can be utilized for implementing this driven-dissipative process using four-wave mixing and lower order nonlinearity. As an additional benefit, since the pair cat code is immune to multiple photon losses on a single oscillator, the leakage error inherent to the cascading protocol does not affect this code. As a result, the pair-cat code has emerged as a prime candidate for realizing fully autonomous and continuous protection against all the error

channels to the first order. We dedicate this chapter to introducing this encoding and developing an experimental proposal for realizing such a logical qubit.

The following section (Sec. 7.1) starts by introducing the pair-cat states and their error correction properties. We put a particular emphasis on the engineered dissipation required for fully autonomous and continuous error correction. The experimental proposal for implementing this engineered dissipation is developed in Sec. 7.2. It becomes clear that the Hamiltonian engineering techniques that we developed in the rest of the thesis can be directly used to achieve our goals.

7.1 Introduction to pair-cat states

The goal of this section is to formally introduce pair-cat code. We begin this introduction by first talking about the basis states of the codes and discussing how the code protects against various channels of errors. This is followed by a discussion about the engineered dissipation required for protecting the encoded information in an autonomous and continuous manner.

7.1.1 Pair-coherent states

The pair-cat states are superpositions of the so called pair-coherent states. These states were first discussed in [Barut and Girardello, 1971] and are also called Barut-Girardello coherent states after the authors of the article. The pair coherent states are defined as simultaneous eigenstates of $\hat{\partial} = \hat{a}_2^\dagger \hat{a}_2 - \hat{a}_1^\dagger \hat{a}_1$, and $\hat{a}_1 \hat{a}_2$. The $\hat{\partial}$ operator is also referred to as the photon number difference operator in our discussions. Note that $[\hat{\partial}, \hat{a}_1 \hat{a}_2] = 0$, i.e. photon number difference and product of destruction operators commute, and hence, they indeed have non-trivial common eigenstates. We denote these states as $|\gamma_\partial\rangle$ where $\gamma^2 \in \mathbb{C}$ is the eigenvalue of the $\hat{a}_1 \hat{a}_2$ operator, and $\partial \in \mathbb{Z}$ is the eigenvalue of the photon-number

difference operator. To summarize

$$\hat{a}_2 \hat{a}_1 |\gamma_\partial\rangle = \gamma^2 |\gamma_\partial\rangle \quad \text{and} \quad \hat{\partial} |\gamma_\partial\rangle = \partial |\gamma_\partial\rangle. \quad (7.1)$$

The representation of these states in the Fock basis is given by

$$\begin{aligned} |\gamma_\partial\rangle &= N_{\gamma,\partial} \sum_{n=0}^{\infty} \frac{\gamma^{2n+\partial}}{\sqrt{n!(n+\partial)!}} |n, n+\partial\rangle, \quad \text{for } \partial \geq 0 \\ &= N_{\gamma,\partial} \sum_{n=0}^{\infty} \frac{\gamma^{2n+|\partial|}}{\sqrt{(n+|\partial|)!n!}} |n+|\partial|, n\rangle, \quad \text{for } \partial < 0. \end{aligned} \quad (7.2)$$

Here $|j, k\rangle = |j\rangle_1 \otimes |k\rangle_2$, and the normalization constant

$$N_{\gamma,\partial} = \frac{1}{\sqrt{I_{|\partial|}(2|\gamma|^2)}}, \quad (7.3)$$

with I_∂ being the modified Bessel function of the first kind. In the particular notation we have utilized, γ and $-\gamma$ return us the same pair-coherent state. From the expression of $|\gamma_\partial\rangle$, it is easy to verify that the relations presented in Eq. (7.1) are satisfied.

Keeping our future discussions in mind, it is helpful to study the overlap of two pair-coherent states as well as the action of single-mode destruction operators on these states.

The overlap is given by

$$|\langle \gamma'_{\partial'} | \gamma_\partial \rangle|^2 = \delta_{\partial,\partial'} \left| N_{\gamma,\partial} N_{\gamma',\partial'} \sum_{n=0}^{\infty} \frac{(\gamma'^* \gamma)^{2n+|\partial|}}{(n+\partial)!n!} \right|^2 = \delta_{\partial,\partial'} \left| \frac{I_\partial(2\gamma'^* \gamma)}{\sqrt{I_{|\partial|}(2|\gamma|^2) I_{|\partial|}(2|\gamma'|^2)}} \right|^2. \quad (7.4)$$

The Kronecker-delta is present since $\langle n, n+\partial' | n, n+\partial \rangle = \delta_{\partial,\partial'}$. This implies that the pair-coherent states with two different eigenvalues of $\hat{\partial}$ are orthogonal to each other irrespective of the value of γ . In effect, these states create orthogonal subspaces for each eigenvalue of $\hat{\partial}$. Moreover, the function $I_{|\partial|}(x)$ asymptotically approaches $2e^x/x$ as $|x| \rightarrow \infty$.

As a result, for $|\gamma|, |\gamma'| \gg 1$, the overlap can be approximated by

$$|\langle \gamma'_{\partial'} | \gamma_{\partial} \rangle|^2 \approx \delta_{\partial, \partial'} e^{-2|\gamma - \gamma'|^2} \quad (7.5)$$

As a result, if $|\gamma - \gamma'| \gg 1$, the pair coherent states are approximately orthogonal.

Next, let us study the effect of the single-mode destruction operators on these states.

It can be easily shown that

$$\hat{a}_1 |\gamma_{\partial}\rangle = \gamma \frac{N_{\gamma, \partial}}{N_{\gamma, \partial+1}} |\gamma_{\partial+1}\rangle, \quad (7.6)$$

and

$$\hat{a}_2 |\gamma_{\partial}\rangle = \gamma \frac{N_{\gamma, \partial}}{N_{\gamma, \partial-1}} |\gamma_{\partial-1}\rangle. \quad (7.7)$$

In fact, such analysis can be extended for powers of destruction operators, \hat{a}_1^l and \hat{a}_2^l .

These operators, act on the pair coherent states as follows:

$$\hat{a}_1^l |\gamma_{\partial}\rangle = \gamma^l \frac{N_{\gamma, \partial}}{N_{\gamma, \partial+l}} |\gamma_{\partial+l}\rangle, \quad (7.8)$$

and

$$\hat{a}_2^l |\gamma_{\partial}\rangle = \gamma^l \frac{N_{\gamma, \partial}}{N_{\gamma, \partial-l}} |\gamma_{\partial-l}\rangle. \quad (7.9)$$

Therefore, \hat{a}_1^l and \hat{a}_2^l change the eigenvalues of the photon number difference operator by l and $-l$ respectively. We could have also reached the same conclusion by noting $\hat{a}_1^l \hat{\partial} = (\hat{\partial} + l) \hat{a}_1^l$ and $\hat{a}_2^l \hat{\partial} = (\hat{\partial} - l) \hat{a}_2^l$.

Finally, to get some more perspective, let us note following similarities and differences between the pair-coherent and the single-mode coherent states:

1. Both coherent states and the pair-coherent states are the eigenstates of the destruction operators. \hat{a} in case of the coherent states and $\hat{a}_1 \hat{a}_2$ in case of the pair coherent states.

2. The amplitudes of the involved Fock-states follow Poisson-like distribution in both the cases.
3. We only have singly infinite coherent states parameterized by the coherent state amplitudes $\alpha \in \mathbb{C}$. In the case of pair-coherent states, however, there are countably infinite orthogonal subspaces enumerated by the eigenvalues of $\hat{\partial}$. Each ∂ -subspace contains a continuous infinity of states parameterized by $\gamma \in \mathbb{C}$.
4. The overlap of coherent states as well as the pair-coherent states is exponentially suppressed as the states go farther apart in phase space and ∂ -subspace respectively.
5. Displacing the single mode vacuum by a displacement operator $e^{\alpha\hat{a}^\dagger - \alpha^*\hat{a}}$ results in a coherent state α . However, a two mode displacement operator $e^{\gamma\hat{a}_1^\dagger\hat{a}_2^\dagger - \gamma^*\hat{a}_1\hat{a}_2}$ acting on the two mode vacuum $|0, 0\rangle$ does not create a pair-coherent state. Instead, such a state is known as the two-mode squeezed state and it is not an eigenstate of $\hat{a}_1\hat{a}_2$.

7.1.2 Pair-cat states and information storage

Photon loss events that affect only one of the two oscillators can be modeled by a set of operators $\mathcal{E} = \{\hat{I}\} \cup \{\hat{a}_1^j, \hat{a}_2^j\}_{j=0}^\infty$. We already know that each of the \hat{a}_1^j and \hat{a}_2^j operators map the ∂ -subspaces to completely orthogonal subspaces with a different eigenvalue of $\hat{\partial}$. Therefore, in order encode information in a manner that is robust to the single-mode photon losses, we need to utilize two orthogonal states in a ∂ -subspace as $|0_L\rangle$ and $|1_L\rangle$ of our codespace. Moreover, these states should also satisfy

$$\langle 0_L | \hat{a}_1^{\dagger j} \hat{a}_1^j | 0_L \rangle = \langle 1_L | \hat{a}_1^{\dagger j} \hat{a}_1^j | 1_L \rangle \quad \text{and} \quad \langle 0_L | \hat{a}_2^{\dagger j} \hat{a}_2^j | 0_L \rangle = \langle 1_L | \hat{a}_2^{\dagger j} \hat{a}_2^j | 1_L \rangle, \quad (7.10)$$

to ensure that the photon loss events do not distort the superposition of the logical states. Taking inspiration from the two-component cat codes, we define the pair-cat states as

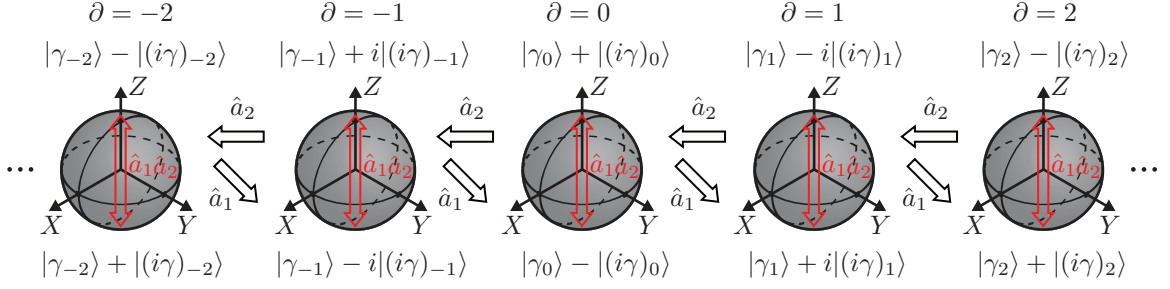


Figure 7.1: Information storage using pair-cat code. We have two orthogonal states at every value of ∂ . The $|0_L\rangle = |\gamma_\partial\rangle + (-i)^k|(-i\gamma)_\partial\rangle$ and $|1_L\rangle = |\gamma_\partial\rangle - (-i)^k|(-i\gamma)_\partial\rangle$ for every \mathcal{C}_∂ are represented in the figure. Here we have ignored the normalization constants for brevity. A photon loss error in the first mode (\hat{a}_1) moves the system from ∂ to a $\partial+1$ -sub-space while also introducing a bit-flip in the system as indicated by the diagonal arrows. This bit flip is the consequence of $(-i)^\partial$ factor in our definition of the logical states. The photon loss in second mode, on the other hand, moves the system from ∂ to $\partial-1$ subspace while introducing no bit-flip. As a result, errors photon loss errors, as long as they only affect a single mode, can be tracked by monitoring the photon number difference between the two oscillators. A loss of photon in both the modes simultaneously, however, introduces a logical bit-flip (red bi-directional arrows) which cannot be tracked since there is no change in value of ∂ .

equal superposition of two pair-coherent states, $|\gamma_\partial\rangle$ and $|(i\gamma)_\partial\rangle$ ¹. Note that both these states have the same eigenvalue ∂ for the photon number difference operator. The formal definition of the pair-cat states is

$$|\mathcal{P}_{\gamma,\partial}^{(k \bmod 2)}\rangle = \frac{N_{\gamma,\partial}^k}{N_{\gamma,\partial}} (|\gamma_\partial\rangle + (-1)^k(-i)^\partial|(i\gamma)_\partial\rangle) \quad (7.11)$$

where the normalization constant $N_{\gamma,\partial}^k$ is given by

$$N_{\gamma,\partial}^k = \frac{1}{\sqrt{2 [I_{|\partial|}(2|\gamma|^2) + (-1)^k J_{|\partial|}(2|\gamma|^2)]}}. \quad (7.12)$$

The function I_∂ again denotes the modified Bessel function of the first kind, and J_∂ denotes the Bessel function of the first kind. For large values of $|\gamma|$, I_∂ goes as $\mathcal{O}(e^{2|\gamma|^2}/|\gamma|)$ and

¹Remember that $|(\pm\gamma)_\partial\rangle$ describe the same states in our notation.

J_∂ as $\mathcal{O}(1/|\gamma|)$ which leads to

$$N_{\gamma,\partial}^k \approx \frac{N_{\gamma,\partial}}{\sqrt{2}} + (-1)^{k+1} \mathcal{O}\left(|\gamma|^{-1} e^{-2|\gamma|^2}\right). \quad (7.13)$$

Therefore, $\frac{N_{\gamma,\partial}^k}{N_{\gamma,\partial}}$ approaches $1/\sqrt{2}$ for large $|\gamma|$ and the k dependence of the normalization is exponentially suppressed just like in the case of cat states. The Fock state expansion of the pair cat states is given by

$$|\mathcal{P}_{\gamma,\partial}^{(k \bmod 2)}\rangle = 2N_{\gamma,\partial}^k \sum_{n=0}^{\infty} \frac{\gamma^{4n+2k+\partial}}{\sqrt{(2n+k)!(2n+k+\partial)!}} |2n+k, 2n+k+\partial\rangle. \quad (7.14)$$

Let us note some of the properties of the pair-cat states. Firstly, by construction, these states are the eigenstates of the photon-number difference operator. Moreover

$$\langle \mathcal{P}_{\gamma,\partial'}^{(j \bmod 2)} | \mathcal{P}_{\gamma,\partial}^{(k \bmod 2)} \rangle = \delta_{j,k} \delta_{\partial,\partial'}. \quad (7.15)$$

As expected, states with different eigenvalues of $\hat{\partial}$ are orthogonal, and we indeed have two orthogonal eigenstates at each eigenvalue of $\hat{\partial}$. Therefore the pair-cat codes can be used as the basis of our ∂ -code-space denoted by

$$\mathcal{C}_{\gamma,\partial} = \text{Span} \left\{ |0_L\rangle = |\mathcal{P}_{\gamma,\partial}^{(0 \bmod 2)}\rangle, |1_L\rangle = |\mathcal{P}_{\gamma,\partial}^{(1 \bmod 2)}\rangle \right\}. \quad (7.16)$$

Similar to pair-coherent states, the single-mode destruction operators introduce a change in the eigenvalue of $\hat{\partial}$. However, there are certain caveats here that deserve close examination. The effect of a photon loss on the first mode is

$$\hat{a}_1 |\mathcal{P}_{\gamma,\partial}^{(k \bmod 2)}\rangle = \gamma \frac{N_{\gamma,\partial}^k}{N_{\gamma,\partial+1}^{k+1}} |\mathcal{P}_{\gamma,\partial+1}^{(k+1 \bmod 2)}\rangle. \quad (7.17)$$

Notice that along with a change in the eigenvalue of $\hat{\partial}$ there is also **an effective bit-flip** here since k changes to $k + 1$. This bit-flip is all the more important since a photon loss in the second mode, described by

$$\hat{a}_2 |\mathcal{P}_{\gamma, \partial}^{(k \bmod 2)}\rangle = \gamma \frac{N_{\gamma, \partial}^k}{N_{\gamma, \partial-1}^k} |\mathcal{P}_{\gamma, \partial-1}^{(k \bmod 2)}\rangle, \quad (7.18)$$

does not display the same bit-flip. Such a bit-flip (or no bit-flip) does not destroy the stored information since the photon loss events can be detected by measuring $\hat{\partial}$ as an error syndrome. On the other hand, it is this asymmetry first and second mode which prevents the correction of photon-gain errors simultaneously with the photon-loss errors. For example, a photon-gain in the first mode (modeled by \hat{a}_1^\dagger) changes ∂ to $\partial - 1$ similar to a photon loss in the second mode. However, \hat{a}_1^\dagger introduces a bit-flip error in addition to the change of ∂ to $\partial - 1$, whereas \hat{a}_2 does not. As a result, we are not protected against photon gain in the first mode simultaneously with the photon loss in the second mode. This is indeed one of the limitations of the pair-cat state encoding. There exist higher order encodings using more than two cavities which can correct for photon gains as well. An interested reader should refer to Albert *et al.* [2019] for more information on those. Generally speaking, in the domain of superconducting circuits, the rate of heating (photon gains) is much slower than the rate of photon loss errors at low temperatures, making the current scheme sufficient for the purpose of first-order error correction. This may change in presence of strong drives in the system due to spurious heating observed in various experiments [Sank *et al.*, 2016, Lescanne *et al.*, 2019a]. Studies [Verney *et al.*, 2019] are underway for addressing such instabilities. However, for the purpose of this thesis, we will only focus on the photon loss errors.

The general result for multiple single-mode photon losses is given by

$$\hat{a}_1^j |\mathcal{P}_{\gamma,\partial}^{(k \bmod 2)}\rangle = \gamma^j \frac{N_{\gamma,\partial}^k}{N_{\gamma,\partial+j}^{k+j}} |\mathcal{P}_{\gamma,\partial+j}^{(k+j \bmod 2)}\rangle. \quad (7.19)$$

and

$$\hat{a}_2^j |\mathcal{P}_{\gamma,\partial}^{(k \bmod 2)}\rangle = \gamma^j \frac{N_{\gamma,\partial}^k}{N_{\gamma,\partial-j}^k} |\mathcal{P}_{\gamma,\partial-j}^{(k \bmod 2)}\rangle. \quad (7.20)$$

It is clear that the error syndrome $\hat{\partial}$ can still detect these photon loss events and hence, such errors can be monitored. Of course, being able to monitor photon loss events is not sufficient for preserving the superpositions. In order to ensure that the photon losses do not distort the superpositions, we need to satisfy Eq. (7.10). This condition translates to

$$\langle \mathcal{P}_{\gamma,\partial}^{(k \bmod 2)} | \hat{a}_1^{j\dagger} \hat{a}_1^j | \mathcal{P}_{\gamma,\partial}^{(k \bmod 2)} \rangle = \left| \frac{\gamma^j N_{\gamma,\partial}^k}{N_{\gamma,\partial+j}^{k+j}} \right|^2 \approx \left| \frac{\gamma^j N_{\gamma,\partial}}{N_{\gamma,\partial+j}} \right|^2 + (-1)^k \mathcal{O}(|\gamma|^{2j} e^{-2|\gamma|^2}), \quad (7.21)$$

and

$$\langle \mathcal{P}_{\gamma,\partial}^{(k \bmod 2)} | \hat{a}_2^{j\dagger} \hat{a}_2^j | \mathcal{P}_{\gamma,\partial}^{(k \bmod 2)} \rangle = \left| \frac{\gamma^j N_{\gamma,\partial}^k}{N_{\gamma,\partial-j}^k} \right|^2 \approx \left| \frac{\gamma^j N_{\gamma,\partial}}{N_{\gamma,\partial-j}} \right|^2 + (-1)^k \mathcal{O}(|\gamma|^{2j} e^{-2|\gamma|^2}). \quad (7.22)$$

The k dependence of the second terms in last two expressions implies that Eq. (7.10) is not satisfied exactly, and the photon jumps introduce slight distortion in the code-space. Similar to the cat codes, these distortions are exponentially suppressed in size $|\gamma|^2$. We verify this further, for different values of ∂ in Fig. 7.2. As a result of this exponential suppression of the distortions introduced by photon-loss events, the pair-cat codes protect against single-mode photon losses. On the other hand, if there is a simultaneous photon loss in both the modes described by $\hat{a}_1 \hat{a}_2$ occurs, then we get

$$\hat{a}_1 \hat{a}_2 |\mathcal{P}_{\gamma,\partial}^{(k \bmod 2)}\rangle = \gamma \frac{N_{\gamma,\partial}^k}{N_{\gamma,\partial}^{k+1}} |\mathcal{P}_{\gamma,\partial}^{(k+1 \bmod 2)}\rangle. \quad (7.23)$$

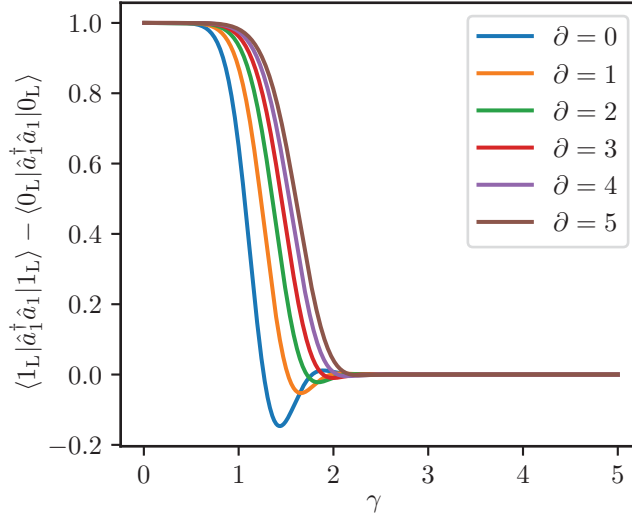


Figure 7.2: In this figure we plot $\langle 1_L | \hat{a}_1^\dagger \hat{a}_1 | 1_L \rangle - \langle 0_L | \hat{a}_1^\dagger \hat{a}_1 | 0_L \rangle$, where $|0_L\rangle = |\mathcal{P}_{\gamma,\partial}^{(0 \bmod 2)}\rangle$ and $|1_L\rangle = |\mathcal{P}_{\gamma,\partial}^{(1 \bmod 2)}\rangle$, as function of γ for different values of ∂ . It is clear that for a sufficiently large value of γ , the pair cat code satisfies Eq. (7.10) approximately. As the value of ∂ increases, the approximation is still valid albeit for slightly higher values of γ .

This is essentially a logical bit-flip since there is no change in the error syndrome $\hat{\partial}$.

Next, we discuss the effect of energy relaxation and dephasing errors on the pair-cat code. These errors are modeled by extending our set of error operators to

$$\mathcal{E} = \{\hat{I}\} \cup \{\hat{a}_1^l, \hat{a}_2^l\}_{l=1}^{\infty} \cup \{\hat{a}_1^\dagger \hat{a}_1^l, \hat{a}_2^\dagger \hat{a}_2^l\}_{l=1}^{\infty} \cup \{\hat{a}_1^\dagger \hat{a}_1^{l+m}, \hat{a}_2^\dagger \hat{a}_2^{l+m}, \hat{a}_1^\dagger \hat{a}_1^l \hat{a}_2^m, \hat{a}_2^\dagger \hat{a}_2^l \hat{a}_1^m\}_{l,m=1}^{\infty} \quad (7.24)$$

The operators in the second bracket are the single mode photon loss errors, operators in second bracket model the dephasing-like errors and the operators in the final bracket model simultaneous dephasing-like errors and the single mode photon loss. It can be checked that the off-diagonal Knill-Laflamme conditions for this extended error set are satisfied trivially. Also most of the diagonal terms are also zero. The non-zero diagonal conditions, on the other hand, are only approximately satisfied. This can be seen by realizing that these conditions are the same as the ones presented in Eq. (7.10), and analyzed in Eq. (7.21) and Eq. (7.22). Similar to the distortions induced by photon loss errors,

the effect of dephasing and energy relaxation is also exponentially suppressed due to the exponential suppression of the k dependent part in Eq. (7.21) and Eq. (7.22).

7.1.3 Tomography and representation

The Wigner function that we used in representation of a single mode oscillator can be extended to two or multiple oscillators as well. Before defining this two-mode Wigner function, let us first define the so called joint parity operator. This operator essentially measures the parity of the sum of photons in both the modes. It is given by

$$\hat{\Pi}_{\text{joint}} = e^{i\pi(\hat{a}_1^\dagger \hat{a}_1 + \hat{a}_2^\dagger \hat{a}_2)}. \quad (7.25)$$

With the help of this operator the two-mode Wigner function is expressed as

$$W(\beta_1, \beta_2) = \frac{2}{\pi} \text{Tr} \left[\hat{\Pi}_{\text{joint}} \hat{D}_1(-\beta_1) \hat{D}_2(-\beta_2) \rho_{12} \hat{D}_2(\beta_2) \hat{D}_1(\beta_1) \right], \quad (7.26)$$

where ρ_{12} is the joint density matrix of the system, and \hat{D}_1, \hat{D}_2 indicate displacements on the respective modes. In words, $W(\beta_1, \beta_2)$ is the expectation value of the joint parity operator after displacing the system by $-\beta_1, -\beta_2$. Note that the joint Wigner function is a four dimensional since $\beta_1, \beta_2 \in \mathbb{C}$. Experimentally speaking, it is time consuming, yet possible to measure such a four-dimensional Wigner function as demonstrated by [Wang *et al.*, 2016]. The displacements β_1, β_2 can be applied on individual cavities with the similar pulses as we have already explored in 5. Measuring the joint parity operator can again be accomplished in a similar manner to the single mode parity measurement, except, it requires an interaction of the form

$$\frac{\hat{H}_\Sigma}{\hbar} = \chi_\Sigma \left(\hat{a}_1^\dagger \hat{a}_1 + \hat{a}_2^\dagger \hat{a}_2 \right) |e\rangle\langle e|, \quad (7.27)$$

with an ancillary qubit mode. Initializing the qubit in the $|+\rangle$ state and allowing the system to evolve under \hat{H}_Σ for π/χ_Σ maps the joint parity of the oscillator modes to the state of the qubit since the unitary under this time evolution is given by

$$\hat{U}_{\text{joint-parity}} = e^{i\pi(\hat{a}_1^\dagger\hat{a}_1 + \hat{a}_2^\dagger\hat{a}_2)|e\rangle\langle e|}. \quad (7.28)$$

In our latter discussions, we will develop techniques to realize a Hamiltonian of the form

$$\frac{\hat{H}_\partial}{\hbar} = \chi_\partial \left(\hat{a}_2^\dagger\hat{a}_2 - \hat{a}_1^\dagger\hat{a}_1 \right) |e\rangle\langle e|, \quad (7.29)$$

for monitoring the error syndrome $\hat{\partial}$. It is interesting to note that such a Hamiltonian also does an equally good job of measuring the joint parity since

$$e^{i\frac{\hat{H}_\partial}{\hbar}t} \Big|_{t=\pi/\chi_\partial} = e^{i\pi(\hat{a}_2^\dagger\hat{a}_2 - \hat{a}_1^\dagger\hat{a}_1)|e\rangle\langle e|} = e^{i\pi(\hat{a}_1^\dagger\hat{a}_1 + \hat{a}_2^\dagger\hat{a}_2)|e\rangle\langle e|} = \hat{U}_{\text{joint-parity}}. \quad (7.30)$$

Although the two-mode Wigner function contains the exact same information as the density matrix of the two-mode system, it is of limited use in visualizing the two-mode states since it is a four-dimensional function. A visualization technique tailored specifically for the pair-coherent and pair-cat states has been developed in [Albert *et al.*, 2019]. The idea is utilize the so called γ -plane Wigner function defined as

$$W(\gamma, \partial) = \int \frac{d^2\eta}{\pi^2} e^{\eta^*\gamma - \gamma^*\eta} \text{Tr} \left(\hat{P}_\partial \rho_{12} e^{\eta\hat{a}_1^\dagger\hat{a}_2^\dagger - \eta^*\hat{a}_1\hat{a}_2} \right) \quad (7.31)$$

where $\gamma \in \mathbb{C}$ and

$$\hat{P}_\partial = \sum_n |n, n + \partial\rangle\langle n, n + \partial| \text{ for } \partial > 0$$

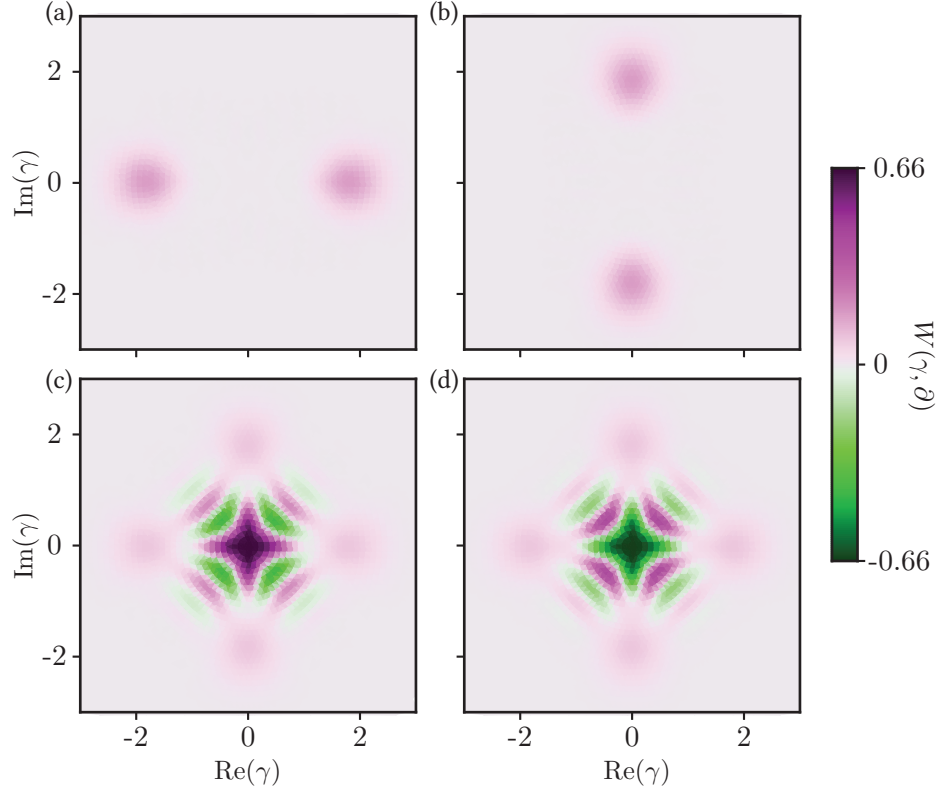


Figure 7.3: (a) γ -plane Wigner function of the pair-coherent state $|(\gamma = 2)_{\partial=0}\rangle$. We have made a deliberate change in the color scheme of the γ -plane Wigners to differentiate them from the regular phase-space Wigner functions. This particular Wigner function has two-blobs since, in our notation, $\pm\gamma$ denotes the same state. Note that there not superposition between two pair-coherent states here and hence, there are no fringes between the two blobs. (b) γ -plane Wigner function of the $|(\gamma = 2i)_{\partial=0}\rangle$ state. Again, similar to the $|(\gamma = 2)_{\partial=0}\rangle$ case, we have two blobs at $2i$ and $-2i$ since they are one and the same states. (c) γ -plane Wigner function of the $|\mathcal{P}_{\gamma=2, \partial=0}^{(0 \bmod 2)}\rangle$ state. Since this is a superposition of $|(\gamma = 2)_{\partial=0}\rangle$ and $|(\gamma = 2i)_{\partial=0}\rangle$ states we have a total of four blobs and the interference fringes between them. The fact that this is an even superposition of the two states is reflected by having the pink color in the center of the Wigner. (d) γ -plane Wigner function of the $|\mathcal{P}_{\gamma=2, \partial=0}^{(1 \bmod 2)}\rangle$ state. We again have four blobs and the interference fringes. Since this state is an odd superposition of the constituent pair-coherent states, we have green color at the center of the Wigner. Figure plotted using scripts provided by Victor Albert

$$= \sum_n |n + |\partial|, n\rangle \langle n + |\partial|, n| \text{ for } \partial < 0 \quad (7.32)$$

is the projector on the ∂ -sub-space. The γ -plane Wigner function is essentially a repre-

sensation of the density matrix for a fixed value of the photon-number difference ∂ . The γ -plane Wigner functions of $|(\gamma = 2)_{\partial=0}\rangle$, $|(\gamma = 2i)_{\partial=0}\rangle$, $|\mathcal{P}_{\gamma=2,\partial=0}^{(0 \bmod 2)}\rangle$ and $|\mathcal{P}_{\gamma=2,\partial=0}^{(1 \bmod 2)}\rangle$ are illustrated in Fig. 7.3. In this figure, we have consciously utilized a different color scheme that typical Wigner function to indicate that we are representing γ -plane Wigner functions. It is clear from panels (a) and (b) of the figure that the pair-coherent states look similar to the two-component cat states in the γ -plane, except there are no fringes. The two blobs in case of pair-coherent states are the consequence of our notation, in which, $|\gamma_{\partial}\rangle$ and $|-\gamma_{\partial}\rangle$ represent the same state. The pair-cat states on the other hand look similar to the the four-component cat states.

7.1.4 Autonomous protection of pair-cats

It is clear from our discussion that pair-cat states have similar error correction properties to the single mode cat states, except for an added protection against multiple single-mode photon loss errors. These single-mode photon loss errors can be monitored by measuring the photon number difference $\hat{\partial}$ between the two modes. However, again similar to single mode cat states, the dephasing and energy relaxation errors only approximately satisfy the Knill-Laflamme conditions and if left uncorrected, these errors tend to accumulate resulting in distortion of the code-space. In order to stabilize the encoding manifold against the photon loss errors, one again needs to utilize a driven-dissipative process.

Before discussing the required driven-dissipative process, let us look into one more property of the pair-cat states. We already know that these states are not the eigenstates of the $\hat{a}_1\hat{a}_2$ operator and which causes a logical bit-flip error for our encoding. However, the picture changes if we consider the $\hat{a}_1^2\hat{a}_2^2$ operator. The constituent pair-coherent states $|\gamma_{\partial}\rangle$ and $|(i\gamma)_{\partial}\rangle$ are both eigenstates of $\hat{a}_1^2\hat{a}_2^2$ operator with the same eigenvalue γ^4 . As a result, any superpositions of these states, including the pair-cat states are the eigenstates

of the $\hat{a}_1^2 \hat{a}_2^2$ with eigenvalue γ^4 . This property offers us a way to protect the pair-cat states from dephasing and energy relaxation errors. An operator of the form $\hat{a}_1^2 \hat{a}_2^2 - \gamma^4$ has the entire $\mathcal{C}_{\gamma, \partial}$ code-space as its Kernel, for any value of ∂ . As a result, a driven-dissipative process described by $\mathcal{D}[\hat{a}_1^2 \hat{a}_2^2 - \gamma^4]$ autonomously protects all of the $\mathcal{C}_{\gamma, \partial}$ code-spaces against the dephasing and energy relaxation errors. Note that this driven-dissipative process essentially involves four photons, two from each mode, which is the same order as the four-photon driven-dissipative process. Indeed we will see in the next section that $\mathcal{D}[\hat{a}_1^2 \hat{a}_2^2 - \gamma^4]$ process can be implemented in the same manner as the four-photon driven-dissipative process.

For building an autonomously protected logical qubit, however, we require protection against all the error channels of the oscillators to the first order. That is, we need to protect against the single mode photon loss errors in an autonomous fashion as well. For building such a protection, we first choose a principle code-space that will be ultimately stabilized. A natural choice for such a code-space is $\mathcal{C}_{\gamma, \partial=0}$, i.e. the code-space with equal number of photons in both the cavities. Note that the ground state of the system $|0, 0\rangle$ also belongs to $\partial = 0$ space and the $|0_L\rangle$ of the system can be simply prepared by turning on the driven-dissipative process. The set of dissipation operators that completely stabilize the $\mathcal{C}_{\gamma, \partial=0}$ against all the correctable errors is then given by

$$\begin{aligned} \mathcal{L}_{\text{eng}} = & \kappa_{2\text{ph}, 12} \mathcal{D}[\hat{a}_1^2 \hat{a}_2^2 - \gamma^4] \\ & + \sum_{k>0} \kappa_{\text{cor}} \mathcal{D} \left[|\mathcal{P}_{\gamma, \partial=k-1}^{(0 \bmod 2)}\rangle \langle \mathcal{P}_{\gamma, \partial=k}^{(1 \bmod 2)}| + |\mathcal{P}_{\gamma, \partial=k-1}^{(1 \bmod 2)}\rangle \langle \mathcal{P}_{\gamma, \partial=k}^{(0 \bmod 2)}| \right] \\ & + \sum_{k<0} \kappa_{\text{cor}} \mathcal{D} \left[|\mathcal{P}_{\gamma, \partial=k+1}^{(0 \bmod 2)}\rangle \langle \mathcal{P}_{\gamma, \partial=k}^{(0 \bmod 2)}| + |\mathcal{P}_{\gamma, \partial=k+1}^{(1 \bmod 2)}\rangle \langle \mathcal{P}_{\gamma, \partial=k}^{(1 \bmod 2)}| \right]. \end{aligned} \quad (7.33)$$

Here subscript 2ph, 12 denotes simultaneous two-photon dissipation on both the oscillators and cor denotes correction against photon loss errors. The dissipators in the second

and third row essentially gravitate the system towards $\mathcal{C}_{\partial=0}$ code-space. This is accomplished by jumping from $\mathcal{C}_{\partial=k}$ to a bit-flipped version of $\mathcal{C}_{\partial=k-1}$ code-space for every $k > 0$ and from $\mathcal{C}_{\partial=k}$ to $\mathcal{C}_{\partial=k+1}$ code-space for every $k < 0$. The reason for including the bit-flip when $k > 0$ is because photon jumps in the first mode themselves introduce bit-flips along with a change in eigenvalue of $\hat{\partial}$. In order to make the implementation of this engineered dissipation easier, we simplify the correction against photon loss errors as follows. Firstly, it is not necessary to correct for all the single-mode photon losses. Correcting the single-mode photon loss events that are less probable than the simultaneous photon loss, does not offer any increase in fidelity of correction, since $\hat{a}_1\hat{a}_2$ always constitutes an uncorrectable error. Therefore, correcting for $\{\hat{a}_1, \hat{a}_2, \hat{a}_1^2, \hat{a}_2^2\}$ is beneficial as well as sufficient for first-order error correction. A further simplification is accomplished by realizing

$$\hat{a}_1^\dagger |\mathcal{P}_{\gamma,\partial}^{(k \bmod 2)}\rangle = \frac{N_{\gamma,\partial}^k}{N_{\gamma,\partial-1}^{k-1}} |\mathcal{P}_{\gamma,\partial-1}^{(k-1 \bmod 2)}\rangle + \mathcal{O}\left(|\gamma|^{-1/2} e^{-|\gamma|^2}\right) \quad (7.34)$$

for $|\gamma| \gg 1$. Moreover, the leakage out of the code-space (the $\mathcal{O}\left(|\gamma|^{-1/2} e^{-|\gamma|^2}\right)$) term, is continuously pumped back into the code-space in presence of $\kappa_{2\text{ph},12} \mathcal{D}[\hat{a}_1^2 \hat{a}_2^2 - \gamma^4]$ term as long as the rate of confinement $|\gamma|^4 \kappa_{2\text{ph},12}$ is much stronger than the rate of leakage out of the code-space. As a result, the dissipation operators in the second row of \mathcal{L}_{eng} can be replaced by

$$\sum_{k=1,2} \mathcal{D} \left[|\mathcal{P}_{\gamma,\partial=k-1}^{(0 \bmod 2)}\rangle \langle \mathcal{P}_{\gamma,\partial=k}^{(1 \bmod 2)}| + |\mathcal{P}_{\gamma,\partial=k-1}^{(1 \bmod 2)}\rangle \langle \mathcal{P}_{\gamma,\partial=k}^{(0 \bmod 2)}| \right] \rightarrow \sum_{k=1,2} \mathcal{D} \left[\hat{a}_1^\dagger \hat{P}_{\partial=k} \right] \quad (7.35)$$

where \hat{P}_∂ is the projector on ∂ -sub-space defined in Eq. (7.32) and we have limited ourselves to correcting one or two photon losses on the first mode. With similar arguments,

the correction against the photon losses on the second mode can be simplified to

$$\sum_{k=-1,-2} \mathcal{D} \left[|\mathcal{P}_{\gamma,\partial=k+1}^{(0 \bmod 2)}\rangle \langle \mathcal{P}_{\gamma,\partial=k}^{(0 \bmod 2)}| + |\mathcal{P}_{\gamma,\partial=k+1}^{(1 \bmod 2)}\rangle \langle \mathcal{P}_{\gamma,\partial=k}^{(1 \bmod 2)}| \right] \rightarrow \sum_{k=-1,-2} \mathcal{D} \left[\hat{a}_2^\dagger \hat{P}_{\partial=k} \right]. \quad (7.36)$$

Combining, the required engineered dissipation is then given by

$$\mathcal{L}_{\text{eng}} = \kappa_{2\text{ph},12} \mathcal{D}[\hat{a}_1^2 \hat{a}_2^2 - \gamma^4] + \sum_{k=1,2} \kappa_{\text{cor}} \mathcal{D} \left[\hat{a}_1^\dagger \hat{P}_{\partial=k} \right] + \kappa_{\text{cor}} \mathcal{D} \left[\hat{a}_2^\dagger \hat{P}_{\partial=-k} \right].$$

This dissipator, under the assumption of $\kappa_{2\text{ph},12} |\gamma|^4 \gg \kappa_{\text{cor}} |\gamma|$ allows us to autonomously and continuously correct, up to first order, all the errors on a logical pair-cat qubit. In the next section we see how to engineer such a dissipator with the techniques that we have already explored.

7.2 Engineering fully autonomous protection

In the last section we constructed the required dissipative processes for autonomously correcting all the errors, to the first-order, on a logical pair-cat qubit. In this section the goal is to give an experimental proposal for implementing the required dissipation. A cartoon of a possible experimental system is shown in Fig. 7.4. We propose to engineer the two high- Q harmonic-oscillator modes, required for storing the pair-cat qubit, with the help of a ‘double post’ cavity. This cavity is essentially a single superconducting enclosure with two identical posts as shown in Fig. 7.4a. These identical posts give rise to two hybridized modes with frequencies ω_1 and ω_2 and field distributions as shown in panel Fig. 7.4b and Fig. 7.4c respectively. The main advantage of utilizing this architecture is the ease of coupling to both the cavity modes simultaneously. A nonlinear device or a coupling port placed at the right or left end of the enclosure, enjoys equal participation

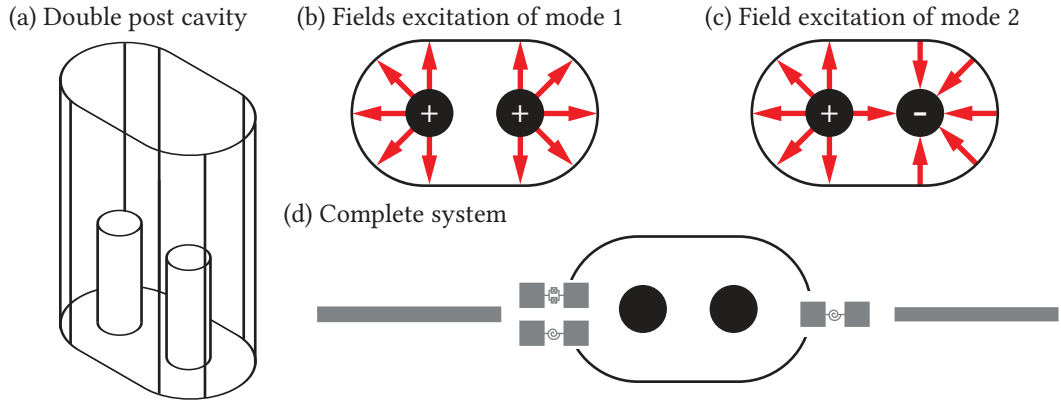


Figure 7.4: (a) Proposal for realizing two high- Q harmonic oscillator modes using a ‘double post’ cavity. The Two identical posts inside an aluminum enclosure gives rise to two $\lambda/4$ -like modes at the same frequencies. These modes hybridize with each others to form two high- Q modes at frequencies ω_1 and ω_2 . The frequency difference $|\omega_1 - \omega_2|$ can be tuned by changing the distance between the posts. (b) Fields of the higher frequency mode (ω_1, \hat{a}_1) in the top view of the cavity. The fields extend radially outward from both the posts. (c) Fields of the lower frequency mode (ω_2, \hat{a}_2) in the top view of the cavity. The fields are 180° out of phase with respect to the two posts. (d) All the parts required for implementing the autonomous stabilization of the pair-cat qubit. The cancellation circuit on the left mainly couples to the left post and the and the SNAIL mode on the right mainly couples to the right post. Since the high- Q harmonic oscillator modes participate equally in the two posts, they participate almost equally in the cancellation circuit, as well as the SNAIL mode. Moreover, the coupling to the cancellation circuit is symmetric for both the harmonic oscillator modes. We assume the bias of the cancellation circuit to be such that the asymmetric mode has four-wave mixing capabilities and a finite anharmonicity, while not having any cross-Kerr with both of the oscillator modes. This mode is then utilized as the nonlinear mode in a modified four-photon exchange. Following our previous convention, we label this mode by the letter b . The SNAIL mode on the right is utilized for measuring the photon loss error syndrome and for engineering autonomous protection against single-mode photon loss errors. We label this mode by the letter c . The two $\lambda/2$ resonators act as low- Q resonators, utilized for extracting entropy of the system. The flux-transformers biasing the cancellation circuit also need to be engineered (not shown).

of both the high- Q oscillator modes. As a result, more complicated transmon designs like a Y-mon [Wang *et al.*, 2016] are not required. The system, with all the required nonlinear modes, is shown in Fig. 7.4d. A cancellation circuit is coupled on the left of the cavity and a SNAIL mode is coupled on the right of the cavity. We utilize the cancellation circuit for

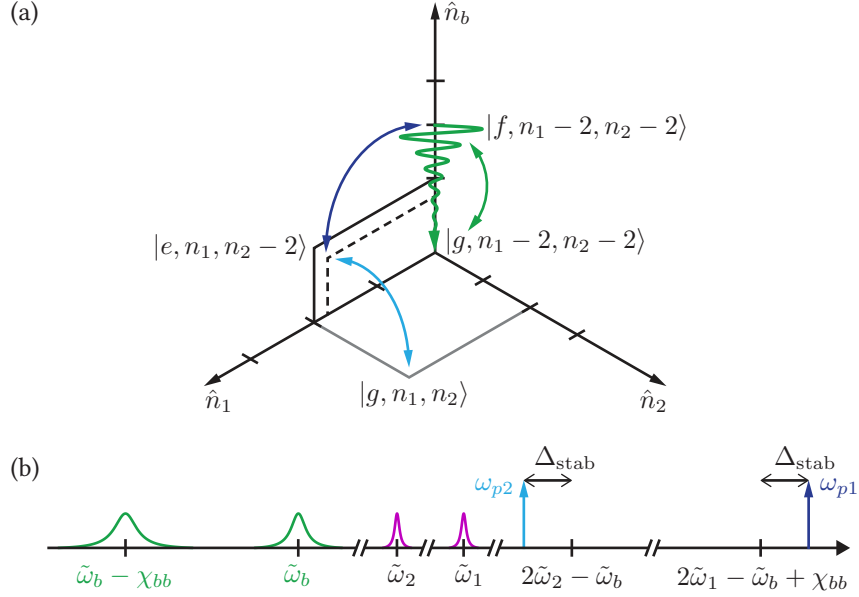


Figure 7.5: (a) 3D energy level diagram showing the Raman-assisted cascading for exchanging two photons from each of the high- Q harmonic oscillator modes, a total of four photons, with an excitation of the conversion mode. Imagine that the system starts in the $|g, n_1, n_2\rangle$ state. A two-photon exchange process, enabled by a pump at frequency ω_{p2} , connects this state with a virtual state detuned from $|e, n_1, n_2 - 2\rangle$ by a detuning Δ_{stab} . Another two-photon exchange process, enabled by pump at frequency ω_{p1} , connects the virtual state with the $|f, n_1 - 2, n_2 - 2\rangle$ state, therefore exchanging two-photons of mode 1 and mode 2 for two-excitations in the nonlinear mode. This modified four-photon exchange, along with the $f \rightarrow g$ direct dissipation of the conversion mode and an $f \leftrightarrow g$ coherent drive on the conversion mode, produces the required $\mathcal{D}[\hat{a}_1^2 \hat{a}_2^2 - \gamma^4]$ process. (b) Frequency distribution of the pumps and the transitions involved in the scheme.

implementing the $\mathcal{D}[\hat{a}_1^2 \hat{a}_2^2 - \gamma^4]$ driven-dissipative process and the SNAIL mode for implementing the correction against single-mode photon losses. A detailed explanation of how the required dissipative processes are engineered is provided in the next two sub-sections. From our discussion it will become clear that this experimental proposal is within reach using the technology developed in this thesis.

7.2.1 Driven-dissipative stabilization

The order of nonlinearity of the $\kappa_{2\text{ph},12}\mathcal{D}[\hat{a}_1^2\hat{a}_2^2 - \gamma^4]$ process is the same as that of the four-photon driven-dissipative process that we have studied previously. As a result, our technique of Raman-assisted cascading can be utilized, with one simple change, to implement the $\kappa_{2\text{ph},12}\mathcal{D}[\hat{a}_1^2\hat{a}_2^2 - \gamma^4]$ process. We utilize the cancellation circuit shown in Fig. 7.4d for obtaining the required nonlinearity in order to engineer this driven-dissipative process. Specifically, we assume that the cancellation circuit is biased such that the asymmetric mode of the circuit has four-wave mixing capability and a finite anharmonicity, however, no cross-Kerr with either of the high- Q harmonic oscillator modes. We hereon call the asymmetric mode as the conversion mode and label it with letter b . This nomenclature is the same as the one we utilized while building the four-photon driven-dissipative process previously.

An explanation of the Raman-assisted modified four-photon exchange used for implementing the driven-dissipative process is provided in Fig. 7.5. The idea is to exchange two-photons of the oscillator mode 2 with a virtual excitation of the conversion mode, followed by an exchange of two-photons from mode 1 while exciting the conversion mode to the f state, and vice versa. Combining this modified four-photon exchange with an $f \rightarrow g$ dissipation and an $f \leftrightarrow g$ coherent drive on the transmon results in the requisite $\mathcal{D}[\hat{a}_1^2\hat{a}_2^2 - \gamma^4]$ dissipation. The calculations behind this modified four-photon exchange and the final driven-dissipative process proceed in a similar manner to the ones presented in Sec. 4.3. Here we simply quote the initial Hamiltonian and the final results without repeating the intermediate steps.

The Hamiltonian of the system in presence of the pumps is given by

$$\frac{\hat{H}_{\text{sys,stab}}}{\hbar} = \tilde{\omega}_1 \hat{a}_1^\dagger \hat{a}_1 + \tilde{\omega}_2 \hat{a}_2^\dagger \hat{a}_2 + \tilde{\omega}_b \hat{b}^\dagger \hat{b} - \frac{\chi_{11}}{2} \hat{a}_1^{\dagger 2} \hat{a}_1^2 - \frac{\chi_{22}}{2} \hat{a}_2^{\dagger 2} \hat{a}_2^2 - \frac{\chi_{bb}}{2} \hat{b}^{\dagger 2} \hat{b}^2$$

$$+ \sum_{k=1,2} \left(g_{\text{stab},k} e^{-i\omega_{pk}t} \hat{a}_k^{\dagger 2} \hat{b} + h.c. \right) + \left(g_{\text{stab},3} e^{-2i\omega_{p3}t} \hat{b}^2 + h.c. \right) \quad (7.37)$$

where the subscript stab is used to indicate that we are only talking about the part of system that is geared towards engineering the driven-dissipative stabilization. In addition, the cross-Kerr term between the oscillators and the conversion mode is left out since we are canceling that term with the help of the cancellation circuit. The frequencies $\tilde{\omega}_1$, $\tilde{\omega}_2$ and $\tilde{\omega}_b$ are the renormalized and Stark-shifted frequencies of the modes as usual. The pump frequencies are given by

$$\begin{aligned} \omega_{p1} &= 2\tilde{\omega}_1 - \tilde{\omega}_b + \chi_{bb} + \Delta_{\text{stab}} \\ \omega_{p2} &= 2\tilde{\omega}_2 - \tilde{\omega}_b - \Delta_{\text{stab}} \\ \omega_{p3} &= \tilde{\omega}_b - \frac{\chi_{bb}}{2}. \end{aligned} \quad (7.38)$$

The master equation governing this part of the system is given by

$$\begin{aligned} \dot{\rho}_{\text{sys,stab}} &= -\frac{i}{\hbar} [\hat{H}_{\text{sys,stab}}, \rho_{\text{sys,stab}}] + \sum_{k=1,2} \kappa_{1\text{ph},k} \mathcal{D}[\hat{a}_k] \rho_{\text{sys,stab}} \\ &+ \Gamma_{\downarrow,b} \mathcal{D}[\hat{b}] \rho_{\text{sys,stab}} + \Gamma_{fg,b} \mathcal{D}[|g\rangle\langle f|] \rho_{\text{sys,stab}}. \end{aligned} \quad (7.39)$$

Utilizing the same tricks that we have previously demonstrated in Sec. 4.3, we get an effective equation of motion for the harmonic oscillators as

$$\dot{\rho}_{12} = -\frac{i}{\hbar} \left[\hat{H}_{\text{eff},12}, \rho_{12} \right] + \sum_{k=1,2} \kappa_{1\text{ph},k} \mathcal{D}[\hat{a}_k] \rho_{12} + \kappa_{2\text{ph},k} \mathcal{D}[\hat{a}_k^2] \rho_{12} + \kappa_{2\text{ph},12} \mathcal{D}[\hat{a}_1^2 \hat{a}_2^2 - \gamma^4] \rho_{12} \quad (7.40)$$

with

$$H_{\text{eff}} = \left(-\frac{|g_{\text{stab},1}|^2}{\Delta_{\text{stab}} + \chi_{bb}} - \frac{\chi_{11}}{2} \right) \hat{a}_1^{\dagger 2} \hat{a}_1^2 + \left(\frac{|g_{\text{stab},2}|^2}{\Delta_{\text{stab}}} - \frac{\chi_{22}}{2} \right) \hat{a}_2^{\dagger 2} \hat{a}_2^2. \quad (7.41)$$

The new dissipation rates $\kappa_{2\text{ph},1}$, $\kappa_{2\text{ph},2}$, $\kappa_{2\text{ph},12}$ and γ are given by

$$\begin{aligned}
\kappa_{2\text{ph},1} &= \left| \frac{g_{\text{stab},1}}{\Delta_{\text{stab}} + \chi_{bb}} \right|^2 \Gamma_{\downarrow,b}, \\
\kappa_{2\text{ph},2} &= \left| \frac{g_{\text{stab},2}}{\Delta_{\text{stab}}} \right|^2 \Gamma_{\downarrow}, \\
\kappa_{2\text{ph},12} &= \frac{4|g_{2\text{ph},12}|^2}{2\Gamma_{\downarrow,b} + \Gamma_{fg,b}}, \\
\gamma &= \frac{\sqrt{2}g_{\text{stab},3}}{g_{2\text{ph},12}}
\end{aligned} \tag{7.42}$$

with

$$g_{2\text{ph},12} = \sqrt{2}g_{\text{stab},1}g_{\text{stab},2} \left(\frac{1}{\Delta_{\text{stab}}} - \frac{1}{\Delta_{\text{stab}} + \chi_{bb}} \right). \tag{7.43}$$

It is clear from this effective equation of motion that, along with the required $\mathcal{D}[\hat{a}_1^2\hat{a}_2^2 - \gamma^4]$ process, we also gain two-photon dissipation on both the modes. However, this is not a problem since the pair-cat code corrects against single-mode two-photon losses as well. In comparison, this was a severe issue for the four-component cat code, since two-photon dissipation is a logical bit-flip error in that case. Finally, notice the denominators in the expressions for $\kappa_{2\text{ph},1}$ and $\kappa_{2\text{ph},2}$. It is clear that $\kappa_{2\text{ph},1} \ll \kappa_{2\text{ph},2}$ when the anharmonicity $\chi_{bb} \gg \Delta_{\text{stab}} > 0$. This asymmetry in the dissipation rates arise due to the particular pump choices we have used. In our case ω_{p1} is selected to off-resonantly exchange two-photons of the first oscillator with the $e \leftrightarrow f$ excitation of the conversion mode while ω_{p2} is selected to exchange two photons of the second oscillator with the $g \leftrightarrow e$ excitation of the conversion mode. This asymmetry in our pumps is essentially translated to the asymmetry in the single-mode two-photon dissipation rates. It is possible to implement the modified four-photon exchange protocol in a more symmetric manner by exchanging one photon from each oscillator ($\hat{a}_1\hat{a}_2$ process) with the $g \leftrightarrow e$ and $e \leftrightarrow f$ transitions of the conversion mode. This will still result in exchanging two-photons from each oscillators

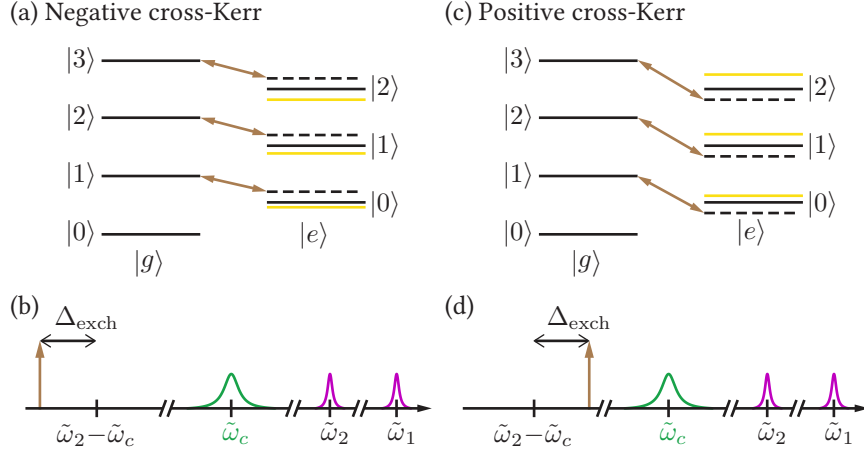


Figure 7.6: (a) Energy level diagram (black lines) of mode the ancillary mode c and the oscillator mode 2 under the influence of a pump at $\tilde{\omega}_2 - \tilde{\omega}_c - \Delta_{\text{exch}}$ shown in panel (b). This pump induces a red detuned beam-splitter interaction ($\hat{a}_1 \hat{c}^\dagger + \hat{a}_2^\dagger \hat{c}$) which off resonantly couples the $|g, n_1, n_2\rangle \leftrightarrow |e, n_1, n_2 - 1\rangle$ as indicated by the double sided brown arrows. As a result of this coupling, the $|e, n_1, n_2 - 1\rangle$ levels are shifted downward (yellow lines) along with some higher-order Stark-shifts (not shown). Moreover, the shift increases linearly as we climb up the ladder, since it is proportional to the square of the $|g, n_1, n_2\rangle \leftrightarrow |e, n_1, n_2 - 1\rangle$ coupling strength, which itself increases as $\sqrt{n_2}$ owing to the stricture of the \hat{a}_2 operator. As a result, a negative detuning induces a negative cross-Kerr between mode 2 and the ancillary mode c . (c) Energy level diagram (black lines) of the system under the influence of a pump at $\tilde{\omega}_2 - \tilde{\omega}_c + \Delta_{\text{exch}}$ as shown in panel (d). The blue detuned beam splitter interaction induced by this pump shifts the $|e, n_1, n_2 - 1\rangle$ levels upwards as shown. The shift again increases linearly as we climb up the ladder. In effect the pump induces a positive cross-Kerr between mode 2 and the ancillary mode c . Thus, off-resonant beam-splitter interaction allows us to engineer cross-Kerr interaction.

with $f \leftrightarrow g$ transition. However, in presence of $\Gamma_{\downarrow, b}$, this leads to a simultaneous photon loss on each mode, i.e. a $\mathcal{D}[\hat{a}_1 \hat{a}_2]$ process. Therefore, our implementation with exchanging two-photons from a single-mode with the $g \leftrightarrow e$ and $e \leftrightarrow f$ transitions of the oscillator is better suited for engineering the desired cascaded process.

7.2.2 Correction against single-mode photon losses

Let us now turn our attention to engineering correction against single-mode photon loss errors. Accomplishing this goal involves three parts: (i) engineering a photon-number difference (∂) dependent frequency shift on an ancillary mode, (ii) utilizing such a frequency shift to selectively add a photon to the appropriate high- Q oscillator mode while exciting the ancillary mode at the same time, and (iii) resetting the ancillary mode to the ground state. In this sub-section we show that executing these three parts simultaneously results in the promised autonomous and continuous correction against photon loss errors. However, let us first discuss, in a step by step manner, how to implement each of these parts.

As we previously discussed, the photon-number difference operator $\hat{\partial} = \hat{a}_2^\dagger \hat{a}_2 - \hat{a}_1^\dagger \hat{a}_1$ acts as the syndrome for the photon loss errors on the pair cat codes. Therefore, engineering the photon-number difference dependent frequency shift on an ancillary mode essentially results in mapping of the error syndrome on the frequency of the ancillary mode. Let us denote the ancillary mode by the letter c and its destruction operator by \hat{c} . The required interaction between the two oscillator modes and the ancilla is then given by $\chi_\partial \hat{\partial} \hat{c}^\dagger \hat{c} = \chi_\partial (\hat{a}_2^\dagger \hat{a}_2 - \hat{a}_1^\dagger \hat{a}_1) \hat{c}^\dagger \hat{c}$. It is clear from this expression that the photon-number dependent frequency shift is nothing but equal and opposite cross-Kerr interaction between the ancillary mode and the high- Q oscillator modes. We propose to accomplish this ‘cross-Kerr engineering’ with the help of the SNAIL mode shown in Fig. 7.4d. We assume that the SNAIL is biased such that $g_{4,\text{sn}}^{\text{eff}} < 0$ and $g_{3,\text{sn}} \neq 0$, where $g_{4,\text{sn}}^{\text{eff}}$ is quoted in Eq. (6.36) and $g_{3,\text{sn}}$ is the one quoted in Eq. (6.35). The Hamiltonian of the ‘syndrome-sub-system’ consisting of the high- Q oscillator modes and the SNAIL mode is then given

by

$$\begin{aligned} \frac{\hat{H}_{\text{sys,syndrome}}}{\hbar} = \sum_{k=1,2} \left(\tilde{\omega}_k \hat{a}_k^\dagger \hat{a}_k - \frac{\chi_{kk}}{2} \hat{a}_k^{\dagger 2} \hat{a}_k^2 \right) - \tilde{\omega}_c \hat{c}^\dagger \hat{c} - \frac{\chi_{cc}}{2} \hat{c}^{\dagger 2} \hat{c}^2 \\ - \chi_{1c} \hat{a}_1^\dagger \hat{a}_1 \hat{c}^\dagger \hat{c} - \chi_{2c} \hat{a}_2^\dagger \hat{a}_2 \hat{c}^\dagger \hat{c}, \end{aligned} \quad (7.44)$$

where we have only kept the diagonal terms of the Hamiltonian. Note that three wave mixing also produces diagonal terms to the second-order in perturbation theory, which can be taken into account by defining the Kerrs in terms of $g_{4,\text{sn}}^{\text{eff}}$. When this ancillary SNAIL mode is only dispersively coupled to the oscillators, the sign of the two cross-Kerr χ_{1c} and χ_{2c} comes out to be the same. Therefore, our task is to reverse the sign of the cross-Kerr with one of the oscillator modes and match it with the absolute value of the cross-Kerr with the other mode. For purpose of illustration we choose to manipulate the cross-Kerr between mode 2 and the SNAIL. This task amounts engineering additional positive cross-Kerr of $\chi_{1c} + \chi_{2c}$ between the two. Note that we cannot simply tune the cross-Kerr by manipulating the flux bias to change the sign and magnitude of $g_{4,\text{sn}}^{\text{eff}}$, since that will change χ_{1c} as well. Instead we utilize an off-resonant pump to accomplish this task. The pump frequency is chosen such that the so called ‘beam-splitter’ interaction between mode 2 and the SNAIL, described by $\hat{a}_2 \hat{c}^\dagger + \hat{a}_2^\dagger \hat{c}$, is addressed in a detuned manner. This interaction off-resonantly addresses the $|g, n_1, n_2\rangle \leftrightarrow |e, n_1, n_2 - 1\rangle$ transitions. If we pump at a frequency lower than that of $|g, n_1, n_2\rangle \leftrightarrow |e, n_1, n_2 - 1\rangle$ transition, then the $|e, n_1, n_2 - 1\rangle$ levels are pushed downwards, creating a negative cross-Kerr as shown in Fig. 7.6a. On the other hand, if we pump higher than the $|g, n_1, n_2\rangle \leftrightarrow |e, n_1, n_2 - 1\rangle$ transition, then the $|e, n_1, n_2 - 1\rangle$ levels are pushed upwards creating the required positive

cross-Kerr. To show this formally, let us extend our system Hamiltonian to

$$\frac{\hat{H}_{\text{driven,syndrome}}}{\hbar} = \frac{\hat{H}_{\text{sys,syndrome}}}{\hbar} + g_{\text{exch}} e^{-i\omega_{p,\text{exch}}t} \hat{a}_2^\dagger \hat{c} + g_{\text{exch}}^* e^{i\omega_{p,\text{exch}}t} \hat{a}_2 \hat{c}^\dagger. \quad (7.45)$$

with

$$\omega_{p,\text{exch}} = \tilde{\omega}_2 - \tilde{\omega}_b + \Delta_{\text{exch}}. \quad (7.46)$$

Here Δ_{exch} can be positive or negative allowing us to situate the pump above or below the resonance frequencies of the $|g, n_1, n_2\rangle \leftrightarrow |e, n_1, n_2 - 1\rangle$ transitions. The off-resonant beam-splitter interaction is essentially a three-wave mixing process, obtained from the $g_{3,\text{sn}}$ term in the potential of the SNAIL mode. In many circuit-QED experiments [Narla *et al.*, 2016, Wang *et al.*, 2016, Axline *et al.*, 2018], the $\hat{a}_2^\dagger \hat{c} + \hat{a}_2 \hat{c}^\dagger$ interaction is obtained from the four-wave mixing nonlinearity by applying two-pumps at appropriate frequencies. However, our application requires $|g_{\text{exch}}| \gg |\chi_{1c}| + |\chi_{2c}|$. Typically, such high interaction strength cannot be achieved by using the four-wave mixing nonlinearity as the χ_{1c} , χ_{2c} are also of the same order in nonlinearity. Instead, a SNAIL mode can be tuned such that $g_{3,\text{sn}} \gg g_{4,\text{sn}}^{\text{eff}}$ allowing us to satisfy $|g_{\text{exch}}| \gg |\chi_{1c}| + |\chi_{2c}|$ for reasonable pump strengths. The effective Hamiltonian of the system in presence of this applied pump can be found by first going into the rotating frame with respect to $\hat{H}_0/\hbar = \sum_{k=1,2} \tilde{\omega}_k \hat{a}_k^\dagger \hat{a}_k - \tilde{\omega}_c \hat{c}^\dagger \hat{c} - \frac{\chi_{cc}}{2} \hat{c}^{\dagger 2} \hat{c}^2$ and then performing the second-order RWA under the assumption of $\Delta_{\text{exch}} \gg |g_{\text{exch}}|$. The result of this calculation is given by

$$\frac{\hat{H}_{\text{eff,syndrome}}}{\hbar} = - \sum_{k=1,2} \frac{\chi_{kk}}{2} \hat{a}_k^{\dagger 2} \hat{a}_k^2 - \chi_{1c} \hat{a}_1^\dagger \hat{a}_1 \hat{c}^\dagger \hat{c} + \chi_{2c}^{\text{eff}} \hat{a}_2^\dagger \hat{a}_2 \hat{c}^\dagger \hat{c}, \quad (7.47)$$

where

$$\chi_{2c}^{\text{eff}} = \left[|g_{\text{exch}}|^2 \left(\frac{1}{\Delta_{\text{exch}}} - \frac{1}{\Delta_{\text{exch}} - \chi_{cc}} \right) - \chi_{2c} \right]. \quad (7.48)$$

It is clear that the cross-Kerr term between the second oscillator mode and the ancillary SNAIL mode is modified due the off-resonant $g_{\text{exch}} e^{-i\omega_p, \text{exch}t} \hat{a}_2^\dagger \hat{c} + h.c.$ interaction². Also, similar to other cascaded processes, the cross-Kerr modification is canceled if $\chi_{cc} = 0$, which implies that we require the SNAIL mode to retain some anharmonicity. By selecting parameters such that

$$\chi_{2c}^{\text{eff}} = \chi_{1c} = \chi_\partial \quad (7.49)$$

the effective Hamiltonian becomes

$$\frac{\hat{H}_{\text{eff, syndrome}}}{\hbar} = - \sum_{k=1,2} \frac{\chi_{kk}}{2} \hat{a}_k^{\dagger 2} \hat{a}_k^2 + \chi_\partial \left(\hat{a}_2^\dagger \hat{a}_2 - \hat{a}_1^\dagger \hat{a}_1 \right) \hat{c}^\dagger \hat{c}. \quad (7.50)$$

Therefore, we have managed to engineer the required photon-number difference dependent frequency shift. The inherited self-Kerr (χ_{11}, χ_{22}) by the high- Q oscillator modes are typically small compared to rate of confinement $\kappa_{2\text{ph},12} |\gamma|^4$ and, hence, can be ignored. Similarly, any mismatch between χ_{2c}^{eff} and χ_{1c} can be ignored as long as $|\chi_{2c}^{\text{eff}} - \chi_{1c}| \ll \kappa_{2\text{ph},12} |\gamma|^4$. As a result, in presence of strong $\kappa_{2\text{ph},12}$, we have a fair amount of flexibility while tuning the cross-Kerr between mode 2 and mode c .

At this point, it is worth mentioning that the cross-Kerr engineering technique presented here is not the only one which allows us to achieve our goals. For example, one could also utilize a detuned four-wave mixing interaction of the form $\hat{a}_2 \hat{c}^{\dagger 2} + \hat{a}_2^\dagger \hat{c}^2$ to manipulate cross-Kerr as demonstrated in [Rosenblum *et al.*, 2018]. As this interaction is simply four-wave mixing, it does not require a SNAIL mode to operate. However, at the same time, it is hard to induce large positive cross-Kerr through this technique since the required pump strengths tend to be high. Another technique that could be utilized for engineering the positive cross-Kerr with an oscillator mode is to place the oscillator in the so

²In addition to the cross-Kerr modification shown in Eq. (7.47), there are some higher order Stark shift terms generated by the off-resonant pumps which we have ignored.

called straddling regime [Schuster, 2007] of an ancillary transmon mode. In this regime, the detuning between the bare oscillator mode and the bare transmon mode is less than the anharmonicity of the transmon. The hybridized oscillator and transmon mode then have a positive cross-Kerr between them instead of the negative cross-Kerr that we get in the typical dispersive regime. As a result, placing one of the oscillator mode in straddling regime and another one in the dispersive regime will allow us to build positive cross-Kerr with one mode and negative with the other. Moreover, by tuning the coupling strengths and frequency of the transmon, we should be able to match the strengths of the cross-Kerr interaction. Availability of multiple possible technique for achieving the same goal is reassuring for the experimental implementation of pair-cat code. From hereon, we assume the presence of photon-number different dependent frequency shift on an ancillary mode c .

Next, in order to correct against single-mode photon loss errors, we need to selectively add a single-photon to the first mode if $\partial = 1, 2$, and to the second mode if $\partial = -1, -2$. To make our correction autonomous, this selective photon addition should be performed without explicitly extracting the value of ∂ . We accomplish this by applying additional pumps at the frequencies

$$\begin{aligned}
 \omega_{\text{cor},1} &= \tilde{\omega}_1 + \tilde{\omega}_c + \chi_\partial \\
 \omega_{\text{cor},2} &= \tilde{\omega}_1 + \tilde{\omega}_c + 2\chi_\partial \\
 \omega_{\text{cor},-1} &= \tilde{\omega}_2 + \tilde{\omega}_c - \chi_\partial \\
 \omega_{\text{cor},-2} &= \tilde{\omega}_2 + \tilde{\omega}_c - 2\chi_\partial.
 \end{aligned} \tag{7.51}$$

The first two pumps resonantly address the $\hat{a}_1^\dagger \hat{c}^\dagger + \hat{a}_1 \hat{c}$ process when $\partial = 1, 2$ and the second two pumps resonantly address the $\hat{a}_2^\dagger \hat{c}^\dagger + \hat{a}_2 \hat{c}$ process when $\partial = -1, -2$. The effect of these resonant processes is illustrated in Fig. 7.6d. As shown, they lead to addition of

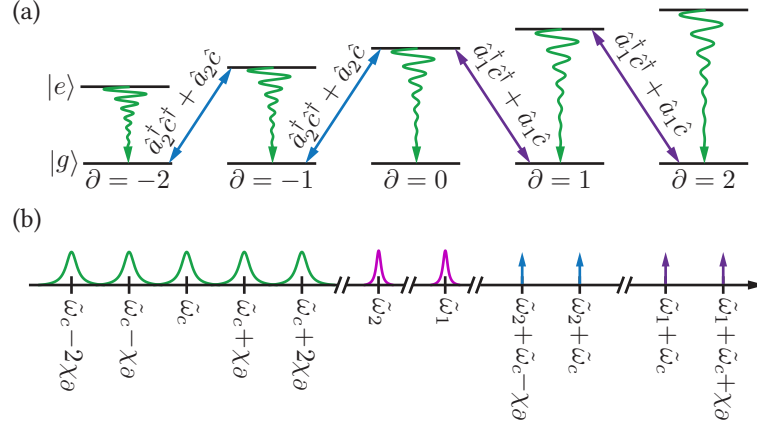


Figure 7.7: (a) Continuous correction against photon loss errors. The level diagram shows the $|g\rangle$ and $|e\rangle$ states of the ancillary mode c for different values of ∂ . The gap between the levels changes due to the $\chi_\partial \hat{\delta} \hat{c}^\dagger \hat{c}$ interaction. In order to correct for the photon loss errors on the oscillator modes, one needs to put a single excitation in the appropriate mode depending on the value of ∂ . Let us consider the scenario when $\partial = 1, 2$ due to photon losses on the first mode. The correction is accomplished by using the resonant two-mode squeezing interactions of the form $\hat{a}_1^\dagger \hat{c}^\dagger + \hat{a}_1 \hat{c}$ between mode 1 and the ancillary mode, induced by applying a pump at $\tilde{\omega}_1 + \tilde{\omega}_c$ and $\tilde{\omega}_1 + \tilde{\omega}_c + \chi_\partial$. These processes take the $|g, \mathcal{P}_{\gamma, \partial=1,2}^{(k \bmod 2)}\rangle$ states to the $|e, \mathcal{P}_{\gamma, \partial=0,1}^{(k-1 \bmod 2)}\rangle$ states by adding an excitation in both the modes. Note that k is changing to $k-1$ which essentially corrects for the extra bit-flip induced by the photon losses on the first mode. A strong dissipation on the ancillary mode then resets that mode to the ground state (wavy green arrows), effectively inducing a dissipation from $|g, \mathcal{P}_{\gamma, \partial=1,2}^{(k \bmod 2)}\rangle$ to $|g, \mathcal{P}_{\gamma, \partial=0,1}^{(k-1 \bmod 2)}\rangle$ as required for autonomous correction. Similarly, for $\partial = -1, -2$ a single excitation is added to the second mode by using resonant beam splitter interactions of the form $\hat{a}_2^\dagger \hat{c}^\dagger + \hat{a}_2 \hat{c}$ induced by pumps at $\tilde{\omega}_2 + \tilde{\omega}_c$ and $\tilde{\omega}_2 + \tilde{\omega}_c - \chi_\partial$. These interactions, combined with the dissipation on the c mode induce continuous correction from $|g, \mathcal{P}_{\gamma, \partial=-1,-2}^{(k \bmod 2)}\rangle$ to $|g, \mathcal{P}_{\gamma, \partial=0,-1}^{(k \bmod 2)}\rangle$ as required. Notice that there is no bit-flip associated with the losses in the second mode and hence k remains unchanged. (b) Frequencies of the transitions and pumps involved in the protocol.

an excitation to the ancillary mode while simultaneously changing ∂ to $\partial - 1$ if $\partial = 1, 2$, and $\partial \rightarrow \partial + 1$ if $\partial = -1, -2$. Therefore one can convert the ∂ dependent frequency shift of the ancillary mode into a correction of the single-mode photon loss errors. However, the story is not finished yet. To begin with, we require the strengths of these processes ($|g_{\text{cor},k}|$) to remain much smaller than χ_∂ for the transitions shown in Fig. 7.6d to remain frequency selective. Moreover, the coherent $\hat{a}_1^\dagger \hat{c}^\dagger + \hat{a}_1 \hat{c}$ and $\hat{a}_2^\dagger \hat{c}^\dagger + \hat{a}_2 \hat{c}$ processes induced

by the pumps will simply lead Rabi oscillations from $\mathcal{C}_\partial \otimes |g\rangle$ and $\mathcal{C}_{\partial\pm 1} \otimes |e\rangle$ spaces, which is not desirable. These oscillations can be eliminated by tuning the amplitudes $g_{\text{cor},k}$ and the time for which the four correction pumps are applied. In addition the ancillary mode needs to be reset after every round of corrections. Combined such pulsed correction and reset will realize a discrete autonomous correction. Engineering continuous autonomous correction, on the other hand, can be accomplished by simply introducing an $e \rightarrow g$ dissipation on the ancillary mode and keeping all four correction pumps on simultaneously. Every time a correction pump becomes resonant, an excitation is added to the appropriate oscillator mode and the ancillary mode. However, for $\Gamma_{eg,c} \gg |g_{\text{cor},k}|$ the SNAIL excitation is quickly dissipated by the strong relaxation of the ancillary mode, resulting in dissipative transfer from $\mathcal{C}_\partial \otimes |g\rangle$ to $\mathcal{C}_{\partial\pm 1} \otimes |g\rangle$. An additional condition for the process to remain ∂ selective, we require $\chi_\partial \gg \Gamma_{eg,c}$ as well. Indeed, it can be formally shown, by adiabatically eliminating the ancillary mode, that the four pumps introduce effective dissipation of the form $\mathcal{D}[\hat{a}_1^\dagger \hat{P}_{\partial=1}]$, $\mathcal{D}[\hat{a}_1^\dagger \hat{P}_{\partial=2}]$, $\mathcal{D}[\hat{a}_2^\dagger \hat{P}_{\partial=-1}]$ and $\mathcal{D}[\hat{a}_2^\dagger \hat{P}_{\partial=-2}]$ when $\chi_\partial \gg \Gamma_{eg,c} \gg |g_{\text{cor},k}|$. We do not go into the details of this derivation.

Finally, let us summarize the time scales involved in realizing the fully autonomous correction for pair cat code. The driven-dissipative process requires $\Delta_{\text{stab}} \gg |g_{\text{stab},k}|$ and $\Gamma_{fg,b} \gg |g_{2\text{ph},12}|$. Similarly, the continuous protection against photon loss errors requires $\Delta_{\text{exch}} \gg |g_{\text{exch}}|$ and $\chi_\partial \gg \Gamma_{eg,c} \gg |g_{\text{cor},k}|$. In order to make sure that both the processes work simultaneously, we also require $\Delta_{\text{stab}} \gg \chi_\partial$ since the frequencies of the high- Q oscillator modes depend on χ_∂ . Furthermore, in order to ensure that the $\hat{a}_k^\dagger \hat{P}_\partial$ do not distort the code-space we need to ensure that $|\gamma|^4 \kappa_{2\text{ph},12} \gg \kappa_{\text{cor}} \gg \kappa_{1\text{ph},k}$. Putting all of these requirements together and assuming $|\gamma| \approx 1$ for the sake of comparison, we have

$$\begin{aligned} \Delta_{\text{stab}}, \Delta_{\text{exch}} &\gg |g_{\text{stab},k}|, |g_{\text{exch}}|, \Gamma_{fg,b} \gg |g_{2\text{ph},12}|, |\chi_\partial| \\ &\gg \Gamma_{eg,c} \gg |g_{\text{cor},k}|, \kappa_{2\text{ph},12} \gg \kappa_{\text{cor}} \gg \kappa_{1\text{ph},k}. \end{aligned} \quad (7.52)$$

Quantity	Symbol	Value
Single-photon dissipation rate for high- Q oscillators	$\kappa_{1\text{ph},1/2}/(2\pi)$	500 Hz
Rate of exchange interaction between mode c and the oscillators	$g_{\text{exch}}/(2\pi)$	2 MHz
Detuning of the exchange interaction	$\Delta_{\text{exch}}/(2\pi)$	10 MHz
Resultant ∂ dependent frequency shift	$\chi_{\partial}/(2\pi)$	≈ 500 kHz
Rate of the correction drives	$g_{\text{cor},k}/(2\pi)$	25 kHz
Rate of reset ($e \rightarrow g$ dissipation) for the ancillary mode c	$\Gamma_{\text{eg},c}/(2\pi)$	100 kHz
Resulting rate of photon-loss correction	$\kappa_{\text{cor}}/(2\pi)$	≈ 5 kHz
Strength of stabilization drives	$g_{2\text{stab},k}/(2\pi)$	2 MHz
Detuning of the stabilization drives	$\Delta_{\text{stab}}/(2\pi)$	10 MHz
Resulting rate of simultaneous two-photon exchange	$g_{2\text{ph}}/(2\pi)$	≈ 500 kHz
Rate of $f \rightarrow g$ dissipation for the stabilization	$g_{2\text{stab},k}/(2\pi)$	2 MHz
Resulting rate of stabilization	$\kappa_{2\text{ph},12}/(2\pi)$	25 kHz

Table 7.1: Here we propose a set of parameters that satisfies the separation of timescales required for implementing pair-cat code based on theoretical considerations. These parameters are well within the range of current cQED technology and hence it is possible to realize fully autonomous quantum error correction. The values quoted of the derived quantities are obtained from the respective formulas. This set of parameters should suppress the dephasing error exponentially as γ increases. Moreover, since κ_{cor} is an order of magnitude greater than rate of photon loss in the modes, we should also suppress photon loss errors by close to an order of magnitude if not beyond.

Table 7.1 presents a plausible set of parameters that satisfy these conditions. Further numerical modeling is required for establishing the fidelity obtained with these parameters. However, an expert would recognize that such parameters can be reasonably obtained using the current cQED technology. Therefore, it should be possible to realize a continuously and autonomously protected pair-cat qubit.

7.3 Summary and prelude to the next chapter

In this chapter we talked about the pair-cat code, a two mode cousin of the cat codes. The important takeaway points from our discussions are as follows:

- (i) Pair-cat code stores information using the superpositions of the pair-coherent states which are defined as the simultaneous eigenstates of the $\hat{a}_1\hat{a}_2$ and the $\hat{\partial} = \hat{a}_2^\dagger\hat{a}_2 - \hat{a}_1^\dagger\hat{a}_1$ operators.
- (ii) The pair-cat states allow for protection against all the single-mode photon loss errors. The error syndrome for monitoring such photon loss is given by the $\hat{\partial}$ operator. As opposed to the four-component cat states, which admit $\hat{\Pi} = e^{i\pi\hat{a}^\dagger\hat{a}}$ operator as the photon loss error syndrome, the pair-cat code offers a massive simplification since $\hat{\partial}$ is simply a bi-linear operator. Moreover, being able to correct for multiple single-mode photon losses is an added benefit for the pair-cat code.
- (iii) In order to protect pair-cat states from dephasing and energy relaxation errors on both the modes, one requires a driven-dissipative process of the form $\mathcal{D}[\hat{a}_1^2\hat{a}_2^2 - \gamma^4]$. This process is similar in the order of nonlinearity to the four-photon driven-dissipative process and offers a similar exponential suppression of the dephasing-like errors as the size of pair-cat state ($|\gamma|$) increases.
- (iv) The driven-dissipative process can be implemented by employing the Raman-assisted cascading of two four-wave mixing processes that we have developed previously in this thesis. The single-mode two-photon dissipation errors inherited from this implementation is not a problem for pair-cat codes since multiple photon losses on single modes are correctable.
- (v) Due to low-order of nonlinearity for the photon loss error syndrome, the photon loss errors can also be corrected in an autonomous and continuous fashion. The

implementation of such continuous correction involves engineering an interaction of the form $\hat{\partial}\hat{c}^\dagger\hat{c}$ with an ancillary mode c . Building such an interaction essentially amounts to engineering cross-Kerr between the ancillary mode and the oscillator modes. We utilize an off-resonant beam splitter interaction to engineer the required cross-Kerr. To convert $\hat{\partial}\hat{c}^\dagger\hat{c}$ interaction into photon loss correction, we need to use frequency selective two-mode squeezing interaction between the appropriate oscillator mode and the ancillary mode, along with a continuous relaxation of the ancillary mode.

- (vi) The driven-dissipative stabilization and continuous correction against the photon loss errors can be combined to engineer a completely autonomous and continuous correction against all the correctable errors of the pair-cat codes.

The complete experimental proposal for engineering an autonomously protected pair-cat qubit presented in this chapter is squarely within the reach of currently available circuit QED technology. We leave such experimental implementation as a future direction.

The next chapter summarizes the conclusion and the immediate future directions for the work presented in this thesis.

Chapter 8

Conclusion and perspective

The goal of this chapter is to provide a conclusion for the work presented in this thesis (Sec. 8.1), and to assemble a ‘to-do’ list for the work that needs to be done in the future (Sec. 8.2). Let us begin our discussion with a summary and conclusion of the thesis.

8.1 Conclusion

In the beginning of this thesis, we set the engineering of hardware efficient, continuous, and autonomous logical qubit as a goal. In Ch. 2 we studied the concepts QEC and surmised that hardware efficient bosonic error correction codes enjoy many advantages over traditional multi-qubit QEC codes, owing to the fewer error channels. In fact, from our discussion about autonomous QEC in the same chapter, it also became clear that having fewer sources errors is better suited for autonomous QEC as well. With this understanding, we studied the Schrödinger’s cat codes in Ch. 3 since it allows one to store information in hardware efficient manner. Here the four-component cat code emerged as the lowest order code that protects against all the error channels affecting a harmonic oscillator to the first order. We studied how the protection against photon loss errors for this code has

been implemented using a measurement based feedback scheme. The protection against the energy relaxation and dephasing errors, on the other hand, is best implemented autonomously by engineering a four-photon driven-dissipative process.

The next three chapters focused on our proposal for engineering such a driven-dissipative process. The Hamiltonian engineering technique, called the Raman-assisted cascading, which allows us to build an eight-wave mixing interaction required for implementing the four-photon driven-dissipative process was introduced in Ch. 4. The next chapter (Ch. 5) focused on experimentally verifying the feasibility of the cascading technique. We accomplished this goal by implementing a cascaded $|g, 4\rangle \rightarrow |f, 0\rangle$ process. Ch. 6 proposed and demonstrated a new superconducting circuit, called the cancellation circuit, which allows four-wave mixing without cross-Kerr. Such cross-Kerr free four wave mixing is essential for the cascaded four-photon exchange process required for implementing the four-photon driven-dissipative process.

The concepts developed in chapters 4 to 6, when put together, are sufficient for engineering the complete stabilization of four-component cat states against dephasing and energy relaxation errors. However, the autonomous protection against photon loss errors for the four-component cat code is still not possible using the current technology. Therefore, in Ch. 7, we changed tactics and attacked the problem of autonomous error correction by simplifying the QEC code itself. We introduced a new kind of hardware efficient QEC code, the pair cat code, which massively simplifies the error correction against photon loss errors by lowering the order of the error syndrome operator. Moreover, the autonomous protection against dephasing and energy relaxation errors is very similar to the four-component cat code and can be implemented with the techniques we developed in the thesis. As a result this code is our answer to engineering fully autonomous protection of a logical qubit.

In conclusion, we have completed the theoretical development for achieving our goal

of engineering a fully autonomous protection of quantum information. We have also experimentally verified two of the Hamiltonian engineering components (cascading and cross-Kerr cancellation) that are necessary for implementing the required driven-dissipative process. The remaining steps for a complete experimental implementation are outlined in the next section as future directions.

8.2 Perspective

Along with a description of what we have accomplished, it is equally important to mention what research needs to be performed in the future. Here we list a few different directions that need detailed exploration:

- (i) Implementation of complete four-photon driven dissipative process using the Raman-assisted cascading and the cancellation circuit.
- (ii) Thorough study of the quality factors of the high- Q harmonic oscillator modes in presence of flux-transformers.
- (iii) Engineering continuous error syndrome measurement for protection of pair-cat code against photon loss errors.
- (iv) Experimental implementation of fully autonomous error correction using the pair-cat code.
- (v) Designing and testing of a universal set of fault-tolerant gates for four-component cat code and the pair-cat code.
- (vi) Autonomous implementation of more elaborate error correction codes that protect against photon-gain errors in addition to the photon-loss and dephasing errors on the high- Q resonators..

The first four goals are the obvious next steps for the work presented in this thesis. The final goal is necessary for processing quantum information using the autonomously protected logical qubits.

Appendix A

Second order RWA in presence of dissipation

In this appendix we illustrate how to perform second order RWA in presence dissipation. The calculations performed here are pertaining to the particular application of four-photon driven-dissipative process developed in Ch. 4. However, the techniques developed here can be carried over to many other applications. For example, the analysis of the fully autonomous error correction against photon-loss errors for the pair cat code, presented in Ch. 7, can also be performed using the technique presented here.

As stated in section 4.3.3, the equation of motion of the transmon-oscillator system is given by

$$\dot{\rho} = -\frac{i}{\hbar} \left[\hat{H}_{\text{sys}}, \rho \right] + \kappa_{1\text{ph}} \mathcal{D}[\hat{a}] \rho + \Gamma_{\downarrow} \mathcal{D}[\hat{b}] \rho + \Gamma_{fg} \mathcal{D}[\hat{\sigma}_{fg}] \rho \quad (\text{A.1})$$

where the system Hamiltonian given by Eq. (4.65) is

$$\begin{aligned} \frac{\hat{H}_{\text{sys}}}{\hbar} = & \tilde{\omega}_a \hat{a}^\dagger \hat{a} + \tilde{\omega}_b \hat{b}^\dagger \hat{b} - \frac{\chi_{aa}}{2} \hat{a}^{\dagger 2} \hat{a}^2 - \frac{\chi_{bb}}{2} \hat{b}^{\dagger 2} \hat{b}^2 - \chi_{ab} \hat{b}^\dagger \hat{a} \hat{b}^\dagger \hat{b} \\ & + \sum_{k=1,2} \left(g_k e^{-i\omega_{pk}t} \hat{a}^{\dagger 2} \hat{b} + g_k^* e^{i\omega_{pk}t} \hat{a}^2 \hat{b}^\dagger \right) + \left(g_3 e^{-2i\omega_{p3}t} \hat{b}^{2\dagger} + g_3^* e^{2i\omega_{p3}t} \hat{b}^2 \right). \quad (\text{A.2}) \end{aligned}$$

In order to perform the RWA in presence of dissipation, we model Γ_\downarrow by extending our system Hamiltonian to

$$\begin{aligned} \frac{H_{\text{tot}}}{\hbar} = & \frac{H_{\text{sys}}}{\hbar} + \sum_k \omega_k \hat{r}^\dagger[\omega_k] \hat{r}[\omega_k] + \sum_k \left(\Omega[\omega_k] \hat{b} \hat{r}^\dagger[\omega_k] + \Omega^*[\omega_k] \hat{b}^\dagger \hat{r}[\omega_k] \right) \\ & + \tilde{\omega}_{r,fg} \hat{r}_{fg}^\dagger \hat{r}_{fg} + \Omega_{p,fg} e^{-i\omega_{p,fg}} \hat{b}^2 \hat{r}_{fg} + \Omega_{p,fg}^* e^{i\omega_{p,fg}} \hat{b}^{*2} \hat{r}_{fg}^\dagger, \end{aligned} \quad (\text{A.3})$$

and changing the master equation to

$$\frac{d}{dt} \rho = -\frac{i}{\hbar} [H_{\text{tot,bath}}, \rho] + \kappa_{1\text{ph}} \mathcal{D}[\hat{a}] \rho + \sum_k \kappa[\omega_k] \mathcal{D}[\hat{r}[\omega_k]] \rho + \kappa_{r,fg} \mathcal{D}[\hat{r}_{fg}] \rho. \quad (\text{A.4})$$

Here $\hat{r}[\omega_k]$ are the destruction operators of low- Q oscillator modes with resonant frequency ω_k and dissipation rates κ_{ω_k} . We assume that the coupling strengths $\Omega[\omega_k] \ll \kappa[\omega_k]$ in our future calculations. Modeling Γ_\downarrow by coupling the system to ancillary oscillators is reminiscent of the Caldeira-Legett model. However, in this case, we have assumed a discrete set of modes instead of a continuum of non-dissipative modes. The justification such discretization comes from the fact that transmon typically dissipates to environment by exchanging photons with other low- Q ‘filter’ modes. We have also modeled the $f \rightarrow g$ direct dissipation explicitly by using a two-photon-exchange coupling between the transmon mode and the low- Q oscillator mode \hat{r} . The frequency $\omega_{p,fg}$ is given by

$$\omega_{p,fg} = 2\tilde{\omega}_b - \chi_{bb} - \tilde{\omega}_{r,fg} \quad (\text{A.5})$$

as we have previously discussed in section 4.3.3. Now, we go into a rotating frame with respect to

$$\frac{\hat{H}_0}{\hbar} = \tilde{\omega}_a \hat{a}^\dagger \hat{a} + \tilde{\omega}_b \hat{b}^\dagger \hat{b} - \frac{\chi_{bb}}{2} \hat{b}^{\dagger 2} \hat{b}^2 + \tilde{\omega}_{r,fg} \hat{r}_{fg}^\dagger \hat{r}_{fg} + \sum_k \omega_k \hat{r}^\dagger[\omega_k] \hat{r}[\omega_k] \quad (\text{A.6})$$

and perform the second order RWA, giving us

$$\begin{aligned}
& \frac{H_{\text{eff,bath}}}{\hbar} \\
& \approx \frac{H_{\text{eff}}}{\hbar} + \left(\Omega_{p,fg} \hat{b}^{2\dagger} \hat{r}_{fg} + h.c. \right) \\
& + \sum_{n=0}^{\infty} \left(\Omega[\tilde{\omega}_b - (n-1)\chi_{bb}] \hat{r}^\dagger[\tilde{\omega}_b - \chi_{bb}] \sqrt{n} \hat{\sigma}_{n,n-1} + h.c. \right) \\
& + \left(g_1^* \Omega[\omega_{+\Delta,0}] \hat{r}^\dagger[\omega_{+\Delta,0}] \hat{a}^2 + h.c. \right) \sum_{n=0}^{\infty} \frac{\chi_{bb} - \Delta}{(n\chi_{bb} + \Delta)((n-1)\chi_{bb} + \Delta)} \hat{\sigma}_{n,n} \\
& + \left(g_2^* \Omega[\omega_{-\Delta,1}] \hat{r}^\dagger[\omega_{-\Delta,1}] \hat{a}^2 + h.c. \right) \sum_{n=0}^{\infty} \frac{2\chi_{bb} + \Delta}{((n-2)\chi_{bb} - \Delta)((n-1)\chi_{bb} - \Delta)} \hat{\sigma}_{n,n} \\
& + \sum_{n=0}^{\infty} \left(\frac{g_1 \chi_{bb} \Omega[\omega_{+\Delta,2n}]}{(n\chi_{bb} + \Delta)((n+1)\chi_{bb} + \Delta)} \hat{r}^\dagger[\omega_{+\Delta,2n}] \hat{a}^{\dagger 2} \sqrt{(n+1)(n+2)} \hat{\sigma}_{n+2,n} + h.c. \right) \\
& + \sum_{n=0}^{\infty} \left(\frac{g_2 \chi_{bb} \Omega[\omega_{-\Delta,2n+1}]}{(n\chi_{bb} - \Delta)((n-1)\chi_{bb} - \Delta)} \hat{r}^\dagger[\omega_{-\Delta,2n+1}] \hat{a}^{\dagger 2} \sqrt{(n+1)(n+2)} \hat{\sigma}_{n+2,n} + h.c. \right).
\end{aligned} \tag{A.7}$$

Here \hat{H}_{eff} is the effective Hamiltonian specified in Eq.(4.73) and n indicates the number states of the junction mode (specifically $n = 0, 1, 2$ correspond to g, e, f levels of the transmon). The frequencies $\omega_{\pm\Delta,n}$ are defined as $\tilde{\omega}_b \pm \Delta - n\chi_{bb}$. Along with the terms presented in Eq.(A.7), we also obtain terms of the form $\hat{\sigma}_{nn} \hat{r}^\dagger[\omega_k] \hat{r}[\omega_k]$ and $\hat{\sigma}_{n+2,n} \hat{r}^\dagger[\omega_k] \hat{r}^\dagger[\omega_m] + h.c.$. The first type of terms corresponds to the dispersive coupling of the junction mode and the bath modes and do not contribute under the assumption of a zero temperature bath. The latter terms become resonant when $\hbar(\omega_k + \omega_m)$ equals the energy difference between the states n and $n+2$ of the junction mode and give rise additional $f \rightarrow g$ dissipation. However, such natural $f \rightarrow g$ dissipation is very small since the coupling strengths $\Omega[\omega_k]$ are typically small. Therefore, we ignore this source of $f \rightarrow g$ dissipation. Next, under the assumption of $\kappa_{r,fg}, \kappa[\omega_k] \gg \|\hat{H}_{\text{eff,bath}}/\hbar\|$ we adiabatically eliminate all the low- Q

oscillator modes to get an effective master equation of the form

$$\begin{aligned}
\frac{d}{dt}\rho = & -\frac{i}{\hbar} [H_{\text{eff}}, \rho] + \Gamma_{fg} \mathcal{D}[\sigma_{fg}] \rho + \kappa_{1\text{ph}} \mathcal{D}[\hat{a}] \rho \\
& + \sum_{n=0}^{\infty} n \Gamma_{\downarrow} [\tilde{\omega}_b - (n-1)\chi_{bb}] \mathcal{D}[\hat{\sigma}_{n,n-1}] \rho \\
& + \sum_{n=0}^{\infty} \left(\frac{|g_1|(\chi_{bb} - \Delta)}{(n\chi_{bb} + \Delta)((n-1)\chi_{bb} + \Delta)} \right)^2 \Gamma_{\downarrow} [\omega_{+\Delta,0}] \mathcal{D}[\hat{a}^2 \hat{\sigma}_{n,n}] \rho \\
& + \sum_{n=0}^{\infty} \left(\frac{|g_2|(2\chi_{bb} + \Delta)}{((n-2)\chi_{bb} - \Delta)((n-1)\chi_{bb} - \Delta)} \right)^2 \Gamma_{\downarrow} [\omega_{-\Delta,1}] \mathcal{D}[\hat{a}^2 \hat{\sigma}_{n,n}] \rho \\
& + \sum_{n=0}^{\infty} \left(\frac{\sqrt{(n+1)(n+2)} |g_1| \chi_{bb}}{(n\chi_{bb} + \Delta)((n+1)\chi_{bb} + \Delta)} \right)^2 \Gamma_{\downarrow} [\omega_{+\Delta,2n}] \mathcal{D}[\hat{a}^{\dagger 2} \hat{\sigma}_{n+2,n}] \rho \\
& + \sum_{n=0}^{\infty} \left(\frac{\sqrt{(n+1)(n+2)} |g_2| \chi_{bb}}{(n\chi_{bb} - \Delta)((n-1)\chi_{bb} - \Delta)} \right)^2 \Gamma_{\downarrow} [\omega_{-\Delta,2n+1}] \mathcal{D}[\hat{a}^{\dagger 2} \hat{\sigma}_{n+2,n}] \rho. \quad (\text{A.8})
\end{aligned}$$

Here

$$\begin{aligned}
\Gamma_{fg} &= \frac{4|\Omega_{fg}|^2}{\kappa_{r,fg}} \\
\Gamma_{\downarrow}[\omega] &= \frac{2|\Omega[\omega]|^2}{\kappa[\omega]}. \quad (\text{A.9})
\end{aligned}$$

Note that under the assumption of white noise

$$\sum_{n=0}^{\infty} n \Gamma_{\downarrow} [\tilde{\omega}_b - (n-1)\chi_{bb}] \mathcal{D}[\hat{\sigma}_{n,n-1}] = \Gamma_{\downarrow} \mathcal{D}[\hat{b}] \quad (\text{A.10})$$

which is the amplitude damping of the transmon mode. Limiting ourselves to only the e, f states of the transmon, the effective master equation becomes

$$\begin{aligned}
\dot{\rho} = & -\frac{i}{\hbar} [H_{\text{eff}}, \rho] + \kappa_{1\text{ph}} \mathcal{D}[\hat{a}] \rho + (\Gamma_{\downarrow} [\tilde{\omega}_b] \mathcal{D}[\hat{\sigma}_{eg}] + 2\Gamma_{\downarrow} [\tilde{\omega}_b - \chi_{bb}] \mathcal{D}[\hat{\sigma}_{fe}]) \rho + \Gamma_{fg} \mathcal{D}[\hat{\sigma}_{fg}] \rho \\
& + (\kappa_{2,gg} \mathcal{D}[\hat{a}^2 \hat{\sigma}_{gg}] + \kappa_{2,ee} \mathcal{D}[\hat{a}^2 \hat{\sigma}_{ee}] + \kappa_{2,ff} \mathcal{D}[\hat{a}^2 \hat{\sigma}_{ff}]) \rho + \kappa_{2,fg} \mathcal{D}[\hat{a}^{\dagger 2} \hat{\sigma}_{fg}] \rho. \quad (\text{A.11})
\end{aligned}$$

The expressions for various dissipation rates can be inferred from Eq. A.8. The adiabatic elimination of the transmon, under the assumption of $\Gamma_{fg} + 2\Gamma_{\downarrow}[\tilde{\omega}_b - \chi_{bb}] \gg \|\hat{H}_{\text{eff}}/\hbar\omega$, then leads to the effective master equation of the oscillator mode, quoted in Eq. (4.79). The validity of this adiabatic elimination is checked in the next appendix.

Appendix B

Validity of adiabatic elimination

This appendix is devoted to checking the validity of the adiabatic elimination of the transmon mode through numerical simulations. As we mentioned in the last sub-section, for the adiabatic approximation to be valid, we require $\Gamma_{fg} + 2\Gamma_{\downarrow} \gg \left\| \frac{\hat{H}_{\text{eff}}}{\hbar} \right\|$ where \hat{H}_{eff} is given by Eq. 4.73. In order to check the validity of this approximation we compare the full dynamics given by Eq. (A.11) and the effective dynamics given by Eq. (4.79) for different values of Γ_{fg} in Fig. B.1a. The black curves have $\Gamma_{fg}/2\pi = 0.6$ MHz and the magenta curves have $\Gamma_{fg}/2\pi = 6$ MHz. The other parameters are kept the same as those utilized in Sec. 4.3.3 with the resulting $g_{4\text{ph}}/2\pi = 41$ kHz and $|\alpha|^2 = 4$. The amplitude damping of the oscillator is ignored and that of the transmon is set to $\Gamma_{\downarrow} = 3$ kHz. For the considered amplitude $|\alpha|^2 = 4$, the choice of $\Gamma_{fg}/2\pi = 6$ MHz satisfies the above separation of time-scales, leading to a good agreement between the dashed and solid magenta lines. The choice of $\Gamma_{fg}/2\pi = 0.6$ MHz leads to a disagreement with the effective dynamics. Note that the full dynamics still converges towards the expected state albeit at a slower rate. To choose the optimum working point, we perform simulations of the full dynamics (Eq. 4.78), while sweeping $\Gamma_{fg}/2\pi$ from 0.1 MHz to 10 MHz. In Fig.B.1b we plot the overlap with the $|\mathcal{C}_{\alpha=2}^{(4\text{mod}0)}\rangle$ cat state as a function of time and Γ_{fg}^{eng} . From this, we extract

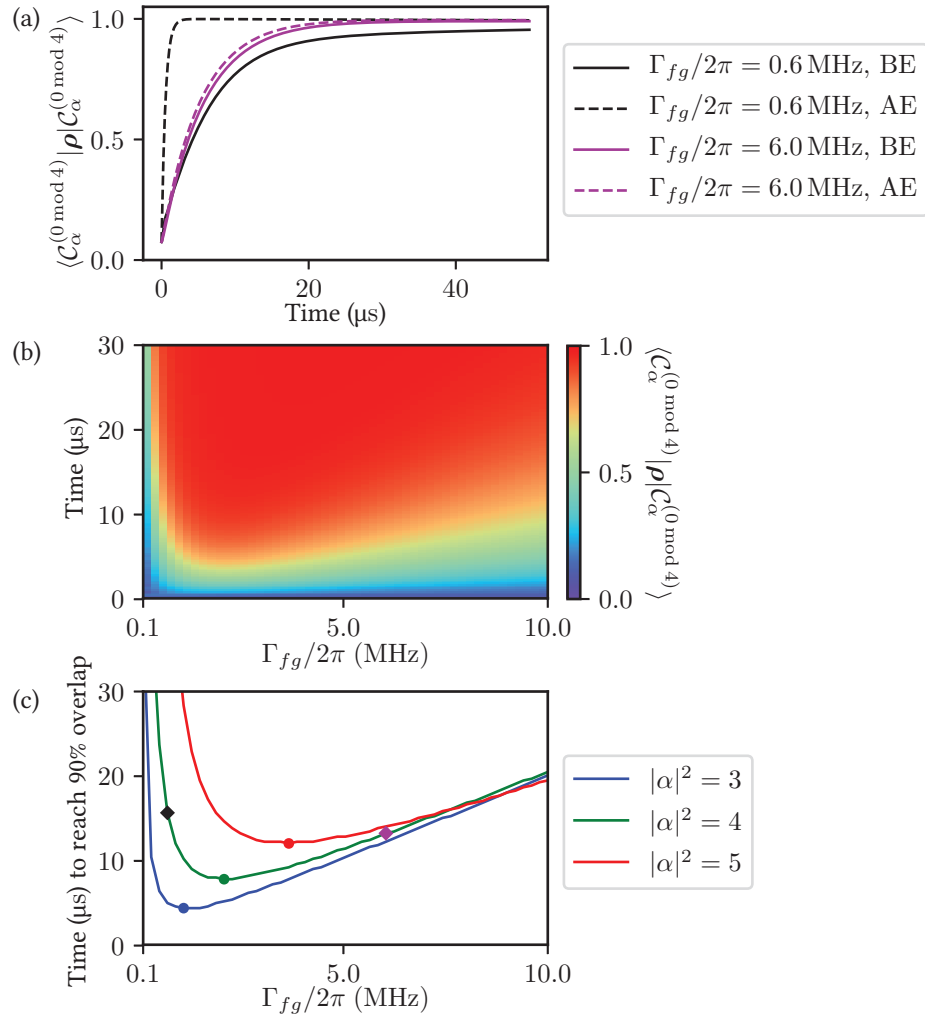


Figure B.1: (a) The system dynamics before (Eq. (A.11)) and after (Eq. (4.79)) the adiabatic elimination, denoted respectively by (BE) and (AE). We use the same parameters as in Fig. 4.8 together with $\Gamma_{fg}/2\pi = 0.6$ MHz (black) and $\Gamma_{fg}/2\pi = 6$ MHz (magenta). The system is initialized in the ground state and the overlap $\langle \mathcal{C}_{\alpha=2}^{(0 \bmod 4)} | \rho | \mathcal{C}_{\alpha=2}^{(0 \bmod 4)} \rangle$ is plotted as function of time. (b) The overlap as a function of time, obtained by simulating (A.11) with $\Gamma_{fg}/2\pi$ ranging from 0.1 MHz to 10 MHz. (c) The time taken to achieve 90% fidelity as a function of Γ_{fg} for $|\alpha|^2 = 3, 4$ and 5. Black and magenta squares indicate the choices $\Gamma_{fg}/2\pi = 0.6$ MHz and $\Gamma_{fg}/2\pi = 6$ MHz, corresponding to the simulations of (a). The dots correspond to the optimum working points for various cat amplitudes.

the time taken to achieve 90% fidelity as a function of Γ_{fg} . This corresponds to the green curve in Fig.B.1c. As illustrated by the green dot, the optimum working point is given by

$\Gamma_{fg}^{\text{eng}}/2\pi = 2$ MHz. Note that the working point of $\Gamma_{fg} = 4$ MHz used in Fig. 4.8 is selected to be well in the region of adiabatic validity while still getting a strong four-photon dissipation ($\kappa_{4\text{ph}}$). The same simulations for $|\alpha|^2 = 3$ and 5 give rise to different working points at 1 MHz and 3.7 MHz respectively. Indeed, the norm $\|\hat{H}_{\text{eff}}\|$, in the assumption $\Gamma_{fg} + 2\Gamma_{\downarrow} \gg \left\| \frac{\hat{H}_{\text{eff}}}{\hbar} \right\|$, corresponds to the norm of the Hamiltonian when confined to the code space $\text{Span}\{|\pm\alpha\rangle, |\pm i\alpha\rangle\}$. This implies a separation of time-scales which depends on the amplitude $|\alpha|$ of the cat state, therefore leading to different optimum working points.

Bibliography

- V. V. Albert, S. O. Mundhada, A. Grimm, S. Touzard, M. H. Devoret, and L. Jiang (2019), “Pair-cat codes: Autonomous error-correction with low-order nonlinearity,” *Quantum Science and Technology* **4** (3), 035007.
- F. Arute, K. Arya, R. Babbush, D. Bacon, J. C. Bardin, R. Barends, R. Biswas, S. Boixo, F. G. S. L. Brandao, D. A. Buell, B. Burkett, Y. Chen, Z. Chen, B. Chiaro, R. Collins, W. Courtney, A. Dunsworth, E. Farhi, B. Foxen, A. Fowler, C. Gidney, M. Giustina, R. Graff, K. Guerin, S. Habegger, M. P. Harrigan, M. J. Hartmann, A. Ho, M. Hoffmann, T. Huang, T. S. Humble, S. V. Isakov, E. Jeffrey, Z. Jiang, D. Kafri, K. Kechedzhi, J. Kelly, P. V. Klimov, S. Knysh, A. Korotkov, F. Kostritsa, D. Landhuis, M. Lindmark, E. Lucero, D. Lyakh, S. Mandrà, J. R. McClean, M. McEwen, A. Megrant, X. Mi, K. Michielsen, M. Mohseni, J. Mutus, O. Naaman, M. Neeley, C. Neill, M. Y. Niu, E. Ostby, A. Petukhov, J. C. Platt, C. Quintana, E. G. Rieffel, P. Roushan, N. C. Rubin, D. Sank, K. J. Satzinger, V. Smelyanskiy, K. J. Sung, M. D. Trevithick, A. Vainsencher, B. Villalonga, T. White, Z. J. Yao, P. Yeh, A. Zalcman, H. Neven, and J. M. Martinis (2019), “Quantum supremacy using a programmable superconducting processor,” *Nature* **574** (7779), 505–510.
- C. J. Axline, L. D. Burkhardt, W. Pfaff, M. Zhang, K. Chou, P. Campagne-Ibarcq, P. Reinhold, L. Frunzio, S. M. Girvin, L. Jiang, M. H. Devoret, and R. J. Schoelkopf (2018), “On-demand quantum state transfer and entanglement between remote microwave cavity memories,” *Nature Physics* **14** (7), 705–710.
- R. Barends, C. M. Quintana, A. G. Petukhov, Y. Chen, D. Kafri, K. Kechedzhi, R. Collins, O. Naaman, S. Boixo, F. Arute, K. Arya, D. Buell, B. Burkett, Z. Chen, B. Chiaro, A. Dunsworth, B. Foxen, A. Fowler, C. Gidney, M. Giustina, R. Graff, T. Huang, E. Jeffrey, J. Kelly, P. V. Klimov, F. Kostritsa, D. Landhuis, E. Lucero, M. McEwen, A. Megrant, X. Mi, J. Mutus, M. Neeley, C. Neill, E. Ostby, P. Roushan, D. Sank, K. J. Satzinger, A. Vainsencher, T. White, J. Yao, P. Yeh, A. Zalcman, H. Neven, V. N. Smelyanskiy, and J. M. Martinis (2019), “Diabatic Gates for Frequency-Tunable Superconducting Qubits,” *Physical Review Letters* **123**, 210501.
- A. O. Barut, and L. Girardello (1971), “New “coherent” states associated with non-compact groups,” *Communications in Mathematical Physics* **21** (1), 41–55.

- M. Boissonneault, J. M. Gambetta, and A. Blais (2009), “Dispersive regime of circuit qed: Photon-dependent qubit dephasing and relaxation rates,” *Physical Review A* **79**, 013819.
- P. Brooks, A. Kitaev, and J. Preskill (2013), “Protected gates for superconducting qubits,” *Physical Review A* **87**, 052306.
- P. Campagne-Ibarcq, A. Eickbusch, S. Touzard, E. Zalys-Geller, N. E. Frattini, V. V. Sivak, P. Reinhold, S. Puri, S. Shankar, R. J. Schoelkopf, L. Frunzio, M. Mirrahimi, and M. H. Devoret (2019), “A stabilized logical quantum bit encoded in grid states of a superconducting cavity,” arXiv preprint arXiv:1907.12487 .
- A. A. Clerk, M. H. Devoret, S. M. Girvin, F. Marquardt, and R. J. Schoelkopf (2010), “Introduction to quantum noise, measurement, and amplification,” *Review of Modern Physics* **82**, 1155–1208.
- J. Cohen, and M. Mirrahimi (2014), “Dissipation-induced continuous quantum error correction for superconducting circuits,” *Physical Review A* **90**, 062344.
- J. Cohen, W. C. Smith, M. H. Devoret, and M. Mirrahimi (2017), “Degeneracy-preserving quantum nondemolition measurement of parity-type observables for cat qubits,” *Physical Review Letters* **119**, 060503.
- N. Earnest, S. Chakram, Y. Lu, N. Irons, R. K. Naik, N. Leung, L. Ocola, D. A. Czaplewski, B. Baker, Jay Lawrence, Jens Koch, and D. I. Schuster (2018), “Realization of a Λ system with metastable states of a capacitively shunted fluxonium,” *Physical Review Letters* **120**, 150504.
- C. Flühmann, T. L. Nguyen, M. Marinelli, V. Negnevitsky, K. Mehta, and J. P. Home (2019), “Encoding a Qubit In a Trapped-Ion Mechanical Oscillator,” *Nature* **566** (7745), 513.
- E. Flurin (2014), *The Josephson mixer : a swiss army knife for microwave quantum optics*, Theses (Ecole normale supérieure - ENS PARIS).
- A. G. Fowler, M. Mariantoni, J. M. Martinis, and A. N. Cleland (2012), “Surface codes: Towards practical large-scale quantum computation,” *Physical Review A* **86**, 032324.
- N. E. Frattini, V. V. Sivak, A. Lingenfelter, S. Shankar, and M. H. Devoret (2018), “Optimizing the nonlinearity and dissipation of a snail parametric amplifier for dynamic range,” *Physical Review Applied* **10**, 054020.
- N. E. Frattini, U. Vool, S. Shankar, A. Narla, K. M. Sliwa, and M. H. Devoret (2017), “3-wave mixing josephson dipole element,” *Applied Physics Letters* **110** (22), 222603.
- C. Gardiner, and P. Zoller (2015), *The quantum world of ultra-cold atoms and light. Book II*, edited by C. Salomon (Imperial College Press).

- C.W. Gardiner, and M.J. Collett (1985), “Input and output in damped quantum systems: Quantum stochastic differential equations and the master equation,” *Physical Review A* **31**, 3761–3774.
- O. Gargiulo, S. Oleschko, J. Prat-Camps, M. Zanner, and G. Kirchmair (2018), “Fast flux control of 3d transmon qubits using a magnetic hose,” arXiv preprint arXiv:1811.10875 .
- D. Gottesman, A. Kitaev, and J. Preskill (2001), “Encoding a qubit in an oscillator,” *Physical Review A* **64**, 012310.
- A. Grimm, N. E. Frattini, S. Puri, S. O. Mundhada, S. Touzard, M. Mirrahimi, S. M. Girvin, S. Shankar, and M. H. Devoret (2019), “The kerr-cat qubit: Stabilization, readout, and gates,” arXiv preprint arXiv:1907.12131 .
- J. Guillaud, and M. Mirrahimi (2019), “Repetition cat-qubits: fault-tolerant quantum computation with highly reduced overhead,” arXiv preprint arXiv:1904.09474 .
- A. Gyenis, P. S. Mundada, A. Di Paolo, T. M. Hazard, X. You, D. I. Schuster, J. Koch, A. Blais, and A. A. Houck (2019), “Experimental realization of an intrinsically error-protected superconducting qubit,” arXiv preprint arXiv:1910.07542 .
- S. Haroche, and J. Raimond (2006), *Exploring the Quantum: Atoms, Cavities, and Photons* (Oxford University Press).
- S. S. Hong, A. T. Papageorge, P. Sivarajah, G. Crossman, N. Dider, A. M. Polloreno, E. A. Sete, S. W. Turkowski, M. P. da Silva, and B. R. Johnson (2019), “Demonstration of a parametrically-activated entangling gate protected from flux noise,” arXiv preprint arXiv:1901.08035 .
- A. Kandala, A. Mezzacapo, K. Temme, M. Takita, M. Brink, J. M. Chow, and J. M. Gambetta (2017), “Hardware-efficient variational quantum eigensolver for small molecules and quantum magnets,” *Nature* **549**, 242.
- A. Y. Kitaev (2003), “Fault-tolerant quantum computation by anyons,” *Annals of Physics* **303** (1), 2 – 30.
- J. Koch, T. M. Yu, J. Gambetta, A. A. Houck, D. I. Schuster, J. Majer, A. Blais, M. H. Devoret, S. M. Girvin, and R. J. Schoelkopf (2007), “Charge-insensitive qubit design derived from the cooper pair box,” *Physical Review A* **76**, 042319.
- P. Krantz, M. Kjaergaard, F. Yan, T. P. Orlando, S. Gustavsson, and W. D. Oliver (2019), “A quantum engineer’s guide to superconducting qubits,” *Applied Physics Reviews* **6** (2), 021318.

- F. Lecocq, I. M. Pop, Z. Peng, I. Matei, T. Crozes, T. Fournier, C. Naud, W. Guichard, and O. Buisson (2011), “Junction fabrication by shadow evaporation without a suspended bridge,” *Nanotechnology* **22** (31), 315302.
- Z. Leghtas, G. Kirchmair, B. Vlastakis, M. H. Devoret, R. J. Schoelkopf, and M. Mirrahimi (2013a), “Deterministic protocol for mapping a qubit to coherent state superpositions in a cavity,” *Physical Review A* **87**, 042315.
- Z. Leghtas, G. Kirchmair, B. Vlastakis, R. J. Schoelkopf, M. H. Devoret, and M. Mirrahimi (2013b), “Hardware-efficient autonomous quantum memory protection,” *Physical Review Letters* **111**, 120501.
- Z. Leghtas, S. Touzard, I. M. Pop, A. Kou, B. Vlastakis, A. Petrenko, K. M. Sliwa, A. Narla, S. Shankar, M. J. Hatridge, M. Reagor, L. Frunzio, R. J. Schoelkopf, M. Mirrahimi, and M. H. Devoret (2015), “Confining the state of light to a quantum manifold by engineered two-photon loss,” *Science* **347** (6224), 853–857.
- R. Lescanne, L. Verney, Q. Ficheux, M. H. Devoret, B. Huard, M. Mirrahimi, and Z. Leghtas (2019a), “Escape of a driven quantum josephson circuit into unconfined states,” *Physical Review Applied* **11**, 014030.
- R. Lescanne, M. Villiers, T. Peronin, A. Sarlette, M. Delbecq, B. Huard, T. Kontos, M. Mirrahimi, and Z. Leghtas (2019b), “Exponential suppression of bit-flips in a qubit encoded in an oscillator,” arXiv:1907.11729 [quant-ph] .
- J. Lihm, K. Noh, and U. R. Fischer (2018), “Implementation-independent sufficient condition of the knill-laflamme type for the autonomous protection of logical qudits by strong engineered dissipation,” *Physical Review A* **98**, 012317.
- V. E. Manucharyan, J. Koch, L. I. Glazman, and M. H. Devoret (2009), “Fluxonium: Single cooper-pair circuit free of charge offsets,” *Science* **326** (5949), 113–116, <https://science.sciencemag.org/content/326/5949/113.full.pdf> .
- M. H. Michael, M. Silveri, R. T. Brierley, V. V. Albert, J. Salmilehto, L. Jiang, and S. M. Girvin (2016), “New class of quantum error-correcting codes for a bosonic mode,” *Physical Review X* **6**, 031006.
- M. Mirrahimi, Z. Leghtas, V. V. Albert, S. T., R. J. Schoelkopf, L. Jiang, and M. H. Devoret (2014), “Dynamically protected cat-qubits: a new paradigm for universal quantum computation,” *New Journal of Physics* **16** (4), 045014.
- M. Mirrahimi, and P. Rouchon (2015), “Modeling and control of quantum systems,” <Http://cas.ensmp.fr/rouchon/QuantumSyst/index.html>.
- F. Motzoi, J. M. Gambetta, P. Rebentrost, and F. K. Wilhelm (2009), “Simple pulses for elimination of leakage in weakly nonlinear qubits,” *Physical Review Letters* **103**, 110501.

- S. O. Mundhada, A. Grimm, S. Touzard, U. Vool, S. Shankar, M. H. Devoret, and M. Mirrahimi (2017), “Generating higher-order quantum dissipation from lower-order parametric processes,” *Quantum Science and Technology* **2** (2), 024005.
- Y. Nam, J. Chen, N. C. Pimenti, K. Wright, C. Delaney, D. Maslov, K. R. Brown, S. Allen, J. M. Amini, J. Apisdorf, K. M. Beck, A. Blinov, V. Chaplin, M. Chmielewski, C. Collins, S. Deb Nath, A. M. Ducore, K. M. Hudek, M. Keesan, S. M. Kreikemeier, J. Mizrahi, P. Solomon, M. Williams, J. D. Wong-Campos, C. Monroe, and J. Kim (2019), “Ground-state energy estimation of the water molecule on a trapped ion quantum computer,” arXiv:1902.10171 [quant-ph].
- A. Narla (2017), *Flying Qubit Operations in Superconducting Circuits*, Ph.D. thesis (Yale University).
- A. Narla, S. Shankar, M. Hatridge, Z. Leghtas, K. M. Sliwa, E. Zolys-Geller, S. O. Mundhada, W. Pfaff, L. Frunzio, R. J. Schoelkopf, and M. H. Devoret (2016), “Robust concurrent remote entanglement between two superconducting qubits,” *Physical Review X* **6**, 031036.
- C. Navau, J. Prat-Camps, O. Romero-Isart, J. I. Cirac, and A. Sanchez (2014), “Long-distance transfer and routing of static magnetic fields,” *Physical Review Letters* **112**, 253901.
- M. A. Nielsen, and I. L. Chuang (2011), *Quantum Computation and Quantum Information: 10th Anniversary Edition*, 10th ed. (Cambridge University Press, New York, NY, USA).
- S. E. Nigg, H. Paik, B. Vlastakis, G. Kirchmair, S. Shankar, L. Frunzio, M. H. Devoret, R. J. Schoelkopf, and S. M. Girvin (2012), “Black-box superconducting circuit quantization,” *Physical Review Letters* **108**, 240502.
- N. Ofek, A. Petrenko, R. Heeres, P. Reinhold, Z. Leghtas, B. Vlastakis, Y. Liu, L. Frunzio, S. M. Girvin, L. Jiang, M. Mirrahimi, M. H. Devoret, and R. J. Schoelkopf (2016), “Extending the lifetime of a quantum bit with error correction in superconducting circuits,” *Nature* **536** (7617), 441–445.
- T.P. Orlando, J.E. Mooij, L. Tian, C.H. van der Wal, L.S. Levitov, S. Lloyd, and J. J. Mazo (1999), “Superconducting persistent-current qubit,” *Phys. Rev. B* **60**, 15398–15413.
- H. Paik, D. I. Schuster, L. S. Bishop, G. Kirchmair, G. Catelani, A. P. Sears, B. R. Johnson, M. J. Reagor, L. Frunzio, L. I. Glazman, S. M. Girvin, M. H. Devoret, and R. J. Schoelkopf (2011), “Observation of high coherence in josephson junction qubits measured in a three-dimensional circuit qed architecture,” *Physical Review Letters* **107**, 240501.
- A. A. Petrenko (2016), *Enhancing the lifetime of quantum information with cat states in superconducting cavities*, Ph.D. thesis (Yale University).

- J. Preskill (2012), “Quantum computing and the entanglement frontier,” arXiv preprint arXiv:1203.5813 .
- J. Preskill (2018), “Quantum computing in the nisq era and beyond,” *Quantum* **2**, 79.
- S. Puri, S. Boutin, and A. Blais (2017), “Engineering the quantum states of light in a Kerr-nonlinear resonator by two-photon driving,” *NPJ Quantum Information* **3** (1), 18.
- S. Puri, L. St-Jean, J. A. Gross, A. Grimm, N. E. Frattini, P. S. Iyer, A. Krishna, S. Touzard, L. Jiang, A. Blais, S. T. Flammia, and S. M. Girvin (2019), “Bias-preserving gates with stabilized cat qubits,” arXiv preprint arXiv:1905.00450 .
- M. Reagor, H. Paik, G. Catelani, L. Sun, C. Axline, E. Holland, I. M. Pop, N. A. Masluk, T. Brecht, L. Frunzio, M. H. Devoret, L. Glazman, and R. J. Schoelkopf (2013), “Reaching 10 ms single photon lifetimes for superconducting aluminum cavities,” *Applied Physics Letters* **102** (19), 192604.
- M. Reed (2013), *Entanglement and Quantum Error Correction with Superconducting Qubits*, Ph.D. thesis (Yale University).
- S. Rosenblum, P. Reinhold, M. Mirrahimi, Liang Jiang, L. Frunzio, and R. J. Schoelkopf (2018), “Fault-tolerant detection of a quantum error,” *Science* **361** (6399), 266–270.
- J. J. Sakurai, and J. Napolitano (2017), *Modern Quantum Mechanics*, 2nd ed. (Cambridge University Press).
- D. Sank, Z. Chen, M. Khezri, J. Kelly, R. Barends, B. Campbell, Y. Chen, B. Chiaro, A. Dunsworth, A. Fowler, E. Jeffrey, E. Lucero, A. Megrant, J. Mutus, M. Neeley, C. Neill, P. J. J. O’Malley, C. Quintana, P. Roushan, A. Vainsencher, T. White, J. Wenner, Alexander N. Korotkov, and J. M. Martinis (2016), “Measurement-induced state transitions in a superconducting qubit: Beyond the rotating wave approximation,” *Physical Review Letters* **117**, 190503.
- J. A. Schreier, A. A. Houck, Jens Koch, D. I. Schuster, B. R. Johnson, J. M. Chow, J. M. Gambetta, J. Majer, L. Frunzio, M. H. Devoret, S. M. Girvin, and R. J. Schoelkopf (2008), “Suppressing charge noise decoherence in superconducting charge qubits,” *Physical Review B* **77**, 180502.
- D. I. Schuster (2007), *Circuit Quantum Electrodynamics*, Ph.D. thesis (Yale University).
- V. V. Sivak, N. E. Frattini, V. R. Joshi, A. Lingenfelter, S. Shankar, and M. H. Devoret (2019), “Kerr-free three-wave mixing in superconducting quantum circuits,” *Physical Review Applied* **11**, 054060.

- S. Touzard, A. Grimm, Z. Leghtas, S. O. Mundhada, P. Reinhold, C. Axline, M. Reagor, K. Chou, J. Blumoff, K. M. Sliwa, S. Shankar, L. Frunzio, R. J. Schoelkopf, M. Mirrahimi, and M. H. Devoret (2018), “Coherent oscillations inside a quantum manifold stabilized by dissipation,” *Physical Review X* **8**, 021005.
- L. Verney, R. Lescanne, M. H. Devoret, Z. Leghtas, and M. Mirrahimi (2019), “Structural instability of driven josephson circuits prevented by an inductive shunt,” *Physical Review Applied* **11**, 024003.
- U. Vool (2017), *Engineering Synthetic Quantum Operations*, Ph.D. thesis (Yale University).
- C. Wang, Y. Y. Gao, P. Reinhold, R. W. Heeres, N. Ofek, K. Chou, C. Axline, M. Reagor, J. Blumoff, K. M. Sliwa, L. Frunzio, S. M. Girvin, L. Jiang, M. Mirrahimi, M. H. Devoret, and R. J. Schoelkopf (2016), “A schrödinger cat living in two boxes,” *Science* **352** (6289), 1087–1091.
- C. S. Wang, J. C. Curtis, B. J. Lester, Y. Zhang, Y. Y. Gao, J. Freeze, V. S. Batista, P. H. Vaccaro, I. L. Chuang, L. Frunzio, L. Jiang, S. M. Girvin, and R. J. Schoelkopf (2019), “Quantum simulation of molecular vibronic spectra on a superconducting bosonic processor,” arXiv:1908.03598 [quant-ph] .
- H.M. Wiseman, and G.J. Milburn (1993), “Quantum theory of field-quadrature measurements,” *Physical Review A* **47**, 642–662.
- H.M. Wiseman, and G.J. Milburn (1994), “Squeezing via feedback,” *Physical Review A* **49**, 1350–1366.
- J. Q. You, X. Hu, S. Ashhab, and F. Nori (2007), “Low-decoherence flux qubit,” *Physical Review B* **75**, 140515.
- B. Yurke, and D. Stoler (1986), “Generating quantum mechanical superpositions of macroscopically distinguishable states via amplitude dispersion,” *Physical Review Letters* **57**, 13–16.